4D PRINTING OF Ni-Mn-Ga MAGNETIC SHAPE MEMORY ALLOY THROUGH LASER POWDER BED FUSION

by

Anastassia Milleret

A thesis submitted to the
University of Birmingham
in partial fulfilment of the
requirements for the degree of
DOCTOR OF PHILOSOPHY

School of Metallurgy and Materials
College of Engineering and Physical Sciences
University of Birmingham

September 2023

Abstract

Ni-Mn-Ga magnetic shape memory (MSM) alloys represent a remarkable class of smart materials capable of undergoing reversible magnetic-field-induced strains (MFIS) of up to 10%. This unique property, characterised by rapid shape changes occurring within milliseconds, positions Ni-Mn-Ga alloys as promising candidates for a wide range of applications, including ultrafast actuators, sensors, micropumps, and energy harvesters. However, the substantial MFIS is predominantly observed in single crystals, primarily because grain boundaries act as barriers against twin boundary motion in polycrystalline materials. To overcome this limitation, research on reducing the impact of grain boundaries by creating porous and highly textured structures has been explored. The largest MFIS in polycrystals, up to 8.7% has been achieved in foam-like samples featuring 'bamboo-like grains'—where grains are stacked on top of each other, spanning the diameter of the struts. These foam-like structures possess random porosity. Another promising approach is the manufacture of structures with 'engineered porosity', such as lattice structures. In these lattices, each strut is composed of a single large grain connected by nodes. This level of design freedom is achievable through additive manufacturing techniques, notably laser powder bed fusion (L-PBF).

This study focuses on the 4D printing (3D printing of smart materials) of Ni-Mn-Ga lattices using L-PBF. Initially, an attempt was made using an in-situ alloying powder blend, in order to gain compositional freedom, but this approach yielded inconclusive results due to segregations in the final part, which would negate the shape memory effect. Subsequently, an optimisation of process parameters was conducted using gas atomised powder for both bulk and lattice samples, with considerations made for Mn evaporation, density, and geometrical integrity. These samples exhibited a 14M crystal structure, not favourable for large MFIS. Following heat treatment, lattices featuring fully dense 200 μm diameter struts with a bamboo-like grain structure were successfully produced.

Further investigations focused on methods to enhance the crystallographic texture and control microstructure to increase the MFIS. These methods encompassed printing on a heated platform, using a double scanning strategy, and varying strut orientation according to the build direction. The study determined that the platform temperature and the double scanning strategy minimally impacted the microstructure and the magnetic behaviour, while the strut orientation had a substantial influence on the crystallographic texture and a small influence on the magnetic behaviour.

Additionally, the research explored the mechanical properties of Ni-Mn-Ga bulk and lattice samples fabricated through L-PBF, particularly in compression loading, with the intention of paving the way for future application prospects. Nanoindentation was used to determine the elastic moduli of both heat-treated and as-built lattices. The findings revealed that the samples exhibited brittle behaviour, with heat treatment increasing ductility but reducing strength. Notably, lattice samples fractured along a 45º diagonal and displayed significantly lower strength.

Lastly, this study underscores the potential of L-PBF in fabricating Ni-Mn-Ga lattices by demonstrating an MFIS of up to 6.6% in a lattice sample with a 10M crystal structure. These findings open up exciting possibilities for the application of functional Ni-Mn-Ga lattices in various fields.

Acknowledgments

I would like to acknowledge the financial support provided by the Defence Science and Technology Laboratory (DSTL) for my PhD Studentship through the UK-French PhD studentship scheme, which made this research endeavour possible. I extend my heartfelt thanks to my technical partners, Sarah Baker and Rebecca Mangham, for their unwavering support and mentorship throughout my academic journey.

My profound gratitude goes to my supervisors, Moataz Attallah, Nouredine Fenineche, and Richard Sheridan, for the opportunities they provided, their guidance, and support throughout the entirety of my thesis journey.

I am grateful to my collaborators who significantly contributed to this work. Special recognition goes to Ville Laitinen, whose immense help was pivotal to the success of this research and who became not just a colleague but also a dear friend. I am also thankful to LUT University and Kari Ullakko's laboratory, as well as all the members of the group who hosted and welcomed me during a 3-month stay. Thanks to all the friends I met at LUT who made my stay memorable. I am also grateful to UTBM, which hosted me for 2 months and allowed me to work during the pandemic. A special thanks to Yoann Danlos who helped me synthetise my powder feedstock and Lucas Dembinski, with whom I have worked since my first year at the university 10 years ago and who introduced me to additive manufacturing. Moreover, I would like to thank the Henry Royce student access scheme, which allowed me to use the facilities at the University of Manchester. I am also thankful to Albert Smith and Jack Donoghue for their tremendous help and expertise.

My research group, AMPlab, played a crucial role in shaping my academic journey. I wish to convey my warmest thanks to all the members for their camaraderie and support, especially to Bonnie, Becky, Donal, Faezeh, Francesco, Dina, and Peter for their valuable assistance, expertise, and engagement in stimulating discussions during my research. My scientific growth has been enriched by the exceptional researchers in the Metallurgy and Materials School. I would like to thank David Collins and Sandy Knowles for making me feel part of their research group and always providing access to their lab. Special thanks to Oliver Brooks, Daniel Reed and Amy Newell for their constant assistance during the course of my research. Thanks to Chris Hamlett for his unwavering support during outreach events and in creating my own workshop on smart materials. I would also like to express my heartfelt thanks to the lunch group at the school and the other PhD student friends at UoB, including Iris, Wakib, Sophia, Adam, Tom, Zak, and Patti, who not only provided a welcoming atmosphere at work and shared their experiences but were also always very helpful in any circumstances.

To my friend Anastasia, who embarked on her PhD journey alongside me, I owe a debt of gratitude. We faced the challenges of the PhD together, even from afar in the US, and your unwavering support, camaraderie, and shared experiences have made this journey more manageable and memorable. Alongside Marianna and David, we weathered the storms of academia as a team, and I cherish the bonds we forged during this time.

Thanks to the members of my gliding clubs in France, ABVV (Belfort) and ATVV (Tarn), who taught me how to fly. Special thanks to the members of the Stratford-upon-Avon gliding club, who became my family in England and kept me grounded by sending me into the sky. Massive thanks to Richard, without whom I would not get to the club. Thanks to my climbing friends, Dutch, Ben, and Kev, and my dance friends, Oksana, Dan, and Stella, for encouraging me to pursue my hobbies and push my boundaries alongside my professional career.

I would also like to express my gratitude to my friends around the world who have always been supportive, no matter the distance. Victoria, Paul, Mathilde, Nasim, Maelis, Nastia, Hugo, Yulia, and Justine have been pillars of support from various corners of the world, including the US, France, Russia, and the Netherlands.

Above all, I would like to thank my parents, Olga, Philippe, and Francoise, for their love and belief in me (et pour m'avoir supporté pendant le confinement). I am grateful for my siblings, Matveil and Julie, and my cousin Adeline, Xavier, Marie, and Baptiste for hosting me during my stay at UTBM. Their understanding, encouragement, and patience sustained me during this demanding project.

In closing, I extend my thanks to all my friends and family members who have been a source of unwavering support throughout my academic journey. Your influence has left an indelible mark on my journey, and for that, I am profoundly thankful to each of you. Thank you all for giving me the strength and courage to chase my dreams.

“La vie est une chose grave. Il faut gravir.”

Pierre Reverdy

In loving memory of my grandmother, Evgenia.

Contents

Nomenclature

Symbol	Definition	Unit
α	Strut angle	^{o}
γ	Monoclinic crystallographic unit cell angle	^{o}
ε_0	Maximum twinning strain of a crystal	-
2Θ	The angle between the incident X-ray and the diffracted X-ray	^{o}
λ	Wavelength	nm
ρ	Density	kg/m^3
σ_{20}	Stress at 20% of the maximum strength	Pa
σ_{70}	Stress at 70% of the maximum strength	Pa
σ_{max}	Maximum strength	Pa
σ_{tw}	Twinning stress	Pa
σ_{mag}	Magnetic driving force	Pa
a, b, c	Crystal lattice parameters	Å
Adj SS	Adjusted sum of squares	-
Adj MS	Adjusted mean squares	-
C	Contour distance	µm
c/a	Crystal tetragonality ratio	-
d_{10}	Point below which 10% of the powder is contained	-
d_{50}	Point below which 50% of the powder is contained	-
d_{90}	Point below which 90% of the powder is contained	-
DF	Degrees of freedom	-
E_r	Reduced elastic modulus	Pa
E	Line energy density	J/mm
E_s	Surface energy density	J/mm^2
F-value	A value on the Snedecor's F-Distribution	-
H_r	Hardness	Pa
H	Magnetic field strength	T
H_c	Coercivity	T
h	Hatching distance	µm
K_u	Magnetic anisotropy	J/m^3
M_s	Saturation magnetisation	Am^2/kg
M_r	Remanent magnetisation	Am^2/kg
P	Laser power	W
P-value	Statistical significance value	-
R2	Coefficient of determination	-
RMSE	Root means square error	-
T	Temperature	°C
t	Layer thickness	µm
T_{AS}	Martensite to austenite transformation start temperature	°C
T_C	Curie temperature	°C
T_{MF}	Austenite to martensite transformation finish temperature	°C
v	Scanning speed	mm/s
VED	Volume energy density	J/mm^3
Y	Elastic modulus	Pa

Abbreviations	Definition
2D	Two-dimensional
3D	Three-dimensional
10M	Modulated five-layered martensite (also referred to as 5M)
14M	Modulated seven-layered martensite (also referred to as 7M)
AB	As-built
AM	Additive manufacturing
ANOVA	Analysis of variance
B2´	Disordered cubic crystal structure
BCC	Body cantered cubic
BD	Build direction
CAD	Computer aided drawings
DIC	Differential interference contrast
DIC	Digital image correlation
DSC	Differential scanning calorimetry
EBSD	Electron backscatter diffraction
EDM	Electrical discharge machining
EDS	Energy-dispersive spectroscopy
HT	Heat-treated
IPF	Inverse pole figure
L21	Ordered cubic crystal structure
LFMS	Low-field AC magnetic susceptibility
L-DED	Laser direct energy deposition
L-PBF	Laser powder bed fusion
LUT	Lappeenranta-Lahti University of Technology
MFIS	Magnetic-field-induced strain
MIR	Magnetically induced reorientation
MSM	Magnetic shape memory
MSMA	Magnetic shape memory alloys
MUD	Multiple of uniform
ND	Normal direction
NM	Non-modulated martensite
SD	Scanning direction
SEM	Scanning electron microscopy
SMM	Shape memory materials
stl	Stereolithography
TB	Twin boundary
UoB	University of Birmingham
UoM	University of Manchester
UTBM	University of Technology of Belfort-Montbéliard
VSM	Vibrating sample magnetometry
VTT	Technical Research Centre of Finland
XRD	X-ray diffraction
XRF	X-ray fluorescence

List of publications

Sections of this work have been published in a peer-reviewed publication or submitted:

- **A. Milleret**, 4D printing of Ni–Mn–Ga magnetic shape memory alloys: a review, Materials Science and Technology, (2022). Doi: 10.1080/02670836.2022.2062655.

This review paper won the Materials Science and Technology Literature Review Prize 2022. To respect the rules of the competition, the paper must be single author.

- **A. Milleret**, V. Laitinen, K. Ullakko, N. Fenineche, M.M. Attallah, Laser powder bed fusion of (14 M) Ni-Mn-Ga magnetic shape memory alloy lattices, Additive Manufacturing 60 (2022) 103231. Doi: 10.1016/j.addma.2022.103231.

***AM** conceived and designed the experiment, performed the experiments, interpreted data, wrote original draft, edited, and reviewed the manuscript. **VL** performed LFMS, XRF and XRD characterisation, interpreted data, wrote, edited, and reviewed the manuscript. **MMA** reviewed the manuscript, provided funding, resources, and supervision. **KU** and **NF** provided funding, resources, and supervision.*

- **A. Milleret**, V. Laitinen, K. Ullakko, N. Fenineche, M.M. Attallah, In-situ alloying laser powder bed fusion of Ni-Mn-Ga magnetic shape memory alloy using liquid Ga, Progress in Additive Manufacturing (2023).

***AM** conceived and designed the experiment, performed the experiments, interpreted data, wrote original draft, edited, and reviewed the manuscript. **VL** performed XRF and XRD characterisation, interpreted data, edited, and reviewed the manuscript. **MMA** reviewed the manuscript, provided funding, resources, and supervision. **KU** and **NF** provided funding, resources, and supervision.*

The following sections of this work are in preparation for publication:

- **Chapter 7: A. Milleret**, V. Laitinen, K. Ullakko, N. Fenineche, M.M. Attallah, First investigation of the mechanical properties under compression loading of Ni-Mn-Ga lattices manufactured through L-PBF.

***AM** conceived and designed the experiment, performed the experiments, interpreted data, wrote original draft, edited, and reviewed the manuscript. **VL** reviewed the manuscript. **MMA** reviewed the manuscript, provided funding, resources, and supervision. **KU** and **NF** provided funding, resources, and supervision.*

- **Chapter 6: A. Milleret**, V. Laitinen, K. Ullakko, N. Fenineche, M.M. Attallah, Influence of strut angle on the crystallographic orientation of Ni-Mn-Ga lattices manufactured through L-PBF.

***AM** conceived and designed the experiment, performed the experiments, interpreted data, wrote original draft, edited, and reviewed the manuscript. **VL** interpreted data, reviewed the manuscript. **MMA** reviewed the manuscript, provided funding, resources, and supervision. **KU** and **NF** provided funding, resources, and supervision.*

- **Chapter 8: A. Milleret**, V. Laitinen, K. Ullakko, N. Fenineche, M.M. Attallah, Magnetic-field-induced twin boundary motion observed in 10M Ni-Mn-Ga lattices fabricated through laser powder bed fusion.

***AM** conceived and designed the experiment, performed the experiments, interpreted data, wrote original draft, edited, and reviewed the manuscript. **VL** performed LFMS, XRF and XRD characterisation, interpreted data, reviewed the manuscript. **MMA** reviewed the manuscript, provided funding, resources, and supervision. **KU** and **NF** provided funding, resources, and supervision.*

This work was presented in the following conferences:

- The Minerals, Metals & Materials Society (TMS2024), Orlando (USA), March 3–7, 2024;
- 9th Anglo-French PhD Scheme Conference, hosted by DSTL (Portsdown West) in conjunction with AID, 24-25 October 2022. Best presentation winner;
- Materials Science and Technology (MS&T2022), Pittsburgh (USA), 9-12 October 2022;
- Royce Student Summit, Henry Royce Institute, hosted by Manchester University,13-14 September 2022;
- Animate Materials Workshop: 4D Printing and Metamaterials, hosted by University of Birmingham in conjunction with DSTL, 27-28 June 2022;
- International Conference on Advanced Manufacturing (ICAM2022), co-organised by ESA and NASA, online, 7-10 March 2022;
- International Student Conference on Metallic Materials (ISCMM2021), hosted by University of Shielfield in conjunction with EPSRC and SFI Centre for Doctoral Training in Advanced Metallic Systems, online, 12-13 July 2021;
- Defence and Security Doctoral Symposium (DSDS21), hosted by Cranfield University in conjunction with DSTL and AWE, online, 9 November 2021;
- Royce Student Summit, Henry Royce Institute, online, 2-3 March 2021;
- Defence and Security Doctoral Symposium (DSDS20), hosted by Cranfield University in conjunction with DSTL and AWE, online, 10 November 2020.

List of Figures

List of Tables

Chapter 1

Introduction

1. Background and motivation

Smart materials, also known as intelligent or responsive materials, represent a novel class of materials capable of controlled and sometimes reversible alterations in response to external stimuli or environmental changes. These materials are designed to adapt, transform, or perform specific functions when subjected to specific triggers. For instance, among the many examples, you will find piezoelectric materials, shape memory alloys, thermoelectric materials, photochromic materials, and self-healing materials.

Additive manufacturing, commonly referred to as 3D printing, has been under intensive investigation since its inception in the late 1980s. This manufacturing method involves the layer-by-layer creation of objects. The convergence of 3D printing with smart materials has given rise to 4D printing, introducing an element of time and change to the printed objects—a fourth dimension. 4D printed objects are designed to alter their shape or behaviour in response to specific external conditions. Here, Ni-Mn-Ga magnetic shape memory (MSM) alloys, which were discovered in the mid-1990s, can undergo significant shape changes when exposed to a magnetic field [1,2]. These alloys exhibit a magnetic-field-induced strain (MFIS) of approximately 6-10% [3,4] in just a few milliseconds. Their applications span various fields, including robotics, aerospace, automotive engineering, and medical devices. Some specific examples include adaptive structures in aerospace, micro-actuators and sensors in microelectromechanical systems (MEMS), and energy harvesters for energy storage.

The MFIS phenomenon arises from the reorientation of crystallographic twins under the influence of a magnetic field. Each twin variant possesses a magnetic domain, and when subjected to a magnetic field, the twin boundaries move to align the magnetic domains with the field. However, twin boundary motion (TBM) is primarily observed in single crystals, as grain boundaries obstruct the TBM [5]. Nonetheless, this limitation can be overcome through the introduction of porosity and texture, achieving a MFIS of up to 8.7% in foam-like structures with bamboo-like grains, where large grains span the diameter of the struts are stacked on top of each other [6].

This is where additive manufacturing assumes a prominent role. By enabling the fabrication of complex geometries, and by controlling the texture through the process parameters, it allows for the production of complex lattice structures with struts composed of bamboo-like grains. Among the various additive manufacturing techniques available, laser powder bed fusion (L-PBF) holds particular interest due to its precision and accessibility. In L-PBF, metallic powders are melted layer by layer using a laser. Certain research gaps remain in the fabrication of polycrystalline Ni-Mn-Ga samples. Notably, functional Ni-Mn-Ga lattices have yet to be successfully produced. Additionally, there are only limited studies examining the impact of lattice geometry factors such as unit cell design, density, strut dimensions (diameter, length, and angle), on the resulting microstructure. Furthermore, there has been an insufficient exploration of grain growth and grain formation in Ni-Mn-Ga samples, and a shortage of research on the mechanical performance of Ni-Mn-Ga porous structures.

2. Research Aims and Objectives

The aim of this work is to develop a processing route for manufacturing functional polycrystalline Ni-Mn-Ga lattices using L-PBF. This aim will be achieved through the fulfilment of the following objectives:

• *Identification of feedstock preparation schemes to create the required alloy chemistry*.

This objective has been addressed in Chapter 4 and Chapter 5. Chapter 4 investigates the production of Ni-Mn-Ga through in-situ alloying, with the results indicating the benefits of using gas-atomised powder for the production of functional components. Consequently, this type of powder is used in Chapter 5 and subsequent chapters.

• *Optimisation of L-PBF technique for processing of Ni-Mn-Ga to create defect-free structures with the required functional behaviour*.

Chapter 5 outlines the design of experiments for the production of bulk and lattice samples using an L-PBF system. Additionally, the appendix of Chapter 5 discusses efforts to optimise parameters on a different L-PBF system.

• *Understanding the influence of thermal post-processing on the microstructure, and the mechanical behaviour of L-PBFed Ni-Mn-Ga*.

Chapter 6 and Chapter 5 delves into the influence of heat treatment on the microstructure, while Chapter 7 explores the mechanical behaviour of both as-built and heat-treated bulk and lattice samples.

• *Identification, design, and testing prototype concepts for functional structures*.

Throughout the chapters, there is an ongoing effort to identify and design the final geometry of the samples. Chapter 8 serves as a proof of concept for the functionality of the developed sample.

3. Scope and limitations

This research is exclusively dedicated to the fabrication of Ni-Mn-Ga alloy using L-PBF. It's worth noting that other alloys, such as Ni-Mn-Fe and Ni-Mn-Ga doped with elements like Co, Cu, Fe, and Cr, also exhibit substantial MFIS effects [7,8]. While Ni-Mn-Ga is the most extensively studied alloy, it's important to acknowledge that this alloy, often with varying compositions, can exhibit additional effects such as the magnetocaloric effect, which are beyond the scope of this study.

Regarding the choice of the additive manufacturing processes, it is notable that other techniques like binder-jetting and direct energy deposition have shown promising results in the literature. However, this study exclusively focuses on L-PBF for three primary reasons: the geometrical precision offered by this process, the avoidance of chemical contamination associated with binder-based processes, and the opportunity to control texture through adjustment of the process parameters.

Consistently, the same heat treatment methodology is applied throughout this research. Alternative post-processing treatments, such as hot isostatic pressing (HIP), cyclic heat treatment, and thermomechanical training, which could potentially enhance the MFIS, are not addressed within the scope of this study.

Due to the pioneering nature of this work, numerous aspects are explored for the first time and lack existing literature references. This particularly pertains to the research on mechanical behaviour (Chapter 7) and the investigation into microstructure and texture (Chapter 6), both of which represent preliminary investigations. Given the limited number of samples, statistical analysis pertaining to the mechanical behaviour of the produced samples is not included. Additionally, it's important to note that this work exclusively examines the compression behaviour, with tensile behaviour and fatigue performance being omitted from the study.

4. Structure of the dissertation

This work consists of a total of nine chapters, with five dedicated to experimental research. Each of these experimental chapters is structured in a paper-style format. In Chapter 2, a comprehensive review is provided on the manufacturing of Ni-Mn-Ga, with a particular emphasis on additive manufacturing techniques. Chapter 3 offers a detailed description of the experimental procedures employed throughout this study, offering more extensive insights than what is presented in individual chapters.

Chapter 4 presents the outcomes of initial experiments involving in-situ alloying, which did not yield conclusive results for the production of functional materials. Consequently, a shift to gas-atomised powder was made for subsequent experiments.

In Chapter 5, the focus shifts to the design of experiments aimed at optimising the parameters of L-PBF for the creation of both bulk and lattice samples. This optimisation encompasses considerations regarding composition, defect mitigation, and geometric integrity. The influence of heat treatment on thermal and magnetic behaviour is also thoroughly examined.

Chapter 6 investigates diverse methods for controlling and manipulating microstructures, including the use of a heated platform, double scanning strategy, and oriented structures. A meticulous analysis of the texture of as-built and heat-treated lattice structures is presented.

Chapter 7 is dedicated to an exploration of the mechanical behaviour in compression loading exhibited by both bulk and lattice structures, both before and after heat treatment.

Finally, Chapter 8 consolidates the knowledge acquired throughout this research to produce a lattice sample capable of achieving approximately 6% deformation, offering a culmination of the insights and findings obtained during the course of this study.

Chapter 9 gives an overall conclusion of this study.

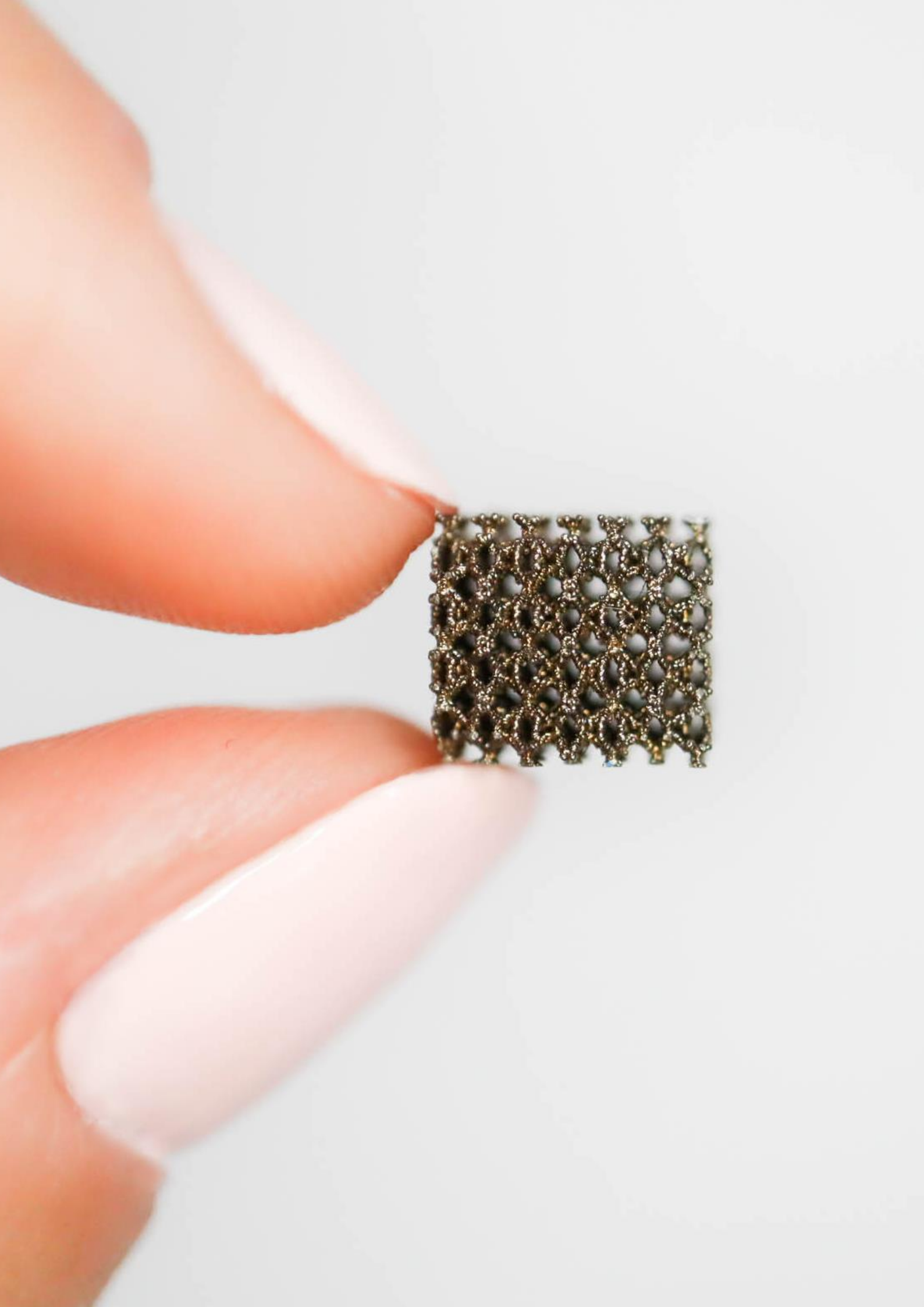

First Ni-Mn-Ga magnetic shape memory lattice
3D printed using L-PBF process.

Chapter 2

Literature review

This chapter gives a critical overview of the existing literature regarding the additive manufacturing of Ni-Mn-Ga. This literature review was published in early 2022, and as a result, does not encompass the most recent papers in the field. For an examination of recent studies relevant to this subject, please refer to the appendix of this chapter. Changes from the published version are added in brackets [] while small spelling mistakes, formatting, changes in acronyms (L-DED instead of DED) or American to English spelling are not highlighted.

Published as:

A. Milleret, 4D printing of Ni–Mn–Ga magnetic shape memory alloys: a review, Materials Science and Technology, (2022). Doi: 10.1080/02670836.2022.2062655.

This review paper won the Materials Science and Technology Literature Review Prize 2022.

Abstract:

4D printing has grown tremendously in the last decade, enabling functional structures made of smart materials to be manufactured. Current metal 4D printing research has focused on thermal shape memory alloys (SMAs), and to a lesser extent on magnetic SMAs. This review assesses the progress in 4D printing of Ni-Mn-Ga, highlighting the key challenges and opportunities for applications. The mechanism of the magnetic SMAs and the influence of 4D printing process parameters on the microstructure and material properties are explored, with an emphasis on laser powder bed fusion processing. Control of porosity, microstructure, texture, and impact of post-processing on the magnetic performance are the key challenges for the development of Ni-Mn-Ga 4D printing.

1. Introduction

Magnetic shape memory alloys (MSMA) are smart materials exhibiting a magnetic-field-induced strain (MFIS). Compared to thermally-activated shape memory alloys, such as NiTi, the response of MSMA is much faster (less than a millisecond compared to few seconds), making them good candidates for actuators [9], sensors [10], micro pumps [11] and energy harvesters [12]. To date, the Ni-Mn-Ga system is the most studied MSMA and is the focus of this study.

The shape memory effect in MSMA is driven by a phase transformation from a high ordered austenitic Heusler phase to a lower symmetry martensitic phase. The change in the shape occurs within the martensitic phase due to the reorientation of the twin variants [13].

The largest MFIS was reported in [a $4 \times 4 \times 6$ mm^3] single crystalline Ni-Mn-Ga exhibiting up to 10% strain [4]. However, in the polycrystalline form, grain boundaries create obstacles for twin boundary motion and thus the shape memory effect is negated. Nevertheless, recent studies show a large MFIS, up to 8.7% [6], in [a $2.3 \times 3 \times 6.2$ mm^3] polycrystalline Ni-Mn-Ga foams. It has been demonstrated that increasing porosity and grain size decreases the grain boundary constraint. MSMA foams have been made using ceramic space holders [6]. However, these techniques create a random distribution and/or size porosity. Additive manufacturing (AM) provides the possibility to create complex geometries, allowing for the design of materials with a specified porosity such as lattice structures [14]. Several techniques have been explored such as binder-jetting [15–18], ink-printing [19,20], laser direct energy deposition (L-DED) [21] and laser powder bed fusion (L-PBF) [22–25].

MSMAs that are additively manufactured are often referred to as 4D printed materials. The fourth dimension added to the 3D printed material is the time dependency of shape memory materials (SMM). SMM can change their shape under the influence of an external stimulus.

This review aims to explore the current state-of-the-art and the challenges that remain in the production of functional Ni-Mn-Ga MSMA through AM routes. To understand all aspects, both Ni-Mn-Ga system and AM techniques are discussed. In the first section, the theory behind MSMA is explained, then a list of current studies of 4D printing of MSMA is analysed such as the influence of different processes on the crystallographic structure. Finally, a short study of heat treatments of AMed Ni-Mn-Ga is conducted.

2. Magnetic shape memory effect

The shape memory effect occurs within a martensite phase, at room temperature. When applying external stress to the material, the structure plastically deforms due to twin boundary motion. In MSMAs, the external stress is a magnetic field, and the deformation is commonly characterised by MFIS.

In Ni-Mn-Ga, the phase transformation (in a range between 40 and 90 °C) occurs from a high symmetry $L2_1$ austenite phase to a lower symmetry martensite structure. Depending on the composition and the thermal history, three different martensitic phases can be distinguished in Ni–Mn–Ga:

- 10M: modulated pseudo tetragonal lattice with c<a (modulation over ten (220) atomic planes along $[\bar{1}10]$ direction), exhibiting 3 twin variants;
- 14M: modulated orthorhombic lattice with c<a (modulation over fourteen (220) atomic planes along $[\bar{1}10]$ direction), exhibiting 6 twin variants;
- NM: non-modulated L10 tetragonal lattice with c>a, exhibiting 3 twin variants.

Figure 2.1 shows the relationship between the parent phase and the martensite structures of Ni-Mn-Ga. The martensitic transformation is a diffusionless first-order structural transition, thus the distribution of the atoms in the martensitic phase is very similar to the austenitic one and often described in the austenite structure.

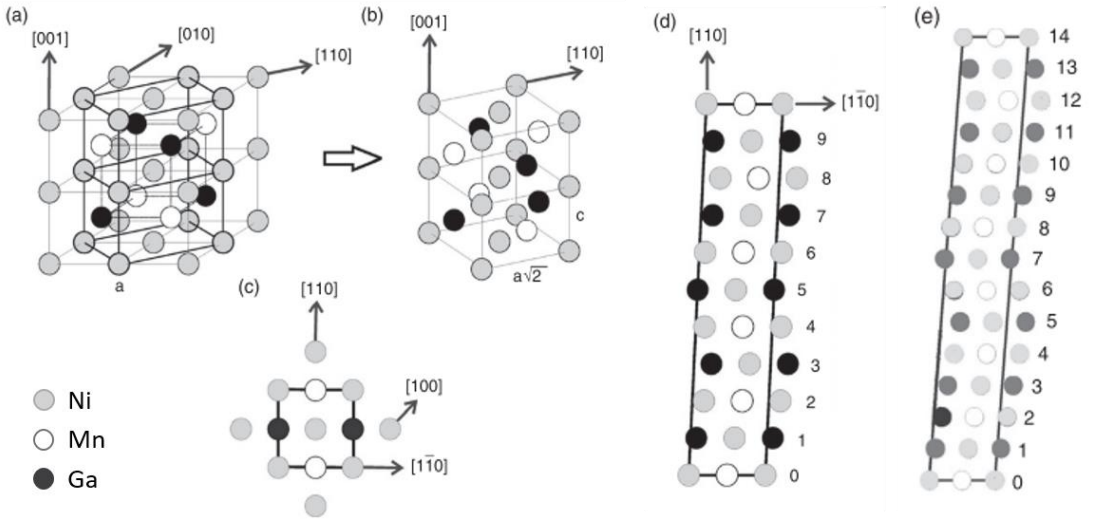

Figure 2.1. *(a) The $L2_1$ Heusler structure showing the relationship with the tetragonal unit cell, which is also shown in part b). (c) The tetragonal unit cell viewed from the top and (d) the 10M and (e) 14M modulated structures obtained by shearing the tetragonal cell,* [26].

The shape memory effect occurs in Ni-Mn-Ga due to the magnetically induced reorientation (MIR) [13]. The MIR effect is governed by twin boundary motion and results in the change of the crystallographic orientation in one phase, without any structural phase transformation. As the unit cell is of low symmetry, crystal reorientation will cause a change in dimensions. Thus, a bigger lattice distortion of the unit cell is favourable to a higher strain. A large strain is obtained by applying a magnetic field perpendicular to the hard axis of magnetisation (the easy axis shown by the small black arrows in Figure 2.2), which corresponds (in Ni-Mn-Ga) to the short crystallographic axis of the martensite cell. If the external field is high enough, the twins in favourable orientation (hard axis along the magnetic field) will nucleate and grow, despite the other variant, until saturation. This causes reorientation of the crystallographic cells, which takes less than a millisecond.

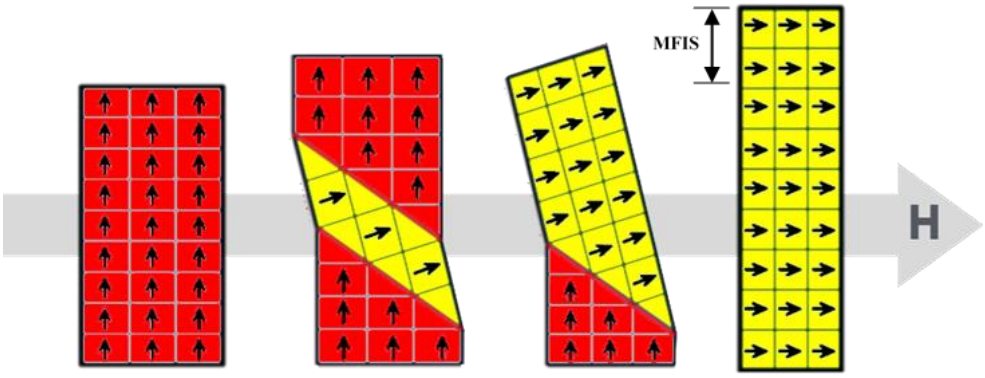

Figure 2.2. *Magnetic-field-induced strain in a single variant crystal.[Black arrows corresponding to the easy axis of magnetisation.]*

The maximum twinning strain allowed by lattice parameter, ε_0, is closely linked to the lattice parameters and is described by the following equation:

$$\varepsilon_0 = |1 - \frac{c}{a}|\,, \tag{1}$$

where *c* and *a* are the lattice constants of the tetragonal or orthorhombic martensite [13].

To activate the twin boundary motion in ferromagnetic materials, the magnetic driving force applied to the twin boundary must be equal to, or greater than, the mechanical driving force, known as the twinning stress, σ_{tw}:

$$\sigma_{tw} \leq \sigma_{mag}\,, \tag{2}$$

Moreover, at the saturation point, when a higher magnetic field (*H*) does not change the magnetisation of the sample, the magnetic driving force can be expressed as a function of the lattice distortion and the magnetic anisotropy energy density K_u as follows [27]:

$$\lim_{H\to\infty} \sigma_{mag}(H) = \frac{K_u}{\varepsilon_0}\,, \tag{3}$$

Recent research has demonstrated that giant magnetic-field-induced strains (when MFIS ~ ε_0) of up to 7% in 10M [28] and 9.5% in 14M martensite [4] can be achieved. Only a very small strain response has been observed in NM martensite as the magnetic driving force is generally not sufficient to exceed the twinning stress [27]. Moreover, modulated martensite (10M and 14M) has thinner twins and thus a higher number of twin and twin boundaries. Hence, more twin boundary motion is possible and the resulting structure exhibits larger MFIS [29].

Table 2.1 summarises the characteristics of the three possible martensitic structures and the properties of the single crystals. [Note that in the case of 14M martensite, the twinning stress energy barrier is slightly higher than the magnetic driving force, not allowing for the material to reach the possible maximum of 11% deformation and saturating at 9.5% MFIS.]

Table 2.1. *Martensitic structures of Ni-Mn-Ga single crystals.*

Structure	10M	14M	NM
	Tetragonal	Orthorhombic	Tetragonal
Easy axis of magnetisation	c	c	ab plane
c/a ratio	0.94	0.89	1.18
ε_0	6%	11%	18%
σ_{tw}	0.6 MPa	2 MPa	6.5 MPa
$K_u/10^5$ [J/m^3]	1.65	1.6	2.03
σ_{mag}	2.75 MPa	1.5 MPa	1 MPa
MFIS	7.1%	9.5%	0.17%
Ref.	[28]	[4]	[27,30]

The structure of the martensitic phase, upon cooling, is difficult to predict and strongly depends upon the thermal history and the valence electron density, (e/a), which in turn is dependent on composition. Figure 2.3 shows the resulting structure as a function of the valence electron density according to Chernenko et al. [30]. A transition

from modulated to non-modulated martensite appears at e/a=7.7, which corresponds to a $Ni_{50}Mn_{30}Ga_{20}$ (at.%) alloy. At this valence electron density, the martensitic transformation temperature [usually in the range of 40 - 90 ºC] is close to the Curie temperature (T_c [usually in the range of 70 - 90 ºC]), meaning that the phase transformation and the magnetic transformation (from paramagnetic to ferromagnetic) occur at approximately the same moment.

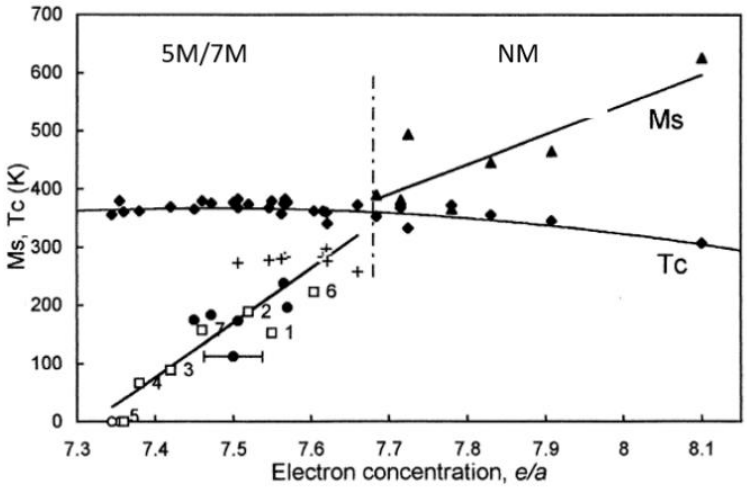

Figure 2.3. *Martensitic transformation temperature (M_s) and Curie temperature (T_C) for the different Ni-Mn-Ga alloys as a function of valence electron concentration (e/a),* [30].

2.1. Influence of the porosity and the size effect

Ni-Mn-Ga alloys exhibit a high shape memory effect in single crystals. However, in polycrystalline form, the shape memory effect is inhibited by grain boundaries that act as a barrier against twin boundary motion. [The twin boundaries are free to move within a grain but get pinned at grain boundaries and cannot move to the next grain.] The growth of a single crystal is costly and slow, therefore, an alternative way to reduce grain boundary constraint is to create oligocrystalline microstructures, consisting of few coarse grains.

Dunand and Mullner [31] studied the geometry effects in foams and laminates by decreasing the size of the constituent foil, fibre, strut and ribbon and/or increasing the grain size. These designs have two effects. Firstly, it creates free space around a grain, decreasing the incompatibilities with neighbouring grains and allows the movement of twin boundary. Secondly, it increases the magnetic anisotropy improving the shape memory effect. Niendorf et al. [32] demonstrated the size effect in the magnetic shape memory alloy Fe-Mn-Al-Ni. They used L-PBF to create bars with different diameters, ranging from 0.5 mm to 5 mm. The bars were printed vertically with the same processing parameters. The electron backscatter diffraction (EBSD) inverse pole figure map, in Figure 2.4, reveals a huge difference in the microstructures of each sample due to the size effect. The thinner bar exhibits strongly textured columnar grains with preferential orientation in the <001> direction perpendicular to the build direction (BD), while the larger bar exhibits a fine-grained microstructure. These differences are due to different thermal gradients and cooling rates. According to Dunand and Mullner [31], a columnar highly anisotropic microstructure, such as the one shown in Figure 2.4a, should exhibit a higher MFIS.

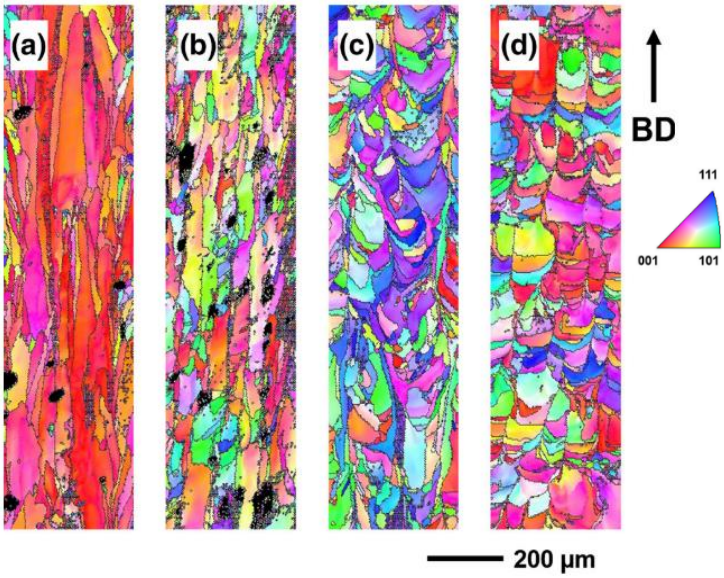

Figure 2.4. *EBSD inverse pole figure maps plotted with respect to the build direction for as-built Fe-Mn-Al-Ni bars of diameter (a) 0.5 mm, (b) 1 mm, (c) 3 mm, and (d) 5 mm,* [32].

Increasing the porosity in the material will also contribute towards decreasing the grain boundary constraint. A porous structure can be depicted as a geometric structure containing nodes and struts in which a size effect can occur. If the grain size is similar to the strut diameter (called bamboo-like structure), a MFIS between 0.1% - 8% can be observed [6,15,17,18,33]. The struts then act as a single crystal and the twin boundaries can move freely within it. The foam structures were produced with space holders [6,33] or through an additive manufacturing process such as binder jetting [15–18] or ink-printing [20]. Figure 2.5 shows a foam structure with twins spanning over the grain boundary.

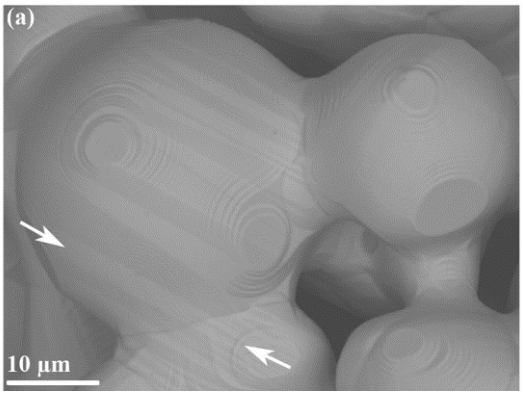

Figure 2.5. *Backscattered electron micrograph showing a twinned martensitic structure with twins spanning grain boundary (arrows) made by binder jetting,* [15].

However, these techniques do not allow a full control of the structure and thus of the shape memory effect. Controlling the porosity distribution and pore size will provide a better understanding of the size effect in MSMAs.

3. Additive Manufacturing of MSMAs

Additive manufacturing has gained significant attention as it is able to create materials with complex geometries. While ink-based techniques to create MSMA have been used in the past (such as inkjet [19,20] or binder jetting [15–18]), laser-based techniques (such as L-PBF [22–25] and L-DED [21]) are currently being studied to provide near net shape structures.

Table 2.2 summarises several examples of additive manufacturing techniques used to produce Ni-Mn-Ga. The type of machine, the composition of the as-built sample and the precursor material are detailed below.

Table 2.2. *List of current publication on additive manufacturing of Ni-Mn-Ga magnetic shape memory alloys.*

Powder composition (at.%)	Powder	Machine type	Author(s)
Binder jet:			
$Ni_{51.5}Mn_{30.7}Ga_{18.4}$	Ball milled	ExOne X1-lab	Caputo et al. [15]
$Ni_{53.3}Mn_{28.5}Ga_{18.2}$	spark eroded Ar	ExOne X1-lab	Caputo et al. [15]
$Ni_{52.3}Mn_{28.1}Ga_{19.5}$	spark eroded N2	ExOne X1-lab	Caputo et al. [15]
$Ni_{49.5}Mn_{27.8}Ga_{22.7}$	Ball milled	ExOne X1-lab	Caputo et al. [16]
$Ni_{49.6}Mn_{30.8}Ga_{19.6}$	Ball milled	custom-made	Mostafaei et al. [18]
$Ni_{49.7}Mn_{30.0}Ga_{20.3}$	Ball milled	ExOne X1-Lab	Mostafaei et al. [17]
Ink-printing:			
$Ni_{50}Mn_{32}Ga_{18}$	non prealloyed Ni-Mn-Ga	Bioplotter EnvisionTec	Taylor et al. [19]
$Ni_{49.5}Mn_{29}Ga_{21.5}$	PLGA + DCM	Bioplotter EnvisionTec	Taylor et al. [20]
L-DED:			
$Ni_{50.6}Mn_{27.2}Ga_{22.2}$	crushed	LENS 450 system	Toman et al. [21]
L-PBF:			
$Ni_{49.3}Mn_{31.2}Ga_{19.0}$	gaz atomised argon	Mlab cusing Concept Laser	Nilsen et al. [24]
$Ni_{49.8}Mn_{28.5}Ga_{21.8}$	gaz atomised argon	custom-made	Laitinen et al. [22]
$Ni_{49.8}Mn_{28.5}Ga_{21.8}$	gaz atomised argon	custom-made	Laitinien et al. [23]
$Ni_{50}Mn_{28.2}Ga_{21.8}$	gaz atomised argon	Mlab cusing Concept Laser	Ituarte et al. [25]

3.1. Binder jetting

Binder jetting is a technique that utilises a liquid binding agent to fuse powders to each other. The as-built parts require post-treatment: curing and sintering, to increase the density and the mechanical properties. Parts made by binder jetting are shown in Figure 2.6. The parts show a magnetic shape memory effect [of 0.01%], as a result of the pores [15]. However, it is extremely difficult to control the porosity with this technique.

There have been two key research groups that have studied binder jet additive manufacturing of Ni-Mn-Ga. Mostafei et al. [17,18] investigated the influence of sintering regimes and atmosphere on the microstructure of

samples made from ball-milled powders. The samples sintered in argon atmosphere demonstrated better results than the samples sintered within a vacuum (Ms = 15.3 Am^2/kg for samples sintered in vacuum and Ms = 68.4 Am^2/kg in argon); a typical 10M structure was observed in samples sintered under argon while samples sintered under vacuum showed a mixture of austenite and Ni-Ti rich phases. They investigated the sintering temperature from 1000 °C to 1100 °C. The sample sintered at 1070 °C with a composition of $Ni_{50.1}Mn_{29.7}Ga_{20.2}$ (at.%) and density of approximately 66 % exhibited the highest saturation magnetisation (Ms ~ 56.5 Am^2/kg). This sample had a martensitic transformation temperature of ~73 °C and a Curie temperature of ~90 °C. Caputo et al. [15,16] investigated the influence of the porosity and the type of powder on the magnetic properties. They compared samples printed from powders made by spark erosion in both liquid nitrogen and liquid argon as well as by ball milling. Parts from ball-milled powders showed 24.08 % porosity (see Figure 2.6) and a MFIS of ~0.01 % [15].

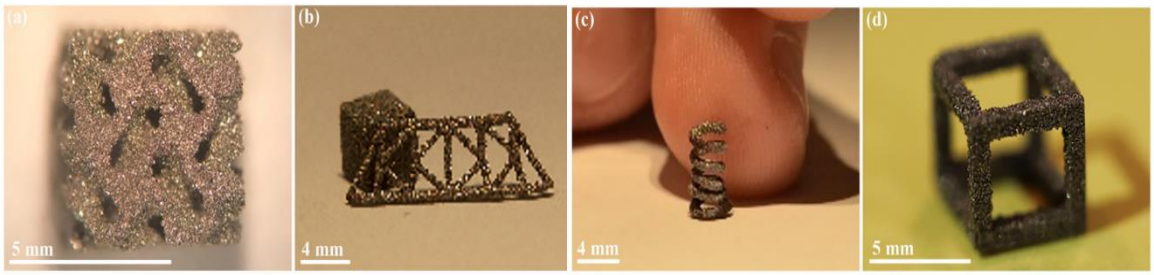

Figure 2.6. *Sintered parts made from ball milled Ni-Mn-Ga powders, [made through binder jetting]* [15].

A recent study on Ni-Mn-Cu-Ga magnetocaloric material made by binder-jet [34] shows foam like structures with pores along the grain boundaries. This would reduce the grain boundary constraint and as a result increase the MFIS, however, this study is not focused on the shape memory effect.
Binder jet additive manufacturing is a suitable method to produce porous parts. However, the size and distribution of the pores is difficult to predict. Moreover, this method requires important post-treatments and does not provide good mechanical properties [due to the high porosity and contamination linked to the binder liquid].

[Vecchis et al. [35] conducted a study to examine the impact of sintering time (ranging from 0 to 8 hours) and temperatures (1070, 1080, and 1090 ºC) in binder jet printed samples produced from ball milled $Ni_{49.9}Mn_{30.0}Ga_{20.3}$ powder. Their findings revealed that the printed samples exhibited a 14M structure with traces of NM. The primary aim was to achieve large grains with interconnected porosity in the sintered samples. Notably, temperature and times smaller than 1080 ºC for 1 hour led to the formation of large interconnected pores, although they were not associated with significant grain growth. While major grain growth was observed at 1090 ºC for 8 hours, but this condition resulted in substantial densification. To strike a balance between densification and grain growth, sintering parameters of 1080 ºC for 2 hours were identified as an optimal compromise.]

3.2. Inkjet printing

Ink printing is an extrusion process, where small metallic powders are mixed inside a polymer binder to create an ink. This ink is then ejected as droplets through a small nozzle onto a substrate. This process requires curing and sintering to extract the polymer binder from the final parts. Taylor et al. [19] used this technique to create porous parts from elemental powders and investigated the influence of the sintering time and temperature on the porosity

and grain size. They created an ink of PLGA + DCM (a copolymer and dichloromethane) containing the elemental powders as shown in Figure 2.7.

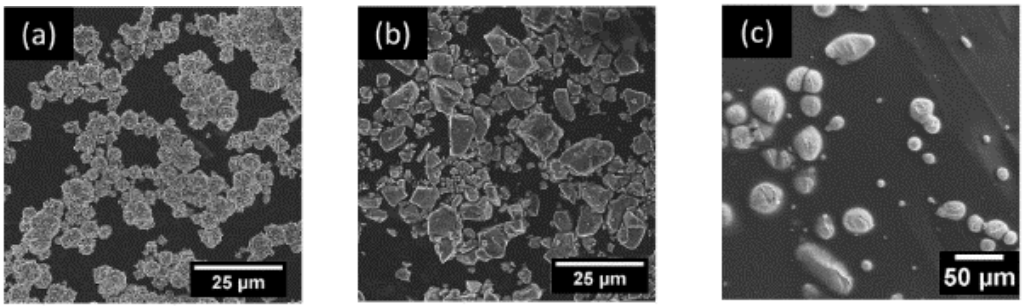

Figure 2.7. *SEM images of (a) Ni and (b) Mn powders, and (c) Ga powders dispersed in a PLGA + DCM slurry,* [19].

Taylor et al. [19] studied the microstructure, the thermal and the magnetic properties of a lattice, which had ~300 µm diameter struts and ~450 µm wide channels, as shown in Figure 2.8. The struts display two types of porosity: pores from incomplete sintering and voids from larger Ga powders that melt and diffuse into the surrounding Ni and Mn powders.

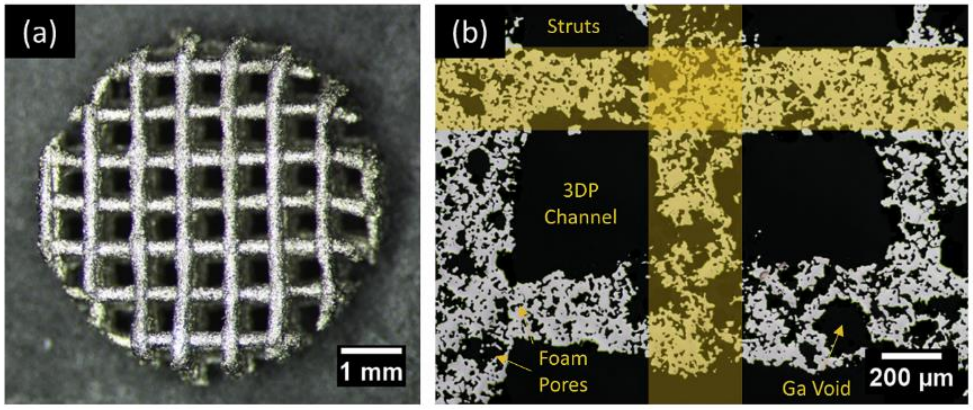

Figure 2.8. *(a) Photograph and (b) optical micrograph of a polished cross-section of a Ni-Mn-Ga micro-truss (after sintering at 1000 °C for 12 h and ordering at 700 °C for 10h),* [19].

The micro-truss with a homogenous composition of $Ni_{50}Mn_{32}Ga_{18}$ (at.%) exhibits a reversible martensitic transformation in the range of 45 and 90 °C, a Curie temperature of 85 - 90 °C, and a saturation magnetisations up to 56 Am^2/kg [19]. These results, which are supported by findings by Mostafaei et al. [17] with binder-jetting, show the feasibility of printing MSMAs from elemental powders.

3.3. Laser Direct Energy Deposition (L-DED)

L-DED is a laser-based process, where metallic powders are spread by a nozzle through a laser beam and melted layer by layer to create the final part. As far as the author is aware, only one study has been performed on L-DED of Ni-Mn-Ga [21]. The crystallographic structure, the phase transformation temperatures and the magnetic properties of a five-layered wall was investigated. In the as-deposited fully dense sample, as shown in Figure 2.9,

columnar grains were observed to extend beyond the deposited layers in epitaxial growth. This allowed twin boundary motion along their long axes [36].

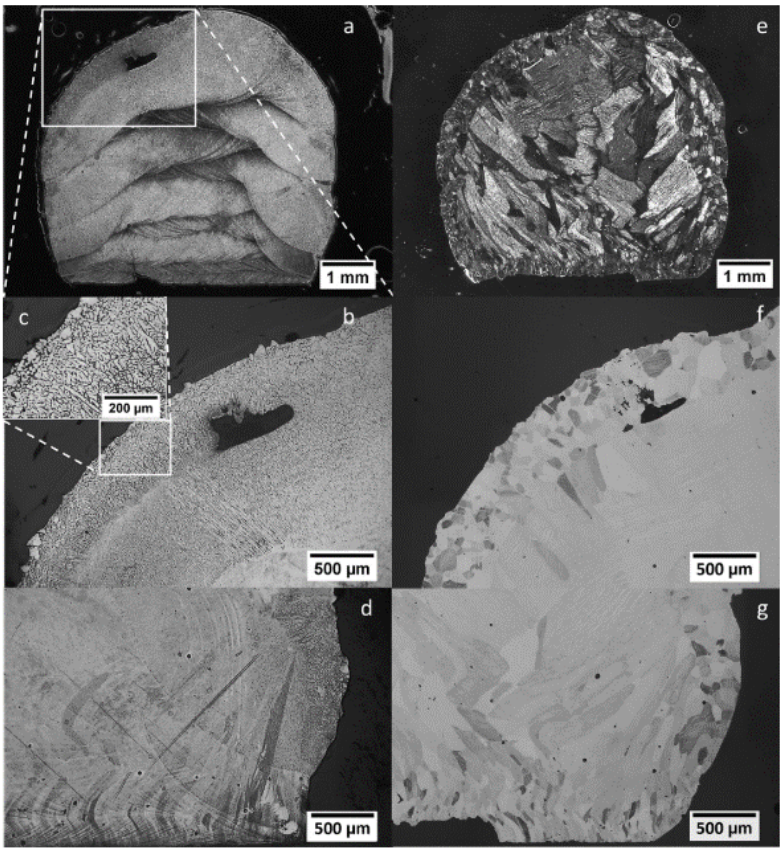

Figure 2.9. *Cross-sectional optical micrographs of the L-DED as-deposited (a-d) and homogenised sample (e-g) after etching,* [21].

The as-built sample with a composition of $Ni_{50.6}Mn_{27.2}Ga_{22.2}$ (at.%) exhibited a martensitic transformation at approximately 56 °C, a Curie temperature at 86 °C and saturation magnetisation ~52 Am^2/kg. After heat treatment, the structure recrystallised and the grains grew, which increased the saturation magnetisation up to 57 Am^2/kg and reduced the degree of ferromagnetic hysteresis. This fully dense material showed good suitability for shape memory application. Further studies could be performed to investigate the effect of controlled porosity on magnetic properties. However, L-DED method is well known to be inaccurate in terms of printing precision relative to L-PBF.

[Flitcraft et al. [37] conducted a study to investigate the impact of solidification rate on microstructure, phase transformation temperature, and magnetic properties in $Ni_{50}Mn_{29}Ga_{21}$ samples produced through arc melting. The objective was to gain insights into replicating and comprehending the solidification rates inherent in L-DED process. They explored a range of solidification rates, spanning from 1.1 x 10^2 to 3.2 x 10^3 K/s. The fastest cooling rate closely approximates the cooling rate observed in L-DED [21]. The findings indicated that higher solidification rates led to a cellular-dendritic solidification pattern, in contrast to slower rates, which resulted in columnar-dendritic structures. The rapid cooling rates also caused a typical 2% Mn evaporation, although this wasn't visible at slower cooling rates. Additionally, Mn partitioning occurred, leading to a crystallographic

structure featuring a mixture of NM+14M and austenite phases, despite the composition corresponding to the 10M crystal structure. After heat treatment, the 10M crystal structure was recovered. Furthermore, increasing solidification rates correlated with a reduction in saturation magnetisation and a change in the shape of the hysteresis loop, resembling a 'wasp-waist' with a double-shifted hysteresis loop. This behaviour was attributed to either higher internal stresses during rapid solidification (notably, in L-PBF, solidification rates can be even higher, up to 10^6 K/s, and do not exhibit this behaviour) or potential ferromagnetic-antiferromagnetic coupling arising from Mn partitioning and the presence of distinct crystal structures [38].]

3.4. Laser Powder Bed Fusion (L-PBF)

L-PBF is a laser-based technique that melts each layer on a powder bed. This process can produce near net shape parts with complex geometries. It is thus interesting to use it for the printing of Ni-Mn-Ga lattices with controlled porosity.

L-PBF of lattice structures often results in geometrical inaccuracy and porosity inside the struts [14]. Moreover, an important heat input can result in preferential evaporation of some elements. Mn has a relatively low boiling point [1962 °C compared to 2403 °C for Ga and 2732 °C for Ni, [39]] making it sensitive to evaporation. In order to avoid these defects, a good optimisation of the printing parameters is required: the laser power (P, in W), the scanning velocity (V, in mm/s), the hatching distance (h, in µm), the layer thickness (t, in µm) and the scanning strategy.

The first trial of L-PBF of Ni-Mn-Ga was made in 2018 by Chmielus and Salminen [40]. They managed to create a cuboid with a lattice structure on a stainless steel 316L substrate, as can be seen in Figure 2.10. The sample exhibited a phase transformation at ~61 °C and a Curie temperature of ~87 °C.

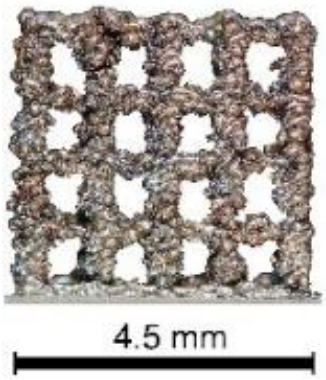

Figure 2.10. *Side view of a Ni-Mn-Ga cuboid sample manufactured by L-PBF,* [40].

Nilsen et al. [24] performed a parameter study over a small range of parameters. They demonstrated that relative density and Mn evaporation are inversely correlated. By increasing the energy input, the relative density increases but the Mn evaporates more. They managed to reach 92.8% density despite the Mn loss. It was found that scan speed and laser power seem to mainly influence the relative density while Mn evaporation is more sensitive to the hatch spacing. The as-printed sample showed a paramagnetic behaviour with low magnetisation; however, heat treatment restored the ferromagnetic behaviour of the sample. The densest sample with a composition $Ni_{50.3}Mn_{30.8}Ga_{18.9}$ (at.%) was made with a laser power of 40 W, a scan speed of 600 mm/s and an energy input of 27.21 J/mm^3. This sample exhibited a saturation magnetisation of 46.3 Am^2/kg, a phase transformation

temperature ~67 °C and a Curie temperature ~92 °C. However, a very narrow parameter window was used, which would not allow for a good evaluation of the optimum parameters. The energy density ranged from 17 to 33 J/mm^3. They performed another study [25] on a larger window, from 26.24 to 44.90 J/mm^3, and got 95.91% dense sample made with a laser power of 55 W and a scan speed of 500 mm/s. Only 0.69 at.% Mn was lost during the process, stabilising a 10M martensite structure at room temperature, with a saturation magnetisation of 56 Am^2/kg, a phase transformation temperature ~50 °C and a Curie temperature ~95 °C . These findings are in accordance with their previous study [24].

Laitinen et al. [23] used a wider range of energy densities, from 56 to 567 J/mm^3. The Mn seems to evaporate at energies above ~75-100 J/mm^3 and the Ga above ~200-250 J/mm^3. The best sample (with the best ratio between relative density and Mn evaporation) was printed with an energy density of 74 J/mm^3 [a laser power of 200 W and a scanning speed of 750 mm/s] with a composition $Ni_{50.9}$ $Mn_{27.4}$ $Ga_{21.7}$ (at.%). This sample had a relative density of 98.3% with 1.1 at.% Mn evaporation. The phase transformation temperature was found to be ~120 °C and the Curie temperature ~60 °C. Although further optimisation of the parameters and scanning strategy is required to avoid cracks (see Figure 2.11).

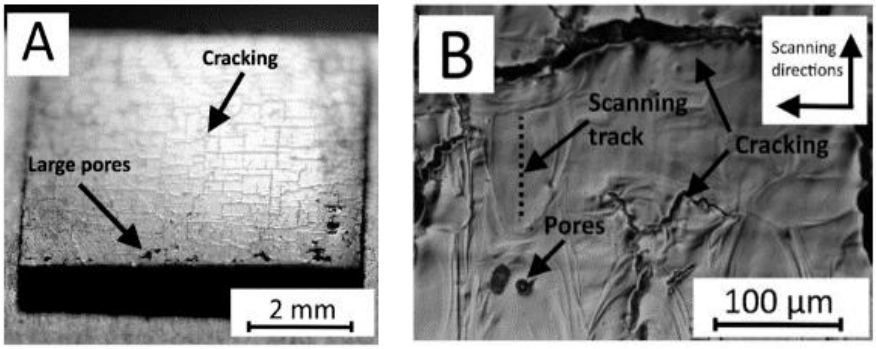

Figure 2.11. *Micro- and macroscale cracks and porosity. (a) Cracks on the surface of the L-PBF sample. (b) Microscale cracks and porosity,* [22].

The printing of thin walls (10 × 0.8 × 5 mm^3) led to a significant decrease of the heat input and a change of the thermal gradient resulting in crack-free samples [41]. After heat treatment, samples with a composition $Ni_{49.71}$ $Mn_{28.92}$ $Ga_{21.37}$ (at.%) exhibited a 10M structure, large mm-sized grains (see Figure 2.12), giant 5.8% MFIS with a phase transformation ~48 °C and a Curie temperature of ~99 °C.

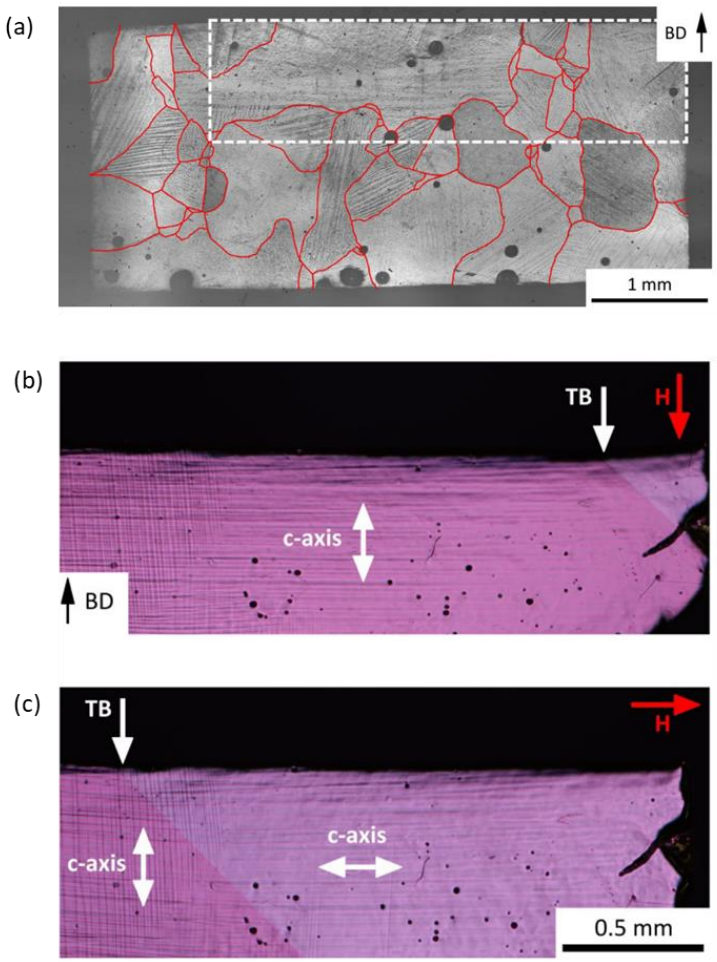

Figure 2.12. *Optical polarised light images of (a) heat- treated and polished L-PBFed sample revealing large single crystalline grains (outlined with red lines) with twins. BD notes the build direction. The white rectangle marks the part of the sample containing the largest grain. This part is magnetically actuated (b-c) under a homogeneous 0.8 T magnetic field, elongated (b) and contracted (c) depending of the direction of the magnetic field (red arrow),* [41].

[Both studies from Laitinen et al. [23] and Nilsen et al. [24] found different optimum parameters for printing Ni-Mn-Ga samples with high density and low Mn evaporation. While Nilsen et al. used a low laser power of 40 and 55 W with a scanning speed of 600 and 500 mm/s, Laitinen et al. used a laser power of 200 W with a scanning speed of 750 mm/s, inevitably increasing the energy input and therefore the risk of cracking. However, this energy input was reduced by using a larger layer thickness of 60 µm instead of 25 µm in Nilsen et al. study.]

In addition, magnetic properties are orientation-dependant. Previous studies have reported the possibility to control the grain orientation via L-PBF by tuning the printing parameters and the scanning strategy [42]. Thus, L-PBF appears to be a potential approach to create near net shape oligocrystalline and foam-structure Ni-Mn-Ga.
As L-PBF seems to be the best technique to produce controlled porosity and near net shape MSMA, the next sections of this paper are putting a particular attention to it.
[Saren et al. [43] conducted a study on twin boundary mobility in a single crystal fabricated through L-PBF, demonstrating a 10M structure with a giant 5.8% MFIS in [41]. Their research included a close examination of twin boundaries, allowing for the calculation of twinning stress and twin boundary velocity, which were found to vary depending on the boundary type. The twinning stress was determined to be approximately 1.4 MPa and 0.6

MPa for different boundary types, values higher than what is typically observed in single crystals of similar composition. The velocity of twin boundaries in these L-PBF-fabricated samples was found to be lower than in conventionally manufactured single crystals, with values of 1.5 m/s and 24 m/s. These differences in results were attributed to the presence of small keyhole defects resulting from trapped argon or oxygen, as well as Mn evaporation. Notably, the twinning stress was found to be much smaller than that reported in L-PBFed polycrystalline samples by Ituarte et al of 10 MPa. The study also revealed that the twin boundaries started moving at a magnetic field strength of 0.1 T and achieved full displacement at 0.7 T. This research offers valuable insights into twin boundary mobility in L-PBFed single crystals.

Wang et al. [44] investigated the microstructure and its impact on the MFIS in Ni-Mn-In samples produced via L-PBF, using two scanning strategies: unidirectional and bidirectional. The unidirectional strategy involved continuous scanning with no rotation between layers, while the bidirectional strategy included a typical 90º rotation between layers. The unidirectional scanning strategy resulted in uniformly sized grains, whereas the bidirectional strategy yielded a bimodal grain distribution. Both strategies led to similar textures, characterised by a typical (100) preferential growth aligned with the building direction, with slightly higher texture intensity observed in the unidirectional strategy. MFIS measurements were conducted in a Physical Property Measurement System (PPMS) equipped with a strain gauge at magnetic fields of up to 7 T. The results indicated that the samples exhibited 0.082% strain for unidirectionally scanned samples and 0.040% strain for bidirectionally scanned samples at 7 T. However, it's important to note that these strain values cannot be entirely attributed to MFIS, as at such high magnetic fields, magnetic phase transformations can also occur.]

4. Effect of AM on the microstructure and composition

L-PBF has a high cooling rate, between ~$10^4$and 10^6 K/s [45] that usually results in highly textured columnar grains. The grain growth is led by the thermal history and can be tuned by several techniques. For example, re-scanning [46] provides longer solidification, and thus grain growth, by passing over the scanned layer a second time, without powder and with different parameters. The use of a heated bed would also minimise the cooling rate and considerably reduce the risk of cracking [47]. However, these two techniques (double scanning and heated bed) could increase the amount of Mn evaporation. Moreover, as the entire process takes place in a closed chamber, the atmosphere can be controlled with argon or nitrogen to reduce the risks of oxidation, and pressurised in order to prevent evaporation. All these methods, added to the process parameters, make L-PBF a very versatile technique to create materials with different microstructures and compositions.

The process parameters are usually evaluated through the equation of volumetric energy density (VED), expressed in J/mm^3 [48]:

$$VED = \frac{P}{h*V*t}, \quad (4)$$

where P is the effective laser power (in Watts), h is the hatch distance (in mm), V is the scanning velocity (in mm /s), and t is the layer thickness (in mm).

The energy input is just an approximate value, which quickly and globally evaluates the parameters. It is therefore important to consider all the parameters individually [49]. Moreover, laser parameters such as spot size, focus point position, laser profile (Gaussian, flat, etc.) and laser wavelength can strongly affect the microstructure and differ from one printer to another.

4.1. Effect on composition and relative density

In general, an increase of VED leads to an increase of the density despite the Mn evaporation. Studies on L-PBF of MSMA demonstrated a Mn evaporation of ~1% – 1.5%, which can be easily compensated for by adding extra Mn to the precursor powder. Table 2.3 summarises the relative density and the Mn evaporation made by the optimum parameters found in the literature.

Table 2.3. *Effect of Laser powder bed fusion on the composition and relative density (only the densest sample is shown in the table).*

	Substrate	VED (J/mm^3)	Relative density	Mn evaporation	Author(s)
$Ni_{49.3}Mn_{31.2}Ga_{19.0}$	Nickel	27.21	91.40%	0.50%	Nilsen et al. [24]
$Ni_{49.8}Mn_{28.5}Ga_{21.8}$	Incoloy	133 80 57	96.80% 94.90% 93.50%	1.30% 1% 1.60%	Laitinen et al. [22]
$Ni_{49.8}Mn_{28.5}Ga_{21.8}$	316L	74	98.30%	1.10%	Laitinen et al. [23]
$Ni_{44.5}Fe_{34}Mn_{14}Al_{7.5}$	-	65	-	1.50%	Niendorf et al. [32]
$Ni_{50}Mn_{28.2}Ga_{21.8}$	-	44.90	95.91%	0.69%	Ituate et al. [25]

Nilsen et al. [24] discovered a strong correlation between the relative density and the power and velocity of the laser. Figure 2.13 shows that a high relative density can be obtained with a high energy density, meaning low speed and high laser power. However, the Mn evaporation follows an opposite pattern but can be controlled by the hatch spacing.

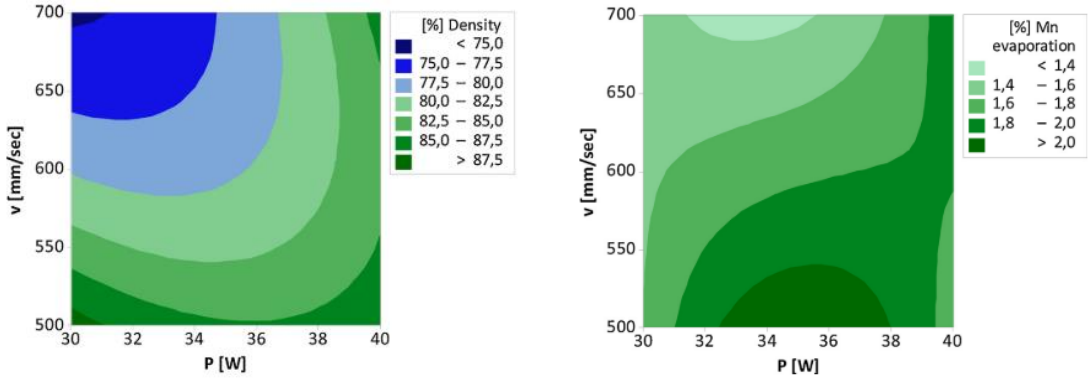

Figure 2.13. *Contour plots for (%) Density and (%) Mn evaporation based on the regression models of HT samples,* [24].

4.2. Effect on the crystallographic structure and grain morphology

4.2.1. Crystallographic structure:

Different techniques and different parameters should result in various structures depending on the thermal history. Table 2.4 summarises the crystallographic structure obtained after AM. However, because of the lack of data, it is difficult to make conclusions on the effect of different processes. We can see in Figure 2.14 that there is no clear relation between the resulting structure (10M, 14M or NM) and the valence electron density (e/a). We deduce that this is probably because the thermal history between different processes is too different and it overcomes the influence of e/a on the resulting structure.

Table 2.4. *Crystallographic structures of Ni-Mn-Ga MSMA made through AM.*

	Powder	Microstructure	e/a	Author(s)
L-DED:				
$Ni_{50.6}Mn_{27.2}Ga_{22.2}$	crushed	14M	7.63	Toman at al. [21]
L-PBF:				
$Ni_{49.3}Mn_{31.2}Ga_{19.0}$	gaz atomised argon	NM	7.68	Nilsen et al. [24]
$Ni_{49.8}Mn_{28.5}Ga_{21.8}$	gaz atomised argon	14M+NM	7.63	Laitinen et al. [23]
Ni_2MnGa	gaz atomised argon	10M	7.5	Chmielus and Salminen [40]
$Ni_{50}Mn_{28.2}Ga_{21.8}$	gaz atomised argon	10M	7.66	Ituate et al. [25]
Binder jet:				
$Ni_{49.5}Mn_{27.8}Ga_{22.7}$	Ball milled	10M	7.58	Caputo et al. [16]
$Ni_{49.6}Mn_{30.8}Ga_{19.6}$	Ball milled	10M	7.70	Mostafaei et al. [18]
$Ni_{49.7}Mn_{30.0}Ga_{20.3}$	Ball milled	14M	7.68	Mostafaei et al. [17]
Ink-printing:				
$Ni_{50}Mn_{32}Ga_{18}$	non prealloyed Ni-Mn-Ga PLGA + DCM	NM	7.78	Taylor et al. [19]

Some studies have found that the structure of the as-built sample differ from the powder. The cast material used to make the powder for L-DED [21] exhibits a 10M martensite structure. However, after processing, the as-deposited material appears to have a 14M orthorhombic structure. This can be due to a slight difference of the composition combined with a different cooling rate.

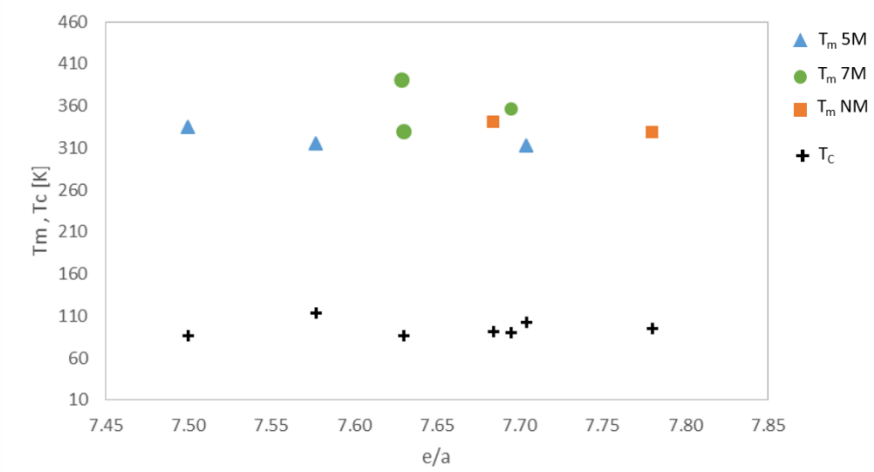

Figure 2.14. *Transition temperature (T_m) and Curie temperature (T_c) as a function of valence electron concentration (e/a) of additive manufactured Ni-Mn-Ga.*

4.2.2. Grains and twins morphology:

The obtained structure in [21] exhibited columnar grains crossing twin boundaries, which is favourable to twin mobility and shape memory effect. Non laser-based processes also create samples with twins extending across the grain boundaries in bamboo-like grains [16,19], as depicted in Figure 2.15 and Figure 2.16.

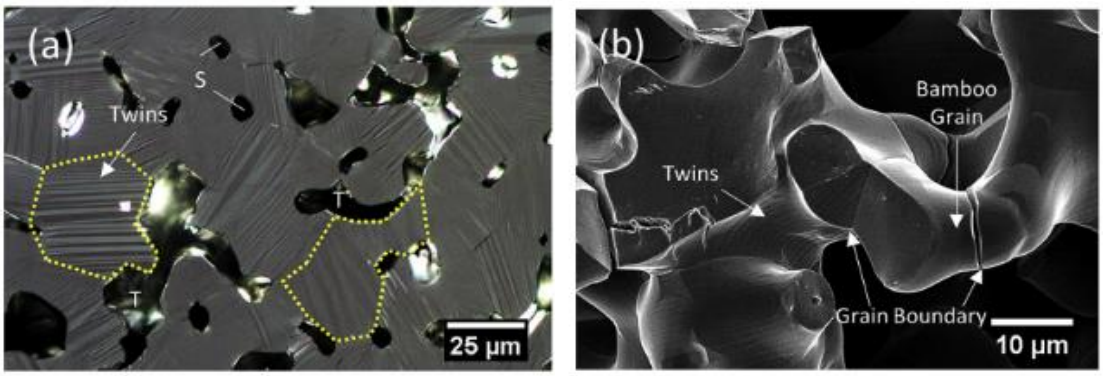

Figure 2.15. *(a) Polarised light optical micrograph of polished cross-section of a Ni-Mn- Ga micro-truss showing martensite twins (arrow) spanning the grains (two of which are outlined with a dashed yellow line). (b) SEM image of the surface of the same specimen, showing martensite twins, grain boundaries that cracked during sample cutting, and a bamboo grain,* [20].

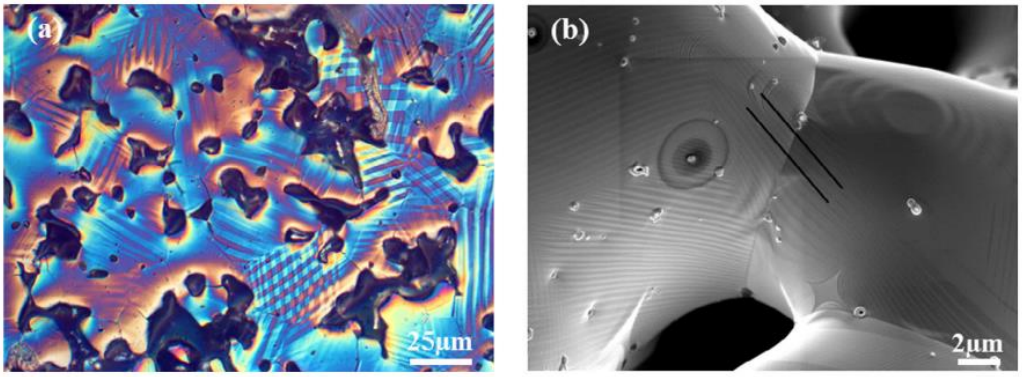

Figure 2.16. *(a) DIC image of polished cross-section of sintered material showing martensitic twins [black lines] extending across entire grains; (b) SE micrograph of two sintered particles,* [16].

The advantage of laser metal forming is to increase grain size in a favourable direction to facilitate the growth of one twin variant. As explained previously, an oligocrystalline structure is beneficial to shape memory effect. By sufficiently decreasing the cooling rate with appropriate parameters, L-PBF can provide grain growth in the build direction.

Several studies have been undertaken on the influence of the processing parameters on grain growth [25,50–53]. Unfortunately, at the time of writing, it is a largely unexplored topic and material dependant.

Recent study has been undertaken to understand the epitaxial growth of re-solidified Ni-Mn-Ga single crystal [54]. The study of different sets of laser parameter (power-velocity) used to remelt a single crystal plate demonstrated that most of these parameter sets do not induce the nucleation of new grains. These results are really promising, and further work needs to be done to investigate epitaxial growth on a single crystal plate with melted powder.

5. Influence of the post-treatment after an AM process

Laser metal forming often creates chemical inhomogeneity and internal stresses due to elevated solidification velocity. To homogenise and release the residual stresses, heat-treatment is necessary.

Several researchers have found that heat treatment can decrease porosity and initiate grain growth. Nilsen et al. [24] studied the influence of a heat-treatment on NM Ni-Mn-Ga samples printed with L-BPF process. The samples were first homogenised for 95 h at 1000 °C and then annealed for 24 h at 800 °C. They highlighted an increase in relative density after heat-treatment, especially for samples printed with a high energy density. Moreover, as-printed samples exhibit a paramagnetic behaviour, and no phase transformation could be observed in the magnetic measurements. After heat-treatment, the ferromagnetic behaviour was recovered for all samples.

Taylor et al. [20] studied the influence of different sintering regimes: from 800 °C to 1050 °C on Ni-Mn-Ga wires. For most of the samples, the pore volume fraction first increased in the first 10 minutes and then dropped significantly, especially for higher temperatures (see Figure 2.17). The first increase was due to the melting of Ga creating large Ga voids. The Ga then diffused into Ni and Mn and the pore volume fraction decreased with bigger rates for higher temperatures. These results are promising for the possibility of in-situ alloying. It shows that a heat treatment could potentially dissolve the segregations in a sample made of elemental powders.

Taylor et al. [20] also studied the influence of the sintering regime on the grain growth. For sintering temperatures of 1000 °C and 1050 °C, grain growth is very quick (Figure 2.17). After 240 minutes at 1050 °C, the grain volume

increased by fifty times. For sintering temperatures below 1000 °C, a longer dwell is necessary to initiate significant grain growth.

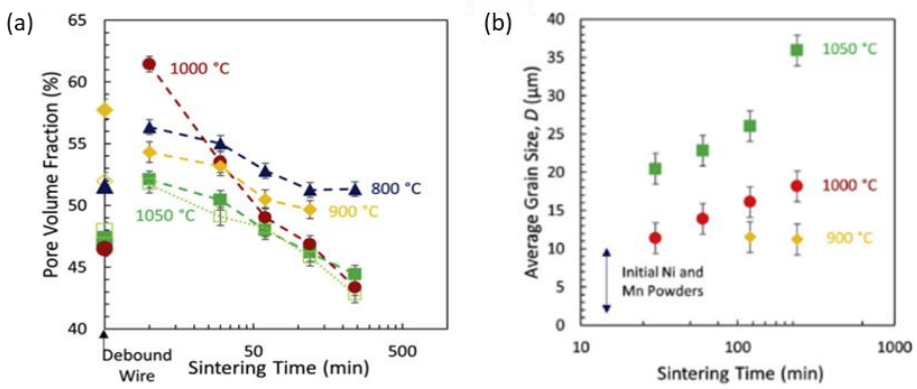

Figure 2.17. *(a) Pore volume fraction vs. sintering time and (b) average grain size, D vs. sintering time for printed Ni-Mn-Ga wires sintered at temperatures between 800 °C and 1050 °C during in situ x-ray tomography scans,* [20].

The melting point of Ni_2MnGa is 1134 °C [55] and closer the homogenisation temperature is to the melting point, the faster and bigger is the grain growth. Laitinen et al. [56] investigated the influence of the heat treatment temperature on the grain growth of L-PBFed samples. Larger grains were also achieved with higher temperatures (1080 °C) as seen in Figure 2.12.

Toman et al. [21] also observed the influence of the post-treatment on L-DED printed samples. The parts were first heated for 24 h at 1000 °C and then homogenised for 12 h at 700 °C. Post-treatment dissolved dendrites and resulted in grain growth (see Figure 2.9). It was also beneficial for magnetic and thermal properties: the saturation magnetisation increased from 51.8 to 57 Am^2/kg and the martensite transformation shifted slightly to higher temperatures (from ~56 °C to ~63 °C). Figure 2.18 shows the DSC and magnetisations curves of as printed and ordered samples. However, post-treatment generated a small Mn evaporation (from 27.5 to 26.9 at.%). With a better comprehension of the influence of heat-treatments on Ni-Mn-Ga laser-based prints, the small Mn evaporation should be easy to control by pre-alloying the initial powders.

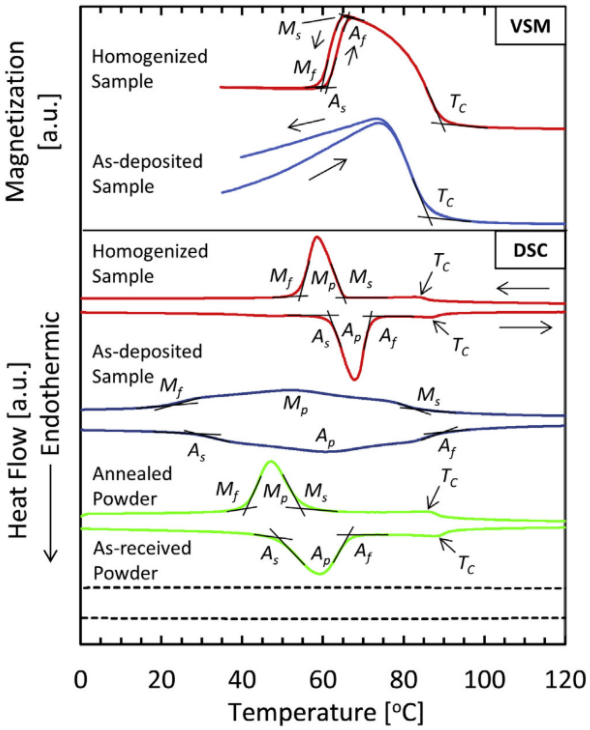

Figure 2.18. *DSC and magnetisation vs. temperature (VSM) results for the as-received and annealed powders, as-deposited sample, and homogenised-and-ordered sample. Amplitudes are not to scale,* [21].

6. Conclusion

Ni-Mn-Ga has exciting potential applications in cutting edge technologies such as fast actuators and energy harvesters. Studies on the MFIS and its correlation with the texture and porosity justify the use of AM processes to enhance the shape memory effect. Binder jetting, ink printing, L-DED and L-PBF have been used to produce near net shape Ni-Mn-Ga samples.

The low cost of ink-based methods (ink printing and binder jetting) to manufacture Ni-Mn-Ga parts is attractive as they do not require powder gas atomisation and binder jetting of ball milled powder is enough to exhibit a 0.01% MFIS [15]. However, ink-based methods require post processing which leads to a low control of the final shape and poor mechanical properties. On the other hand, laser-based techniques provide a high accuracy and control of the porosity by printing lattices. Moreover, the texture is easier tuneable to create bamboo-like grains and graded structures with some areas actuated or not, depending on the process parameters. Nevertheless, two concerns need to be raised on laser printing of Ni-Mn-Ga MSMA:

- The control of the composition and Mn evaporation. This problem can be solved by over-alloying the initial powder with ~1 or 2 at.% of Mn according to the previous studies [22–25].
- The high amount of residual stresses due to the rapid solidification of laser-based methods causing an increase of the twinning stress. As shown in [41], the residual stresses can be released by heat treatment leading to a 5.8% MFIS.

To conclude, among the four techniques studied, L-PBF appears to be the most suitable way to create near net shape lattices with large bamboo-like grains. Other AM processes such as electron beam melting (EBM) are yet to be studied. However, considering the relatively high vapor pressure of Mn, this process is likely not to be suitable for the manufacture of Ni-Mn-Ga. This process is carried out within a vacuum chamber, which may alter

the alloy chemistry and accordingly the magnetic performance even if minor Mn-evaporation occurs. Heat treatment such as homogenisation at temperatures between 1000 °C and 1100 °C, would lead to a further increase in the size of the grains and thus of the MFIS.

[It is important to note that two distinct approaches exist for producing porous Ni-Mn-Ga structures via additive manufacturing. The first approach leverages the intrinsic porosity generated by the manufacturing process itself. For instance, Caputo et al. employed binder jetting, achieving a 0.01% MFIS in their research [15,35]. Similarly, Ituarte et al. used the island scan strategy in L-PBF to generate porous structures [25]. The second approach involves the deliberate creation of lattice structures with "engineered" porosity, offering greater control over both the size and distribution of pores [40]. There has been no research that quantified the MFIS in lattice structures fabricated through L-PBF.]

Acknowledgements

AM acknowledges the financial support from the Defence Science and Technology Laboratory (DSTL) for her PhD Studentship, through the UK-French PhD studentship scheme.

Declaration of interest statement

The author declares that they have no known competing financial interests or personal relationships that could have appeared to influence the work reported in this paper.

Appendix – Literature review

Some information below has been added to the literature review post publication in order to have a better understanding of:

- The solidification mechanism and epitaxial growth involves in small structures;
- The magnetic energies that act in the formation of magnetic domains in Ni-Mn-Ga.

Solidification and epitaxial growth in small structures

L-PBF often results in a pronounced anisotropic grain structure characterised by columnar grains aligned along the build direction, owing to the rapid solidification inherent in the process. It is well established that the microstructure of L-PBF printed components is influenced not only by the process parameters but also by the build orientation and the part size. These factors impact the thermal gradient and resulting crystallographic texture [57]. Many studies have explored the impact of build direction on mechanical properties in bulk materials [58], yet there has been comparatively less research focused on understanding how both build direction and part size affect texture. With growing interest in lattice structures and the emergence of topological optimisation, understanding the spatial variation of microstructure becomes crucial. Complex lattices composed of thin struts oriented at various angles relative to the build direction experience differing thermal gradients and solidification rates.

While existing research has explored how strut angles affect defects, geometric integrity, and mechanical properties of lattices [59–61], fewer investigations have delved into their implications on microstructure. For instance, Jia et al. [59] examined the influence of strut angle on the mechanical properties of AlSi10Mg samples, observing an inverse correlation between increasing strut angle (angle with the platform) and elastic modulus, while yield and ultimate strength exhibited positive trends. A subtle reduction in average grain size with increasing strut angle was also observed, seemingly contradictory to expectations of large columnar grains aligned with the vertical strut direction.

Moreover, the size of the printed structure determines the melt pool size, significantly influencing the final microstructure. Several studies have explored the influence of size on microstructure, examining parameters like wall thickness [62–64] and strut diameter [65–69]. For instance, Takata et al. [62] studied the microstructure in AlSi10Mg thin walls ranging from 0.3 to 10 mm in thickness. They found no strong correlation between texture and wall thickness, possibly due to the presence of two phases. However, they noted variations in the ratio between α-Al grains and Si eutectic particles, affecting the mechanical behaviour of the final part. Leicht et al. [63] investigated stainless steel 316L walls ranging from 0.2mm to 3 mm, observing random texture in thin samples (<0.4 mm) and elongated grains with a <110> texture in thicker samples. Ahn et al. [64] similarly observed these outcomes in stainless steel 316L samples with wall thicknesses of 0.3 mm, 0.5 mm, 1 mm, and 1.5 mm. They noted that increasing wall thickness led to a reduction in overall cooling rate. This phenomenon is attributed to thicker samples undergoing more reheating during each layer scan, thereby maintaining warmth in adjacent tracks, and diminishing the overall cooling rate. Consequently, promoting epitaxial growth of columnar grains, resulting in higher texture.

Research on single struts has yielded diverse outcomes with thinner parts exhibiting higher texture. For example, Wang et al. [65] examined the microstructure and the mechanical properties in stainless steel 316L vertical struts ranging from 0.25 mm to 5 mm, producing a single crystal in 250 µm struts with a strong ⟨110⟩ texture along the build direction. Sanchez-Mata et al. [67] also achieved a single crystalline structure in 250 µm struts made of Hastelloy X, displaying a ⟨110⟩ texture along the build direction. Both studies observed that reducing strut diameter led to the formation of a single melt pool, reducing cooling rates and promoting epitaxial growth, resulting in near-single crystalline structures. Peyre et al. [68] confirmed experimentally and numerically that a single melt pool forms below 0.5 mm diameter struts in Inconel 625, with a strong <001> texture along the build direction. Niendorf et al. [69] also observed higher texture in smaller struts made of 316L, with a critical diameter for epitaxial growth between 0.65 mm and 1.1 mm.

There appears to be a discrepancy between studies investigating microstructure in walls, where thicker walls exhibit higher texture, and studies on single struts, where smaller diameters (<300 µm) display higher texture. This difference likely arises from the formation of a single melt pool in small struts, which is not the case in thick walls due to their length. Consequently, there's likely a threshold in strut diameter below which a single melt pool forms, resulting in a robust, near-single crystalline structure that would be beneficial for giant MFIS in Ni-Mn-Ga.

Magnetic energy in Ni-Mn-Ga

Ni-Mn-Ga alloys are ferromagnetic, meaning that within a certain temperature range, they exhibit spontaneous small magnetisation and long-range ordering of magnetic moments. This ferromagnetic interaction arises from the exchange coupling between neighbouring magnetic moments of Ni, Mn, and Ga atoms. Their magnetisation however is really weak and considered as soft magnets. Due to their orthorhombic crystal structure with one axis (c-axis in 10M and 14M) shorter than the other ones, they exhibit a strong magneto-crystalline anisotropy with the easy axis of magnetisation along the short crystallographic axis [70,71]. The formation of magnetic twins, which are regions with different magnetic orientations, contributes significantly to the overall magnetic anisotropy of the material. The anisotropy is one of the key elements for magnetic-induced reorientation (MIR) strongly linked to the presence of the martensite phase. The Zeeman energy is also a significant factor in Ni-Mn-Ga magnetic shape memory alloys. It refers to the energy associated with the interaction of magnetic moments with an external magnetic field. When an external magnetic field is applied, it causes the magnetic moments within the material to align with the field [72]. Several studies have modelled the behaviour of Ni-Mn-Ga and it seems that the formation of magnetic domains withing the crystallographic twins is still not fully understood [73]. Veligatla et al. [74] determine that at lower fields (0.02 T) the formation of magnetic domain is attributed to the magneto-crystalline anisotropy while at higher fields (0.06 T) it is attributed to the Zeeman energy. Moreover, due to the lattice geometry, Ni-Mn-Ga lattices should exhibit some magnetostrictive energy which occurs when the magnetic moments are arranged non-uniformly within the material, and generate a magnetic field, which in turn affects neighbouring magnetic moments. This interaction leads to the storage of energy within the material, known as magnetostatic energy. This is particularly important to consider for energy harvesting applications and is taken into account in some modelling studies on single crystal without a big impact [75].


RIMPLab
Homenaje
Tesis
2022

Part printed for the international women in materials science day 2022
Aluminium alloy using L-PBF process.

Chapter 3

Experimental procedure

This chapter describes the experimental procedure used during the entire project. The equipment is more detailed in this chapter than in the method description in each experimental chapter.

1. Material

Four batches of Ni-Mn-Ga powder were used during this research. The initial batch consisted of a blend of elemental powders; the mixing details are described in Chapter 4. Subsequent batches were procured through gas atomisation processes: one from Nanoval (used in Chapter 5), another from the University of Technology of Belfort-Montbéliard (UTBM, used in Chapter 5, Chapter 6, and Chapter 7), and the final batch from the Technical Research Centre of Finland (VTT, used in Chapter 8). The salient characteristics of each powder batch, including their compositions and granulometry, are summarised in Table 3.1. Uniformity was assessed by calculating the ratio of d_{90} to d_{10}. Particle size analyses were conducted in accordance with ISO13320 standards, employing a Malvern Mastersizer 2000 (Malvern, UK) and a Sync particle analyser (Microtrac MRB). Compositional analysis was performed using an x-ray fluorescence (XRF) analyser X-Strata 960 (Oxford Instruments) calibrated with a reference sample of known composition and with a 300 µm diameter collimator.

All batches were deliberately over-alloyed with excess Mn to counteract the anticipated evaporation phenomena inherent to the L-PBF.

Table 3.1. *Compositions and granulometry of the powder used.*

	Ni (at.%)	Mn (at.%)	Ga (at.%)	d_{10}	d_{50}	d_{90}	Uniformity
Elemental powder blend	~49	~31	~20	17.51	49.42	213.20	12.18
Nanoval initial (1)	49	31	21	13.12	27.49	63.32	4.83
Nanoval sieved (2)	49	31	21	28.36	47.67	78.08	2.75
UTBM	48.8	31.2	19.9	19.32	39.14	73.07	3.78
VTT	48.7	30.7	20.6	13.66	32.75	69.52	5.09

1.1. Elemental powder blend

The initial experiments involved the in-situ alloying of an elemental powder blend. The Ga ingots, with a purity of 99.99999% and a melting point of 30ºC, were purchased from NewMet (UK). The Ni powder, with a purity of 99.8%, was gas atomised by TLS Technik (Germany), while the Mn flakes, possessing a purity >99%, was acquired from Sigma-Aldrich (UK). The elements were blended through a procedure elaborated upon in Chapter 4 and subsequently sieved to obtain a batch within the 20-80µm range.

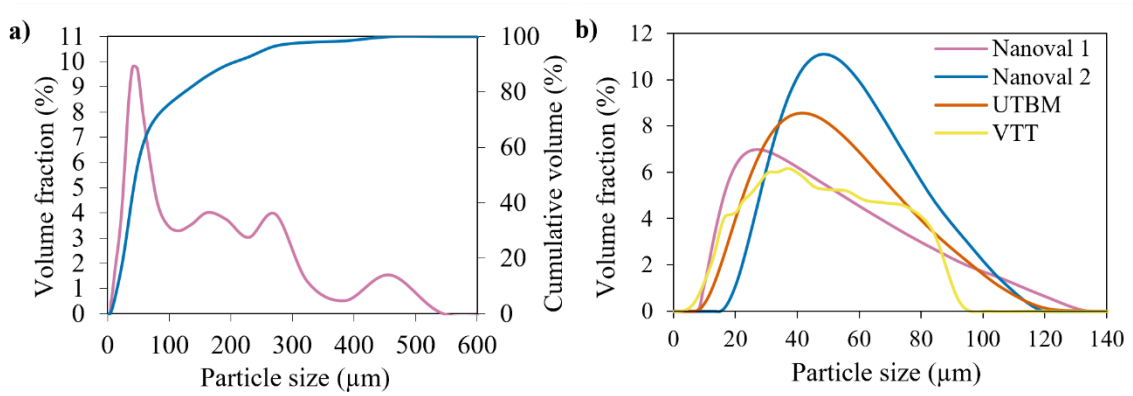

Figure 3.1. *Particle size distribution of (a) the elemental powder blend and (b) the gas atomised powder batches.*

1.2. Atomised powder

All gas atomised powders exhibited a spherical morphology, with some dendritic microstructure originating from the fast cooling of the gas atomisation and generally small number of satellites. Their respective particle size distributions are depicted in Figure 3.1.

A first gas atomised powder batch was obtained from Nanoval (Germany) and comprised Ga (99.99% purity), Ni (99.8% purity), Mn (99.877% purity), and was atomised with argon utilising the Nanoval process, targeting a typical fraction of 15-63 µm for L-PBF powder. First trials with this powder were not successful due to the poor flowability of the powder which was a result of the high amount of small particles, shifting the particle size distribution curve to the left. Consequently, the powder was sieved with a 30 µm mesh to eliminate fine particles resulting in a shift of d_{10}, d_{50} and d_{90} towards higher sizes (Table 3.1). Both curves are depicted in Figure 3.1. Because of the sieving process, the amount of powder left was too small to carry all experiments.

The second batch was produced through argon atomisation at UTBM in France. A total of 26 kg of powder, within the 20-90 µm size range, were generated from 41.5 kg of raw materials. The particle size distribution with specific d_{10}, d_{50} and d_{90} (Table 3.1) allow a good flowability. The Ni balls were procured from Goodfellow (UK) with a purity of 99.98%, the Mn flakes from Hauner (Germany) with 99.90% purity, and the Ga ingots from a Chinese supplier with 99.99% purity. These materials were melted in a zirconium crucible at 1390 ºC and atomised using a De Laval nozzle. The autoclave was pressurised at 8 bar and the chamber at 4 bar. A video of the atomisation process can be found here. However, the composition of this powder was slightly offset resulting in 14M microstructure instead of 10M (see Chapter 5 for more details).

The powder manufactured by VTT was also produced through argon gas atomisation employing precursor materials Ni (99.95%), Mn (99.99%), and Ga (99.99%). Subsequently, the atomised powder underwent mechanical sieving to obtain particles within the 15-80 µm size range.

2. Sample geometry and file preparation

Various sample geometries were investigated during this study.

Initial parameter optimisation occurred using bulk samples with cubic shapes of dimensions 7 × 7 × 7 mm³ and 10 × 10 × 10 mm³. Subsequently, the parameters were also optimised for lattices 2D geometries of dimensions 7.4 × 0.25 × 8 mm³ and 3D lattices measuring 8 × 8 × 8 mm³, all possessing 200 µm diameter struts. The selection of the 3D lattice geometry aimed to streamline optimisation efforts; it was deliberately anisotropic to facilitate orientation identification for sample preparation. Moreover, the lattice struts were aligned parallel to the sample's edges, allowing for easy microscopic observation on cut samples.

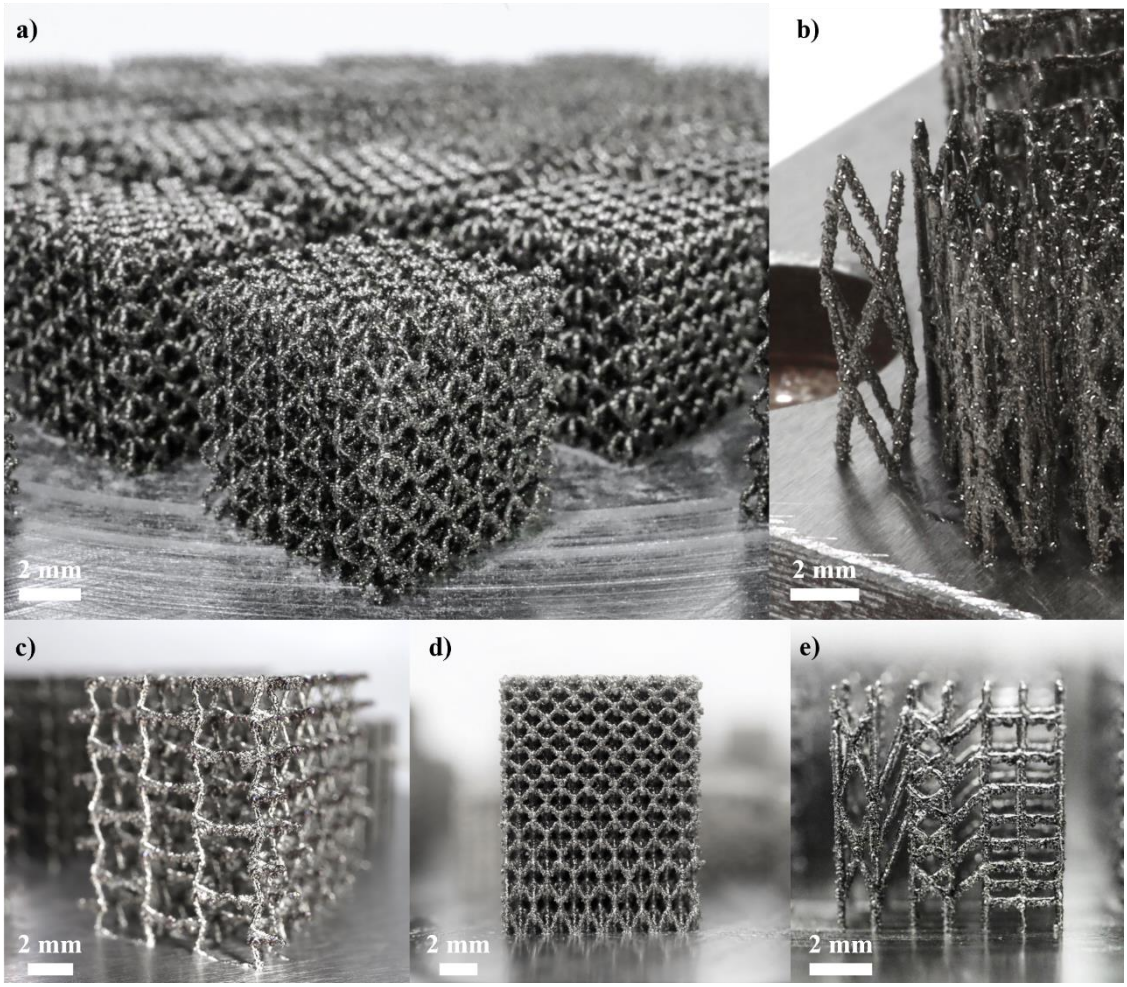

Figure 3.2. *Pictures of lattices sample with different geometries: (a) 3D lattice, (b) helix, (c) auxetic, (d) graded, and (e) 2D.*

Following parameter optimisation, additional lattice designs were generated, a subset of which is illustrated in Figure 3.2. On the image we see (from top left) a 3D lattice Figure 3.2a used for parameter optimisation (Chapter 5), a helix lattice with 75° struts Figure 3.2b used for the MFIS measurements (Chapter 8), an auxetic negative Poisson geometry Figure 3.2c (Chapter 7), a graded lattice to study the strut angle Figure 3.2d (Chapter 6) and a 2D lattice Figure 3.2e used for optimisation (Chapter 5). The design of all structures was accomplished using CAD software, namely CATIA V5 and nTopology. Subsequently, CAD files underwent conversion into

stereolithography files (STL files), encompassing layer-specific geometry and process parameters, employing Materialise Magics.

3. Manufacturing process

The majority of the samples were fabricated using the M2 Concept laser system located at the University of Birmingham (UoB). Nevertheless, a subset of samples was produced at UTBM employing a ReaLizer SLM250 system. Both printers operate based on the L-PBF process. Their primary distinction lies in their laser systems; specifically, the ReaLizer uses a pulse wave laser system, while the M2 employs a continuous wave laser system.

3.1. M2 concept laser system

3.1.1. Machine specifications

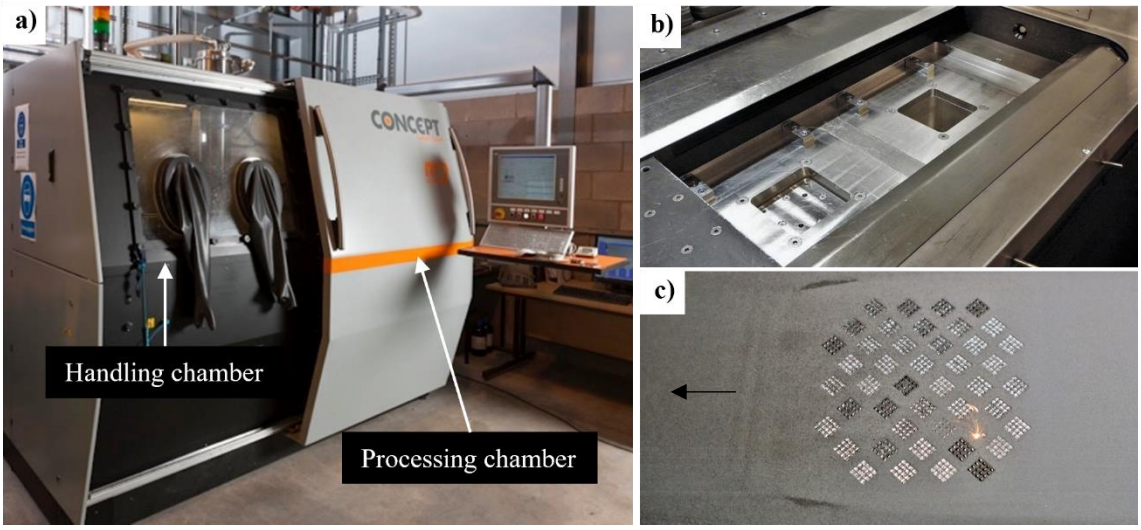

Figure 3.3. *M2 Concept laser L-PBF system with a picture of (b) the handling chamber and (c) the processing chamber. The black arrow represents the air flow and the recoater direction.*

Figure 3.3 illustrates the system comprising two chambers: a handling chamber for build preparation and setup (depicted in Figure 3.3b), and a smaller processing chamber for the manufacturing process (illustrated in Figure 3.3c). In the image, the machine is configured with a reduced kit tailored for 90 × 90 mm² substrates. With the large substrate kit installed, the system offers a maximum build envelope measuring 250 × 250 × 280 mm³, and the airflow direction is from right to left as shown in Figure 3.3c. The system is equipped with a continuous wave 400 W Yb-fibre laser, emitting at a wavelength of 1.064 µm, with a maximum beam transverse speed of 4 m/s. The laser beam has a fixed focal point diameter of approximately ~67 µm, characterised by a Gaussian irradiance profile. The layer thickness can be adjusted within the range of 25 µm to 50 µm, and the maximum scanning speed reaches 7000 mm/s. Powder distribution is achieved using a soft rubber recoater, which is replaced between each experiment. The entire process is conducted under a protective argon atmosphere, maintaining O_2 content less than 100 ppm. Following the process, the used powder is sieved through an 80 µm mesh to eliminate powder agglomerates and contaminants (such as broken parts detaching from the build), rendering it suitable for subsequent builds where composition and oxygen content are less critical. In this study, the reduced kit was

consistently employed, and all substrates used were of 316L stainless steel, varying in size from 40 × 40 mm² to 90 × 90 mm². The machine can be fitted with an in-house developed heating stage system that goes to temperatures between 100 ºC and 400 ºC and described in Chapter 6. The process can be seen in a video here.

3.1.2. Parameters and scanning strategy

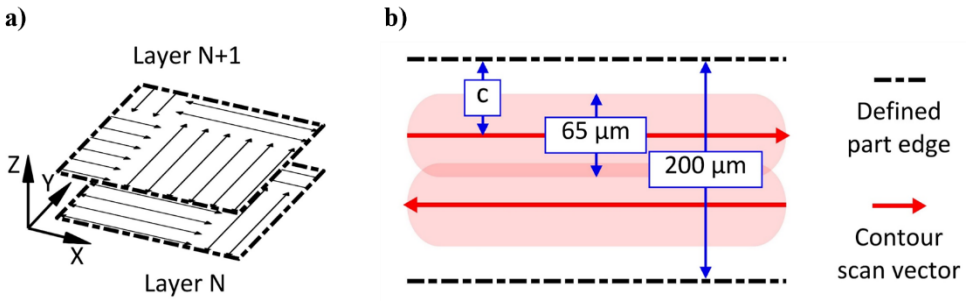

Figure 3.4. *Scanning strategies of (a) the bulk samples and (b) the lattice samples.*

All samples were manufactured with a uniform 25 µm layer thickness, denoted as *t*. Bulk cubes followed the default scanning strategy of the M2 Concept Laser, employing an island scan approach with 5 mm² islands and a 1mm shift in both x and y directions. Between each layer, a 90º rotation direction was applied, as depicted in Figure 3.4. The hatch spacing, *h*, varied within the range of 50 to 130 µm. In the case of lattice structures, a single contour scan strategy was employed, as illustrated in Figure 3.4. The contour distance *C* represents the distance from the design's edge to the middle of the laser track, essentially signifying the offset of the laser track. For analysis and parameter optimisation, the line energy density (*E*, J/mm) was used and calculated using the following equation:

$$E = \frac{P}{v}, \tag{1}$$

where *P* is the average laser power (W) and *v* is the scanning speed (mm/s).

Table 3.2 summarises the parameters employed on the M2 system, encompassing the optimised parameter set used for subsequent experiments.

Table 3.2. *Summary of the used parameters on the M2 Concept Laser.*

Parameter	Bulk samples	Lattice samples	Optimised lattices
t (µm)	25	25	25
P (W)	80, 90, 100, 150, 200, 250, 300	60, 65, 70, 75, 80, 90, 100	70
v (mm/s)	100–500 (50)	150–750 (50)	450
h (µm)	50, 75, 100, 130	-	-
C (µm)	-	25, 50, 75, 100	75
E (J/mm)	0.16–3.00	0.08–0.67	0.16

Statistical analysis was conducted using MiniTab and MATLAB software. Analysis of variance (ANOVA) statistical analysis was used to represent the influence of the printing parameters (P, v, C and h) on the Mn content, the strut size and the struts internal density. Each input data has one degree of freedom (DF). The adjusted sums (Adj SS), the adjusted mean squares (Adj MS), and the F-value (value indication the association of the input to

the response) are used to determine the P-value which corresponds to the statistical significance of the model. Typically, a P-value larger than 0.05 indicates that there is a significant correlation between the specific input and the response. More information can be found here [76].

3.2. ReaLizer system

3.2.1. Machine specifications

Figure 3.5 shows the ReaLizer SLM250 system equipped with a 400 W quasi-pulsed/modulated near-IR fibre laser. The laser spot size is 34-250 µm, a maximum built envelope of 250 × 250 × 300 mm^3, a layer thickness varying from 5 to 100 µm, and a heated building plate that goes up to 100 ºC. The chamber is filled with a protective argon atmosphere down to 0.1% O_2.

The powder is fed onto the build plate by a feeding system on top of the recoater that loads the powder on the front of the build and then the powder is spread by a circular rubber recoater that is changed in between each builds. The process can be seen in a video here.

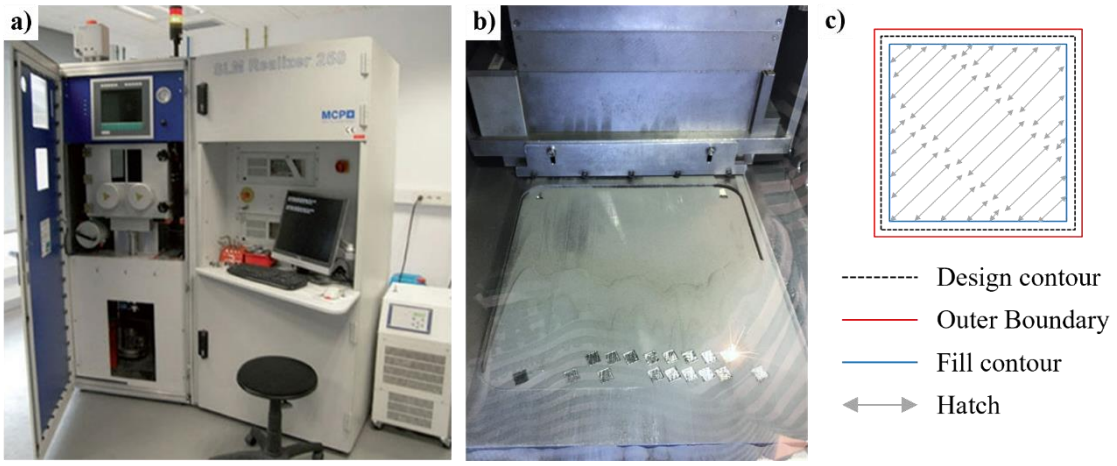

Figure 3.5. *(a) ReaLizer SLM250 L-PBF system with a picture of (b) the processing chamber, and (c) the scanning strategy used for bulk materials.*

3.2.2. Parameters and scanning strategy

All experiments were conducted employing a 25 µm layer thickness on 316L stainless steel substrates and using a 36º rotation between every layer.

The scanning speed (v) follows the following equation:

$$v = \frac{P_{dist}}{T_{expo}+\frac{P_{dist}}{V_{eng}}}, \quad (1)$$

with P_{dist} the distance between 2 points, T_{expo} the exposure per point and V_{eng} the speed of the engine constant.

The parameters used are described in Table 3.3.

Table 3.3. *Summary of the used parameters on the ReaLizer system.*

Parameter	Single tracks	Bulk samples	Lattice samples
t (µm)	-	25	25
P (W)	100, 150, 200, 250, 300	150, 200, 250, 300	150, 200, 250, 300
P_{dist} (µm)	20, 25, 30, 35, 40	25	25
T_{expo} (µs)	35, 45, 55, 65, 75	32, 40, 52, 74, 115	32, 40, 52, 74, 115
v (mm/s)	440, 443, 448, 455, 465	200, 300, 400, 500, 600	200, 300, 400, 500
h (µm)	-	130, 150, 170, 190, 210	130, 150, 211
E (J/mm)	0.215 to 0.682	0.3 to 3.5	0.3 to 1.5

4. Post processing

4.1. Sample preparation

To prepare the samples, they were initially detached from their substrates, either manually for thin lattices or via electrical discharge machining (EDM) for others. Subsequently, the samples underwent a thorough cleaning in an ultrasonic bath containing ethanol, effectively removing any loose powder particles. For microstructure observation, the samples were cut using EDM and certain were cold mounted in epoxy resin. The samples were ground and polished using a Tegramin Struers polisher, employing the following method:

- Griding on a diamond-grit disc P220, corresponds to a removal rate of 75 µm, with water;
- Fine griding on a P2000 disc (equivalent to 10 µm removal) with water;
- Polishing on a woven acetate cloth with a 3 µm diamond suspension;
- Final polishing on a flocked viscose cloth with a 1 µm diamond suspension.

Notably, the polishing of un-mounted lattice samples posed challenges due to the detachment of unmelted powders from the struts, which could contaminate the polishing cloth. Consequently, the fine griding step was used with water to flush loose particles, deviating from the typical use of a diamond suspension in common polishing procedures. Moreover, both polishing methods were kept short, and the cloth was meticulously cleaned under water between each sample to prevent contamination.

In addition to mechanical preparation, selected samples underwent electropolishing, applying a constant voltage of 12 V at -20 °C within an electrolyte solution comprising a volumetric ratio of 3:1 ethanol to 60% HNO_3. In this process, the samples served as the anode, while a stainless-steel component acted as the cathode. Magnetic stirring was employed to facilitate solution mixing.

4.2. Heat-treatment

A subset of samples underwent heat treatment according to the methodology established in [56], utilising the equipment illustrated in Figure 3.6. The furnace employed for this purpose was an in-house system at LUT university (Finland), based on an MTI OTF-1200X furnace operating under pressurised argon conditions (~300 mbar at ambient temperature) to prevent chemical evaporation. The furnace core consisted of a 60 mm length tube, ensuring a temperature precision of ±1 ºC. The heat treatment process included the following steps, illustrated in Figure 3.7:

- Heating at a rate of 250 ºC per hour from room temperature;
- Homogenisation step at either 1040 ºC, 1060 ºC, or 1080 ºC (depending on the sample) for a duration of 12 hours;
- Cooling to the ordering temperature at a rate of 100 ºC per hour;
- Maintaining an ordering temperature of 800 ºC for 4 hours;
- Gradual furnace cooling.

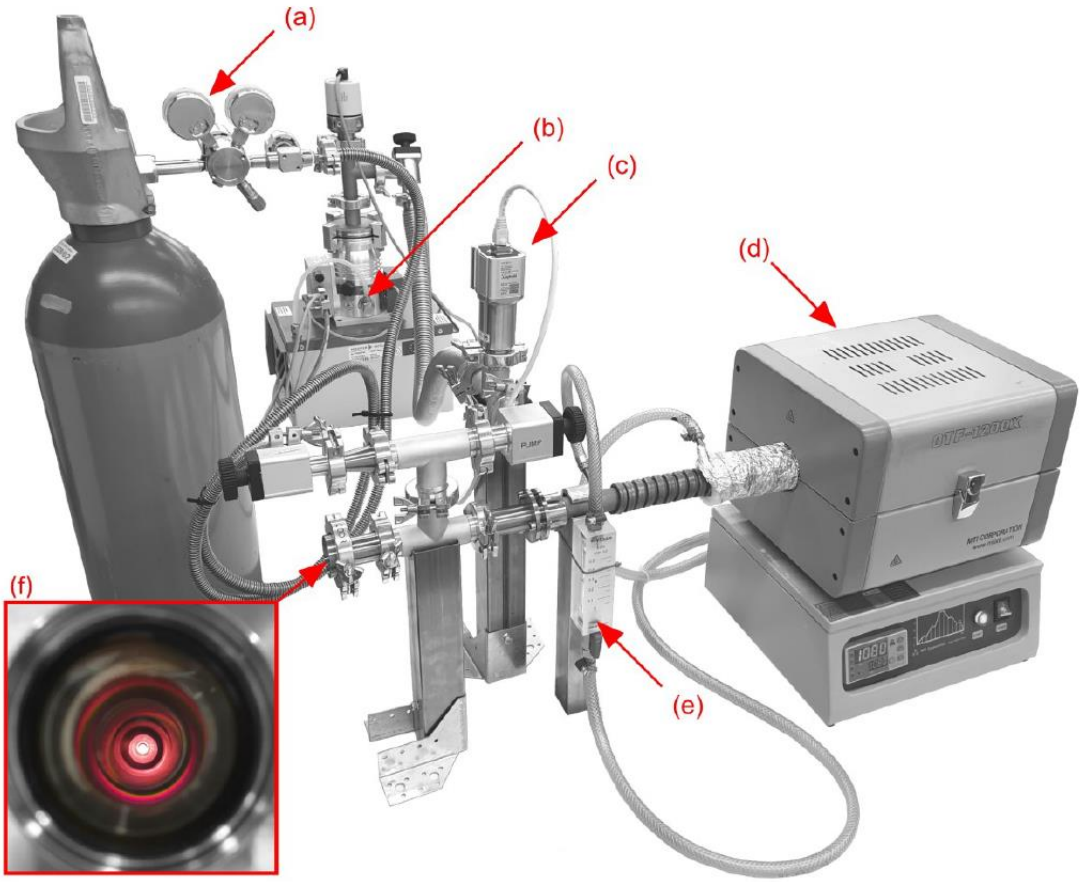

Figure 3.6. *The in-house-developed heat-treatment system from* [77]. *(a) high-purity argon inlet, (b) turbopump, (c) vacuum meter, (d) heat-treatment furnace, (e) coolant flow meter, and (f) access to the main tube of the heat-treatment system with a vacuum window allowing direct observation of the heat-treated samples.*

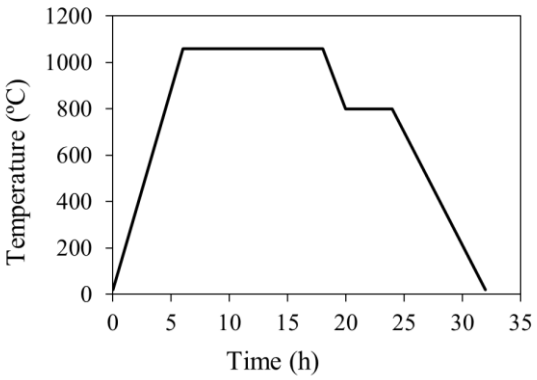

Figure 3.7. *Heat treatment procedure with homogenisation step followed by ordering and furnace cooling.*

5. Characterisation

Characterisation were conducted across four distinct academic institutions: primarily at UoB, with supplementary work carried out at LUT, UTBM, and electron backscatter diffraction (EBSD) analysis performed at The University of Manchester (UoM). If not specified, the experiment was conducted at UoB.

5.1. Density and composition

Density assessments were conducted in adherence to ASTM B962-17 standards, employing the Archimedes principle in ethanol. Results were corroborated through image analysis using Image J software. The density of the lattice struts was determined through optical imaging.

Chemical composition analysis was executed at LUT with an absolute accuracy of 0.3 at.% using an x-ray fluorescence (XRF) analyser X-Strata 960 (Oxford Instruments). Calibration was achieved employing a Ni-Mn-Ga reference sample of known composition, and a 300 µm beam diameter was employed.

The O_2 content of the powder was quantified using a LECO TC400 Series Elemental Analyzer at UTBM.

5.2. Microstructure

Optical micrographs were obtained employing a Zeiss Axioscope 5 microscope at UoB, a Meiji Techno MT7000 trinocular metallurgical microscope equipped with polarised light contrast lenses at LUT, and a Keyence VHX-7000 4K digital microscope also equipped with polarised light and e (DIC) at UoB and UTBM.

For more precise imaging at higher magnifications, a desktop Hitachi TM3000 scanning electron microscope (SEM) fitted with an energy dispersive spectroscopy (EDS) detector was used at UoB, along with a JEOL JSM 7800F SEM equipped with a Bruker X Flash 5130 EDS detector at UTBM.

For orientation and texture analysis, EBSD was performed at UoM, facilitated by the Henry Royce student equipment access scheme, utilising a TESCAN Clara FEG-SEM system equipped with a NewTec Scientific FurnaSEM oven and an Oxford Symmetry 2 EBSD camera. The sample was affixed to the oven using conductive carbon paste, and tests were conducted at temperatures approximately ranging from 150 to 200 ºC, employing a beam current of 20nA and step size ranging from 0.5 µm to 1.5 µm. The analysis of EBSD data was made using the software Atex.

5.3. Crystal structure

X-ray diffraction (XRD) was performed at LUT using a PANalytical Empyrean 3 diffractometer (Cu tube, $\lambda = 0.15406$ nm and Co tube, $\lambda=0.17890$ nm) equipped with poly-capillary optics, a PIXcel3D-Medipix3 detector, and a heating stage.

The Cu tube was used in Chapter 5 while the Co tube was used in Chapter 4 and Chapter 6.

The martensite peaks were indexed within the crystal coordinate system of the $L2_1$ austenite parent phase. The analysis assumes that the martensite phases exhibit distortion (elongation or contraction) along the a-, b-, and c-axes, with a small gamma angle typically around 90.33 for 10M and 90.55 for 14M. These distorted phases are considered as variations of a standard four-layered cell of the $L2_1$ phase. This approach does not account for modulation, leading to the non-indexing of peaks originating from the superstructure. This method enables a direct estimation of the theoretical maximum MFIS through the c/a ratio. This approach is widely adopted within the MSM community. More information can be found here [78].

5.4. Magnetic and thermal properties

Phase transformation temperatures were ascertained employing a low-field AC magnetic susceptibility device (LFMS) developed in-house at LUT, operating under a constant ~5 mT field and a heating/cooling rate of 6 °C/min. Differential scanning calorimetry (DSC) was performed at UoB, employing a Netzsch STA 449 F3 Jupiter instrument with a temperature range of -150 °C to 2400 °C using a heating/cooling rate of 5 °C/min.

Magnetic properties were further characterised using a LakeShore 8600 Series Vibrating Sample Magnetometer (VSM), which could apply a maximum constant field of 5 T in the configuration employed, along with a furnace setup with a maximum temperature of 1000 °C. Each hysteresis loop was performed 10 times to avoid any error in the measurements. The demagnetisation factor was determined with the shape of the samples considering the envelope of the lattice samples as a rectangle or a cylinder.

5.5. Mechanical properties

Compression experiments were performed using an Instron 3345 testing machine equipped with a 5kN load cell at room temperature (approximately 20 ºC). The stroke rate was set at 1.3 mm/min. To minimise radial friction, lubrication grease was applied to the contact surface between the samples and the compression plates. A digital image correlation (DIC) system was used to observe macroscale fracture and to measure strain. The surface roughness of the bulk samples and the lattice pattern provide sufficient contrast for DIC analysis. The images were analysed using the MATLAB-based 2D DIC software package 'Ncorr' [79]. The mechanical properties of the lattices were calculated according to ISO13314:2011. The estimated elastic modulus of the lattices was considered as the slope of linear fits between the two stress values σ_{20} and σ_{70}. The first maximum stress σ_{max} and the related strain, ε_{max}, are summarised in Table 3.2.

Nanoindentation was performed to determine the elastic modulus and hardness using a NanoTest system (Micro Materials, UK) equipped with a Berkovich tip and applying a maximum load of 20 mN, a holding time of 5 s, and a distance between points of 15 µm.

5.6. MFIS measurements

An experimental setup was created to capture MFIS using the VSM and a high-speed camera. This setup involved recording a sample rotating in a magnetic field using a high-speed camera, which would provide data on the activation angle and strain. However, the results obtained were inconclusive due to camera alignment issues. Nevertheless, this set-up is described here for future reference. Figure 3.8 illustrates the setup, with the high-speed camera positioned beneath the magnetic poles of the VSM. Two significant challenges were encountered during these experiments. Firstly, the magnetic field affected the camera's lens, causing slight movement. Secondly, the positioning of the lens beneath the sample made it impossible to achieve perfect alignment. A potential solution to both issues involves using a mirror-based system with more precise alignment. A test was conducted on a single crystal, and the video footage can be found here. Ultimately, the MFIS was measured ex-situ by magnetising the sample in various directions within the VSM and observing it under a microscope between each magnetisation step.

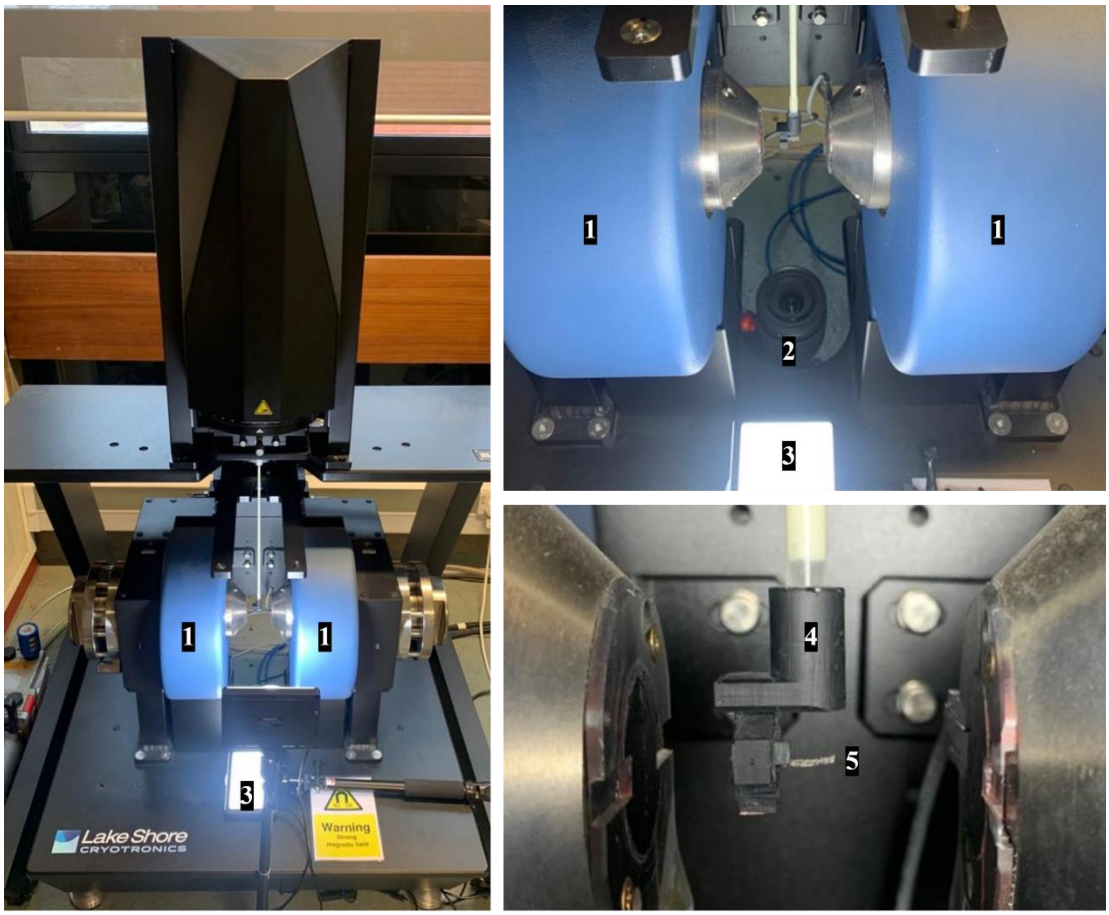

1. VSM electromagnet poles
2. High speed camera
3. Lights (another one was placed in front)
4. Sample holder
5. Sample

Figure 3.8. *Setup with the VSM and high-speed camera for MFIS recording.*

Top: Voronoi cube necklace made of Ti6Al4V
Bottom: mountains ring with intended high surface roughness made of stainless steel
3D printed using L-PBF process.

Chapter 4

In-situ alloying laser powder bed fusion of Ni-Mn-Ga magnetic shape memory alloy using liquid Ga

This chapter outlines the results from in-situ alloying of Ni-Mn-Ga powder for L-PBF. The paper was submitted to Progress in Additive Manufacturing journal on the 3rd of July 2023.

Submitted as:

A. Milleret, V. Laitinen, K. Ullakko, N. Fenineche, M.M. Attallah, In-situ alloying laser powder bed fusion of Ni-Mn-Ga magnetic shape memory alloy using liquid Ga, Progress in Additive Manufacturing (2023).

Author contributions:

AM: Conceptualisation, Methodology, Investigation, Formal analysis, Data curation, Visualisation, Writing - original draft preparation. **VL:** Investigation, Formal Analysis (characterisation by XRF and XRD), Data curation, Visualisation, Writing - review & editing. **KU:** Supervision, Resources, Funding acquisition. **NF:** Supervision, Resources, Funding acquisition. **MA:** Writing – review & editing,Supervision, Resources, Funding acquisition.

Abstract:

Ni-Mn-Ga-based magnetic shape memory alloys can exhibit large magnetic-field-induced strains (MFIS). Recently, additive manufacturing techniques, especially laser powder bed fusion (L-PBF), have been successfully used to manufacture functional polycrystalline Ni-Mn-Ga with complex geometries, such as 'bamboo-grained' lattice structures. However, previous approaches of L-PBF of Ni-Mn-Ga have used pre-alloyed powders, which can limit the compositional freedom of the manufactured devices. This study explores, for the first time, the feasibility of an in-situ L-PBF alloying approach using a powder blend of elemental Ni, Mn, and Ga. Promising results were obtained despite the significant differences between the elemental Ni and Mn powders and the liquid Ga. The microstructure of the as-built sample showed distinct stripe patterns from the 14M structure confirmed by XRD analysis. Heat-treatment significantly improved chemical homogeneity, dissolved the Ni-rich phase but couldn't dissolve MnO hindering the shape memory effect.

1. Introduction

Ni-Mn-Ga-based magnetic shape memory (MSM) alloys have received much attention since their discovery in 1996 [1] due to their ability to exhibit large magnetic-field-induced strains (MFIS). This straining phenomenon occurs at ambient temperature due to the magnetic-field-induced reorientation of the martensite twin variants and is subsequently observable as twin boundary motion. Large MFIS is typically observed in single crystals [3,4,8] or individual grains [41] as grain boundaries obstruct twin boundary motion. However, adding porosity to polycrystalline Ni-Mn-Ga reduces grain boundary constraints, leading to increase the MFIS. Research by Chmielus et al. [6] showed that using sodium aluminate as a spaceholder in a cast polycrystalline Ni-Mn-Ga foam resulted in an MFIS of 8.7%. Additive manufacturing techniques have also been used to increase the MSM effect in polycrystals by printing lattices and bamboo-grained structures, with binder-jetting [15–18], ink-printing [19,20], laser-based directed energy deposition [21], and laser powder bed fusion (L-PBF) [23,24,41,43,80] being investigated. Of these, L-PBF has been shown to be the most suitable process for producing 'bamboo-grained' lattice structures [80,81].

Previous research on L-PBF of Ni-Mn-Ga used pre-alloyed gas atomised powders, however, gas atomisation is a costly process with limited composition freedom. Studies have revealed that the evaporation of Mn in L-PBF Ni-Mn-Ga samples is greatly impacted by the process parameters, thus affecting the MSM effect [23,80]. An elemental approach, using Ni, Mn, and Ga blend, offers greater composition freedom and can mitigate evaporation issues, modify properties, and manage microstructural development. This approach has already proven successful in creating Ni-Mn-Ga thin films [82], microtubes [83], and micro-trusses through ink printing and sintering [19].

In the L-PBF process, using powder blends has been associated with issues such as low repeatability, unmelted powders, and segregation. The final microstructure is largely dependent on the degree of mixing and the size of the laser beam. In order to minimise composition gradients, the powder elements must be of similar melting temperatures, particle size, and flowability [84]. Despite these challenges, the use of powder blends has gained popularity for its cost-effectiveness and versatility in adjusting chemical composition, especially in the development of high entropy alloys [84,85]. In the case of Ni-Mn-Ga, Ga's low melting point (~30 °C) may pose difficulty in blending with other elements, but it readily forms alloys with both Ni and Mn. This study explores, for the first time, L-PBF of Ni-Mn-Ga from an elemental powder blend.

2. Experimental procedure

2.1. Powder blend

The blend was made from elemental gas atomised Ni powder, crushed Mn, and liquid Ga. The elements were blend together to obtain a composition of $Ni_{49}Mn_{31}Ga_{20}$ (at.%) with an additional 2 at.% of Mn to compensate from the typical evaporation of Mn during the L-PBF process [22,24,80]. The melting temperature of the purchased Ga was approximately ~30 °C, therefore the Ga was incorporated as a liquid into the blend of Ni and Mn using different steps schematised in Figure 4.1. First, a bottled mixture of Ni (spherical powder) + Mn (crushed powder) + Ga (liquid) was placed onto a rotational mill for two hours, with a reheating step (up to 40 °C) every 5 min. The bottle was heated by placing in hot water during approximately 3 min and shook several times. Second,

the bottle was placed on a vibrational table for two hours, with a reheating step every 5 min. Third, the bottle was heated up again at 40 °C and placed on the rotational table for an hour with a doubled vibration speed.

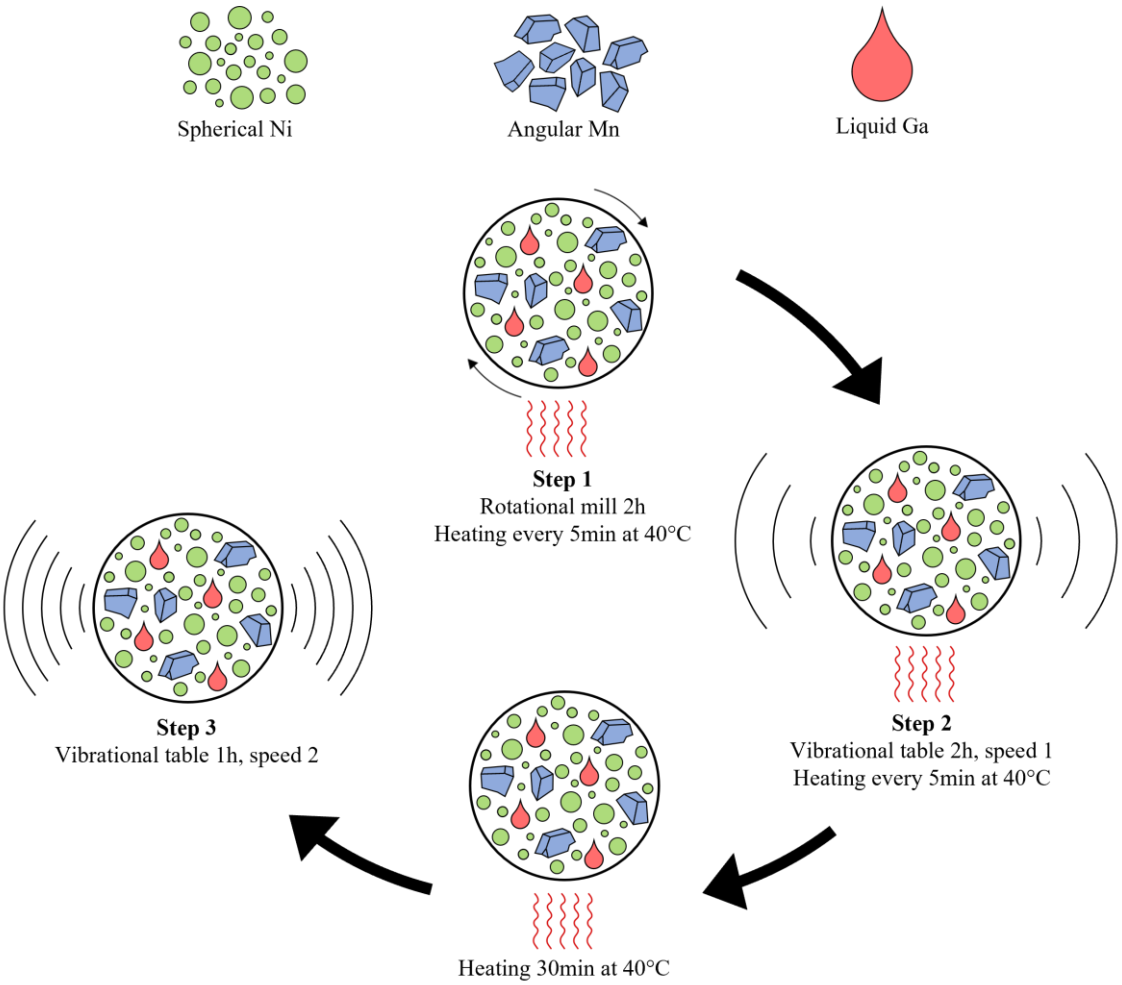

Figure 4.1. *Schematic diagram representing the steps during the powder blend preparation.*

Scanning electron microscopy (SEM) was performed after each step using a Hitachi TM3000 microscope equipped with energy dispersive spectroscopy (EDS). Figure 4.2 shows a micrograph and an EDS map after each step. It is observed that a simple ball milling step leads to large Ga spherical aggregates (Figure 4.2a) and low vibration leads to large plane aggregates (Figure 4.2b). Only an increase of the vibration speed causes the Ga to break into smaller particles although remaining larger than the Ni and Mn ones. All weighting and powders collection were performed inside a glovebox filled with argon atmosphere to prevent oxidation.

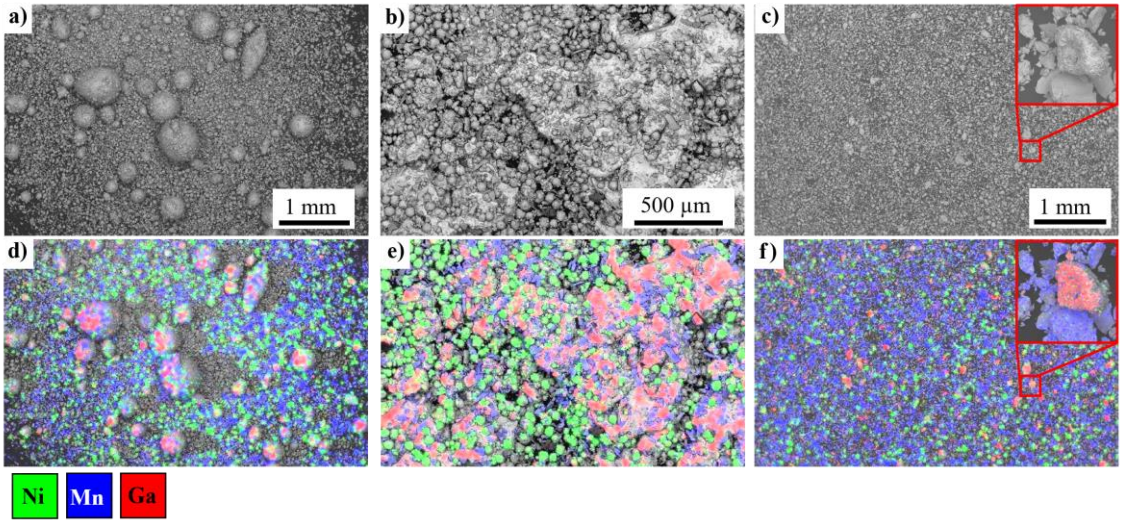

Figure 4.2. *SEM images of the powder blend after the (a) first, (b) second, and (c) third step, and (d, e, f) their respective EDS maps. The red outlined inset images in (c) and (f) show a Ga particle.*

The particle size distribution (d_{10} = 17.51 µm, d_{50} = 49.42 µm, and d_{90} = 213.2 µm) of the blended powder was measured by laser diffraction (Sync particle analyser, Microtrac MRB) and shown in Figure 4.3. The powder includes a relatively large distribution of different particle sizes. Two distinct distribution peaks are observable, the first one corresponding to the Ni and Mn particles at 39.75 µm, and the second one corresponding to Ga particles at 151.10 µm.

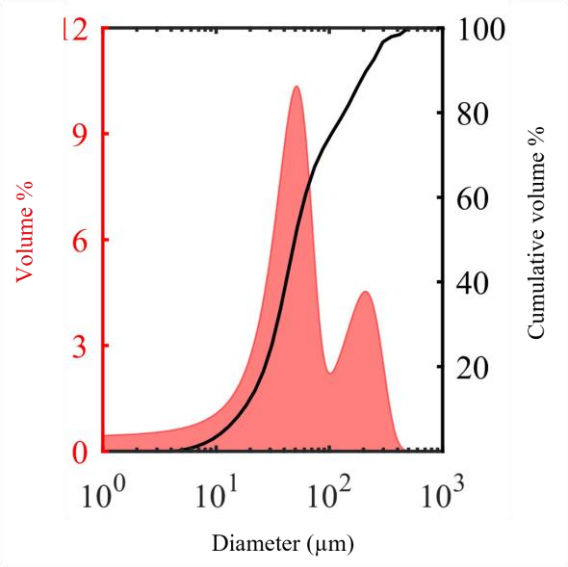

Figure 4.3. *Particle size distribution of the Ni-Mn-Ga powder blend.*

2.2. L-PBF process and design of experiment

L-PBF samples were fabricated using a Concept Laser M2 Cusing system, operated using a 400 W continuous-wave fibre laser, with a wavelength of 1.064 µm, a maximum beam speed up to 4 m/s and a fixed focus diameter of ~67 µm. The samples were built under a protective argon atmosphere to obtain the minimum O_2 content of

100 ppm. A unidirectional scanning strategy was adopted, as illustrated schematically in Figure 4.4a, with a 25 µm layer thickness.

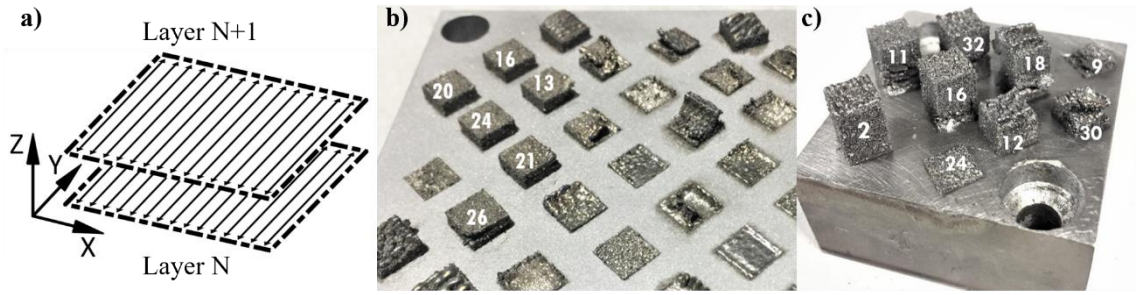

Figure 4.4. *(a) Unidirectional strategy used for building the samples, (b) the first batch of samples on the larger substrate, and (c) the second batch of samples on the smaller substrate. The labels correspond to the same sets of parameters (listed in table 2) in both batch 1 and 2.*

The process parameters used in the design of experiment are summarised in **Table 4.1**. Cuboids of 7 × 7 × 4 mm^3 were printed on a 90 × 90 mm^2 316L substrate and cut from the substrate using electrical discharge machining (EDM). The small amount of powder blended resulted in a small print (4 mm height) therefore the samples were analysed in the XY plane. A second build was made with the recycled powder on a smaller 40 × 40 mm^2 316L substrate. Cuboids of 5 × 5 × 10 mm^3 were printed, cut, and analysed in the build direction. The two builds were printed with a 25 µm layer thickness and are shown in Figure 4.4b, c. The surface energy density (E_s, J/mm^2) was calculated using the following equation:

$$E_s = \frac{P}{h * v}, \quad (1)$$

where P is the average laser power (W), h is the hatching distance (mm), and v is the scanning speed (mm/s).

Table 4.1. *Summary of the used parameters.*

P (W)	v (mm/s)	h (µm)	E_s (J/mm^2)
100	1000	15	0.37-20
150	2000	45	
200	3000	90	
250			
300			

2.3. Sample preparation and analysis

The samples were metallographically polished to a mirror-like finish and etched for less than 1 second with Kalling's II reagent to reveal the martensite twins. The relative density was evaluated through image analysis using ImageJ software. One of the samples with the highest relative density was heat-treated according to [56] by first homogenising them at 1060 °C for 12 hours, followed by atomic ordering treatment at 800 °C for 4 hours, after which the samples were furnace cooled to ambient temperature. The composition and homogeneity was evaluated by the aforementioned EDS system and by x-ray fluorescence (XRF) on 16 points with an absolute accuracy of 0.3 at.% using a X-Strata 960 (Oxford Instruments) analyser calibrated with a reference Ni-Mn-Ga sample of known composition. X-ray diffraction (XRD) measurements were performed using a PANalytical Empyrean 3 diffractometer (Co tube, λ = 0.179031 nm) equipped with parallel beam x-ray mirror optics for the

incident beam, a PIXcel3D-Medipix3 detector (scanning line detector mode, 0.5° anti-scatter slit), and a zero-background sample holder. Differential scanning calorimetry (DSC) was conducted from 20°C to 200°C upon heating and cooling (DSC – 5 °C/min heating/cooling rate) on a Netzsch STA 449 F3 Jupiter to determine the phase transformation temperatures.

3. Results and discussion

Figure 4.4 presents a picture of the two builds done with the powder blend. Only a limited set of parameters were effective in producing cubes. Samples with high energy density (E > 4 J/mm^2) overheated and delaminated while samples with low energy density (E < 0.74 J/mm^2) did not stick to the substrate due to lack of melting. The successful samples exhibited a high level of porosity (20 – 30 %) with a rough surface finish. The second batch was conducted with the aim of controlling repeatability in taller samples, however, only one set of parameters from the first batch proved successful. This lack of repeatability can be attributed to the poor flowability of the powder blend, as Ga particles are larger in size compared to Ni and Mn particles. Samples 20 (250 W, 3000 mm/s, 45 µm) and 24 (150 W, 3000 mm/s, 45 µm) were successful in the first batch, but showed signs of delamination in the second, potentially due to an overheating caused by the larger height or insufficient wettability with the substrate. Another factor could be a smaller heat dissipation due to the smaller substrate in the second batch. Table 4.2 lists the parameters of the successful samples. A favourable energy density of around 1 J/mm^2 was observed, however, further optimisation of parameters is necessary to fully understand their individual impact.

Table 4.2. *Parameters of the selected samples built in the first and the second batch using the elemental powder blend. The numbering corresponds to the same set regardless the batch number.*

	Sample #	P (W)	v (mm/s)	h (µm)	E_s (J/mm^2)
Batch 1	13	200	3000	90	0.74
	16	300	3000	90	1.11
	20	250	3000	45	1.85
	21	100	3000	15	2.22
	24	150	3000	45	1.11
	26	150	2000	90	0.83
Batch 2	2	200	2000	45	2.22
	11	200	2000	90	1.11
	16	300	3000	90	1.11
	32	250	2000	90	1.39

The XRF results presented in Table 4.3 demonstrate that the chemical composition of the sample is highly heterogeneous, with a significant variation of Ga observed throughout. Ga readily forms alloys with Mn and Ni, as evidenced by the presence of Ga-rich regions observed throughout sample 20 (250W, 3000mm/s, 45µm). This is apparent in Figure 4.5a, which was captured under an optical microscope and reveals dark needle structures. EDS analysis confirms the presence of Ga-Mn and Ga-Ni compounds. Segregations of Ni and Mn have also been noted in other areas, which may be a result of unmelted powders or insufficient heat input to blend the melt pool. The variation in Ga content is also related to the build layer thickness compared to the Ga powder particles. According to Figure 4.3, the second peak (corresponding to Ga particles) is approximately at 151.1 µm whereas the layer thickness used during printing was only 25 µm. Consequently, the recoater may push some of the larger

Ga particles from the build plate, which can result in selective removal of Ga from the blend. Additionally, some Ga particles may melt prematurely due to the heat accumulation during L-PBF, which may also contribute variation of the Ga content and formed microstructures locally within the sample.

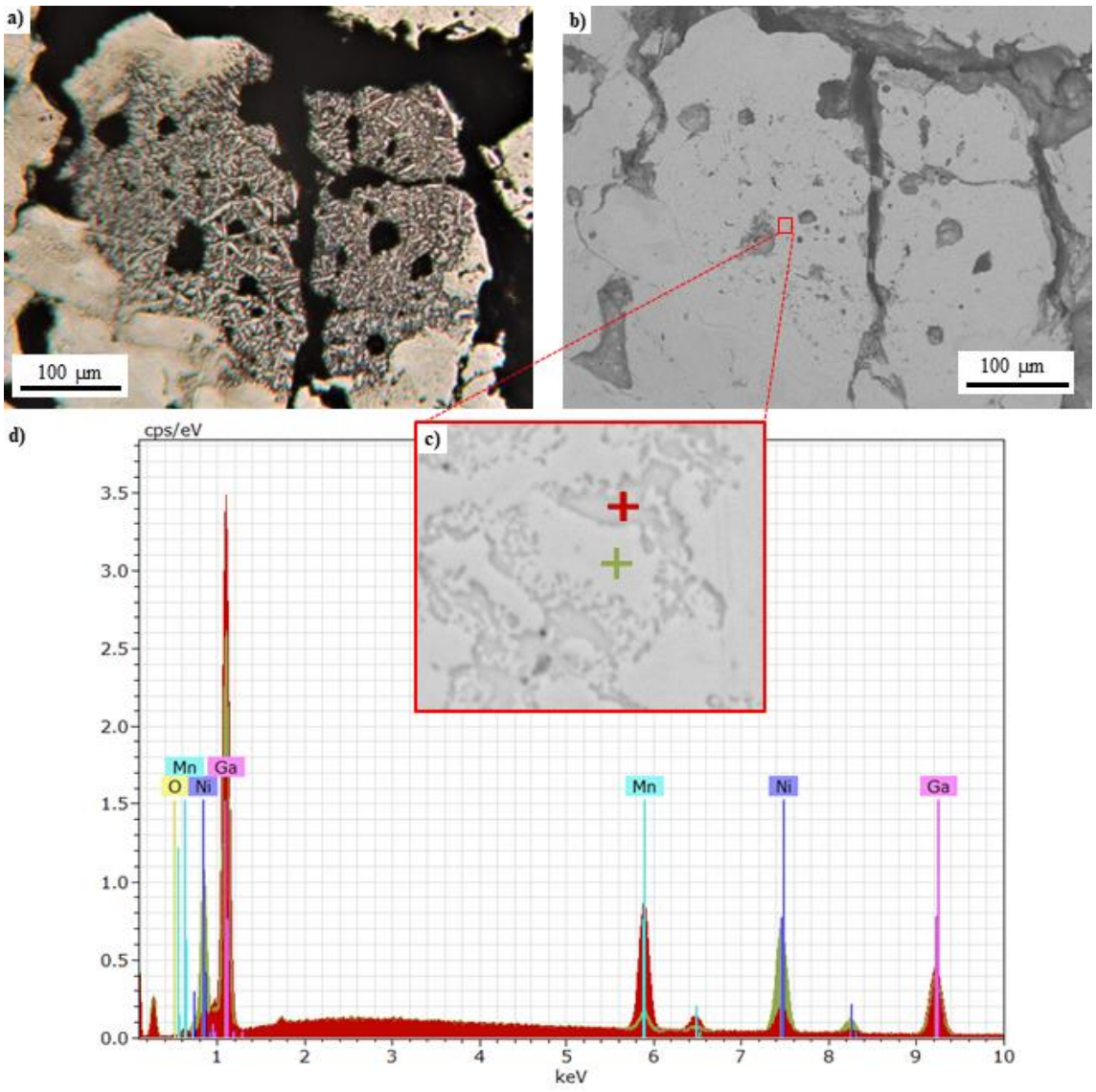

Figure 4.5. *(a) An optical micrograph, (b,c) SEM images, and (d) EDS analysis of a Ga-rich region in the XY plane. (d) Ga-Mn compound is shown in red and a Ga-Ni compound in green.*

Heat treatment resulted in elemental diffusion and the subsequent increase in chemical homogeneity. Despite this improvement, however, the standard deviation remains substantial when compared to experiments using pre-alloyed powder [86]. Specifically, the standard deviation here is on the order of 1 at.% when using a powder blend, whereas when using pre-alloyed powders, it is on the order of 0.1 at.% while previous studies have established that achieving final homogeneity is critical to observe a MFIS. To further improve homogeneity, several L-PBF process related approaches could be adopted, such as using slower scanning speed and/or lower laser power, using double scanning, or the implementation of a heated platform during the fabrication process. These methods would allow for longer exposure and reduction of the thermal gradients, ultimately helping to dissolve the chemical segregations and therefore, further enhancing homogeneity. Another approach would be to use pre-alloyed Ga. Preferably Ni-Ga as the Mn is the element which the composition is the most likely to fluctuate and would be easier to control as an elemental powder.

Table 4.3. *Composition analysis (XRF) of sample 20 (250 W, 3000 mm/s, 45 µm) before and after heat-treatment.*

	As-built		
	Ni (at.%)	Mn (at.%)	Ga (at.%)
Average	48.79	35.28	15.93
Standard deviation	4.40	2.81	6.28
Range	16.56	11.32	23.58
	Heat-treated		
	Ni (at.%)	Mn (at.%)	Ga (at.%)
Average	50.63	36.43	12.94
Standard deviation	0.80	0.97	0.96
Range	2.80	3.53	3.35

Figure 4.6 shows the x-ray diffractograms obtained at ambient temperature for sample 20 (250 W, 3000 mm/s, 45 µm) before and after heat-treatment. By examining the diffraction peaks present in the samples, we were able to identify the crystalline phases and determine their average lattice parameters, as shown in Table 4.4.

Table 4.4. *Approximate lattice parameters of the crystalline phases detected from the sample 20 (250 W, 3000 mm/s, 45 µm) before and after heat-treatment. All lattice parameters are presented with an approximate accuracy of ± 0.02 Å.*

	As-built			**Heat-treated**		
Phase	**a (Å)**	**b (Å)**	**c (Å)**	**a (Å)**	**b (Å)**	**c (Å)**
MnO	4.44	4.44	4.44	4.44	4.44	4.44
Ni-rich	3.62	3.62	3.62	-	-	-
Cubic $L2_1$	5.85	5.85	5.85	5.93	5.93	5.93
14M	6.06	5.90	5.50	-	-	-
NM	-	-	-	5.38	5.38	6.65

The lattice parameters of seven-layered modulated (14M) orthorhombic and non-modulated (NM) tetragonal martensites are presented in the coordinate system of the parent phase (cubic $L2_1$ austenite). Only the main diffraction peaks were considered in calculating the lattice parameters. The as-built sample exhibited a complex diffraction pattern with a large quantity of peaks originating from multiple different crystalline phases. After

conducting a thorough examination, it was determined that most of the peaks belonged to the MnO and cubic $L2_1$ austenite phases. Nonetheless, some low-intensity peaks indicate the presence of Ni-rich γ phase and 14M martensite in the sample. The 14M peaks' relatively low intensity compared to the background noise made it impossible to estimate the monoclinic angle, resulting in the use of an orthorhombic approximation with a gamma-angle of 90° to calculate the phase's lattice parameters. Foremost, the presence of multiple crystalline phases was expected based on the large compositional variations observed in the sample using XRF. The existence of the γ phase can be attributed to the presence of the Ni-rich segregations within the as-built sample, whereas MnO was likely introduced into the sample as surface oxides of the used Mn-powder prior to L-PBF. Additionally, the presence of multiple phases can be partially attributed to the inherent chemical composition inhomogeneity that typically occurs in the anisotropic microstructures developed during L-PBF. The heat-treated sample exhibited a markedly different diffraction pattern, as the peaks originating from the 14M martensite and Ni-rich γ phases were no longer present, and instead, the diffraction peaks originating from NM martensite were observed. As mentioned in the XRF section, heat treatment at 1060 °C for 12 hours resulted in significant chemical homogenisation, effectively dissolving the 14M martensite and Ni-rich γ phase. The heat-treated sample was primarily composed of the cubic $L2_1$ austenite, NM martensite and the previously observed MnO. The sample displayed a little variation in the lattice parameters of MnO, which was expected due to its relatively high melting temperature of 1842 °C [87], preventing it from dissolving during the heat treatment. The presence of Mn-oxide is most likely to pin the twin boundary motion and cancel the MSM effect. Additionally, the final composition of the heat-treated sample is largely deviated from the ideal compositions [41] for obtaining large MFIS. However, the advantage of in-situ alloying is that the composition could be easily tuned by adapting the proportions of the elemental powders.

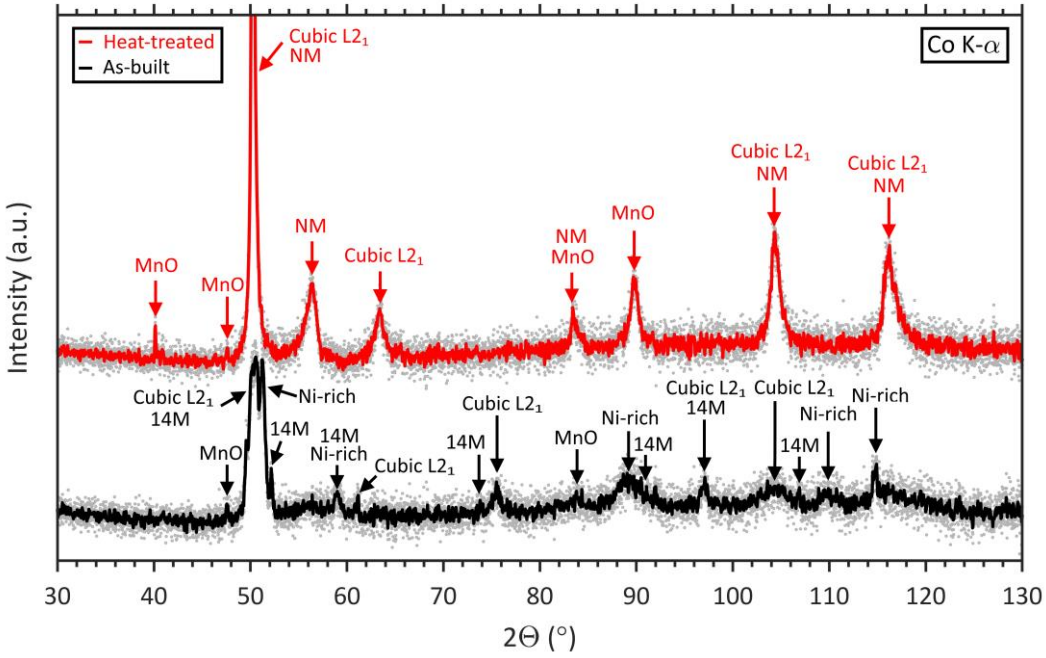

Figure 4.6. *XRD diffractograms of sample 20 (250 W, 3000 mm/s, 45 µm) in as-built and heat-treated conditions.*

Sample 20 (250 W, 3000 mm/s, 45 µm) was inspected using optical microscopy and SEM before and after heat-treatment (Figure 4.7). The relative density of the as-built sample 20 was determined to be ~70 % using image analysis. Upon etching, the as-built sample exhibited stripe-like patterns associated with martensitic twins, consistent with the XRD analysis that identified the presence of 14M martensite in the sample. No segregation can be seen in Figure 4.7. Following heat treatment, the grain structure of the sample was more clearly observed, consisting predominantly of equiaxed grains with an average size of 62 nm. Each grain exhibited a distinct martensite twin structure, consistent with the XRD results indicating a predominantly martensitic (NM phase) in the heat-treated sample, with some twins spanning grain boundaries. These findings suggest a high degree of chemical homogenisation and recrystallisation of the microstructure. EDS analysis of various regions of the heat-treated sample showed no evidence of element segregation. However, DSC analysis before and after heat treatment did not reveal any distinct phase transformations. Despite the absence of discernible segregation in the EDS analysis and the SEM observations, the XRD analysis showed that the sample was not crystallographically uniform after heat treatment. The presence of multiple crystal structures and chemical heterogeneities (as shown by XRF results) effectively hinders the detection of the phase transformations in the DSC results.

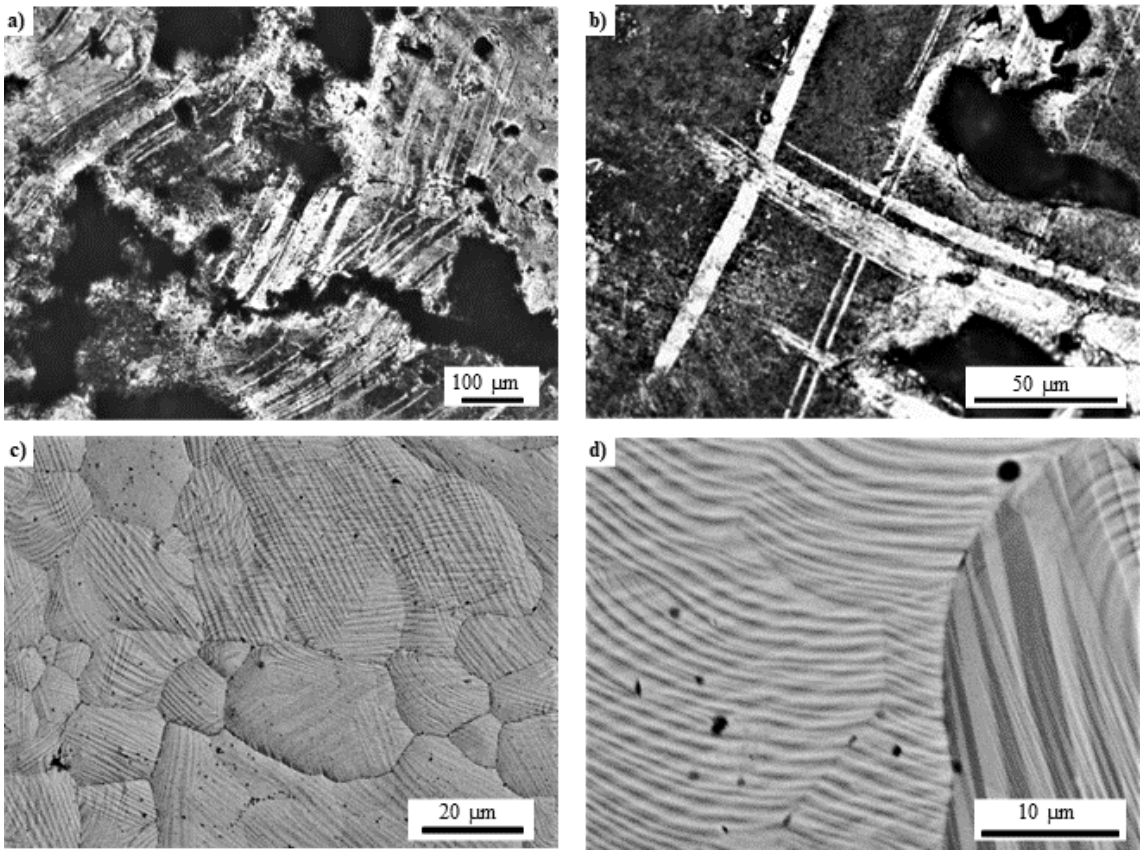

Figure 4.7. *(a, b) Optical micrographs showing twins in as-built sample 20 (250 W, 3000 mm/s, 45 µm), and (c, d) SEM micrographs showing grains and twins in heat-treated sample 20.*

4. Conclusion

This research represents a preliminary investigation of Ni-Mn-Ga manufactured using L-PBF from a blend of elemental powders. Despite the significant differences between the elemental powders and liquid Ga, the results are promising. The microstructure features distinctive stripe patterns originating from the 14M crystallographic structure, as confirmed by XRD analysis. Although heat-treatment improved chemical homogeneity, and dissolved the Ni-rich phase, it was unable to dissolve the MnO phase, which impedes the shape memory effect. Further studies should focus on dissolving the segregations through adapted heat treatment, different scanning strategy, double scanning, or pre-alloying of two elements such as Ni-Ga or Ni-Mn. Furthermore, the in-situ alloying process provides the opportunity to explore adding additional elements such as Co, Cu, Cr or Fe [7] to reduce segregation through alloying with Ni.

Acknowledgements

This work was financially supported by the Defence Science and Technology Laboratory (DSTL), the Strategic Research Council of Finland (grant number 313349), the Academy of Finland (grant number 325910), and the AMBI (Analytics-based Management for Business and Manufacturing Industry) research platform of Lappeenranta-Lahti University of Technology LUT.

Declarations

On behalf of all authors, the corresponding author states that there is no conflict of interest.

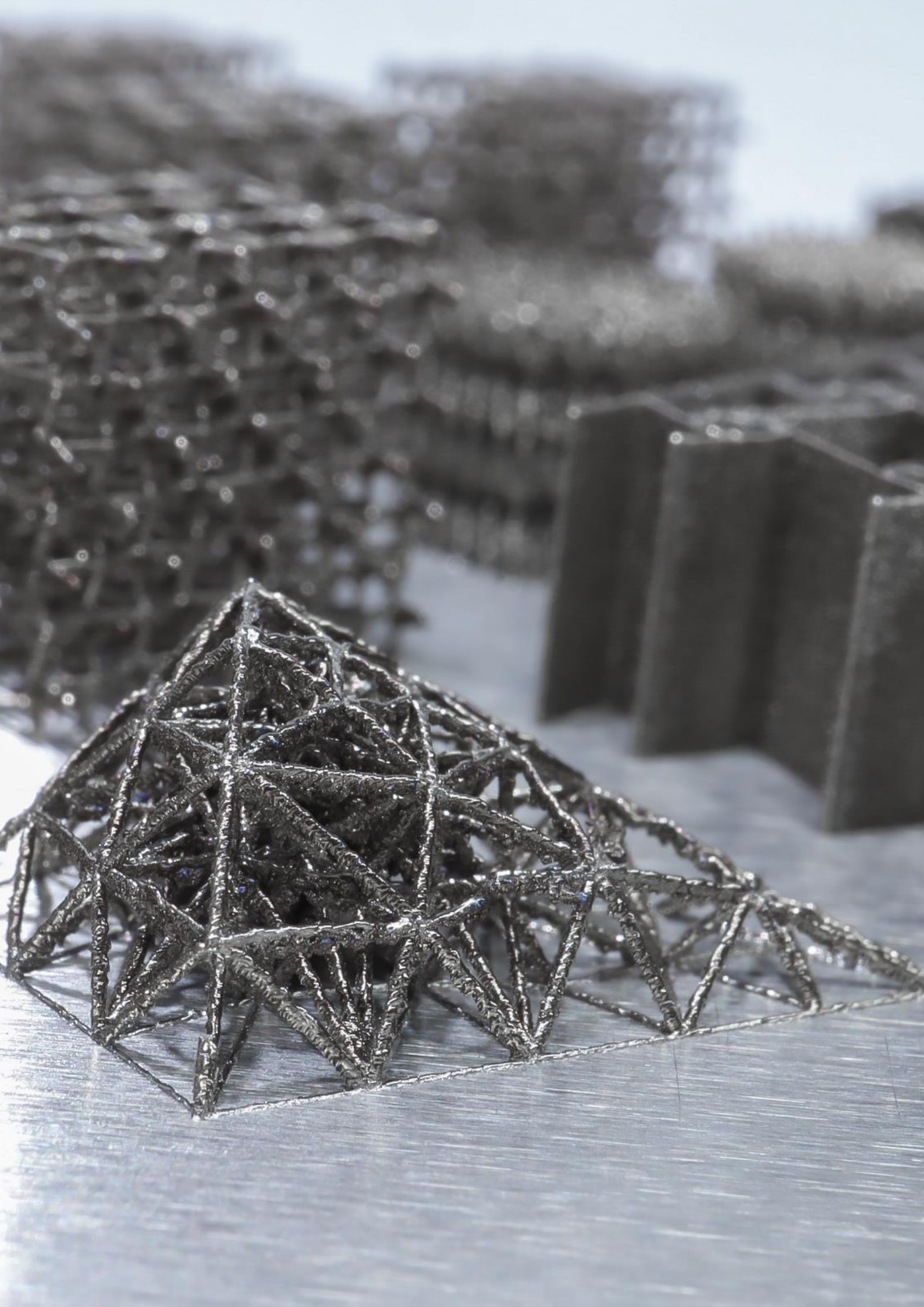

Lattice structure made of Ni-Mn-Ga
3D printed using L-PBF process.

Chapter 5

Laser powder bed fusion of (14 M) Ni-Mn-Ga magnetic shape memory alloy lattices

This chapter describes the design of experiment conducted to optimise the process to produce bulk and lattice samples through L-PBF. Part of this chapter has been published in Additive Manufacturing journal. Preliminary experiments were done at UTBM with a ReaLizer SLM500 L-PBF system while the paper describes experiments done on a M2 Concept Laser. The preliminary experiments are described in the supplementary work at the end of this chapter.

Published as:

A. Milleret, V. Laitinen, K. Ullakko, N. Fenineche, M.M. Attallah, Laser powder bed fusion of (14 M) Ni-Mn-Ga magnetic shape memory alloy lattices, Additive Manufacturing 60 (2022) 103231. Doi: 10.1016/j.addma.2022.103231.

Author contributions:

AM: Conceptualisation, Methodology, Investigation, Formal analysis, Data curation, Visualisation, Writing - original draft preparation. **VL:** Methodology, Investigation, Formal Analysis (characterisation by XRF, LFMS and XRD), Data curation, Visualisation, Writing - review & editing. **KU:** Supervision, Resources, Funding acquisition. **NF:** Supervision, Resources, Funding acquisition. **MA:** Writing – review & editing,Supervision, Resources, Funding acquisition.

Abstract:

Recent developments in the additive manufacturing of magnetic shape memory (MSM) alloys have demonstrated the high potential of laser powder bed fusion (L-PBF) process for the manufacture of functional polycrystalline Ni-Mn-Ga-based actuating devices with complex geometries. This research utilises a systematic experimental approach to develop and optimise an L-PBF process for manufacturing Ni-Mn-Ga lattices. Experiments were conducted in two distinctive stages: firstly, to characterise the selective Mn evaporation in bulk samples built; secondly, to investigate the influence of the applied process parameters on the relative density and geometrical integrity of the lattice struts. The lattices manufactured using optimised parameters had a high internal density of ~99% and were heat-treated for chemical homogenisation, grain growth, and atomic ordering. The heat-treated lattices exhibited a seven-layered modulated (14 M) martensite structure at ambient temperature with the phase transformation temperatures and magnetic properties corresponding to the chemical composition. Primarily, the results demonstrate that the beneficial 'bamboo-grained' structure can be obtained in individual lattice struts via post-process heat treatment. Plus, they also confirm that the use of thinned-down structures, such as lattices, can effectively prevent the cracking previously observed in bulk samples. Although there remains plenty of room for further research on this topic, these results highlight the high potential of L-PBF for the manufacture of a new generation of MSM-based actuating devices.

1. Introduction

Ni-Mn-Ga-based magnetic shape memory (MSM) alloys [1] exhibit large magnetic-field-induced strains (MFIS) of up to 6% [3] in five-layered modulated (5M/10M) martensite, 10% [4] in seven-layered modulated (7M/14M) martensite, and 12% [8] in (elementally-doped) non-modulated (NM) martensite. These large MFIS have been reported in oriented single crystals and are driven by twin boundary motion that occurs when the easy magnetisation axis of the crystal lattice of the low-symmetric martensitic phase reorientates along an applied magnetic field. Compared to thermally activated shape memory alloys, such as Ni-Ti, the response of MSM alloys is much faster (even few microseconds [88]) making them good candidates for ultrafast actuators [9], sensors [10], micro-pumps [11], and energy harvesters [12].

Grain boundaries in polycrystalline Ni-Mn-Ga alloys act as barriers to twin boundary motion and increase the stress required for such movement. Subsequently, most polycrystalline Ni-Mn-Ga alloys do not exhibit large MFIS [5]. Nevertheless, some conditions exist in which polycrystalline Ni-Mn-Ga alloys can exhibit moderate or even large MFIS. Research by [6] shows that high MFIS – up to 8.7% – can be obtained in polycrystalline Ni-Mn-Ga foams made using a special casting replication technique. In these Ni-Mn-Ga foams, large MFIS is enhanced by the formation of a so-called 'bamboo-like grain structure' [6], in which individual grains form a hierarchical structure with connecting nodes and crystallographically-oriented single crystalline struts. Strong crystallographic texture and unconstrained struts allow for the free motion of twin boundaries in those grains, resulting in large MFIS throughout the entire foam [31,36]. This mechanism can also be effective on a larger size-scale when applied to bulk Ni-Mn-Ga polycrystals with strong crystallographic texture and coarse grain structure [6,41].

The utilisation of polycrystalline Ni-Mn-Ga alloys in functional MSM-based devices opens up new opportunities for the application of novel advanced manufacturing methods, such as additive manufacturing (AM) techniques. Most research has focused on binder-based processes, such as binder-jetting [15–18] and 3D ink-printing [19,20], with being interested in the production of polycrystalline Ni-Mn-Ga foams. The primary disadvantage associated with these processes concerns the use of water-soluble binding materials that result in residual oxygen and titanium, which can compromise the processed alloy's functional properties [18,89]. Additionally, these techniques create random distribution and/or size porosity, resulting in poor mechanical behaviour that, in combination with the generally low force-output of the polycrystalline Ni-Mn-Ga foams, makes the efficacy of these processes less viable.

Nevertheless, laser additive manufacturing techniques, such as laser powder bed fusion (L-PBF) and laser-based directed energy deposition (L-DED), enable the manufacture of polycrystalline Ni-Mn-Ga without sacrificing compositional integrity [81,90]. Plus, these processes are highly suited to the manufacturing of bulk polycrystalline materials with high relative densities and crystallographic textures [91]. Indeed, a recent article [41] demonstrated the feasibility of L-PBF for the AM of functional polycrystalline Ni-Mn-Ga samples that can, after sufficient reduction of grain boundary constraints, develop up to 5.8% MFIS. The obtained MFIS is similar to that of conventionally manufactured single crystals featuring the same crystal structure. Furthermore, it is considerably larger than the 0.01% MFIS previously reported in additively manufactured (by binder-jetting) Ni-Mn-Ga [15], or the ~1–4% MFIS obtained in conventionally manufactured bulk polycrystalline Ni-Mn-Ga

[18,89]. Moreover, the Mn evaporation in L-PBF can be used for in-situ alloy tailoring, which is not possible in ink-based processes. Hence, L-PBF is by far considered the most suitable AM process for the manufacture of functional polycrystalline Ni-Mn-Ga devices.

To date, scientific research on the L-PBF of Ni-Mn-Ga has primally focused on parameter optimisation for enabling the manufacture of bulk structures [23,24], thin walls [41], and lattice-like structures [40]. The foremost observation made in the cited literature is the selective evaporation of Mn, which occurs during L-PBF melting. The evaporation levels are dependent on the applied process parameters and can be used for in-situ tailoring of the final component's chemical composition, which also enables for controlling the crystal structure and the resulting MSM-related properties [41]. Crucially, however, the grain structure of L-PBF-built Ni-Mn-Ga bulk samples typically prevents the free motion of the twin boundaries and considerably reduces the potential MFIS. Consequently, [20,41] propose that future research should focus on the systematic development of the L-PBF process towards the manufacturing of 'bamboo-grained' lattice structures, wherein neighbouring grains are less constrained and pose fewer obstacles to twin boundary motion.

Additively manufactured lattices often exhibit design inaccuracies as a result of: the machine's minimum manufacturable strut size, the melt pool size, the struts' inclination with respect to the substrate, the resulting surface roughness (e.g. staircase effect), and the number of residual particles sintered around the struts [14]. Consequently, the optimum parameters for bulk and lattice samples differ. The aim of this study is to develop an L-PBF process for the manufacture of Ni-Mn-Ga lattices, wherein the beneficial 'bamboo-grained' structure can be obtained via post-process heat treatment.

2. Material and methods

2.1. Powder feedstock

$Ni_{48.83}Mn_{31.24}Ga_{19.93}$ powder was synthesised by argon gas atomisation using a Nanoval atomisation system equipped with a DeLaval nozzle. The powder was over-alloyed (prior to atomisation) with approximately 1.3 at.% of additional Mn by substituting Ni in order to obtain the desired final composition ($Ni_{50}Mn_{30}Ga_{20}$) to compensate for the typical Mn evaporation occurring during the L-PBF process [23]. The powder composition was measured with an absolute accuracy of 0.3 at.% using the x-ray fluorescence (XRF) analyser X-Strata 960 (Oxford Instruments) calibrated with a reference sample of known composition. The O_2 content of the powder was measured using a LECO TC400 Series Elemental Analyzer as 283±12 ppm. This oxygen level is within the range (<500 ppm) to allow large MFIS [41]. The particle size distribution (d_{10} = 19.315 µm, d_{50} = 39.140 µm, and d_{90} = 73.074 µm) of the powder was measured by the laser diffraction powder sizer (Mastersizer 2000, Malvern Instruments Ltd., UK) and shown in Figure 5.1a. The powder's surface morphology is shown in Figure 5.1b and a cross-section features in Figure 5.1c. Both scanning electron microscope (SEM) images depict dense spherical particles with a low number of observable satellites.

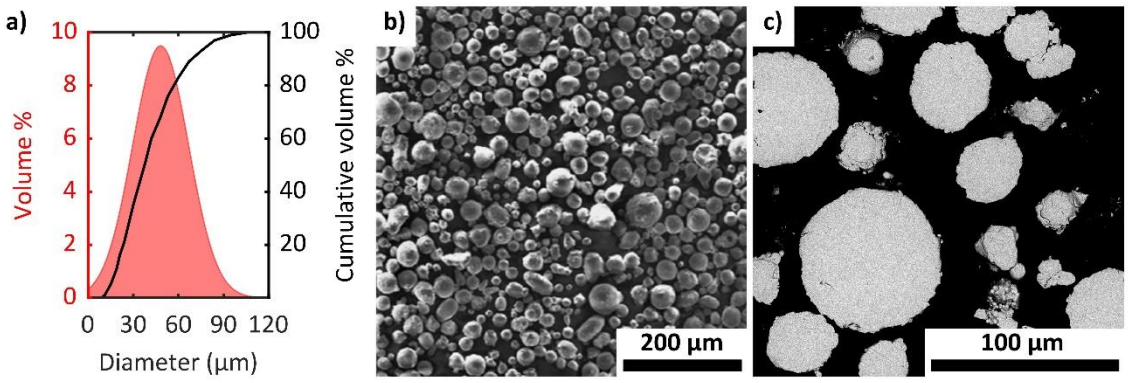

Figure 5.1. *(a) particle size distribution of the Ni-Mn-Ga powder; (b) SEM image of the powder; (c) SEM image of the cross-sectioned powder.*

2.2. Laser powder bed fusion process and design of the experiments

L-PBF samples were built using a Concept Laser M2 Cusing system, operated using a 400 W continuous-wave fibre laser with a wavelength of 1.064 µm, a maximum beam transverse speed of 4 m/s, and a fixed laser beam focal point diameter of ~67 µm. The samples were built under a protective argon atmosphere to obtain the minimum O_2 content of 100 ppm.

The first set of samples – 7 × 7 × 7 mm^3 cubes with small supports – was built on a stainless steel 316L substrate using a constant powder layer thickness (t) of 25 µm. An island scan strategy (5 mm island size) with a 1 mm shift in x- and y-directions and a 90° rotation direction between each layer was used to reduce overheating [92]. As shown in Figure 5.2ab, no contour scan was used. The cubes were built according to the parameters listed in Table 5.1, with chemical composition determined to establish a baseline for the Mn evaporation and to calibrate the used L-PBF system with respect to previous studies [23].

The second set of samples – lattices with two distinct geometries (see Figure 5.2cd) – were built to adapt the optimal parameters obtained from experiments with the cube geometry for the manufacture of 3D lattices. All lattices were built on a stainless steel 316L substrate using a constant powder layer thickness of 25 µm. No propagation of the elements from the stainless steel substrate could be observed in the produced samples, likely due to the build's low layer thickness. The first lattice geometry (7.4 × 0.25 × 8 mm^3 2D lattices exhibiting variable strut angles of 0°, 45°, and 70°) was used to study the influence of the applied parameters and the strut angle (with respect to the build platform) on the built struts' geometrical integrity. The second lattice geometry (8 × 8 × 8 mm^3 3D lattices) was used to study the struts' internal density and chemical composition. Additionally, the magnetic and crystallographic properties of the as-built and heat-treated 3D lattices, made according to the optimum parameters, were investigated. All lattices were made using the designed strut thickness of 200 µm, which was found to be a feasible size based on preliminary experiments conducted using a single contour scanning strategy – see Figure 5.2e. For this approach, the parameter 'contour distance' (C, µm) denotes the spatial distance between the edge of the designed strut in the computer-aided design (CAD) 3D model and the scan path of the laser beam. The parameters used for building the lattices are summarised in Table 5.1.

For modelling the effects of the varied parameters on the selected properties, line energy density (E, J/mm) was employed and calculated using the following equation:

$$E = \frac{P}{v}, \quad (1)$$

where P is the average laser power (W) and v is the scanning speed (mm/s).

Table 5.1. *Summary of the used parameters.*

Parameter	Bulk samples	Lattice samples	Optimised lattices
t (µm)	25	25	25
P (W)	80, 90, 100, 150, 200, 250, 300	60, 65, 70, 75, 80, 90, 100	70
v (mm/s)	100–500 (50)	150–750 (50)	450
h (µm)	50, 75, 100, 130	-	-
C (µm)	-	25, 50, 75, 100	75
E (J/mm)	0.16–3.00	0.08–0.67	0.16

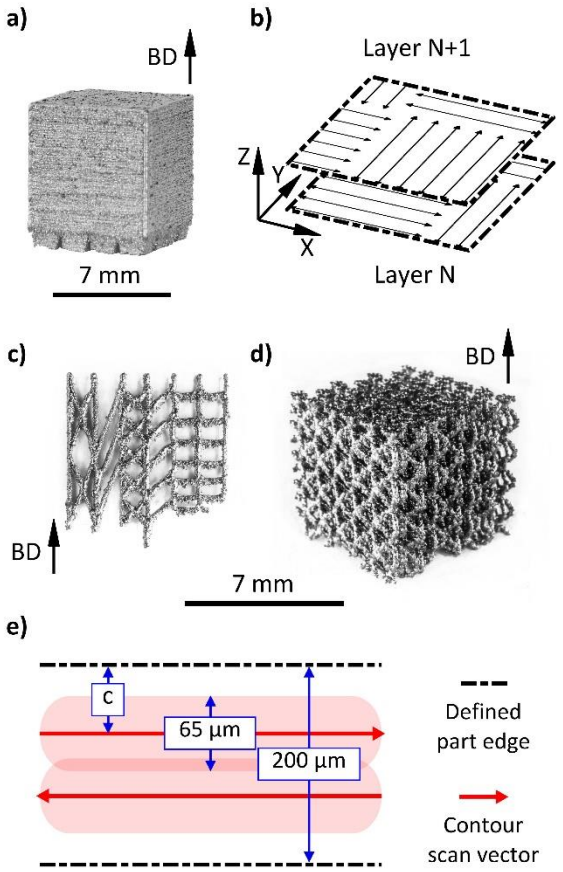

Figure 5.2. *(a) cube sample; (b) island scan strategy; (c) 2D lattice; (d) 3D lattice; (e) single contour scan strategy.*

2.3. Sample preparation and analysis

All samples were separated from the build platform using electrical discharge machining (EDM) and subsequently cleaned in an ultrasonic ethanol bath to remove the loose powder particles. The cubes and 3D lattices were cut in half along the build direction by using the EDM, then mounted in epoxy resin, and finally incrementally polished to a mirror-like finish. The chemical compositions of these samples were determined using the aforementioned XRF system (using a 300 µm diameter collimator) by averaging the results of nine consecutive measurements conducted on a polished cross section oriented along the build direction of each sample. The morphology of the 2D lattices was characterised using a Hitachi TM3000 scanning electron microscope (SEM). All image analysis was computed using ImageJ software, while statistical analysis was achieved using Minitab and Matlab software.

3D lattices built using optimised parameters (see Table 5.1) were electropolished under a constant 12 V voltage at -20 °C in an electrolyte solution containing a 4:1 volumetric ratio of ethanol to 70% HNO_3. The samples were heat-treated according to [56] by first homogenising them at 1060 °C for 12 hours, followed by atomic ordering treatment at 800 °C for 4 hours, after which the samples were furnace cooled to ambient temperature. The compositional homogeneity of these samples was evaluated using energy dispersive spectroscopy (EDS) in the aforementioned SEM. X-ray diffraction (XRD) was performed using a PANalytical Empyrean 3 diffractometer (Cu tube, λ = 0.15406 nm) equipped with poly-capillary optics, a PIXcel3D-Medipix3 detector, and a heating stage. Microstructural characterisation and imaging were conducted using a polarised optical microscope (Meiji

Techno, Japan) and the aforementioned SEM. The phase transformation temperatures were determined using an in-house-developed low-field AC magnetic susceptibility device (LFMS– constant ~5 mT field and 6 °C/min heating/cooling rate) and differential scanning calorimetry (DSC – 5 °C/min heating/cooling rate) on a Netzsch STA 449 F3 Jupiter. Magnetic properties were further characterised using a LakeShore 8600 Series vibrating sample magnetometer (VSM) [at room temperature and up to 1T].

3. Results and discussion

3.1. Bulk samples

Previous research [23] has demonstrated the dependency of Mn evaporation with respect to the applied process parameters. As this effect also depends on the equipment, the cubes' chemical composition was determined to establish a baseline for Mn evaporation and to calibrate the L-PBF system. Taking this approach facilitated the Mn evaporation effects comparisons between cubic bulk samples and lattices.

Figure 5.3a shows an optical micrograph obtained along the build direction from a bulk sample with a relative density of 98.26%. The observable porosity consists of spherical gas voids (see inset 1 in Figure 5.3a) and some irregular lack-of-fusion pores. The gas pores can form due to argon entrapment and/or as a consequence of Mn evaporation, whereas the lack-of-fusion pores are typically caused by unstable process conditions involving insufficient energy input [23]. Some cracking within the sample can be observed, as expected based on previous research conducted using bulk samples. Most of the cracks appear to be oriented along the build direction (see inset 2 in Figure 5.3a). This type of cracking is stress-induced and strongly related to the large thermal gradients in L-PBF and the subsequent residual stresses observed in L-PBF-built Ni-Mn-Ga samples [21,22,56].

The relative densities of the successfully built samples varied between 88.33% and 98.26%. Although some porosity originated from differences between parameter combinations, a systematic effect that originated from the used scanning strategy was also apparent. Each sample exhibited large lack-of-fusion type pores at the intersections of the melted islands. However, the samples were not precisely cut at the same location, leading to varying cross-sectional views from one sample to another. As a result, some samples exhibit more or less of lack-of-fusion between the islands. Subsequently, the interpretation of the relative density results was considered biased and, consequently, the effects of the process parameters on the cubes' relative densities were not analysed further. The practical implications of this, however, were considered minimal, since the cubes were only intended for the initial L-PBF system calibration and to facilitate the comparison between the results obtained from 'conventional bulk geometry' and the built lattices.

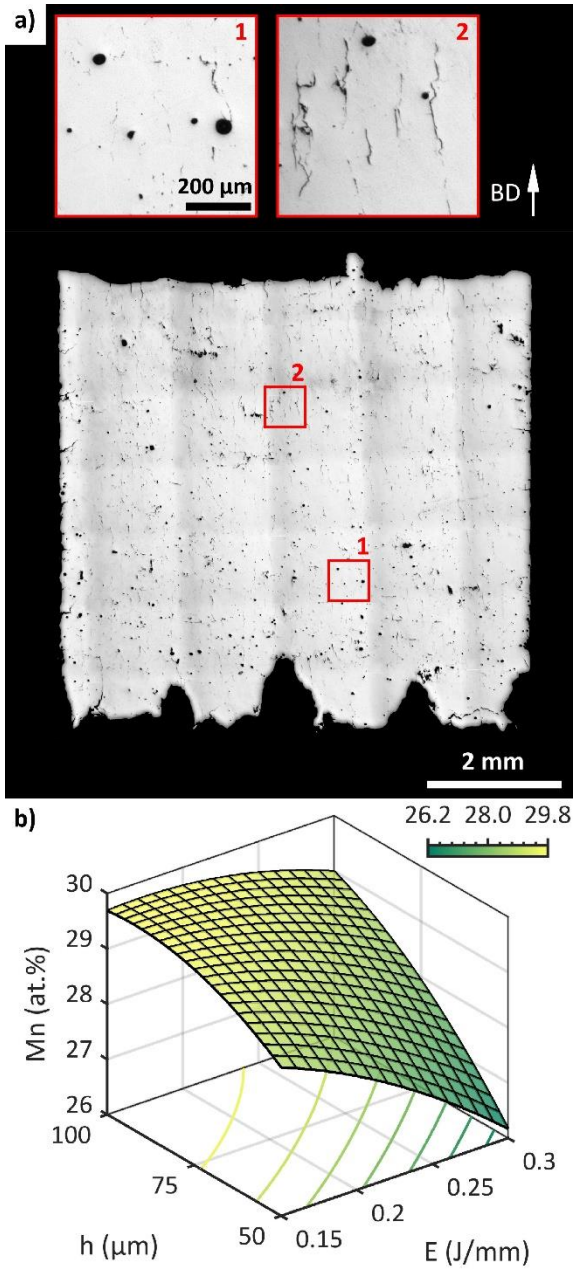

Figure 5.3. *(a) the optical micrograph of a polished cross-section along the build direction obtained from a bulk sample made following the parameters: laser power of 90 W, scanning speed of 500 mm/s, and hatch distance of 75 µm; and (b) the effect of the applied line energy density and the hatch distance on the bulk samples' Mn content (2nd-degree polynomial model: R^2 = 0.8674, adjusted R^2 = 0.8639, RMSE = 0.1623).*

Figure 5.3b shows the effect of the process parameters on the evaporation of Mn in as-built bulk samples. Foremost, all samples exhibited a minimum of ~1.5 at.% decrease in Mn content with respect to the initial Ni-Mn-Ga powder. As can be observed in the Table 5.2 analysis of variance (ANOVA) table shown in Table 5.2, all primary parameters exhibited *p*-values below the 0.05% threshold and so were considered statistically significant for the Mn content. The observations made here correspond to previous studies [23,24]. Plus, the applied quadratic polynomial model shows a strong correlation between the Mn evaporation and process parameters.

Table 5.2. *ANOVA for the Mn content with laser power, scanning speed, and hatch distance as continuous variables.*

Source	DF	Adj SS	Adj MS	F-value	P-value
P	1	0.1116	0.11157	6.75	0.010
v	1	4.7744	4.77441	288.68	0.000
h	1	9.3824	9.38237	567.29	0.000
P^2	1	0.3467	0.34669	20.96	0.000
v^2	1	0.9741	0.97410	58.90	0.000
h^2	1	1.8111	1.81107	109.50	0.000
*P*v*	1	0.0560	0.05598	3.38	0.067
*P*h*	1	0.0053	0.00528	0.32	0.573
*v*h*	1	0.8213	0.82132	49.66	0.000
Error	188	3.1093	0.01654		
Total	197	39.3294			

3.2. Lattice samples

The geometry of the 2D lattices (shown earlier in Figure 5.2c) was designed to study the effects of the applied laser power, contour distance, and scanning speed, together with the angle of the struts with respect to the substrate. The essential results of these experiments are summarised in Figure 5.4.

The first observation made on the experiments conducted on 2D lattices concerns the dissimilar behaviour of the Ni-Mn-Ga in comparison to other common engineering materials featured in the scientific literature [93]. Although the horizontal struts in 2D lattices were only 1 mm long, most of them were not fully melted and subsequently collapsed during manufacture. This observation was made consistently for each 2D lattice, occurring without an apparent connection to the particular set of applied process parameters. Only the 2D lattices, which were made using combinations of processing parameters that produce overall large energy densities, appeared to produce the horizontal struts successfully, mostly due to the excessive thickness of the feature with these lattices. However, as can be observed from Figure 5.4, the vertical struts and the struts built using the 45° and 70° angles appear smoother and more regular. Future lattice designs, therefore, should favour the use of angled struts while avoiding horizontal ones.

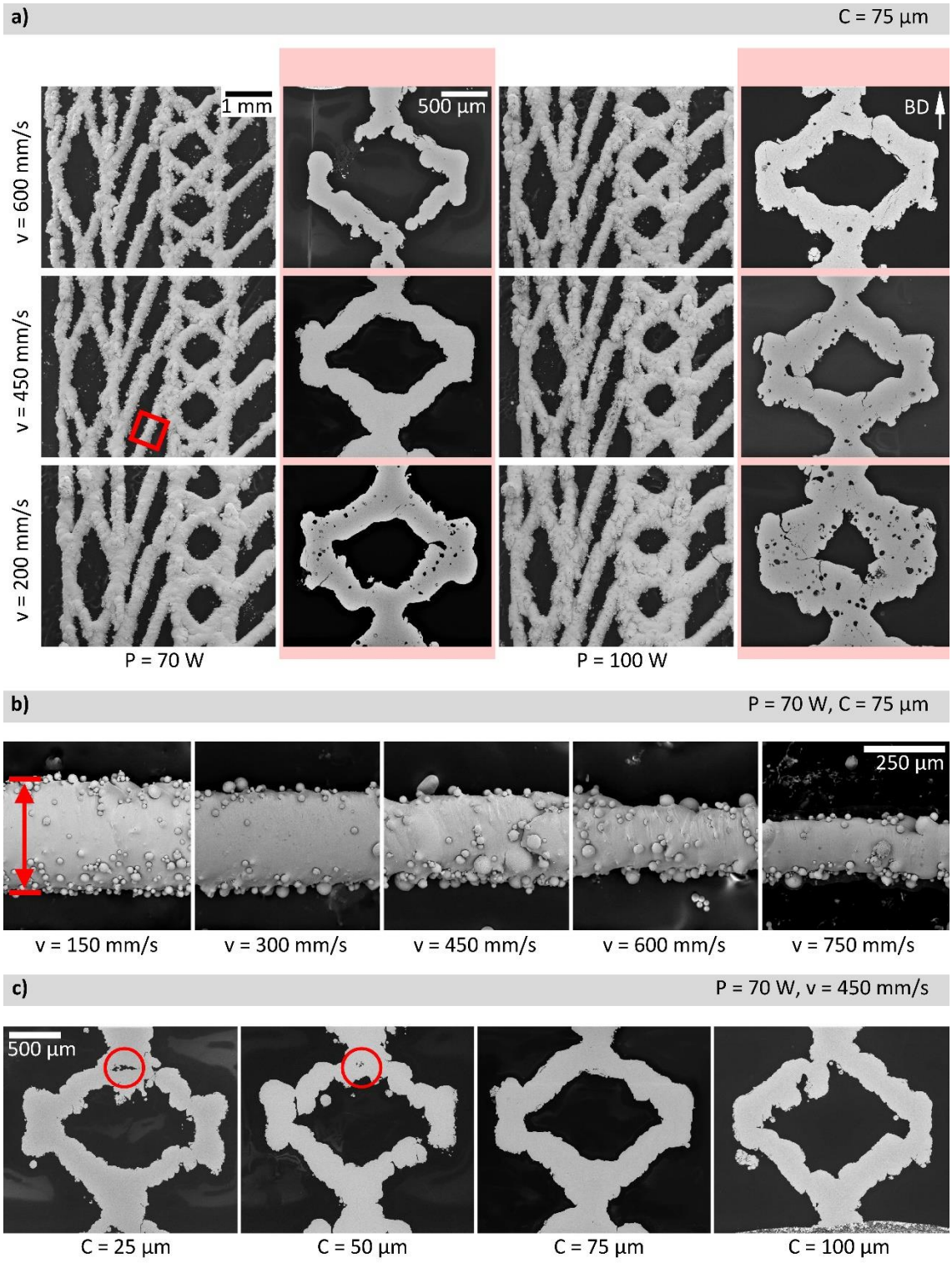

Figure 5.4. *BSE images showing the selected characteristics of the 2D and 3D lattices. (a) The effect of the applied laser power and scanning speed with a constant contour distance of 75 µm. Cross-sections obtained from 3D lattices (light red background colour); (b) The effect of applied scanning speed on 2D lattices' strut size with a constant laser power of 70 W and contour distance of 75 µm. The shown images correspond to the red inset square in section 'a'; the red arrow denotes the strut size; (c) Cross-sections obtained from 3D lattices showing the effect of contour distance with a constant laser power of 70 W and scanning speed of 450 mm/s. Red circles denote systematic lack-of-fusion defects.*

Figure 5.5 shows the effect of the applied line energy density and contour distance on the average strut size (see red arrow in Figure 5.4b) of 70° struts in each 2D lattice. Table 5.3 shows a statistical analysis of the effects of the applied process parameters on the strut size. An observation can be made that strut size is mostly influenced by the scanning speed and the laser power, whereas contour distance is not statistically significant for this feature. This is particularly clear in Figure 5.5, where the response surface has a steep slope in the direction of the line energy density axis but only a mild slope in the direction of the contour distance axis.

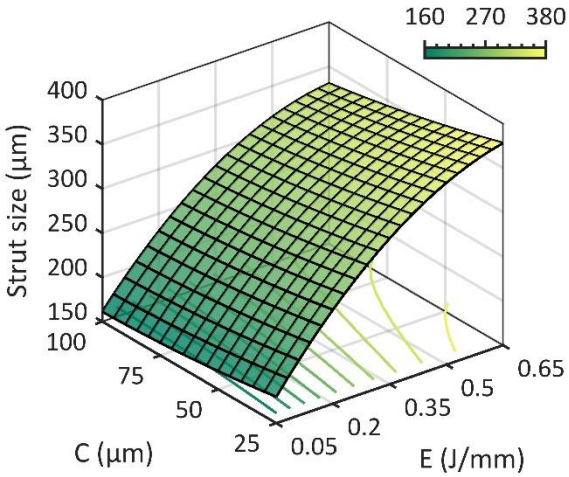

Figure 5.5. *The effect of the applied line energy density and the contour distance on the strut size of the 2D lattices (2nd-degree polynomial model: R^2 = 0.8172, adjusted R^2 = 0.8023, RMSE = 19.7705).*

Table 5.3. *ANOVA for the strut size and internal density of struts with laser power, scanning speed, and contour distance as continuous variables.*

	Strut size (2D lattices)					Internal density of struts (3D lattices)				
Source	DF	Adj SS	Adj MS	F-value	P-value	DF	Adj SS	Adj MS	F-value	P-value
P	1	29500	29499.7	90.12	0.000	1	4.338	4.3383	10.76	0.002
C	1	1019	1018.8	3.11	0.083	1	1.771	1.7706	4.39	0.041
v	1	74982	74982.1	229.06	0.000	1	14.361	14.3608	35.63	0.000
P^2	1	2792	2792.4	8.53	0.005	1	3.108	3.1083	7.71	0.008
C^2	1	1439	1439.2	4.40	0.040	1	0.318	0.3184	0.79	0.378
v^2	1	5730	5729.8	17.50	0.000	1	3.835	3.8354	9.52	0.003
*P*C*	1	30	30.1	0.09	0.763	1	3.445	3.4453	8.55	0.005
*P*v*	1	3147	3147.5	9.62	0.003	1	4.072	4.0720	10.10	0.002
*C*v*	1	13	13.0	0.04	0.843	1	1.085	1.0853	2.69	0.107
Error	57	18658	327.3			54	21.763	0.4030		
Total	66	143288				63	107.756			

Most of the samples exhibited strut sizes larger than the designed size of 200 µm in the initial CAD 3D model, whereas a few samples were clearly under-melted (too low line energy density). For example, high scanning speeds of >600 mm/s resulted in a balling effect, lack of fusion, and subsequent collapse of the structure – as seen in the sample built with 70 W and 600 mm/s (Figure 5.4a). Plus, a similar effect can be seen in the Figure 5.4c sample built using a 100 µm contour distance, with the contour distance creating a double scan melting the strut

twice (the designed strut width being 200 µm). Figure 5.4a shows that any laser power of ≥100 W leads to a melt pool increase, resulting in thicker struts and some cracking. The same effect is seen when using low scanning speeds of ≤200 mm/s. A further laser power increase above 200 W results in over-melting and, subsequently, leads to filling the designed porosity of the 3D lattices. Additionally, cracks and keyhole porosity were both observed in all samples built using higher line energy densities.

Table 5.3 shows applied parameters to be statistically significant for the internal density of the 3D lattices. This implies that the overall energy input of the process has a telling impact on the lattices' final internal density. It can be noted that small contour distances of 25 µm and 50 µm are not sufficient for the two scanning paths to coincide, resulting in a lack of fusion in the nodes (as highlighted in Figure 5.4c). This effect could be compensated for by applying an additional contour or hatch to the nodes. However, these two strategies would likely result in a significant strut size increase and also lead to overheating. Foremost, the 3D lattices built using the successful parameter combinations did not exhibit cracking. In fact, all lattices exhibited fewer cracking signs overall when compared to the bulk samples. The main cause of cracking in L-PBF-built Ni-Mn-Ga is the large residual stresses that occur due to the large thermal gradients characteristic of the process [21,22]. It is logical, therefore, to assume that residual stresses in the lattice samples must be lower in comparison to their bulk counterparts. This is expected as, when manufacturing fine structures such as lattices, the heat input of each layer significantly decreases, resulting in less cracking and a diminution of internal porosity [14].

Table 5.4 shows the chemical compositions of the 3D lattices (previously shown in Figure 5.4a). When compared to the initial powder, the lattices built with 70 W laser power at 450 mm/s scanning speed exhibit ~1.3 at.% of Mn loss, while the sample with the highest amount of Mn evaporation exhibits Mn content decrease of ~2.7 at.%. Similar to the bulk sample experiments, the general trend of decreasing Mn content can be observed when laser power is increased or scanning speed is decreased.

Table 5.4. *Chemical composition of the selected 3D lattices.*

P (W)	v (mm/s)	C (µm)	Ni (at.%)	Mn (at.%)	Ga (at.%)	e/a (-)	Internal density of struts (%)
70	200	75	51.09 ± 0.18	28.53 ± 0.21	20.39 ± 0.06	7.72	97.31
70	450	75	49.88 ± 0.08	29.91 ± 0.10	20.21 ± 0.08	7.69	98.94
70	600	75	49.97 ± 0.09	29.70 ± 0.15	20.33 ± 0.09	7.69	98.90
100	200	75	51.09 ± 0.22	28.51 ± 0.21	20.39 ± 0.04	7.72	94.04
100	450	75	50.34 ± 0.08	29.28 ± 0.11	20.38 ± 0.06	7.70	97.36
100	600	75	50.00 ± 0.06	29.61 ± 0.08	20.40 ± 0.06	7.68	97.92

3.3. Characterisation of the optimised lattices

The optimum parameters (P = 70 W, v = 450 mm/s, and C = 75 µm) for the manufacture of final 3D lattices for materials characterisation were determined as the parameters producing struts with minimal internal defects and close to the designed struts thickness (200 µm). These parameters produced samples with a chemical composition of $Ni_{49.88}Mn_{29.91}Ga_{20.21}$. An EDS scan (Figure 5.6) was performed on a polished section of an as-built optimised 3D lattice cut along the build direction. The figure shows a homogeneous distribution of the elements Ni, Mn, and Ga within the strut. The minor segregation of Ga observed on the strut's lower edge is within the error range of

the EDS system and, thus, the produced material can be considered homogenous. Additionally, the EDS do not show any apparent oxygen pickup, which was also confirmed by additional measurement using the aforementioned LECO system that determined the O_2 content of the lattices as 215±59 ppm for the 2D lattices and 249±34 ppm for the 3D lattices. The surface oxygen observable in Figure 5.6 is mostly originating from the sample preparation and exposure to atmospheric oxygen prior to the SEM/EDS measurement. The lattices' O_2 content is roughly the same as in the initial powder and the sample was heat-treated according to the procedure described earlier in the methods section – to induce chemical homogenisation, increase the long-range order of the atomic lattice, and induce grain growth. After heat-treatment, the sample exhibited a composition $Ni_{50.15}Mn_{29.25}Ga_{20.61}$, very close to the as-built one.

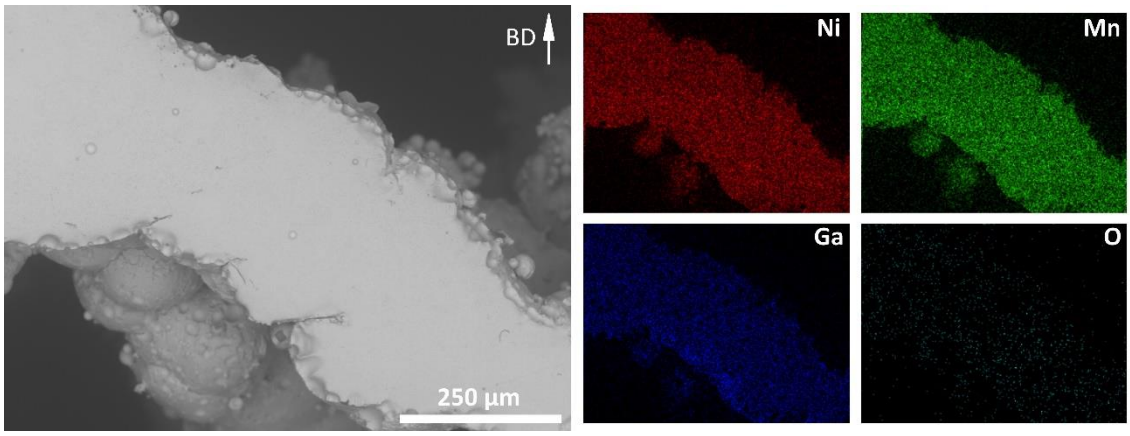

Figure 5.6. *BSE image and the corresponding EDS area mappings of the selected elements in a section in the middle of the heat-treated 3D lattice strut cut along the build direction.*

Figure 5.7abc show optical micrographs of an as-built and the heat-treated 3D lattices along the build direction. The pores featured appear larger because of the effects of the electro-polishing process used during sample preparation. Primarily, it can be seen from the figure that the applied heat treatment worked to induce considerable grain growth. In some struts – see Figure 5.7c – this growth resulted in the formation of the beneficial 'bamboo-grained' structure, in which the neighbouring grains span the thickness of the struts and make them partially unconstrained from the sides. The largest grains observed in the struts were ~0.5 mm long (along the strut length). In this type of structure, individual grains may (theoretically) act as functional single crystals with mobile twin boundaries, providing that the grains have the correct crystal structure and crystallographic orientation. In some areas (e.g. nodes that connect individual struts to each other), the grains remained smaller, which the BSE image in Figure 5.7d shows an example of. Here, the twins belonging to the martensite structure can be clearly seen as contrasting parallel lines. Overall, the twin structure observed in the sample is very fine – a structure typically observed in Ni-Mn-Ga 14M polycrystals [56] and next confirmed via XRD. The obtained 'bamboo-grained' structure is not homogenous throughout the produced sample and more studies need to be done to understand the grain growth and the grain election mechanisms during heat-treatment. Moreover, the lattice geometry and the applied L-PBF parameters also influence the crystallographic texture.

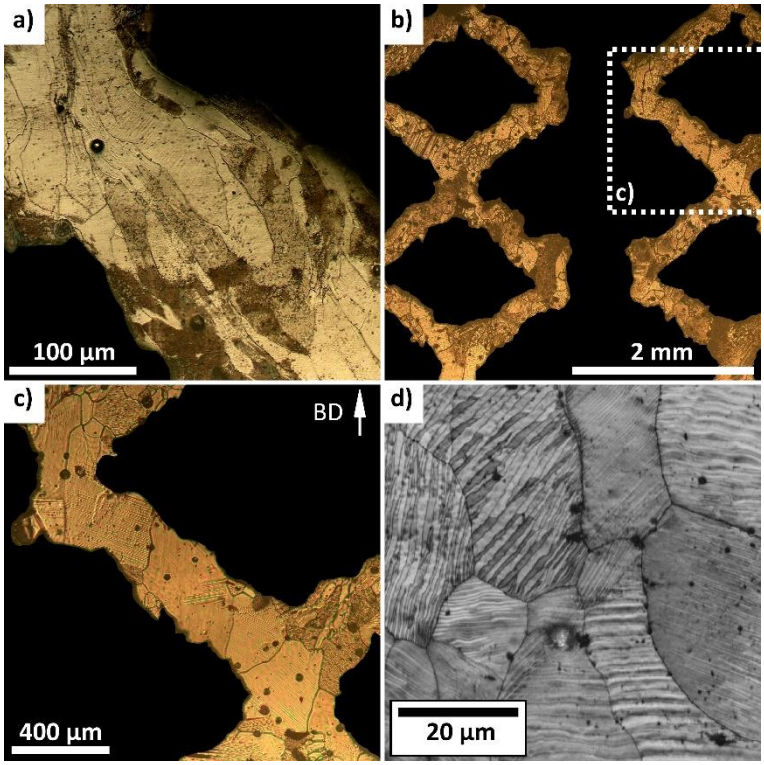

Figure 5.7. *Optical micrograph of the cross-section of the (a) as-built strut and (b) heat-treated 3D lattice cut and electropolished along the build direction; (c) Optical micrograph showing a relatively coarse 'bamboo-grained' structure in a strut – the contrasting parallel straight lines are martensitic twins; (d) BSE image of the finer twinned grain structure in a node.*

L-PBF-built materials exhibit unique thermal histories due to the repetitive melting and rapid cooling of the processed material. In the case of Ni-Mn-Ga, this has been shown to significantly affect the chemical composition and the resulting magneto-structural properties of the built material [23,24,56]. Consequently, heat-treatment is necessary to recover the typical (composition dependent) functional properties in L-PBF-built Ni-Mn-Ga polycrystals [41,56]. Therefore, further characterisation shown here mostly focuses on the heat-treated sample, whereas the properties of the as-built samples are not discussed extensively. It is worth pointing out that the DSC curves for the as-built samples did not show any phase transformations, more likely due to excessive residual stresses. Magnetisation measurements done with the aforementioned VSM system on the as-built samples provided information about the phase transformation (crystallographic and magnetic), however, the curves were too blunt to provide accurate results. The XRD scan performed on as-built samples showed the same crystal structure as the heat-treated samples with wider and lower peak intensities. This is due to the smaller crystallite size (and grain size) and slightly lower homogeneity of the as-built samples.

The XRD analysis – shown in Figure 5.8 – was performed according to two distinctive stages. Firstly, the sample was inspected at 120 °C (above the martensite-to-austenite transformation temperature) to analyse the diffraction pattern originating from the cubic $L2_1$ parent phase (austenite). The lattice parameters of the cubic phase were determined as $a = b = c = 5.84$Å. Secondly, to inspect the crystal structure of the martensitic phase, the sample was cooled down to 30 °C (below the austenite-to-martensite transformation temperature). The initial diffraction pattern inspection showed the splitting of the main cubic $L2_1$ (400) peak (at 63.8°) into three distinctive orthorhombic 14M martensite (400), (040), and (004) peaks (at 60.3°, 63.9°, and 67.7°). The intensity of the 14M

martensite (040) peak was very low, possibly due to a strong texture induced by the L-PBF process and to the sample's local twin variant configuration. The lattice parameters of the 14M martensite were determined as a = 6.14Å, b = 5.82Å, c = 5.54Å, and γ = 90.53°. The c/a-ratio of this lattice is approximately 0.90, implying that the theoretical maximum MFIS is approximately 10%. The obtained crystal structure and the lattice parameters are well within expectations compared to polycrystalline Ni-Mn-Ga samples of similar composition [94].

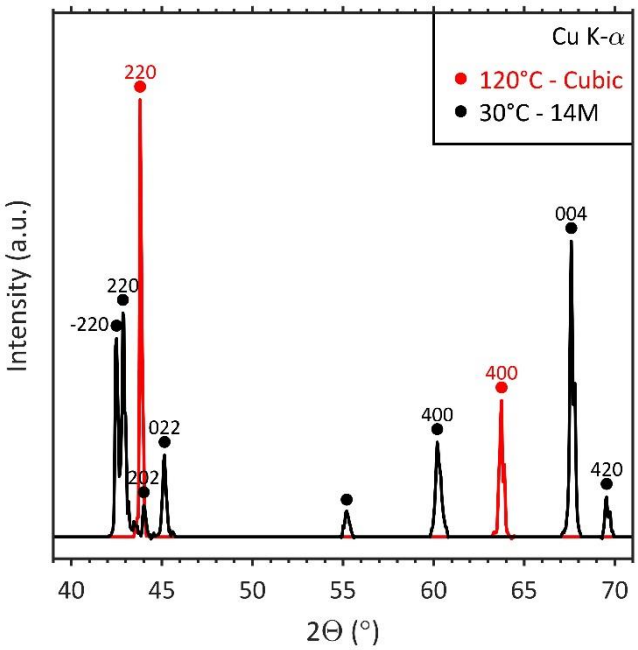

Figure 5.8. *X-ray diffractograms obtained from the heat-treated 3D lattice. The background has been removed and the baseline is offset. The red line (cubic $L2_1$) shows the measurement at 120 °C, whereas the black line (14M martensite) shows the measurement at 30 °C. All peaks have been indexed with respect to the unit cell coordinate system of the cubic parent phase. Unindexed peaks originate from the modulated superstructure.*

Figure 5.9ab displays the temperature-dependent measurements of the phase transformations (DSC and LFMS) of a heat-treated 3D lattice. Based on the DSC measurement shown in Figure 5.9a, the austenite start temperature (T_{AS}) is ~85 °C. The LFMS measurement – see Figure 5.9b – showed slightly different temperature of T_{AS} ~84 °C and a martensite finish of T_{MF} ~80 °C. These values are really similar to the transformation temperatures of samples with comparable composition in [17,94]. Previously ink-printed samples fabricated by [17] exhibited a 14M structure with similar martensite phase transformation temperature and Curie temperature at 73 °C and 90 °C respectively. Here, the approximate width of the transformations is 9 °C, which is close to the expected value for a polycrystalline 14M martensite sample [41,94]. The hysteresis of the phase transformations was ~8 °C for the DSC measurement and ~4 °C for the LFMS measurement, which may occur due to differences in the applied methods and equipment. The phase transformations overlapped the transformation from ferromagnetic order to paramagnetic order (Curie temperature, T_C), for which reason the transformation from 14M martensite to cubic $L2_1$ structure cannot be fully observed in the LFMS measurement. This observation was also made in [94] on samples with similar composition. The first derivative of the magnetisation dM/dT gives the temperatures T_C ~ 89.4 °C upon heating and T_C ~ 88.3 °C upon cooling. In contrast to previous studies [41,56], the martensite transformation temperatures here are abnormally high, mostly because of the composition difference of the initial

powder when compared to the typical functional 10M/14M compositions. Typical functional compositions exhibit the martensite-to-austenite transformation (and the reverse transformation) around 35-50 °C to minimise twinning stress at ambient temperature. This difference in chemical composition, together with the subsequent difference in martensite transformation temperatures, results in high twinning stress [95,96], which effectively reduces the twin boundary mobility and the maximum obtainable MFIS.

Additional barriers to twin boundary motion originate from the structure itself, as the preferable bamboo-grained structure was not yet obtained homogenously in all sections of the tested samples. Consequently, the samples produced in this study did not exhibit measurable MFIS. This is a problem subject to further study, which will require the initial powder's composition to be adjusted to enable the manufacture of the functional 10M/14M compositions.

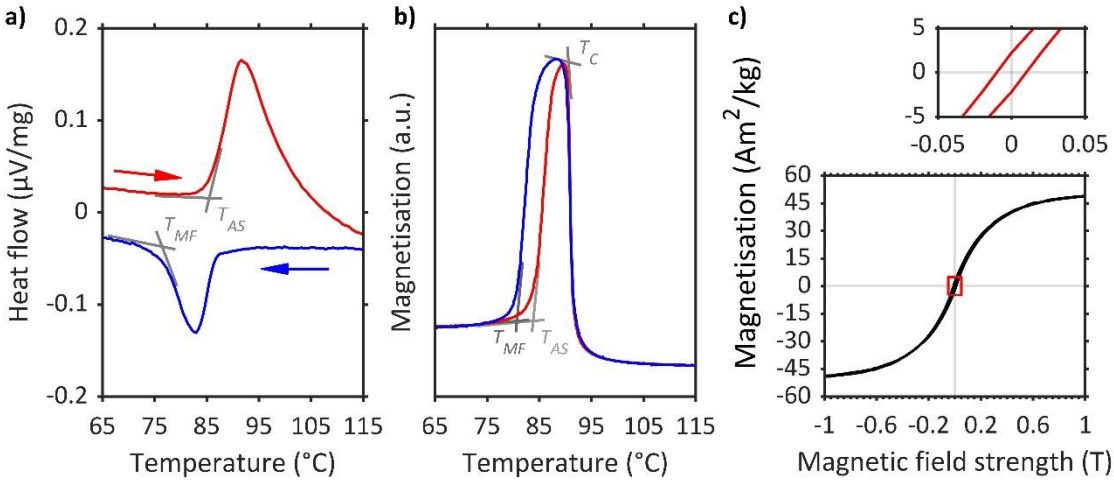

Figure 5.9. *Phase transformations of the heat-treated 3D lattice as measured via (a) DSC and (b) LFMS. The red arrow shows the transformations occurring during heating, whereas the blue arrow shows the cooling; (c) magnetisation hysteresis loop obtained at ambient temperature from the VSM measurement.*

Figure 5.9c shows the VSM magnetisation hysteresis loop at ambient temperature obtained for the heat-treated sample. The hysteresis loop shows a saturation magnetisation of 48.5 Am^2/kg at the field of 1 T, a coercivity of 0.010 T, and remanent magnetisation of 2.233 Am^2/kg. The saturation magnetisation and coercivity are close to similar composition samples made by binder-jetting in [17], where the samples exhibited a saturation magnetisation of 56.5 Am^2/kg and a coercivity of 0.028 T. It is worth pointing out that the magnetic remanent magnetisation is difficult to compare with the literature as it also depends on the demagnetisation factor and therefore on the sample geometry. Overall, the values reported here characterise a soft ferromagnetic behaviour typical to Ni-Mn-Ga-based MSM alloys. We can note that they are close to values previously reported by [21,56], whereas the saturation magnetisation appears to be slightly lower than the expected value of ~68 Am^2/kg [56]. This difference mainly relates to variations in chemical compositions but may also be affected by the lattice samples' designed porosity. Due to the small size and low mass of the lattice sample in comparison to conventional bulk samples used in this type of studies, the difference in magnetic measurements might also originate from a sample mass measurement error.

4. Conclusion

This study features a systematic experimental approach to develop and optimise an L-PBF process for the manufacture of polycrystalline Ni-Mn-Ga MSM alloy lattices. The primary results can be summarised as follows:

- The experiments using 2D and 3D lattice geometries were used to determine the effects of the applied process parameters on the lattice struts' relative density and geometrical integrity. The results show that a 200 µm strut size with ~99% internal density can be obtained by using the optimised parameters: laser power of 70 W, scanning speed of 450 mm/s, and contour distance of 75 µm. The lattices fabricated in this study using L-PBF, exceed from far the geometrical accuracy and internal density of the lattices previously made by binder-jetting and ink printing [15,19].

- The bulk samples exhibited cracking relating to the excessive residual stresses originating from the process while the lattice samples were crack free. The results obtained using 3D lattice geometry confirm the previous notion that using thinned-down structures (such as lattices) can effectively prevent the cracking previously observed when using bulk geometries [23].

- The heat-treated lattices manufactured using optimised parameters exhibited a 14M martensite structure at ambient temperature. The lattice exhibited a saturation magnetisation of 48.5 Am^2/kg at the field of 1 T and phase transformations with austenite start temperature at ~85 °C and martensite finish temperature at ~77 °C. Foremost, the optimised lattices demonstrated that the beneficial 'bamboo-grained' structure can be obtained from some individual lattice struts via post-process heat treatment. However, the growth of bamboo-like grains does not occur in the entire sample and more investigation needs to be done to understand this process.

The results obtained here highlight the high potential of L-PBF for the manufacture of a new generation of MSM-based actuating devices. Nevertheless, plenty of room remains for further research on this topic. Primarily, the initial powder's composition should be further adjusted to increase Ga content by ~1 at.% to enable the manufacture of the functional 10M/14M compositions. Additionally, future research should focus on the development and testing of different lattice geometries, scanning strategies (such as double scanning), and substrate pre-heating to investigate the crystallographic texture in L-PBF-built Ni-Mn-Ga lattices.

Acknowledgements

This work was financially supported by the Defence Science and Technology Laboratory (DSTL), the Strategic Research Council of Finland (grant number 313349), the Academy of Finland (grant number 325910), and the AMBI (Analytics-based Management for Business and Manufacturing Industry) research platform of Lappeenranta-Lahti University of Technology LUT.

Supplementary work - Chapter 5

The research presented here was conducted at UTBM prior to the experiments conducted on the M2 Concept laser system. The investigations involved the use of a pulsed wave laser system, which introduces a temporal dimension to the energy input. In this system, energy is delivered to the material in brief, high-intensity bursts or pulses, typically on the order of microseconds. This characteristic enables precise control over the heat input, minimising the creation of heat-affected zones. In contrast, a continuous laser wave delivers a steady stream of energy without interruption, resulting in consistent and wider melting pools. Consequently, a pulsed wave laser is particularly advantageous for printing small features such as lattices, as noted in studies by [97,98]. Additionally, the use of a pulsed wave laser can impact the thermal gradient, thereby influencing the resulting microstructure. For instance, Biffi et al. [99] observed higher macrotexture in AlSi10Mg samples produced using a pulsed wave laser, characterised by large columnar grains exhibiting a strong <100> orientation aligned with the build direction.

5. Experimental procedure

The powder used for these experiments was argon gas atomised by Nanoval (Germany), with a composition of $Ni_{49}Mn_{31}Ga_{21}$ (at.%). More information about the powder can be found in Chapter 3.

Single tracks, 10 × 10 × 10 mm^3 cuboids, and lattice samples were manufactured using a ReaLizer SLM250 equipped with a 400 W quasi-pulsed/modulated laser system. All experiments were conducted under a protective argon atomosphere, employing a 25 µm layer thickness on 316L stainless steel substrates and using a 36° rotation between every layer. Figure 5.10 shows a picture of the system and the processing chamber.

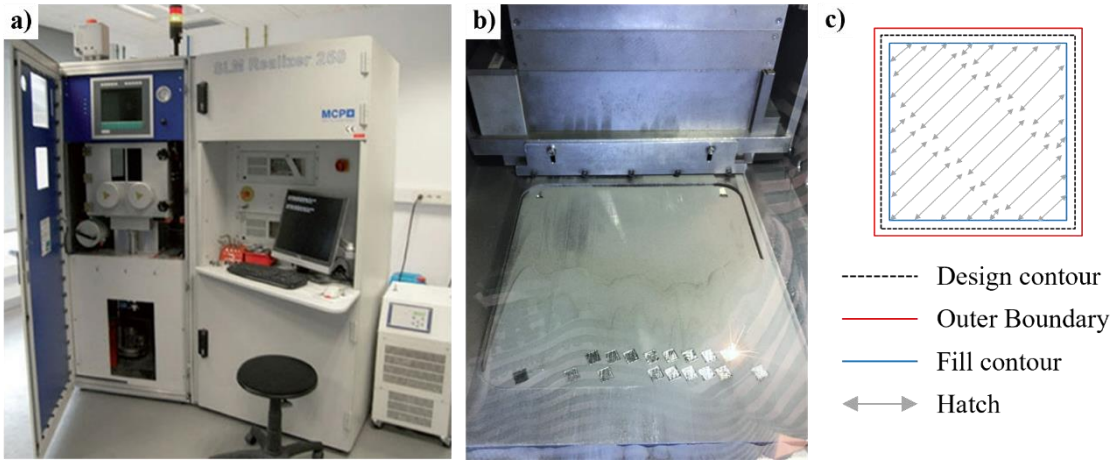

Figure 5.10. *(a) ReaLizer SLM250 L-PBF system with a picture of (b) the processing chamber, and (c) the scanning strategy used for bulk materials.*

The scanning speed (v) follows the following equation:

$$v = \frac{P_{dist}}{T_{expo}+\frac{P_{dist}}{V_{eng}}}, \quad (1)$$

With P_{dist} the distance between 2 points, T_{expo} the exposure per point and V_{eng} the speed of the engine constant.

For analysis and parameter optimisation, both line energy density (E, J/mm) and surface energy density (E_s, J/mm^2) were employed and calculated using the following equations:

$$E = \frac{P}{v}, \tag{2}$$

$$E_s = \frac{P}{v*h}, \tag{3}$$

where P is the laser power (W), v is the scanning speed (mm/s), and h is the hatch distance (mm). Table 5.5 summarises the used parameters. The parameters were choose using a design of experiment generated via Taguchi methods.

Table 5.5. *Summary of the used parameters on the ReaLizer system.*

Parameter	Single tracks	Bulk samples	Lattice samples
t (µm)	-	25	25
P (W)	100, 150, 200, 250, 300	150, 200, 250, 300	150, 200, 250, 300
P_{dist} (µm)	20, 25, 30, 35, 40	25	25
T_{expo} (µs)	35, 45, 55, 65, 75	32, 40, 52, 74, 115	32, 40, 52, 74, 115
v (mm/s)	440, 443, 448, 455, 465	200, 300, 400, 500, 600	200, 300, 400, 500
h (µm)	-	130, 150, 170, 190, 210	130, 150, 211
E (J/mm)	0.215 to 0.682	0.3 to 3.5	0.3 to 1.5

The single tracks were made with a 2 mm spacing between each other. The bulk materials were manufactured with a stripe scanning strategy and two contour scans as shown in Figure 5.10c. To minimise potential contamination from sparks during recoating, the samples were positioned at the front of the substrate in one or two rows, as depicted in Figure 5.10b. Small supports were built into the bulk samples to facilitate sample removal from the substrate. Lattice samples were designed using the lattice module in Materialise Magics. Bulk and lattice samples were detached from the substrate using a chisel, followed by sectioning along the build direction with a Buehler cutting machine equipped with a diamond disc. Afterward, they were embedded in epoxy resin, and polished to achieve a mirror-like finish using SiC abrasive paper. The samples were then etched using Kallings II reagent for approximately 10 s. Imaging was conducted using a Keyence VHX-7000 4K digital microscope and a JEOL JSM 7800F SEM fitted with a Bruker X Flash 5130 EDS detector. Sample density assessments were performed using Archimedes' principle and image analysis via Image J software.

6. Results and discussion

6.1. Single tracks

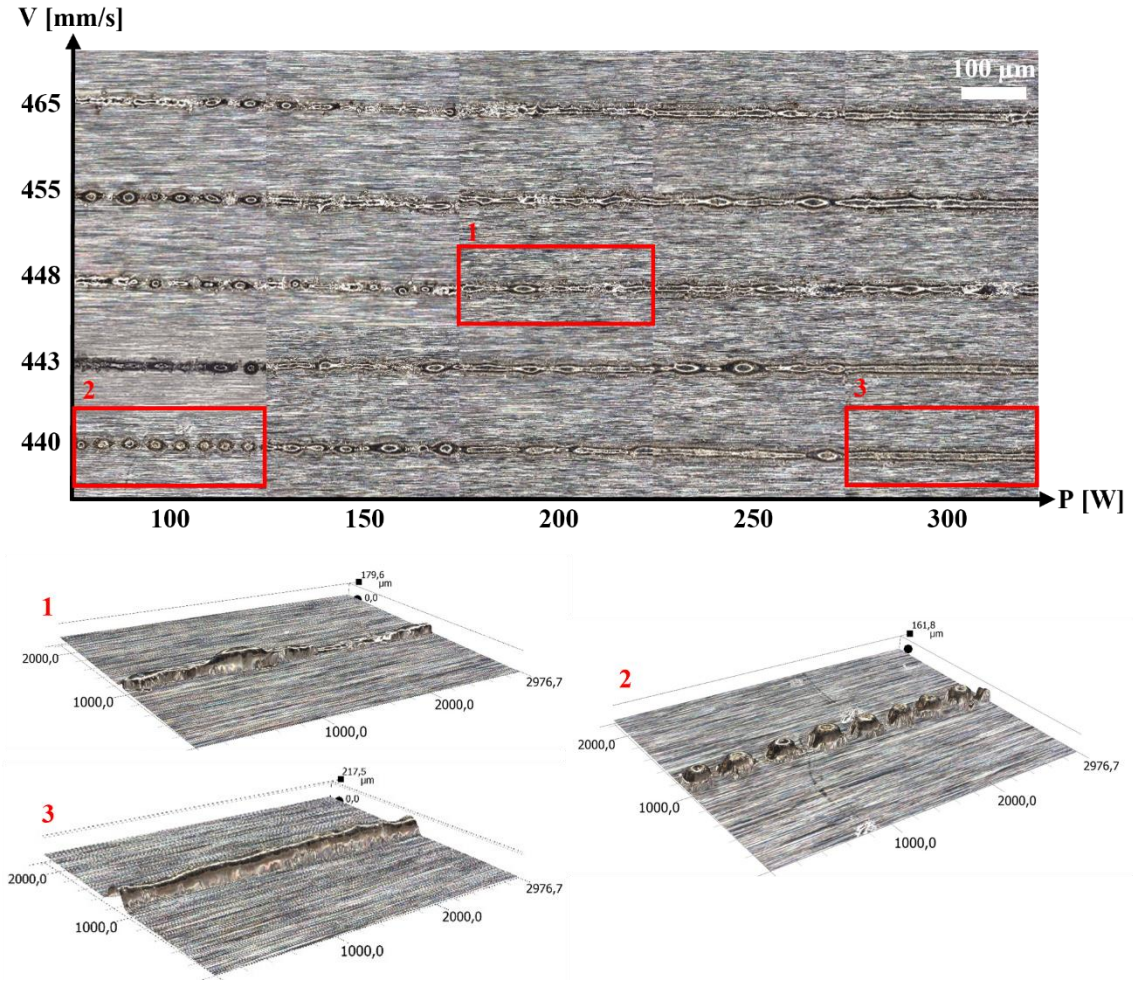

Figure 5.11. *Micrographs of single tracks at different scanning speed and laser power.*

Figure 5.11 shows micrographs of individual tracks conducted at various scanning speeds and laser power. Table 5.6 provides a detailed account of the P_{dist} and T_{expo} parameters employed throughout the manufacturing process. The parameters were selected in proximity to the optimised parameters of Laitinen et al. [22], which originally recommended a laser power of 200 W and a scanning speed of 450 mm/s. However, this parameter set, when applied with the experimental system in this study, resulted in the formation of discontinuous tracks, as represented in inset 1 of Figure 5.11. Inset 2 also showcases a discontinuous track, attributed to a larger P_{dist}, as evidenced by the individual laser shots within the track. Notably, the same P_{dist} can generate continuous tracks if the laser power is elevated sufficiently, as illustrated in inset 3. In general, individual tracks tend to display enhanced continuity at higher laser power levels (200 W, 300 W), resulting in a track thickness ranging between 20 and 25 µm. This thickness is notably smaller than what was previously reported in [22] and falls below the minimum laser spot size of 34 µm. This deviation from the norm can be attributed to the use of a pulsed wave laser, which typically generates narrower tracks due to localised high-energy discharges [98].

Table 5.6. *Scanning speed parameters used for the single tracks.*

P_{dist} (µm)	T_{expo} (µs)	v (mm/s)
40	75	440
35	65	443
30	55	448
25	45	455
20	35	465

6.2. Bulk samples

For both bulk samples and lattices, P_{dist} was maintained at 25 µm while T_{expo} was varied.

Table 5.7 provides the parameters used for the samples that successfully completed the building process, and Figure 5.12 includes pictures and micrographs of these samples. The coloration observed on the samples suggests the presence of oxidation during the manufacturing process, detrimental for the MFIS.

We can observe that the three samples with hatch distances of 0.13 mm and 0.15 mm exhibited the lowest density, which is an intriguing result, given that the individual tracks were only 15-20 µm wide. A smaller hatch distance would theoretically aid in filling the spaces between each track. However, the observed increase in density can likely be attributed to the 36º rotation between layers, which leads to the remelting of the previous tracks and the homogenisation of the structure. A significant number of cracks were evident in most of the samples. Higher energy settings resulted in fewer cracks but an increased number of keyholes, as observed in sample 13, Figure 5.12c probably due to Mn evaporation. Moreover, columnar elongated grains were readily discernible in high-energy samples such as sample 13 and 21, with twins manifesting as stripe-like patterns. Some samples displayed signs of delamination on their corners, which may have resulted from overheating due to the two contour scans.

Table 5.7. *Parameters of the successfully printed bulk samples.*

Sample #	P (W)	T_{exp} (µs)	v (mm/s)	h (mm)	E (J/mm)	E_s (J/mm²)	Density (%)
6	150	70	300	0.17	0.50	2.94	91.00
9	200	70	300	0.13	0.67	5.13	86.10
12	350	70	300	0.21	1.17	5.56	92.84
13	150	240	100	0.13	1.50	11.54	87.90
15	200	110	200	0.21	1.00	4.76	91.40
19	200	40	500	0.17	0.40	2.35	91.50
21	300	70	300	0.15	1.00	6.67	87.50
25	150	40	500	0.21	0.30	1.43	91.80

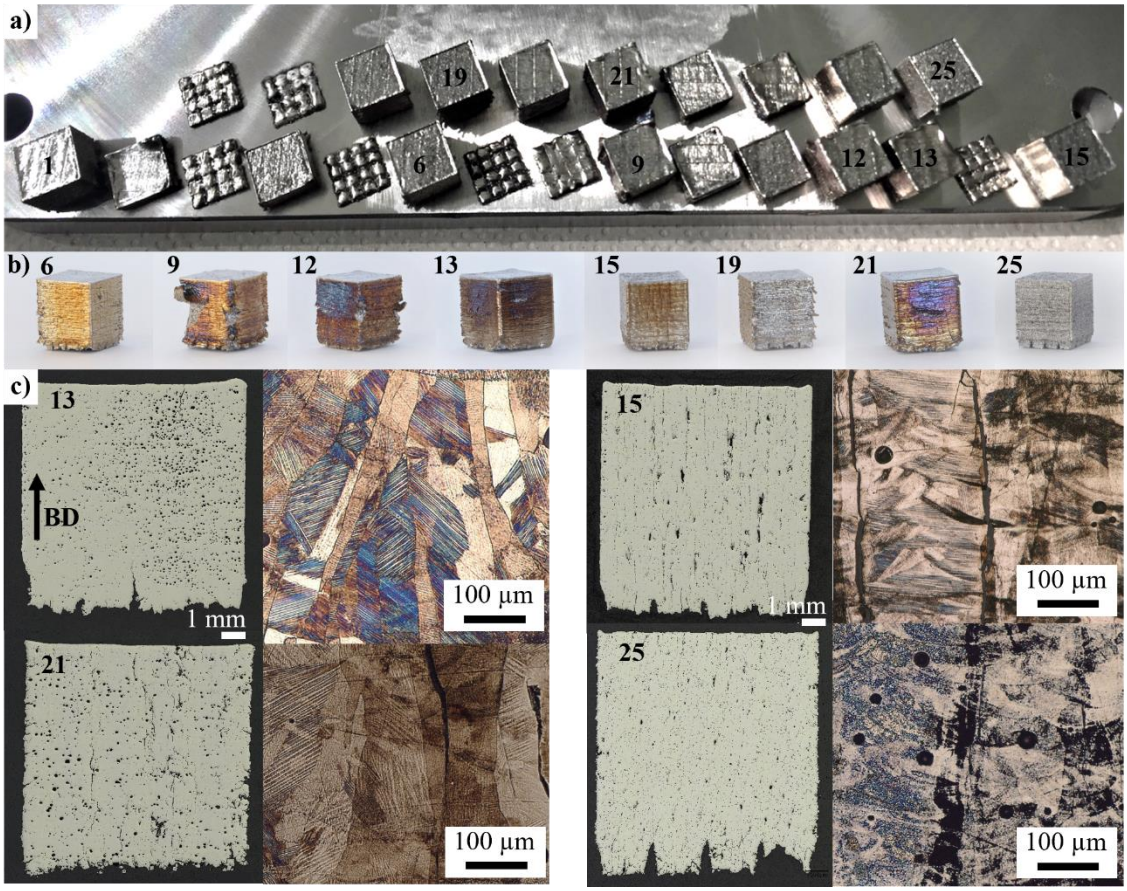

Figure 5.12. *(a) picture of the substrate with the bulk samples, (b) picture of the samples, and (c) corresponding micrographs.*

Figure 5.13 depicts an EDS scan performed at the centre of a polished section of sample 25, oriented along the build direction. The scan illustrates a uniform distribution of the three elements Ni, Mn, and Ga. The minor presence of oxygen, which may be observed, is in the range of the EDS error.

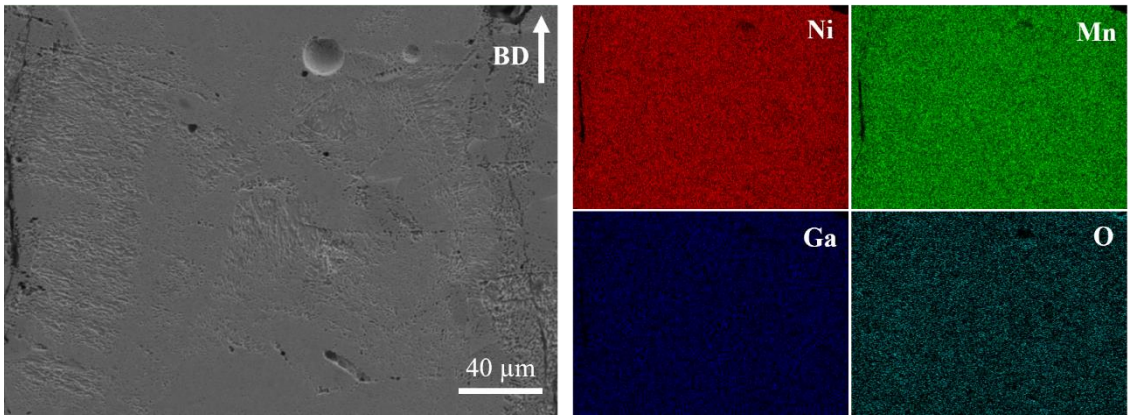

Figure 5.13. *BSE image and the corresponding EDS area mappings of the selected elements in a section in the middle of bulk sample 25 cut along the build direction.*

6.3. Lattice samples

Two different lattice geometries were employed in this study: one featuring angled struts (Figure 5.14b) used for samples 1 to 9, and another with only vertical and horizontal struts (Figure 5.14c), used for samples 10 to 13. Two distinct scanning strategies were applied: one involving two contour scans and the other using a hatching approach exclusively. A summary of all parameters and scanning strategies employed can be found in Table 5.8. Figure 5.14 provides pictures of the build plate and the resulting lattice samples.

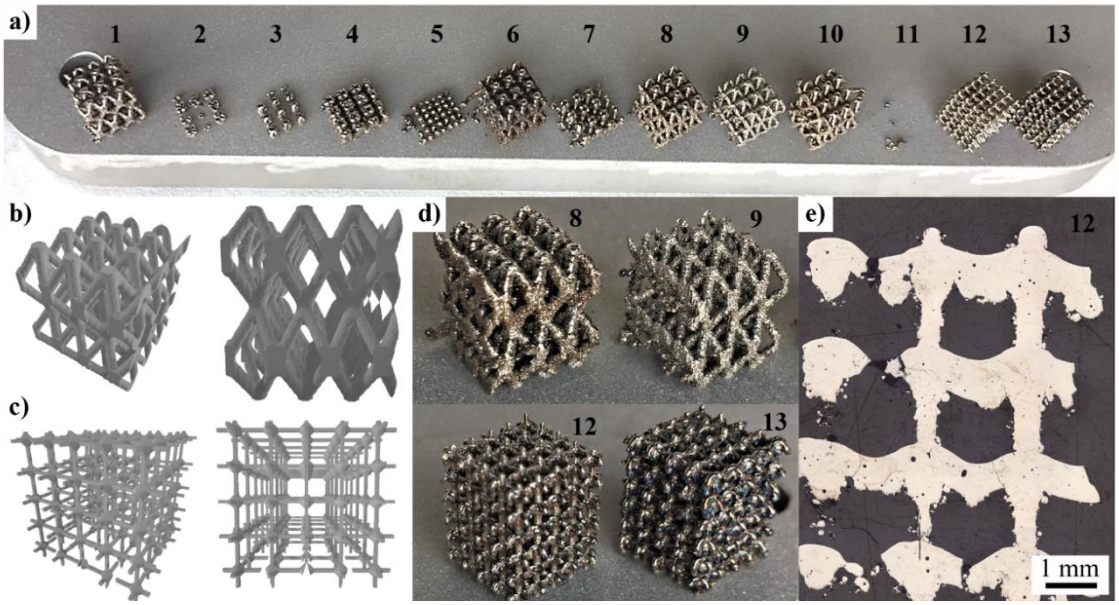

Figure 5.14. *(a) picture of the substrate with the lattice samples, (b, c) design of the two lattice geometries, (d) picture of the lattice samples, and (e) sample 12 micrograph.*

Table 5.8. *Parameters used for the lattice samples.*

Sample #	Scanning strategy	P (W)	v (mm/s)	h (mm)	E (J/mm)
1	Hatch	200	417	0.15	0.48
2	Double contour	200	417	-	0.48
3	Hatch	300	313	0.15	0.96
4	Double contour	300	313	-	0.96
5	Hatch	150	100	0.13	1.50
6	Double contour	150	100	-	1.50
7	Hatch	150	500	0.21	0.30
8	Double contour	150	500	-	0.30
9	Hatch	200	313	0.13	0.64
10	Double contour	200	313	-	0.64
11	Hatch	200	417	0.15	0.48
12	Double contour	200	417	-	0.48
13	Double contour	150	100	-	1.50

In general, lattices manufactured with a contour scanning strategy exhibited better surface finishing, and the struts appeared more continuous compared to those produced with the hatching strategy alone. There was no apparent

correlation between the parameters and the overall success of the lattice samples, suggesting the need for further optimisation. It is worth mentioning that the use of the contour strategy resulted in hollowed struts in sample 8, visible at the top of the struts in Figure 5.14d. This issue was not observed in the other lattice geometry (Figure 5.14e). The problem of hollowed struts was subsequently addressed through the reduction of strut size.

7. Conclusion

These initial experiments provided us with the opportunity to explore an alternative system employing a pulsed wave laser instead of a continuous wave laser. The operation of this system offers additional parameters to manipulate, allowing adjustments to both the P_{dist} and T_{expo}. The single tracks produced were approximately 20 µm wide. The samples printed with the lowest energy densities gave the most favourable results (in terms of geometry accuracy and density), aligning with findings from experiments conducted using the continuous wave laser system (using energies of 0.15 and 0.18 J/mm for bulk and lattice samples, respectively).

It would be interesting to investigate the transferability of parameters between the two systems and assess the impact of the pulsed wave laser system on the resulting microstructure in lattice samples. More extensive dataset, involving a larger number of samples, is required to establish robust conclusions in this regard.

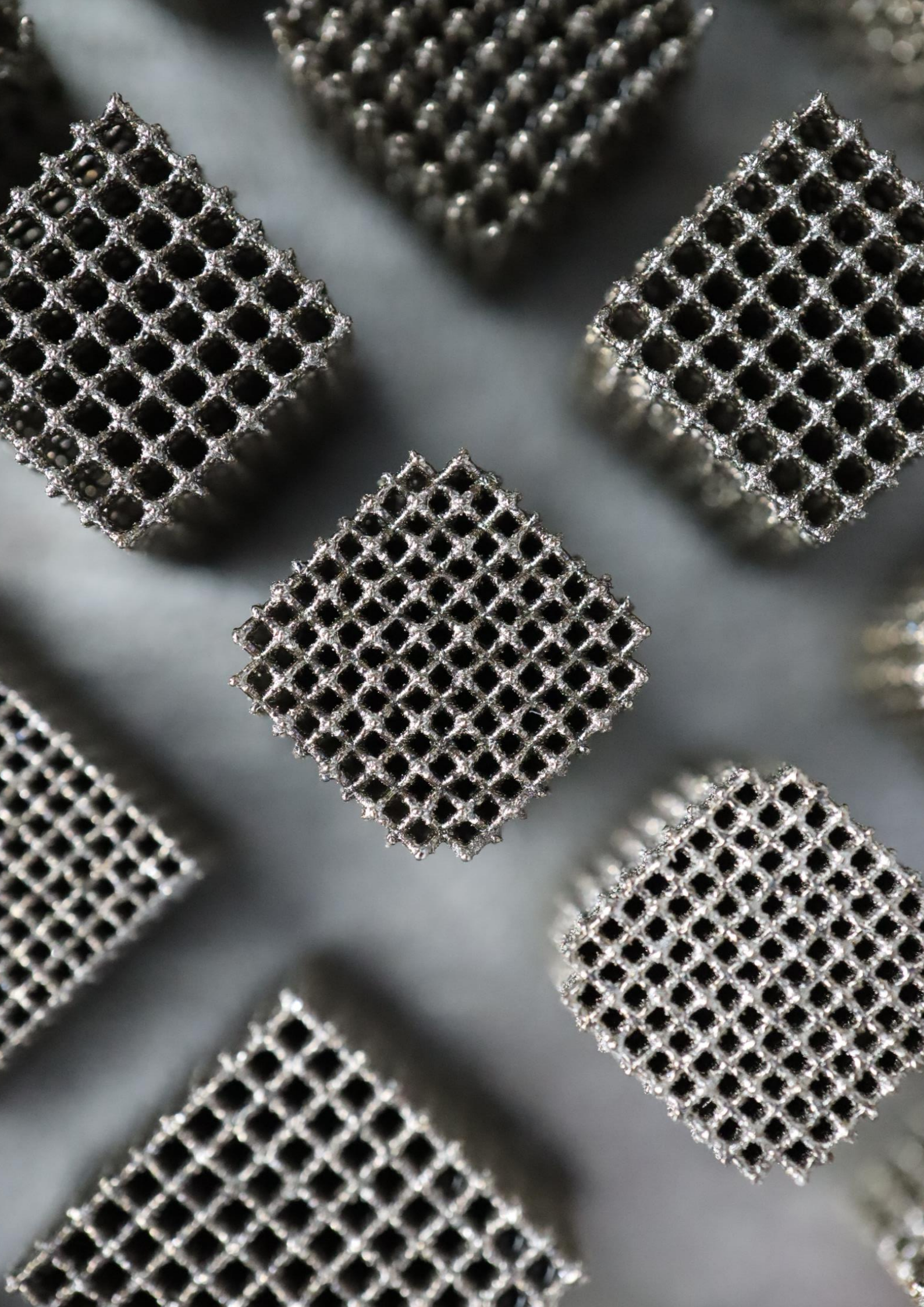

Various shapes Ni-Mn-Ga magnetic shape memory lattices
3D printed using L-PBF process.

Chapter 6

Microstructure control in Ni-Mn-Ga lattices through the use of heated platform, double scanning strategy and oriented structures

This chapter explores the influence of heated platform temperature, double scanning strategy, and strut orientation on the microstructure and magnetic properties of Ni-Mn-Ga magnetic shape memory alloys fabricated using laser-powder bed fusion (L-PBF). Some of the data on strut angle influence may be part of a future publication.

Abstract:

Prior research has established the importance of grain texture in achieving large magnetic-field-induced strain (MFIS) in Ni-Mn-Ga magnetic shape memory alloys. The study investigates two methodologies for controlling microstructure: the use of a heated platform and a double scanning strategy. Additionally, the research examines the impact of strut angle on texture evolution. The influence of platform temperature on microstructure and magnetic behaviour is minimal within the tested range (up to 400 ºC). The double scanning strategy, involving two scans on each layer at reduced energy density, results in compositions similar to single scanning. Pre-sintering at 700 mm/s slightly affects magnetic saturation. Strut orientation significantly impacts crystallographic texture, with struts aligned closer to the building direction exhibiting a stronger texture. Heat treatment induces grain growth and increases texture, but the precise mechanisms during heat treatment remain unclear, warranting further investigation to understand the role of strut angle during annealing. This study lays the groundwork for exploring microstructure control through L-PBF and geometry for Ni-Mn-Ga alloys, with potential implications for other materials and applications.

1. Introduction

Previous research has established the important role of texture and bamboo-like grain in the fabrication of Ni-Mn-Ga magnetic shape memory alloys with large magnetic-field-induced strain (MFIS) [31,100–102]. Laser-powder bed fusion (L-PBF) additive manufacturing typically results in materials with a distinct texture with columnar grains aligning along the build direction [65,103]. While prior investigations on L-PBF have predominantly concentrated on mitigating process-related anisotropy, this study uses its favourable consequences on the MFIS. It has been demonstrated that the thermal gradient and concomitant crystallographic texture can be controlled through process parameters, scanning strategies, and other process variables [91,103]. In this context, this study explores two methodologies for influencing the microstructure, the use of a heated platform and a double scanning strategy. Additionally, the research explores the impact of strut angle on texture evolution. It is important to note, however, that modifications of the thermal gradient inherently induce changes in chemical composition, with consequence on Mn evaporation [22,80].

1.1. Heated platform

Employing a heated platform within the L-PBF process has an effect of reducing the thermal gradient by uniformly heating the powder throughout the fabrication process. This has a consequence on reducing the residual stresses (detrimental for the MFIS) and mitigating crack formation that typically arises due to the rapid solidification of the process. Preceding investigations have demonstrated substantial reductions in thermal stresses (up to 80%) in M2 Tool Steel, accomplished through the utilisation of a 200 ºC platform [104]. Analogously, reductions of 50% (Ti6Al4V with 300 ºC) [105] and 40% (standard chrome molybdenum steel with 160ºC) [106] have been achieved. The effect of the heated platform, however, is strongly material dependant [107]. Martens et al. [107] highlighted that significant microstructural changes manifest when a phase transformation occurs beneath the preheating temperature (enhance uniformity in Al7075), a phenomenon of significance for Ni-Mn-Ga alloys given the austenite-martensite transition range of 60-110 ºC.

1.2. Double scanning

The technique of double scanning represents another method for controlling the thermal gradient within the L-PBF process. This approach is characterised by executing two scans on each layer, generally at a reduced energy density, thereby diminishing the heat input per unit area and retarding the cooling kinetics. The secondary scan (with the lowest energy) may be positioned either preceding the principal scan, serving as a pre-sintering step [108], or after it, serving as an in-situ heat treatment [109,110]. For instance, Obeidi et al. [109] observed a decrease in hardness and elastic modulus due to the annealing effects attributed to the re-melting scan in stainless steel 316L samples. This method has demonstrated its potential in diminishing residual stresses (in chrome molybdenum steel and stainless steel 316L samples) [106,111], improving surface finish [112], and controlling microstructure [112,113]. However, Yasa et al. [112,113] demonstrated that re-scanning each layer several times results in refined lamellar microstructure in stainless steel 316L samples.

1.3. Influence of the strut orientation

The orientation of the build in relation to the platform has a strong influence on crystallographic texture [58]. Consequently, struts oriented at different angles relative to the platform experience disparate thermal gradients and solidification rates. While extant studies have examined the impact of strut angles on defects, geometrical integrity, and mechanical properties of lattices [59,60], limited investigations have delved into its implications on microstructure. For example, Jia et al. [59] explored the influence of strut angle on the mechanical properties of AlSi10Mg samples, observing an inverse correlation between strut angle increase (angle with the platform) and elastic modulus, while yield and ultimate strength displayed positive trends. A subtle reduction in average grain size with increasing strut angle was also observed, seemingly contradictory to expectations of large columnar grains aligned with the vertical strut direction. Further research has addressed the impact of strut diameter on microstructure, with studies revealing highly textured crystallography for small 250 μm struts [65] and even approaches to single crystal texture [66,67] in various materials such as steel 316L and nickel superalloys.

2. Experimental procedure

The fabrication of the samples was made utilising a Concept Laser M2 Cusing system, operated by a 400 W continuous-wave fibre laser with a 1.064 μm wavelength, with a maximum beam transverse speed of 4 m/s and a laser beam focal point diameter of approximately 67 μm. The manufacturing process occurred within a protective Argon atmosphere to ensure a minimal O_2 content of 100 ppm. The L-PBF parameters employed were as follows: a laser power setting of 70 W, a scanning speed of 450 mm/s, a contour distance of 75 μm, and a layer thickness of 25 μm. The samples were then cut off the substrate and sectioned along the build direction by electro-discharge machining (EDM).

2.1. Heated platform

A custom-designed heated platform system, illustrated in Figure 6.1, and designed by Luke Carter (University of Birmingham) was used to heat up a 65 × 65 × 8 mm^3 steel substrate. Four distinct temperatures were tested, 100 ºC, 200 ºC, 300 ºC, and 400 ºC. Precise temperature control was achieved using K type thermocouples, and the printing process was initiated 15 minutes subsequent to the attainment of the desired temperature. The powder used in these experiments (from UTBM) was recycled from prior parameter optimisation experiments (Chapter 5) and subjected to sieving using a 90 μm sieve to eliminate any residual contaminants from prior builds. Various sample geometries were fabricated, encompassing 8 × 8 × 8 mm^3 cubes, 2D wall lattices, and three lattices with different unit cells. The geometry studied here is the same as the one studied in Chapter 5. The colour alteration of the substrate in Figure 6.1, suggest the presence of oxygen within the chamber.

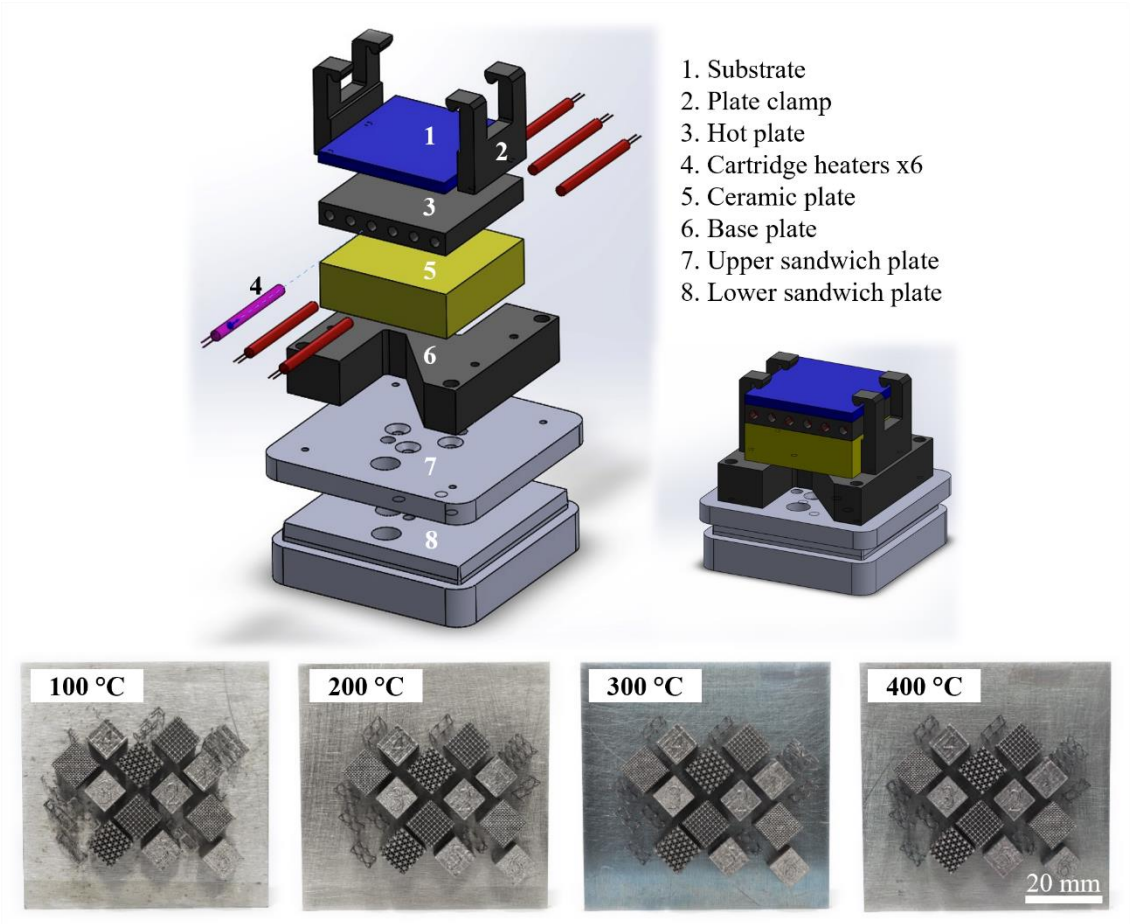

Figure 6.1. *Heated platform set-up and picture of the four builds at different platform temperature.*

2.2. Double scanning

The double scanning was made by loading two stereolithography files (STL files) on top of each other in the printer software. The optimised laser power was already close to the lower limit of the printer; therefore, the scanning speed was varied for this experiment. The scanning parameters are summarised in Table 6.3, three test samples were printed with a single scan (top left, tilted ones on Figure 6.2). The build was performed on a 90 × 90 mm^2 stainless steel 316L substrate and is shown in Figure 6.2.

Figure 6.2. *Picture of the build plate with the single scanned samples.*

2.3. Influence of strut angle

To study the influence of the strut angle (α) on the microstructure, graded bcc lattices, illustrated in Figure 6.3 were manufactured. The angle of the strut varied from bottom to the top from α = 30º to 70º. The design was created using the nTopology software with a continuous ramp field. After sample preparation, the graded sample was scanned heat-treated, and scanned again. Additionally, samples with constant strut angle 15º, 45º and 75º with the platform were produced.

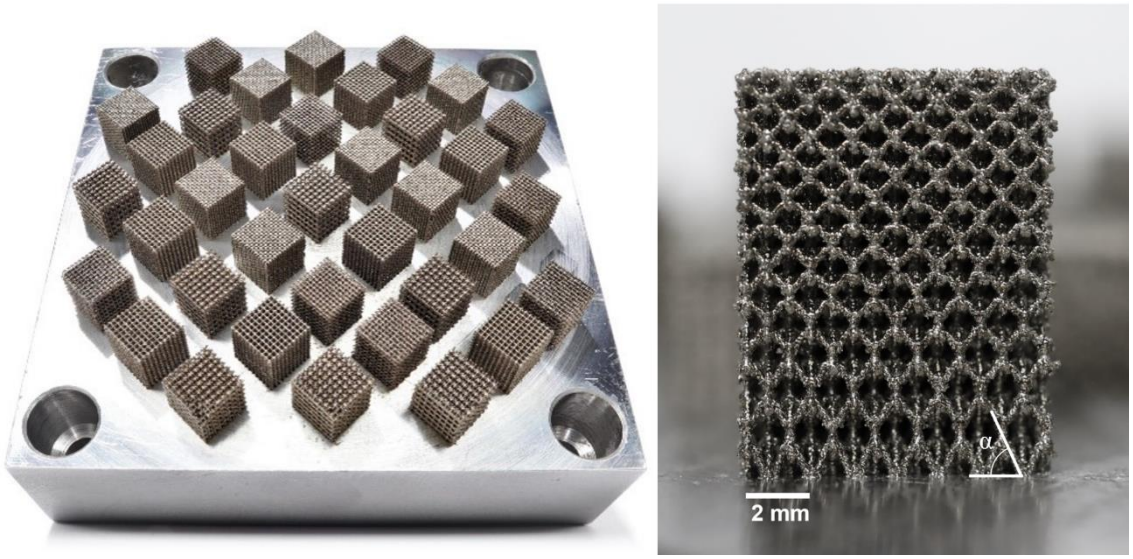

Figure 6.3. *Picture of the build plate with the lattices with variable strut angle α and a picture of a graded lattice.*

2.4. Sample preparation and characterisation

The specimens underwent an initial ultrasonic cleaning phase to remove loose powder particles. Subsequently, the samples were subjected to manual grinding and polishing, resulting in a mirror-like surface finish. Following this, electropolishing was conducted under a constant 12 V voltage at a temperature of -20 °C, employing an electrolyte solution comprised of a 4:1 volumetric ratio of ethanol to 70% HNO_3. Some samples were subjected to thermal etching at 800 °C for 1 hour to facilitate the examination of the microstructure. Other samples were subjected to a heat treatment according to [56] an initial homogenisation stage at 1060 °C for 12 hours, followed by an ordering stage at 800 °C for 4 hours.

Microstructural examination and imaging procedures were conducted employing a polarised optical microscope (Meiji Techno, Japan) and a Hitachi TM3000 Scanning Electron Microscope (SEM). Chemical compositions were ascertained using an x-ray fluorescence (XRF) analyser X-Strata 960 (Oxford Instruments), calibrated through reference to a known composition Ni-Mn-Ga sample, and equipped with a 300 µm diameter collimator. The magnetic properties were investigated utilising a LakeShore 8600 Series vibrating sample magnetometer (VSM). The hysteresis loops were repeated 10 times, no differences were observed between the curves. The demagnetisation factor was considered by assuming the sample shape as a cube. X-ray diffraction (XRD) analyses were executed utilising a PANalytical Empyrean 3 diffractometer (Cu tube, $\lambda = 0.15406$ nm) fitted with poly-capillary optics and a PIXcel3D-Medipix3 detector. Additionally, electron backscatter diffraction (EBSD) analysis was conducted using a TESCAN Clara FEG-SEM system equipped with a NewTec Scientific FurnaSEM oven and an Oxford Symmetry 2 EBSD camera. The sample was affixed to the oven using conductive carbon paste, and tests were conducted at temperatures ranging approximately from 150 to 200 ºC to ensure a full transformation to austenite. The scan was made with a beam current of 20 nA and a step size ranging from 0.5 µm to 1.5 µm. The analysis of the EBSD data was made using the software, Atex.

3. Results and discussion

3.1. Heated platform

Table 6.1 provides an overview of the final composition of heat-treated lattices fabricated on different temperature platforms. Prior XRF measurements on as-built lattice specimens exhibited a considerable standard deviation. This variability was partially attributed to the measurement of high Mn content unmelted powders adhering to the strut surfaces. This phenomenon was unavoidable during measurements due to the overlap between the XRF spot size (approximately 300 µm) and the strut diameter (250 µm). Consequently, the measurements presented here specifically concern electropolished and heat-treated samples that exhibit less amount of unmelted powder particles on their surface.

Table 6.1. *Chemical composition of heat-treated lattices fabricated on the heated platform measured by XRF.*

Platform temperature (°C)	at.% Ni		at.% Mn		at.% Ga	
100	50.92	± 0.18	28.50	± 0.28	20.58	± 0.11
200	50.77	± 0.10	28.69	± 0.18	20.55	± 0.12
300	50.58	± 0.17	28.83	± 0.33	20.59	± 0.19
400	50.52	± 0.05	28.95	± 0.17	20.52	± 0.13

A visual representation of the Mn content's sensitivity to platform temperature is depicted in Figure 6.4. A noticeable trend is apparent, indicating a reduction in Mn evaporation with higher platform temperatures. Nevertheless, the recorded values exhibit minimal divergence, with overlapping standard deviations. The marginal Mn content elevation at higher temperatures might arise from a larger amount of high Mn content particles attached to the strut surface due to increased temperatures; however, this hypothesis requires further investigation.

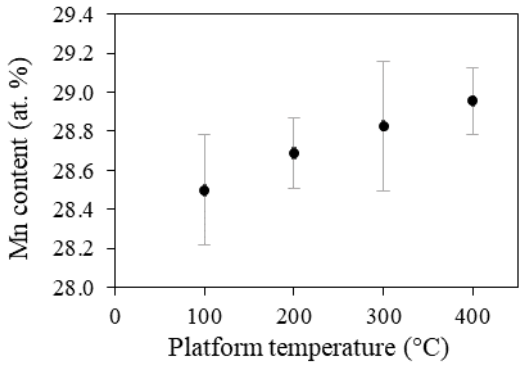

Figure 6.4. *Influence of the platform temperature on the Mn content (as-built condition) measured by XRF.*

Figure 6.5 shows optical micrographs of thermally etched as-built lattice samples. Although the precise characterisation of grain morphology presents challenges due to the low contrast of the grain boundaries, a comparative analysis of the four micrographs distinctly indicates that significant changes resulting from platform temperature variations are not present. Additionally, SEM observation of the struts size shows that the platform temperature does not exert a discernible influence on sample geometry.

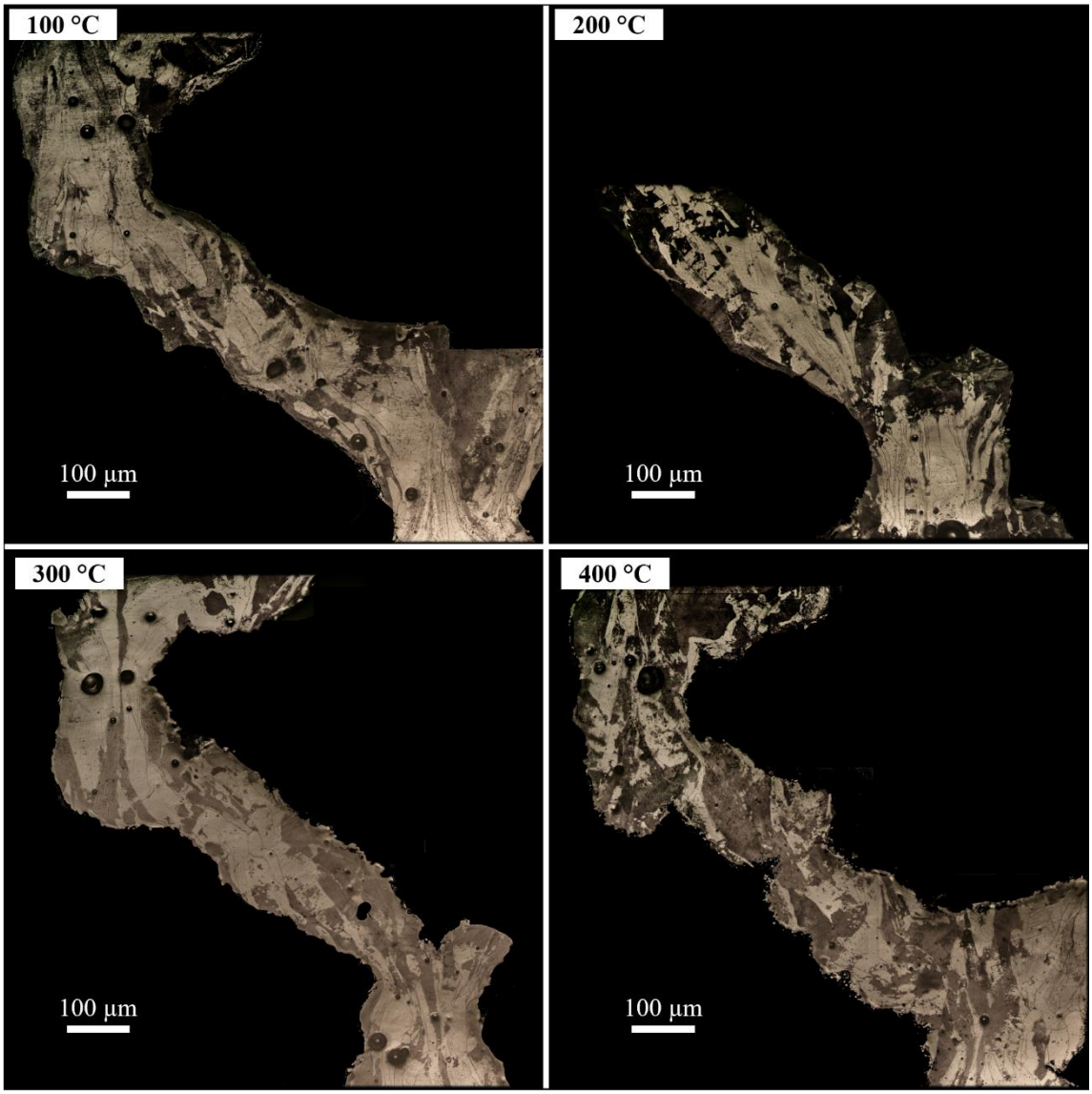

Figure 6.5. *Stitched optical micrographs of lattice samples built on different platform temperature.*

Figure 6.6 presents the results of VSM measurements. The coercivity and remanence values remain consistent across all samples. Only a marginal difference in saturation magnetisation becomes apparent—lattices built on 200 ºC and 300 ºC platforms exhibit slightly higher saturation magnetisation (64 Am^2/kg) compared to those fabricated on 100 ºC and 400 ºC platforms (61 Am^2/kg). Overall, the magnetic behaviour of all four samples is very similar, suggesting similar characteristics in their microstructure and composition.

Figure 6.7 depicts the normalised XRD data across a range of 46º to 74º. Each sample exhibits discernible NM and 14M phases, along with minor traces of 10M phase, consistent with established literature and chemical composition of this material. Table 6.2 summarises the lattice parameters with a precision of 0.005 Å. The crystallographic patterns of the four samples display a large similarity, with only small differences in the sample from the 400 ºC platform, like slightly wider peaks and different peak intensities (higher 14M (040) peak around 64º and lower NM (400) peak around 68º), attributed to subtle texture variations or small compositional heterogeneity with plausibly a larger fraction of 14M.

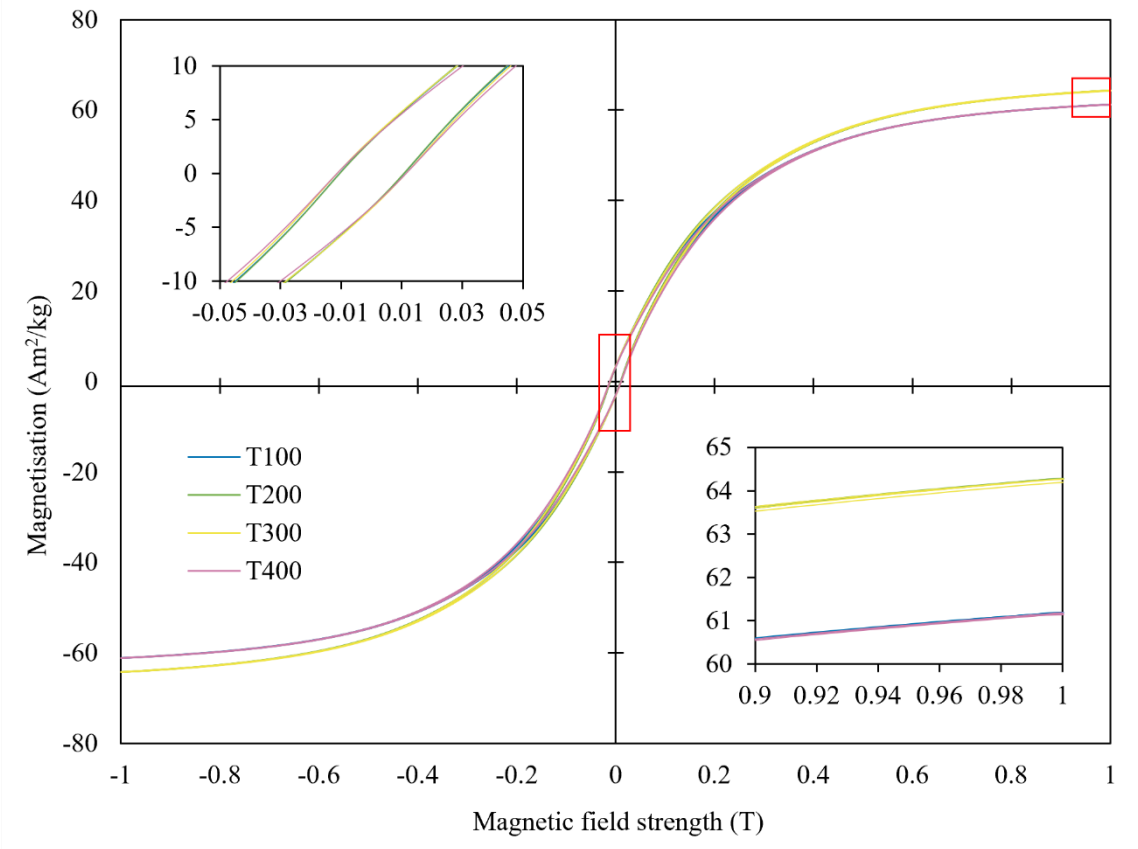

Figure 6.6. *Magnetisation hysteresis loop obtained at ambient temperature from the VSM measurements on heat-treated lattices fabricated with different platform temperature (in ºC). The insets show a magnified view of the two red squares.*

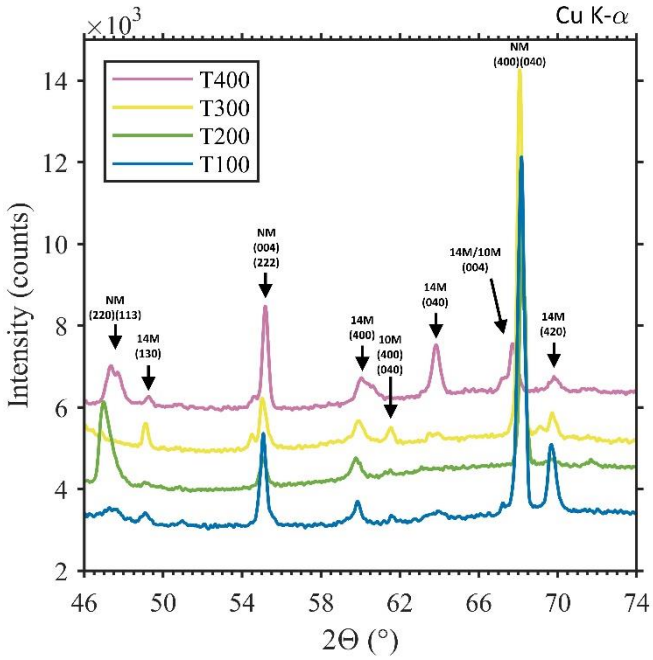

Figure 6.7. *X-ray diffractograms obtained from the heat-treated lattices fabricated with different platform temperature (in ºC). The background has been removed and the baseline is offset. All peaks have been indexed with respect to the unit cell coordinate system of the cubic parent phase.*

Table 6.2. *Lattice parameters of the NM, 14M and 10M crystallographic structure present in the lattice samples made on the heated platform.*

	a	b	c	γ
NM	5.499	5.499	6.651	90º
14M	6.117	5.831	5.53	90.56º
10M	5.999	5.983	5.568	90.33º

Collectively, these findings suggests that a platform temperature of 400 ºC may not be sufficient to induce substantive disparities in the microstructure and correspondingly, magnetic behaviour. To evoke substantial changes, a platform temperature above the $L2_1$ austenite-to-B2' phase transition (approximately 760 ºC in this material) is probably required, however the set-up used did not reach higher temperatures.

3.2. Double scanning

The chemical composition of the samples printed with a double scanning strategy are summarised in Table 6.3. From these results, we can see that a combination of 700 mm/s and 900 mm/s, no matter the order, results in compositions very close to the single scanned sample composition. It seems that this behaviour follows a rule of:

$$v_0 = \frac{1}{4}(v_1 + v_2) \quad (1)$$

where v_0 is the scanning speed used for a single scan strategy, v_1 and v_2 the scanning speeds used for a double scan strategy.

Table 6.3. *Scanning speed values and chemical composition of the double scanned heat-treated lattices measured by XRF.*

Scan speed v_1 (mm/s)	Scan speed v_2 (mm/s)	at.% Ni	at.% Mn	at.% Ga
450	700	50.60 ± 0.16	29.01 ± 0.32	20.39 ± 0.20
450	900	50.78 ± 0.33	28.79 ± 0.39	20.43 ± 0.20
450	1350	50.52 ± 0.27	29.04 ± 0.26	20.43 ± 0.07
700	900	49.98 ± 0.15	29.73 ± 0.15	20.29 ± 0.09
900	450	50.95 ± 0.31	28.82 ± 0.29	20.22 ± 0.08
1350	450	50.42 ± 0.18	29.25 ± 0.16	20.34 ± 0.10
700	450	50.84 ± 0.22	28.83 ± 0.27	20.33 ± 0.11
700	700	50.49 ± 0.40	29.30 ± 0.36	20.21 ± 0.11
900	700	50.09 ± 0.39	29.72 ± 0.32	20.19 ± 0.22
450	450	51.36 ± 0.35	28.45 ± 0.37	20.19 ± 0.06
Powder		48.83	31.24	19.93
Single scan		49.88	29.91	20.21

Figure 6.8 illustrates the relationship between the deviation of Mn content from that of the single-scanned sample (where 100% signifies identical Mn composition) and the secondary expression of equation 1. The observed correlation appears to align with a linear pattern. Further experiments incorporating scanning speed parameters based on equation 1 would present insightful results and contribute to the establishment of robust conclusions.

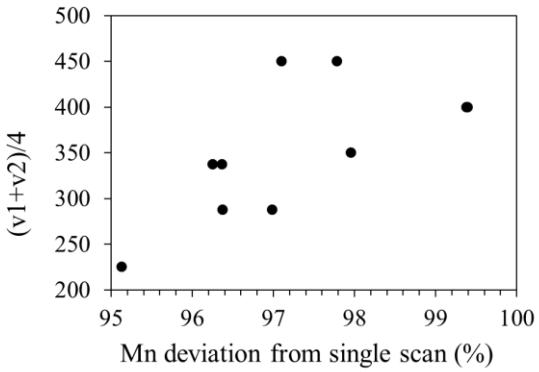

Figure 6.8. *Mn deviation from Mn content of the single scanned sample against scanning speeds.*

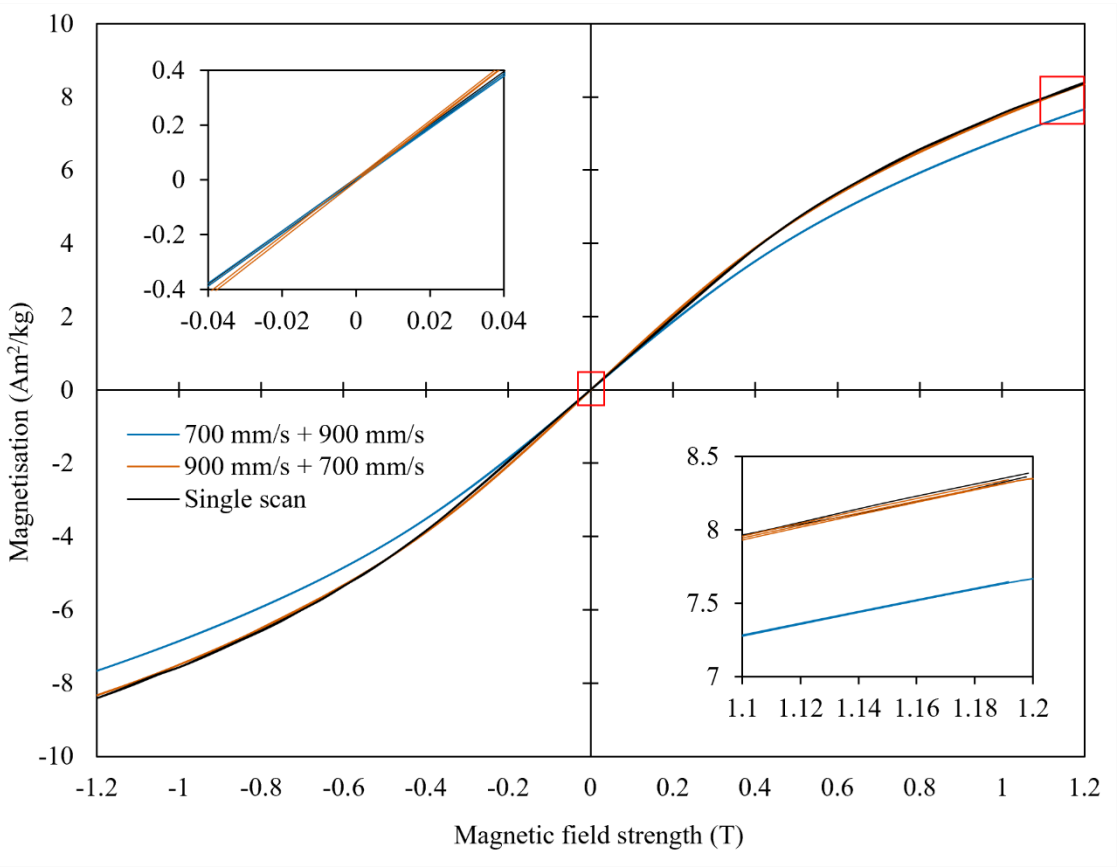

Figure 6.9. *Magnetisation hysteresis loop obtained at ambient temperature from the VSM measurements on as-built lattices fabricated with a double scan strategy and single scan as a reference. The insets show a magnified view of the two red squares.*

Figure 6.9 presents the results of VSM measurements conducted on two samples fabricated using scanning speeds of 700 mm/s and 900 mm/s, alongside a single-scanned sample. These measurements were performed on samples in their as-built state, resulting in relatively weak signals and no significant hysteresis. The samples did not reach saturation, even after increasing the magnetic field to 1.2 T, the maximum strength possible in the configuration used (due to sample size). However, it is noteworthy to observe a minor distinction in magnetisation between the pre-sintered sample (700 mm/s + 900 mm/s) and the re-melted sample (900 mm/s + 700 mm/s). Specifically, the pre-sintered sample displays a magnetisation of 7.66 Am^2/kg, while the re-melted one displays 8.34 Am^2/kg

(similar to the single-scanned sample), at a magnetic field strength of 1.2 T. This discrepancy implies a subtle alteration in either texture or homogeneity.

It is crucial to highlight that adopting a double scan strategy would inevitably lead to increased oxygen absorption, detrimental to the shape memory effect. Consequently, this study did not progress further in this direction.

3.3. Influence of the strut orientation

The chemical composition of the graded lattice sample was measured at 42 distinct points across the specimen and averaged to $Ni_{50.82}Mn_{28.46}Ga_{20.72}$. Six points were sampled for each row of the sample, corresponding to a certain strut angle (angle with respect to the platform). These values are graphically presented in Figure 6.10. By omitting the top row, which corresponds to struts at a small angle, a subtle linear tendency can be observed. This trend indicates a slight elevation in Mn evaporation with an increase in the strut angle. Nevertheless, the values remain very close to each other, and this correlation is not really significant.

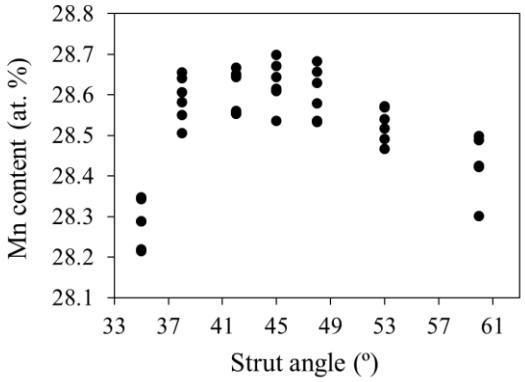

Figure 6.10. *Influence of the strut angle on the Mn content measured on the graded as-built lattice, measured through XRF.*

EBSD analysis was conducted on the identical sample both before and after heat treatment, with both scans performed in the austenite cubic phase (a = b = c). The resulting inverse pole figure (IPFz, normal to the build direction, ND) maps are presented in Figure 6.11.

The surface area of each individual grain was determined using Atex software, with grain size represented as the equivalent circle area corresponding to this surface area. However, considering the strong anisotropy of the grains, especially after heat treatment, it is important to note that the grain size value may not be fully representative. Therefore, Table 6.4 provides additional details on the surface area, grain aspect ratio, and the equivalent ellipse long axis length denoted as *a*. Furthermore, the presence of numerous small grains significantly reduces the average grain size, particularly notable in the heat-treated condition. In this state, the arithmetic average grain size is approximately 67 µm, whereas the area-weighted average is approximately 265 µm. Consequently, the grain size parameters are expressed here in terms of the area-weighted average, where larger grains contribute more than smaller ones. The heat treatment has a substantial impact on grain size, increasing the average surface area by a factor of 16, from an initial average of around 555 µm² in the as-built state to approximately 9,196 µm² after heat treatment. The heat-treated sample map reveals the presence of advantageous bamboo-like grains spanning the strut diameter, with the largest grain measuring up to 733 µm in length. However, it is expected that the aspect

ratio would decrease in the heat-treated conditions, as grains tend to lose some of their columnar structure during heat treatment going from around 4 to 2.

Table 6.4. *Grain surface area, grain size, aspect ratio and equivalent ellipse long axis length values for as-built and heat-treated graded lattice.*

		Grain surface area (μm^2)	Grain size (µm)	Aspect ratio (a/b)	a (µm)
Arithmetic average	AB	555.26	18.26	3.07	16.90
	HT	9195.93	66.93	2.04	46.89
Area-weighted average	AB	-	69.11	4.13	69.20
	HT	-	264.74	2.14	196.24
Max value	AB	69367.50	297.11	100	395.92
	HT	309532.00	627.98	51	733.20
Min value	AB	9.00	3.39	1	1.70
	HT	16.00	4.51	1	2.26
Standard deviation	AB	1655.35	19.32	2.46	21.09
	HT	23195.70	85.03	1.25	63.70

The IPFz maps were further partitioned into eight sections along the build direction to investigate the influence of the strut angle on the texture and the grain size. Pole figures were generated for each individual row along the entire length of the samples and are shown in Figure 6.12 along with a small part the corresponding row. In general, the sample exhibits a weak texture with maximum intensities between 2 and 4. The highest multiple of uniform (MUD) values predominantly appeared in the (100) pole figures. Figure 6.13 provides insight into the effects of the strut angle on the average grain size and the MUD. There is no significant impact of the strut angle on average grain size; however, it does influence the texture. First, the heat-treated condition exhibits a higher texture, suggesting that specific grain orientations are favoured during grain growth. Second, in the as-built condition, the MUD increases as the strut angle (α) rises, with an inverse trend observed in the heat-treated condition. The orientation of the struts influences the thermal gradient by orienting it along the struts. During the process, the heat flow along the struts impacts grain nucleation, resulting in an increase of the texture with increasing α, reaching a maximum texture when the angle is closer to the 90º build direction. However, during heat treatment, the texture decreases with increasing α. The development of grains during heat treatment is linked to both the heat flow and the stress relief processes. The observed impact of strut angle on texture during heat treatment suggests an anisotropic diffusion, possibly due to grain boundaries pinned during annealing depending on the strut angle. This is corroborated by the presence of clusters of small grains in the heat-treated condition. However, it is worth noting that the length of the struts also varies with longer lengths at higher α that could influence the grain boundary motion during annealing. To delve deeper into the diffusion process during heat treatment, it is advisable to undertake investigations at a smaller scale, such as in-situ synchrotron experiments. Third, it can be observed in Figure 6.12 that some inherent texture seen in the as-built condition is lost after heat-treatment. Such as for the highest angle, where a strong pole can be seen at $[0\bar{1}0]$ in the as-built condition, while it is weaker in the heat-treated condition, with grain alignment preferably associating to $[0\bar{2}1]$. Figure 6.12 reveals that a gradual decrease in the strut angle progressively modifies the pole locations shown in the (100) pole figures. It appears that as the long axis of the grains tends to align with the build direction in the highest angle strut (bottom

one), a single pole develops and approaches the $[0\bar{1}0]$, which is the behaviour expected for a bulk material where the grains and crystal orientations are aligned with the building direction. In contrast, as the strut angle decreases and therefore get further from the build direction, the pole moves further from the $[0\bar{1}0]$, and its intensity decreases. This trend is less apparent in the heat-treated condition, but the rotation of the poles is still observable.

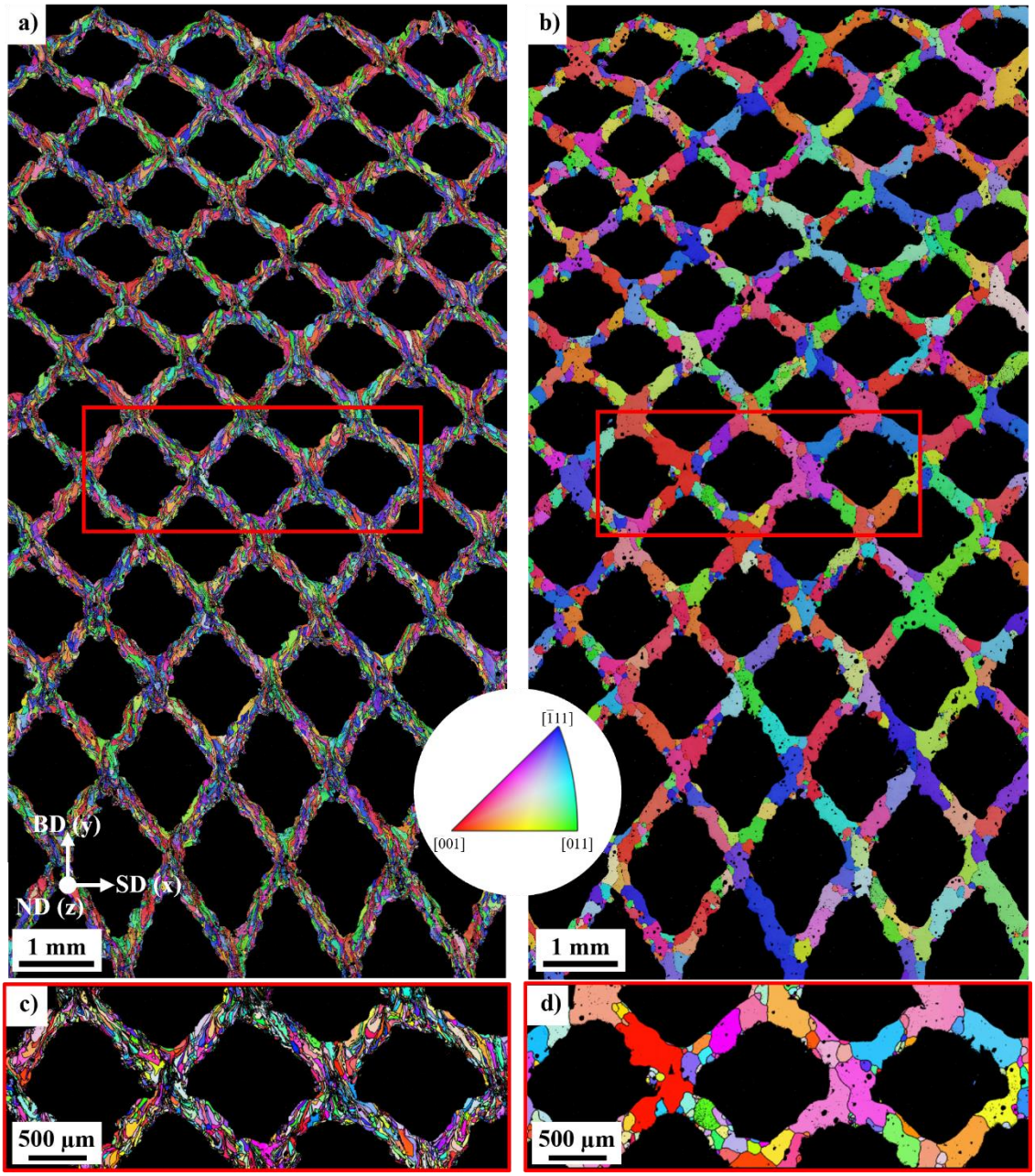

Figure 6.11. *IPFz maps of a cross section of the as-built (a,c) and heat-treated (b,d) graded lattice in the austenite phase.BD corresponds to the building direction, SD to the scanning direction and ND the normal direction.*

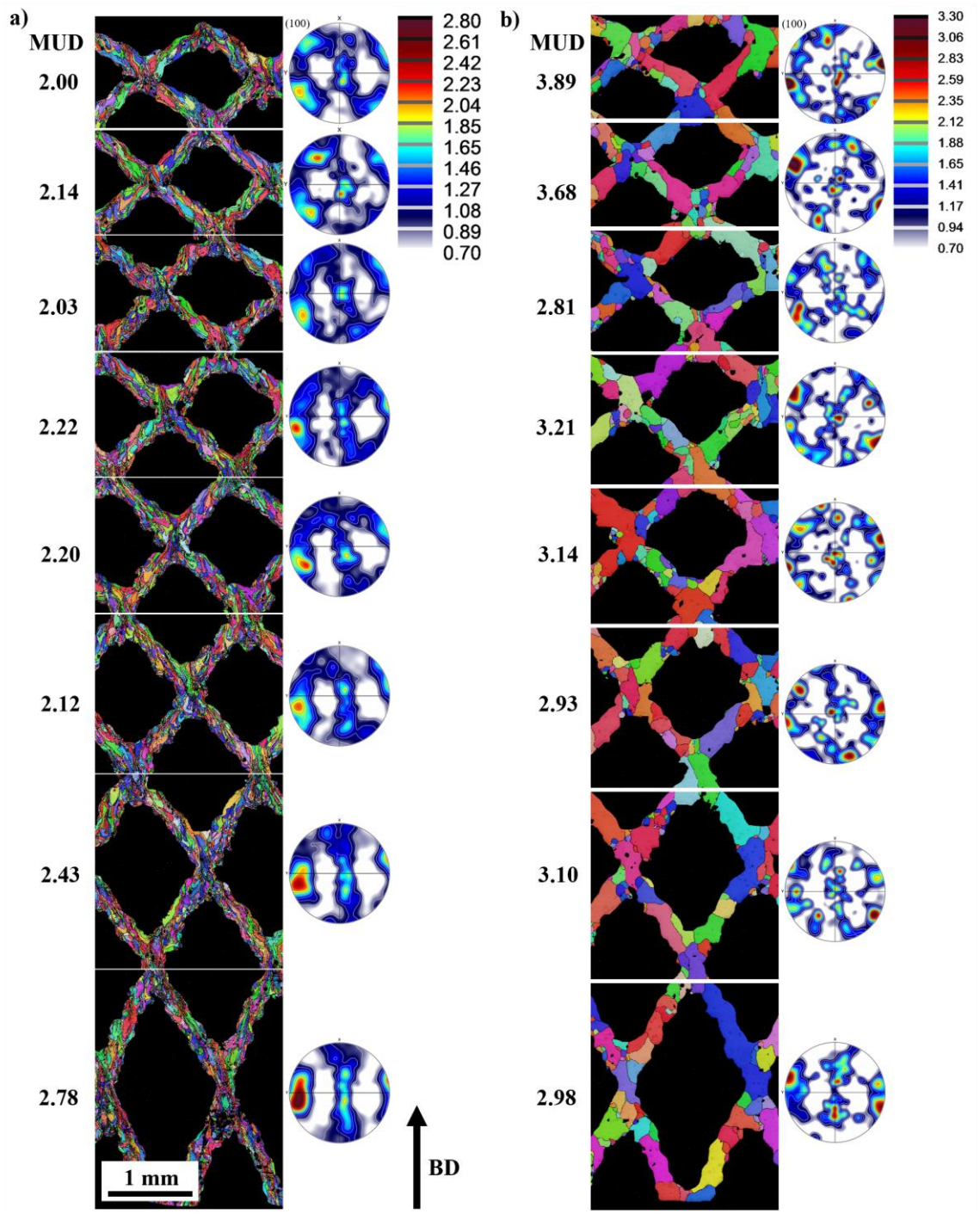

Figure 6.12. *(100) pole figures of each row of the sample in the (a) as-built and (b) heat-treated conditions.*

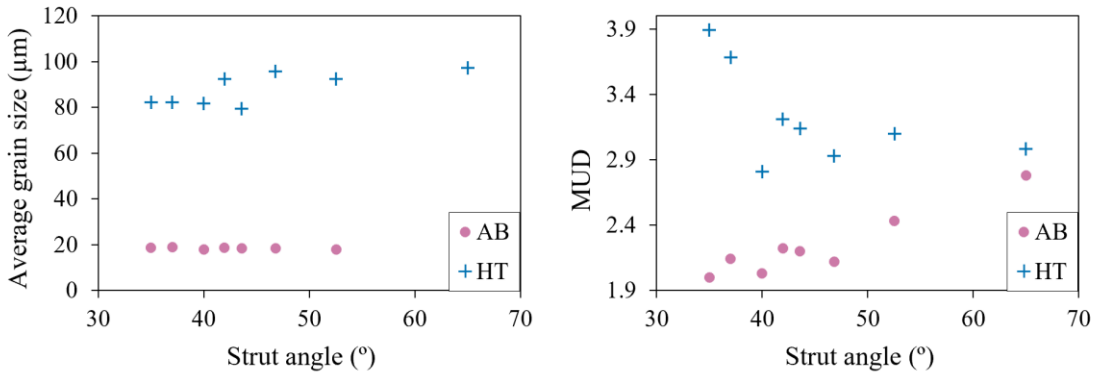

Figure 6.13. *Influence of the strut angle on the average grain size and the MUD in as-built (AB) and heat-treated (HT) graded lattice.*

The presence of neighbouring struts exerts an influence on the solidification behaviour of adjacent struts. Struts built at different angles can interact with each other, affecting their thermal profiles and potentially leading to different grain growth patterns. To overcome this microstructural constraint, samples with uniform strut angle (15º, 45º, and 75º) have been fabricated.

The sample with α = 15º strut angle exhibited a poor surface finish, likely attributed to entrapped loose particles in the narrower interstices, resulting in surface scratching during the polishing process. Figure 6.14 illustrates the inverse pole figure from BCC 45, BCC 75 and the graded samples. A clear texture in the BCC 75 in the [001] direction is observed while BCC 45 depict a weak texture in the [101] direction. This is in accordance with the observations made in the graded sample with the crystal orientation aligning with the struts and resulting in a stronger texture along the build direction when α is closer to the 90º build direction.

Figure 6.15 illustrates the pole figures of samples with α at 45º (denoted as BCC 45) and 75º (denoted as BCC 75) in the heat-treated condition. It is discernible that the pole figure for sample BCC 45 bears resemblance to that corresponding to α = 45º in the graded lattice (after heat treatment) but with a smaller MUD value of 2.03 (versus 3.14 in the graded lattice). In contrast, the texture for BCC 75 is more pronounced, with a MUD of 3.79, indicating a preservation of texture following the heat treatment. Small differences between the texture of these samples and the corresponding one of in the graded sample can be attributed by the different thermal profiles related to the graded geometry, however both show the same tendency.

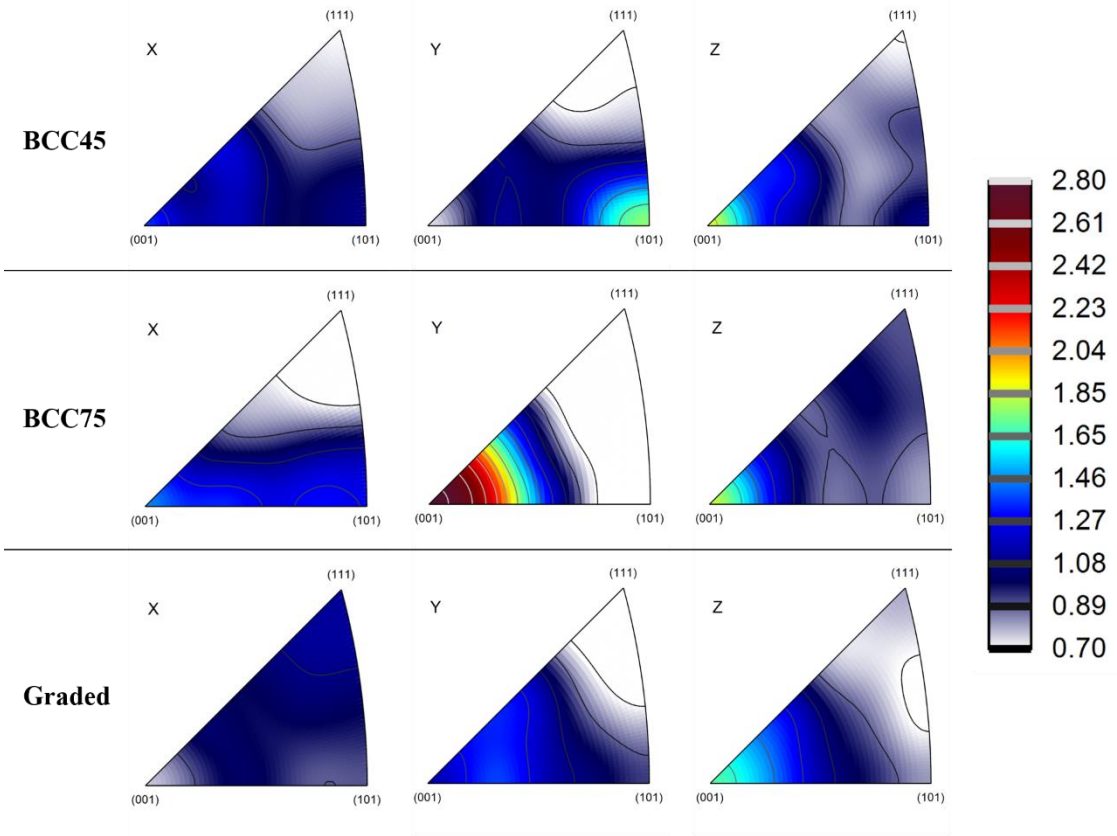

Figure 6.14. *Inverse pole figures of the heat-treated samples BCC 15, BCC 75 and graded.*

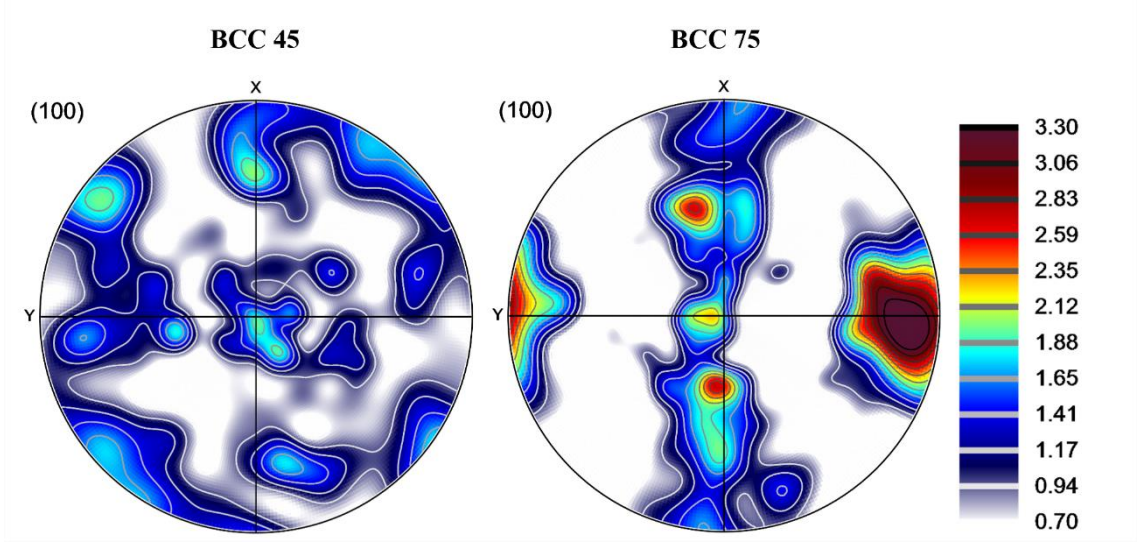

Figure 6.15. *(100) pole figures of the entire heat-treated samples BCC 45 and BCC 75.*

Magnetic measurements were carried out on the as-built samples with fixed strut angles, and the corresponding hysteresis loops are presented in Figure 6.16. An increase in magnetisation is evident with increasing strut angle, with the 15º strut angle sample exhibiting a magnetisation of 8 Am²/kg at 1.2 T, compared to 11 Am²/kg for the 75º strut angle sample.

It is important to consider that the densities of the three samples differ, potentially introducing an additional influence on crystal orientation and magnetisation. Furthermore, the length of the struts varies, with lattices

featuring higher angle struts also possessing longer struts, as observed in Figure 6.11 of the graded lattice that could also have an influence.

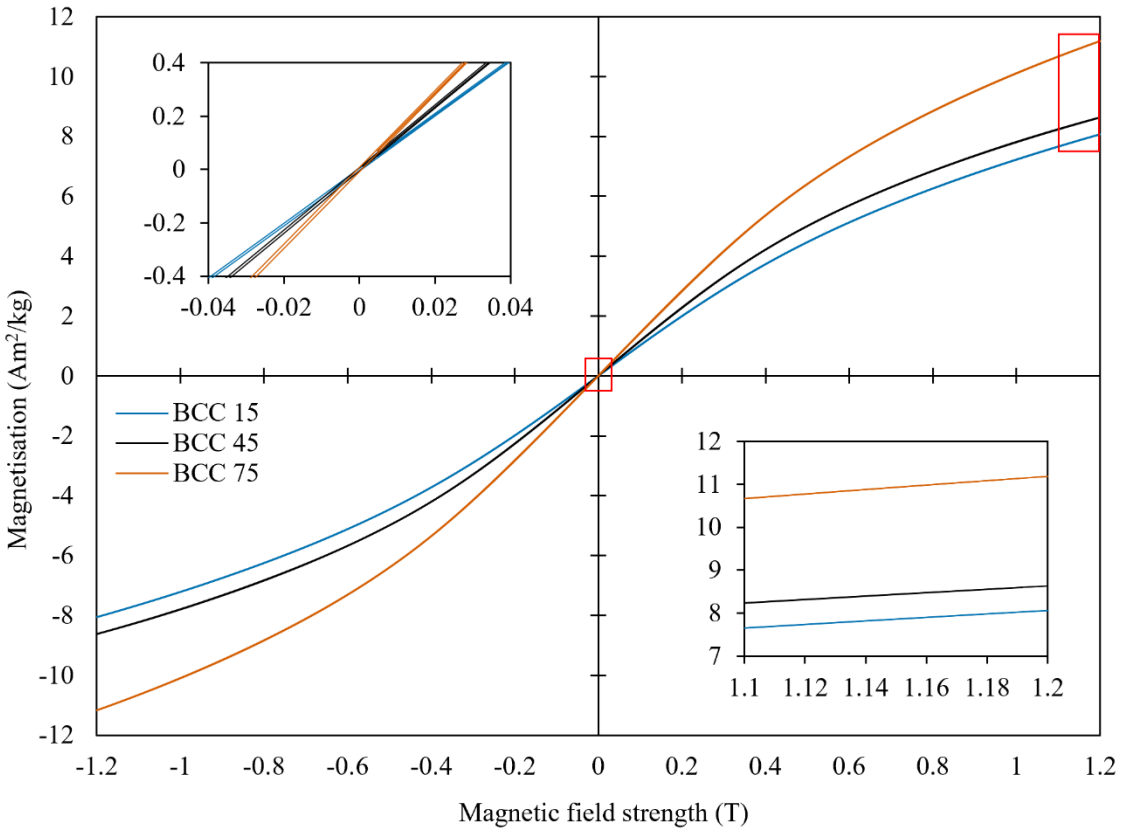

Figure 6.16. *Magnetisation hysteresis loop obtained at ambient temperature from the VSM measurements on as-built lattices fabricated with different strut angle. The insets show a magnified view of the two red squares.*

4. Conclusion

In summary, this study investigates the texture and grain structure of Ni-Mn-Ga magnetic shape memory lattices, aiming to understand their microstructural evolution within the context of L-PBF processing. The research encompasses the manipulation of thermal gradients through techniques like heated platforms and double scanning, along with an exploration of strut angle effects. This comprehensive investigation draws several key conclusions:

- The use of a heated platform, up to 400 ºC, appears to have no significant influence on the microstructure or magnetic behaviour. To induce substantial changes, a platform temperature exceeding the $L2_1$ austenite-to-B2' phase transition (approximately 760 ºC for this material) may be necessary.
- Employing a combination of scanning speeds at 700 mm/s and 900 mm/s results in a composition similar to that of a single scanned sample. Pre-sintering at 700 mm/s appears to marginally reduce magnetic saturation.
- Strut angle exerts a notable influence on crystallographic texture, with struts aligned closer to the building direction exhibiting a stronger texture.

- Heat treatment induces significant grain growth and generally increases texture. However, the precise mechanisms during heat treatment remain incompletely understood, warranting further investigation to comprehensively elucidate the role of strut angle during annealing.

Additional scanning strategy parameters may also affect the thermal gradient. Promoppatum et al. [114] have previously demonstrated the influence of scan lengths on microstructure and mechanical response. However, in the present study, due to the selection of a small strut diameter (200 µm) to encourage the formation of bamboo-like grains, certain scanning strategies like hatch strategies were not feasible. Consequently, a single contour scanning strategy was employed to ensure accurate geometry, thereby reducing the number of variables that could be altered.

Moreover, all these techniques potentially impact residual stresses. Unfortunately, this study lacks measurements of residual stresses, which could be a valuable avenue for future research.

Acknowledgments

This work was financially supported by the Defence Science and Technology Laboratory (DSTL), the Strategic Research Council of Finland (grant number 313349), the Academy of Finland (grant number 325910), and the AMBI (Analytics-based Management for Business and Manufacturing Industry) research platform of Lappeenranta-Lahti University of Technology LUT. The EBSD work was supported by the Henry Royce Institute for Advanced Materials, funded through EPSRC grants EP/R00661X/1, EP/S019367/1, EP/P025021/1 and EP/P025498/1

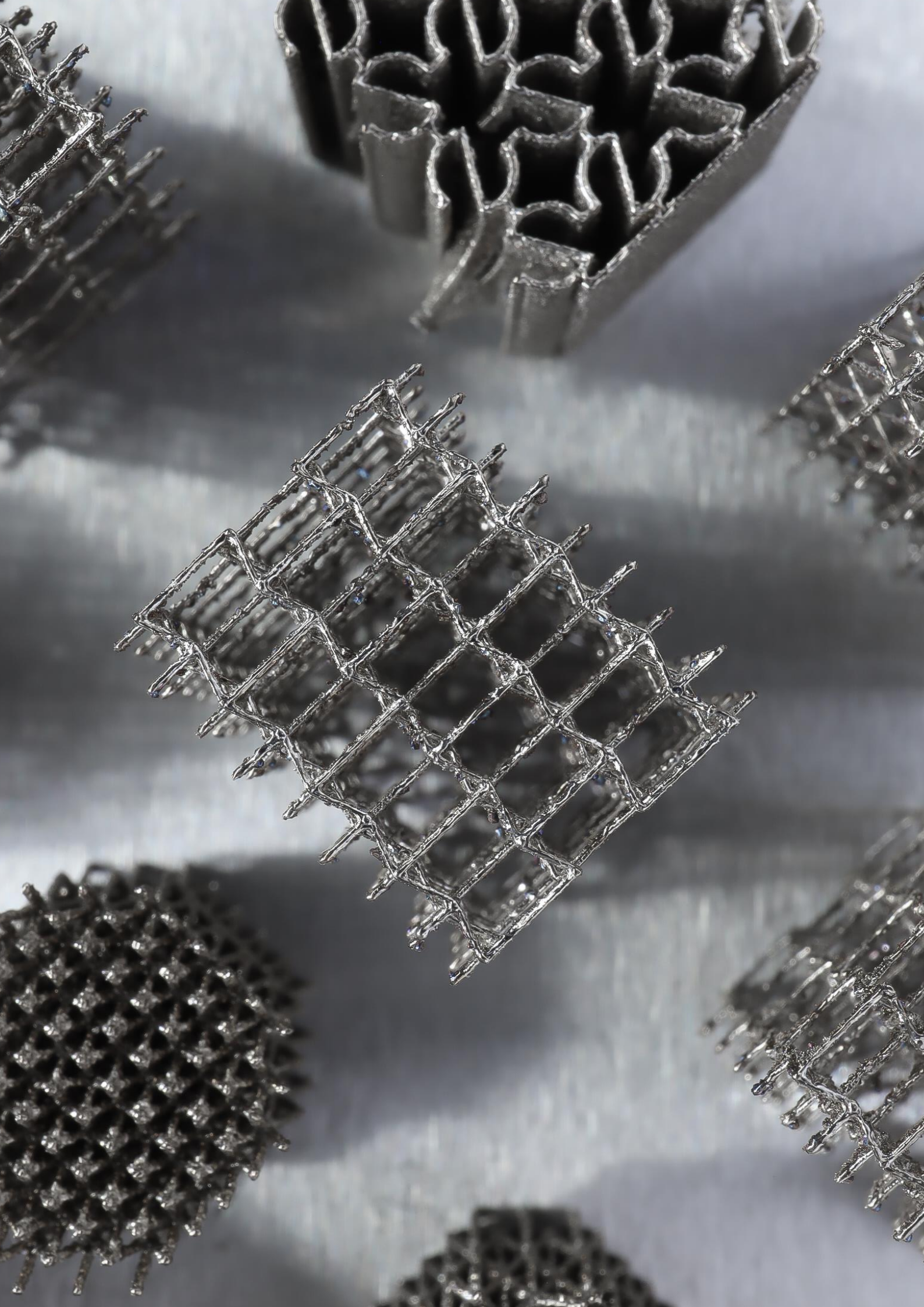

Auxetic Ni-Mn-Ga magnetic shape memory lattices
3D printed using L-PBF process.

Chapter 7

First investigation of the mechanical properties under compression loading of Ni-Mn-Ga lattices manufactured through L-PBF

This chapter provides a comprehensive overview of the mechanical properties exhibited by Ni-Mn-Ga lattices manufactured via Laser Powder Bed Fusion (L-PBF). The specimens employed in this study are identical to those produced during the design of experiments (Chapter 5), taking the form of cuboids, and therefore subjected to compression testing. This chapter is intended to be part of a forthcoming publication.

Abstract:

This study presents the first comprehensive investigation into the mechanical properties of Ni-Mn-Ga lattices fabricated through Laser Powder Bed Fusion (L-PBF). Ni-Mn-Ga alloys are known for their giant magnetic-field-induced strain (MFIS), making them promising materials for various applications, including actuators and sensors. This study focuses on the compression behaviour of bulk and lattice samples of Ni-Mn-Ga, exploring the influence of L-PBF manufacturing and heat treatment on their mechanical performance. The results reveal that bulk samples exhibit a brittle behaviour, with heat treatment increasing ductility but decreasing strength. Lattice samples show unique fracture patterns with a fracture at 45º and significantly lower strength. Furthermore, the research delves into the potential for structural optimisation using the Gibson-Ashby model, explores the mechanical behaviour of an auxetic geometry, and quantifies the elastic modulus at 111.77 GPa in the struts of as-built lattice structures by nanoindentation.

1. Introduction

Giant magnetic-field-induced strain (MFIS) up to 8.7% has been demonstrated in foam-like Ni-Mn-Ga polycrystals [6]. The remarkable increase of MFIS is attributed to the presence of bamboo-like grains, which facilitates twin boundary motion within the grains. In contrast, monolithic materials exhibit nearly null strain due to the high constraint imposed by grain boundaries [5]. Laser powder bed fusion (L-PBF) of Ni-Mn-Ga has been previously studied to manufacture complex lattice geometries wherein the struts are made of a bamboo-like grain structure [80]. However, the mechanical performances of Ni-Mn-Ga lattices have not yet been studied.

Previous research shows good fatigue performance under compression loading exhibited by monolithic Ni-Mn-Ga despite its inherently brittle nature. It has been observed that a 10M single crystal can endure cyclic loading up to 2×10^9 compression cycles without experiencing fracture [115] and by keeping the same magnetic response. However, investigations into the mechanical properties of Ni-Mn-Ga polycrystals, particularly in cellular solids/lattices is limited. While significant fundamental research has been conducted to understand the twinning/detwinning mechanisms in both 10M [116] and 14M [117] martensite structures, thereby providing insights into the deformation behaviour of the material, only a limited number of studies have offered a comprehensive overview of the general mechanical properties from an engineering standpoint.

To promote a single variant structure and enhance the MFIS in single crystals and foam-like structures, mechanical training involving repetitive compression loading and unloading of Ni-Mn-Ga samples under a magnetic field has been investigated [118]. This training process has been found to reduce the yield stress after multiple cycles. No studies have been conducted on the mechanical behaviour of Ni-Mn-Ga lattices, with the closest study conducted by Zheng et al. [119], who investigated the mechanical properties of Ni-Mn-Ga microwires with bamboo-like grain structures under tensile loading. These microwires, with a diameter of 368 µm, a nominal composition of $Ni_{54.1}Mn_{26.2}Ga_{19.7}$, and a NM martensite structure exhibited an elastic modulus ranging from 5 to 8 GPa. To date, only one study has explored the mechanical behaviour of Ni-Mn-Ga samples fabricated through L-PBF [25]. Tension tests were conducted on 10M samples with a nominal composition of $Ni_{50.11}Mn_{28.16}Ga_{21.73}$ and a density of 88.16%. These samples exhibited a small plastic strain of approximately 0.02%, a total strain of 0.13% at a stress of 19.89 MPa, and a yield strength above 10 MPa.

As additive manufacturing processes continue to evolve, numerous studies have delved into the mechanical properties of lattice samples with varying geometries. The mechanical characteristics of lattices can be finely tuned by altering their geometry, such as unit cell type, cell size, strut thickness, and density, to suit specific applications [120,121], for instance enhancing energy absorption [122]. Extensive research has investigated the failure mechanisms of different types of lattices under compression loading [123–127]. Studies by McKown et al. [125] and Choy [127] have examined shear band formation in bending-dominated lattices made of primary ductile materials. Liu et al. [126] also explored shear band failure resulting from crack propagation in struts with high stress concentration and successfully mitigated it through slight adjustments to the unit cell's geometric parameters. Gu et al. [123] investigated the brittle fracture of octet-truss lattices and observed that the strength and modulus were strongly influenced by lattice geometry, leading to distinct failure behaviour. Qiu et al. [124] investigated the impact of strut diameter on strength, with smaller diameter struts (256 µm) reaching a nominal peak stress of 1 MPa, whereas larger diameter struts (800 µm) achieved a maximum stress of approximately

35 MPa. Among the various lattice geometries explored, auxetic structures garnered significant interest due to their negative Poisson's ratio [128,129]. However, these geometries pose printing challenges due to overhanging components or horizontal struts. To address this issue, Li et al. [130] adapted the unit cell design to conform to L-PBF process constraints. The same strategy was used in this study.

The association of Ni-Mn-Ga magnetic shape memory effects with the design versatility offered by L-PBF and the ability to manipulate mechanical properties through metamaterials holds substantial promise for applications such as ultra-fast actuators [9], sensors [10], and energy harvesters [12]. Nonetheless, for industrialisation and real-world applications, a comprehensive understanding of the mechanical behaviour is imperative. This study represents a preliminary investigation, focusing on the compression behaviour of Ni-Mn-Ga bulk and lattice samples manufactured using L-PBF. Both as-built and heat-treated samples are investigated through compression testing and nanoindentation.

2. Experimental procedure

2.1. L-PBF system

The specimens were fabricated using a pre-alloyed powder (for additional information on the powder, refer to [80]) with a Concept Laser M2 Cusing system. The system operated using a 400 W continuous-wave fibre laser with a wavelength of 1.064 µm, a maximum beam transverse speed of 4 m/s, and a fixed laser beam focal point diameter of ~67 µm. To ensure minimal oxygen (O_2) content, a protective argon atmosphere was employed, maintaining O_2 levels below 100 ppm. The samples were cut from a 316L stainless steel substrate using electrical discharge machining (EDM).

2.2. Sample preparation

Five cubic samples were tested under compression to obtain an approximation of the elastic modulus of bulk L-PBFed Ni-Mn-Ga. The process parameters are given in Table 7.1. The line energy density (E, J/mm) was used according to the formula:

$$E = \frac{P}{v}, \quad (1)$$

where P is the average laser power (W) and v is the scanning speed (mm/s).

Table 7.1. *Process parameters, relative density, chemical composition, and elastic modulus of bulk samples.*

Cube	Process parameters				Density	Composition (at.%)			Y (GPa)	
	P (W)	v (mm/s)	h (µm)	E (J/mm)		Ni	Mn	Ga	As-built	Heat-treated
1	90	500	75	0.18	98%	49.72 ± 0.24	29.29 ± 0.12	20.98 ± 0.25	1.27	1.55
2	80	400	75	0.20	97%	50.16 ± 0.22	29.30 ± 0.18	20.52 ± 0.11	2.87	1.54
3	100	450	75	0.22	95%	50.28 ± 0.14	29.22 ± 0.08	20.49 ± 0.10	3.70	1.45
4	80	300	75	0.27	99%	51.17 ± 0.24	28.32 ± 0.22	20.50 ± 0.05	1.43	1.04
5	80	300	75	0.27	98%	51.22 ± 0.24	28.16 ± 0.33	20.62 ± 0.11	2.70	1.97

The samples were cut in two and one half was heat-treated at 1060 °C for 12 hours followed by an ordering step at 800 °C for 4 hours, followed by furnace cooling. The density of the bulk samples was determined through the Archimedes method. Samples 1 to 4 were tested in the building direction while sample 5 was tested in the scanning direction, perpendicular to the build direction. The lattice samples were all fabricated according to the optimum parameters described in [80], with a 200 µm strut size, employing a single contour scan strategy with a laser power of 70 W, scanning speed of 450 mm/s, and contour distance of 75 µm. These parameters resulted in the production of 14M martensite structures with a final composition of $Ni_{49.88}Mn_{29.91}Ga_{20.21}$ and an internal strut density of 99%. Two different lattice geometries were tested. The first geometry was previously investigated in [80], while the second was an auxetic re-entrant geometry, slightly modified to adhere to conventional additive manufacturing rules. The re-entrant geometry was chosen as it has been extensively studied, exhibiting a high negative Poisson's ratio of -1.5 to -2 [14,128,131], which makes it particularly interesting for MSM materials application. The design of the re-entrant cell's geometry shown in Figure 7.1 followed the guidelines presented in [130] with θ = 75º, L = 15 mm and H = 30 mm. The unit cell was then modified slightly according to [132] by adding some material on the overhanging struts with a ~15º angle as shown in grey in Figure 7.1a.

The chemical composition was measured in several points across the samples using an x-ray fluorescence (XRF) analyser X-Strata 960 (Oxford Instruments) calibrated with a reference sample of known composition using a 300 µm beam size.

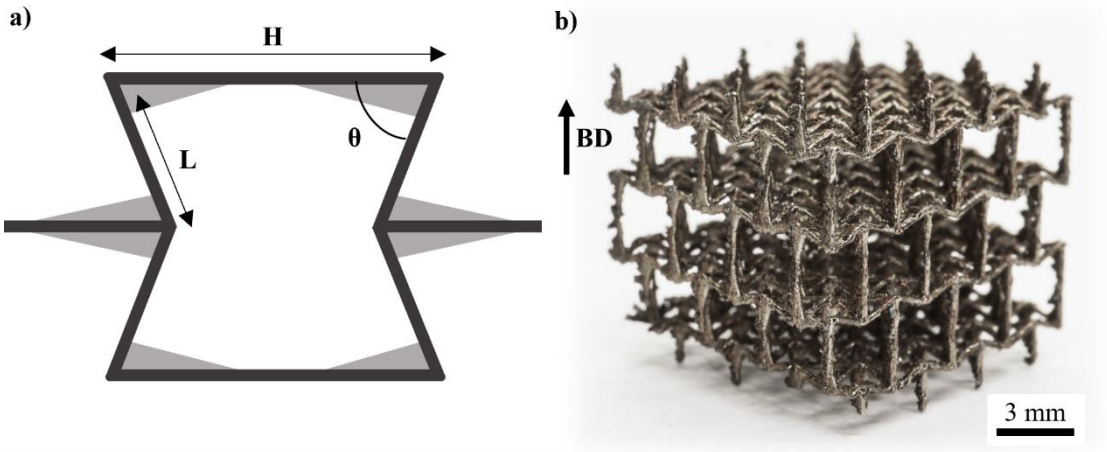

Figure 7.1. *(a) modified design of the unit cell's re-entrant lattice, (b) picture of L-PBFed re-entrant lattice.*

The microstructure was analysed using electron backscatter diffraction (EBSD) analysis using a TESCAN Clara FEG-SEM system equipped with a NewTec Scientific FurnaSEM oven and an Oxford Symmetry 2 EBSD camera. The sample was affixed to the oven using conductive carbon paste, and tests were conducted at temperatures approximately ranging from 150 to 200 ºC to ensure a full transformation to austenite, to make the analysis easier compared to the martensite phase. The scan was made with a beam current of 20 nA and a step size ranging of 1.5 µm. The analysis of EBSD data was made using the software Atex.

2.3. Mechanical testing

Compression experiments were performed using an Instron 3345 testing machine equipped with a 5 kN load cell at room temperature (approximately 20 ºC). The stroke rate was set at 1.3 mm/min. To minimise radial friction, lubrication grease was applied to the contact surface between the samples and the compression plates. A digital Image Corelation (DIC) system was used to observe macroscale fracture and to measure strain. The surface roughness of the bulk samples and the lattice pattern provide sufficient contrast for DIC analysis. The images were analysed using the MATLAB-based 2D DIC software package 'Ncorr' [79]. The mechanical properties of the lattices were calculated according to ISO13314:2011. The estimated elastic modulus of the lattices was considered as the slope of linear fits between the two stress values σ_{20} and σ_{70}. The first maximum stress σ_{max} and the related strain, ε_{max}, are summarised in Table 7.2.

Nanoindentation was performed to determine the elastic modulus and hardness on both, as-built and heat-treated lattice using a NanoTest system (Micro Materials, UK) equipped with a Berkovich tip and applying a maximum load of 20 mN and a holding time of 5 s. A total amount of 30 points, separated by 15 µm were measured on the as-built sample to make sure to hit many different grains. For heat-treated samples, large grains were targeted in order to associate the values to a specific crystallographic orientation. The lattice samples were mounted in epoxy resin for nanoindentation to avoid any bending of the struts.

3. Results and discussion

3.1. Bulk samples

Table 7.1 summarises the process parameters, relative density, chemical composition, and elastic modulus of the bulk samples. Among the samples, only sample 3 fractured before reaching the maximum capacity of the load cell, likely due to its lower density. The normalised stress-strain curves of the compression test of sample 3 are depicted in Figure 7.2a. In the as-built condition, the sample exhibited a maximum strain of 11% at a stress of 374 MPa, while in the heat-treated condition, it reached a maximum strain of 18.5% at a stress of 260 MPa. The heat treatment typically increased ductility but reduced the strength. Both stress-strain curves demonstrated a linear relationship and indicates brittle behaviour. Since the samples consist of a single phase (see Chapter 5), the increase in ductility can be attributed to stress relief and grain growth that occurred during the heat-treatment.

Figure 7.2b illustrates the correlation between the elastic modulus and the process parameters for samples 1 to 4. In the as-built condition, a relationship can be observed between the elastic modulus and the relative density of the samples, reflecting their respective process parameters. The values ranged from 1.2 to 3.7 GPa. However, in the heat-treated condition, the elastic modulus values stabilised within a narrower range of 1.0 to 1.6 GPa (not taking in account the sample tested in the scanning direction). This stabilisation of the data could potentially result from the stress relief and grain growth occurring during the heat treatment. While different energy input will induce different thermal gradients, affecting grain formation and stress accumulation differently, the homogenisation treatment relieves the stresses and increase the grain size. Consequently leading to an elastic modulus that is less sensitive to minor fluctuations in energy density compared to the as-built state.

Samples 4 and 5 were fabricated using identical parameters but loaded in different directions. The results presented in Table 7.1 demonstrate that the material exhibited greater stiffness in the scanning direction compared to the

build direction. These findings indicate the presence of an anisotropic texture, consistent with the characteristic grain morphology observed in the L-PBF process, where larger grains are typically present in the build direction [58]. Consequently, this anisotropic structure facilitates the propagation of cracks more readily in the build direction. After heat-treatment, a slight difference in the elastic modulus persists between the two samples. Specifically, sample 4, tested in the build direction, exhibited an elastic modulus of 1.04 GPa, while sample 5, tested in the scanning direction, had an elastic modulus of 1.97 GPa. This residual discrepancy suggests the continued presence of a minor anisotropic texture following the heat-treatment process.

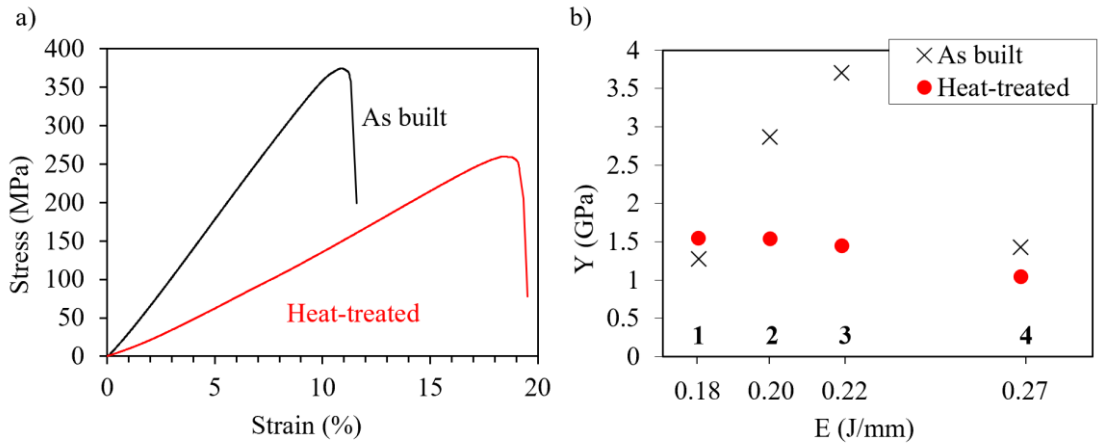

Figure 7.2. *(a) compressive stress-strain curves of as-built and heat-treated bulk sample 3, (b) influence of the printing parameters on the elastic modulus of bulk samples.*

3.2. Lattice samples

Figure 7.3 shows EBSD micrographs of a lattice unit cell both before and after heat treatment, with both scans conducted in the austenite phase. The micrographs reveal elongated grains along the struts, with the presence of bamboo-like grains extending across the diameter of the struts. The heat treatment exerted a substantial influence on grain growth, resulting in an 80% increase in the average grain size. Specifically, the average grain size expanded from an initial 18 µm in the as-built state to 88 µm following heat treatment.

Six lattice samples with the same unit cell were subjected to compression testing, some of the samples were divided for heat-treatment, resulting in variations in their overall geometry. The corresponding results of the nominal engineering stress-strain curves for all the as-built lattices are presented in Figure 7.4. Overall, the samples exhibited a similar behaviour but with different amplitudes due to their different sizes, with all of them displaying a highly brittle fracture attributed to the thin struts (200 µm). The figure was annotated following the guidelines in the ISO 13314 standard. The elastic modulus was calculated in the elastic gradient, i.e. as the straight line between 20 % and 70 % (I) of the maximum strength, denoted as σ_{20} and σ_{70}, respectively. Upon reaching the first maximum strength, certain struts experience fracture, resulting in a drop in strain (II) and post-yield softening. Further compression induces the lattice cells to stack atop one another, thereby elevating the strain until another layer fracture (III), consequently contributing to densification ans sequential local collapses. Only a small densification was observed in the samples.

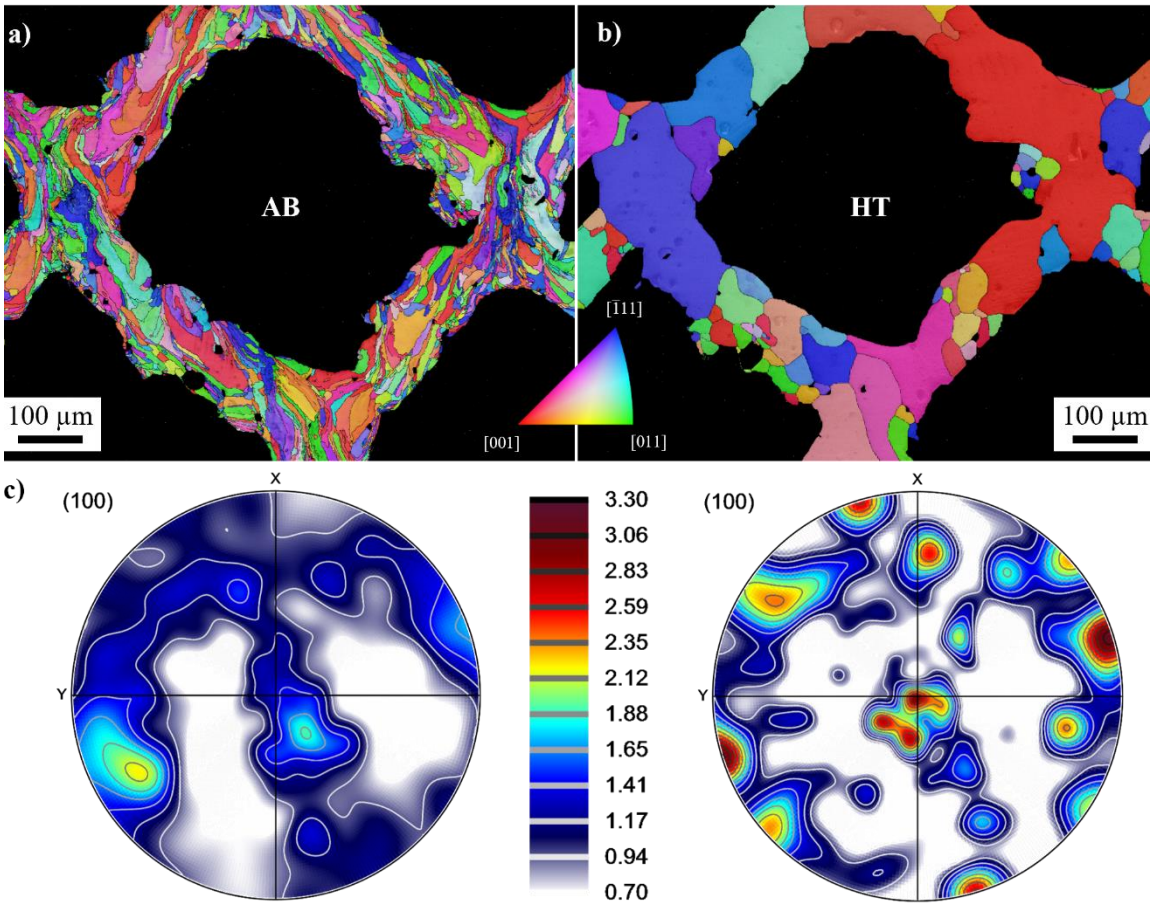

Figure 7.3. *IPFz maps of a cross section of a as-built (a) and heat-treated (b) lattice unit cell in the austenite phase and (c) corresponding (100) pole figures.*

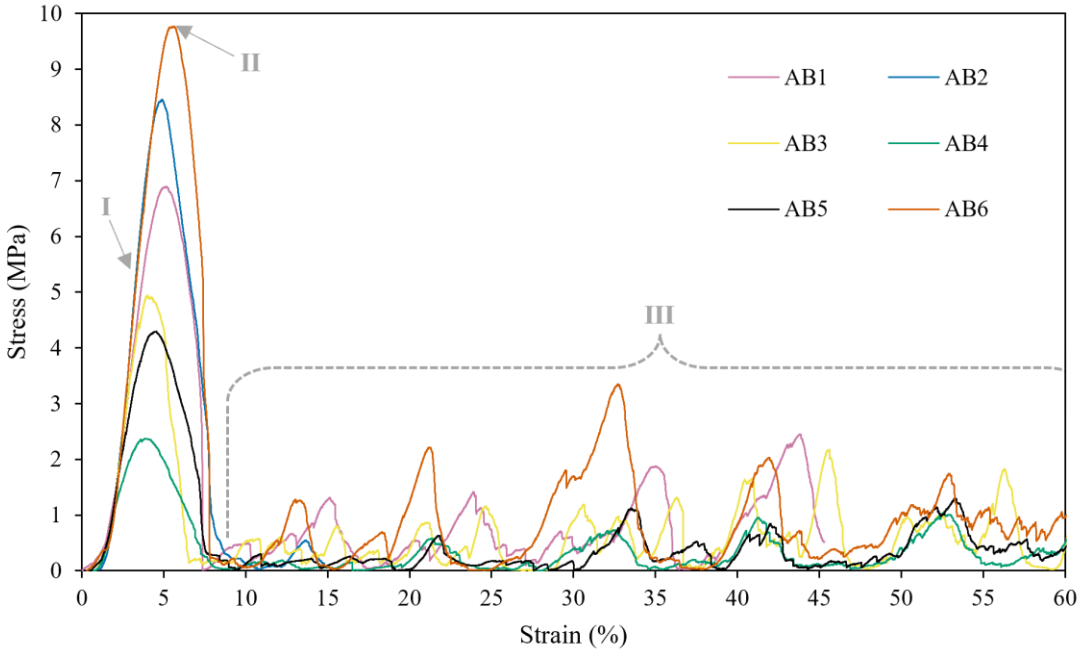

Figure 7.4. *Compression stress-strain curves of as-built lattices. With I: the elastic gradient taken from σ_{20} and σ_{70}, II: the first maximum compressive strength and III: the densification.*

The mechanical properties are summarised in Table 7.2. The as-built lattices demonstrated a maximum strain of only 6 MPa (± 2.5 MPa) at a strain level of roughly 4 % (± 0.8 %), and an average elastic modulus of 228 MPa (± 64 MPa). These values were notably lower than any previously reported for Ni-Mn-Ga [119], which can be attributed to the lattice structure's influence.

Table 7.2. *Summary of the mechanical properties of the lattice samples tested in compression.*

Performance Metric	AB1	AB2	AB3	AB4	AB5	AB6	HT1	HT2	Auxetic1	Auxetic2
σ_{max} (MPa)	6.89	8.46	4.94	2.37	4.30	9.77	2.63	1.61	0.55	0.51
$\varepsilon(\sigma_{max})$ (%)	5.15	3.89	3.18	3.16	4.04	5.27	4.81	4.20	4.44	3.38
Y (σ_{20}-σ_{70}) (MPa)	234	303	219	113	200	300	86	51	18	20

Figure 7.5 shows the stress-strain curve of sample AB2, along with images captured during the test. Initially, the stress increased sharply until it reached a maximum load-bearing capacity of 8.46 MPa at nearly 4 % strain. Subsequently, cracks initiated in the struts (Figure 7.5c, red circle), leading to the development of a 45º fracture relative to the compression axis, shown as a red line. Consequently, there was a sudden drop in stress (Figure 7.5d). Further compression caused the lattice to fracture along the 45º band, inducing slight densification before ultimate failure of the structure. This behaviour aligns with the findings of previous studies [126], which extensively investigated the typical shear-band formation in lattice structures. A 45º fracture is observed due to the formation of small cracks in localised regions in the lattice struts owing to the stress concentration and is probably related to the geometry of the unit cell.

The power law of the Gibson-Ashby model [120,121] establishes a relation between the mechanical characteristics of a lattice structure and those of the corresponding bulk material, expressed as follows:

$$\frac{Y}{Y_0} = A\,(\frac{\rho}{\rho_0})^n,$$

where Y represents the elastic modulus of the lattice structure, Y_0 is the elastic modulus of the parent material, ρ represents the volume density of the lattice, ρ_0 is the density of the parent material, and A and n are geometric constants.

Figure 7.6 illustrates the relationship between the two expressions within this model, suggesting adherence to a model with A = 10^4 and n = 1.39. To quantify the error in the elastic modulus, the curve is discretised into 30 segments between σ_{20} and σ_{70}, with the elastic modulus measured in each segment. The error is then computed as the deviation between these values. This equation holds the potential for inverse designing lattice structures with specific desired mechanical properties.

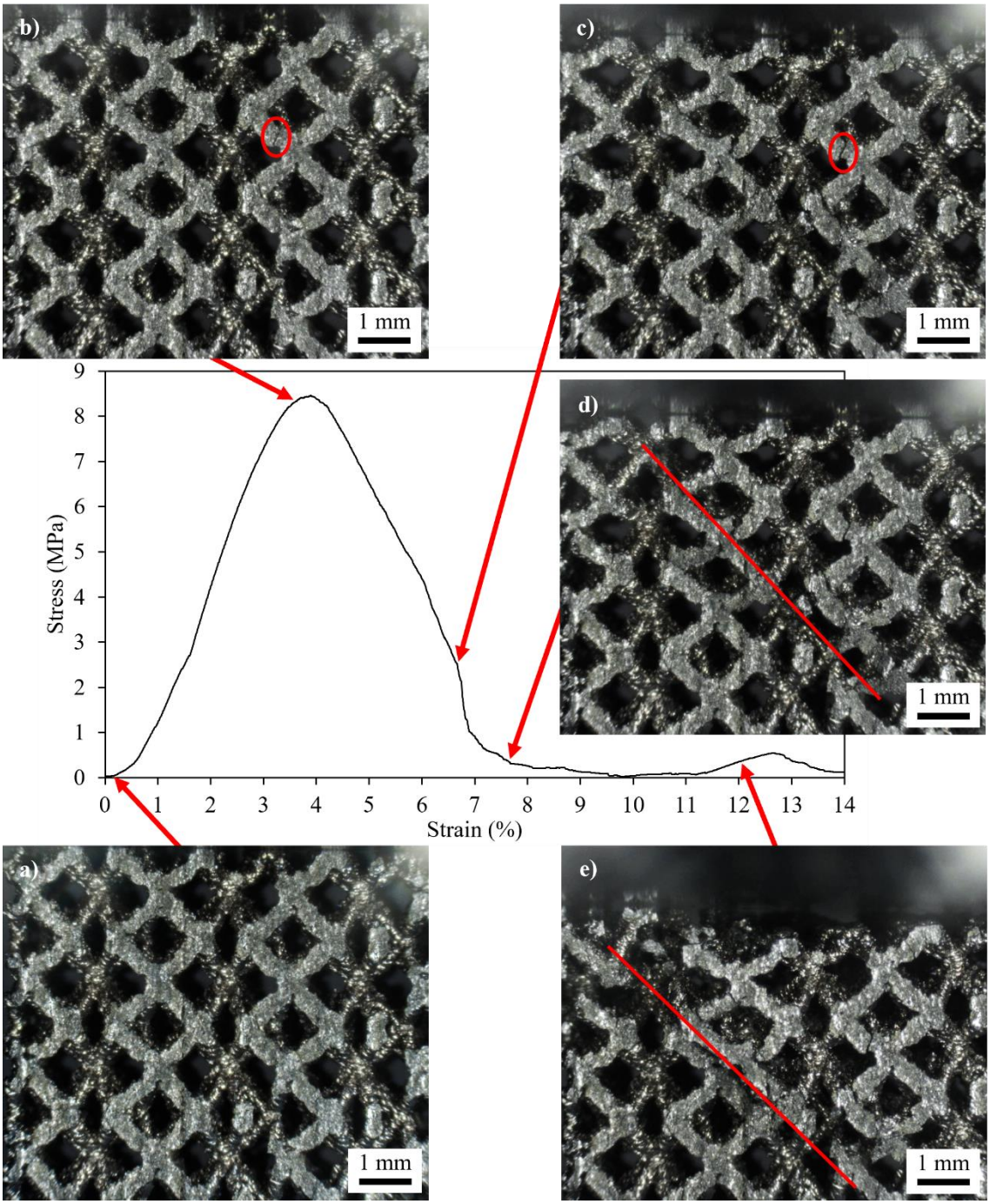

Figure 7.5. *Compression stress-strain curve of sample AB2 with corresponding pictures of the lattice. The red circles are pointing crack initiation while the red line depict the 45° shear band.*

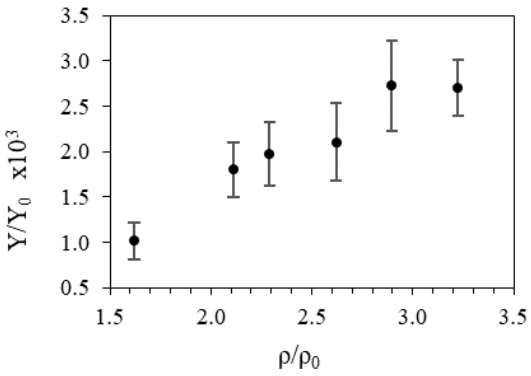

Figure 7.6. *Gibson-Ashby model for as-built lattice samples.*

In Figure 7.7, the stress-strain curves of the heat-treated sample are presented alongside the one from sample AB3 for comparison purposes. The heat-treatment exhibited a comparable effect on the lattice as observed in the bulk material: a reduction in strength, a slight increase in ductility, and a decrease in elastic modulus. Notably, both samples collapsed layer-by-layer, with one sample (HT1) initiating collapse from the top and the other sample (HT2) from the bottom, without apparent shear band formation. However, it is essential to conduct more tests on a larger number of samples to understand if the layer-by-layer fracture of the heat-treated samples is repeatable.

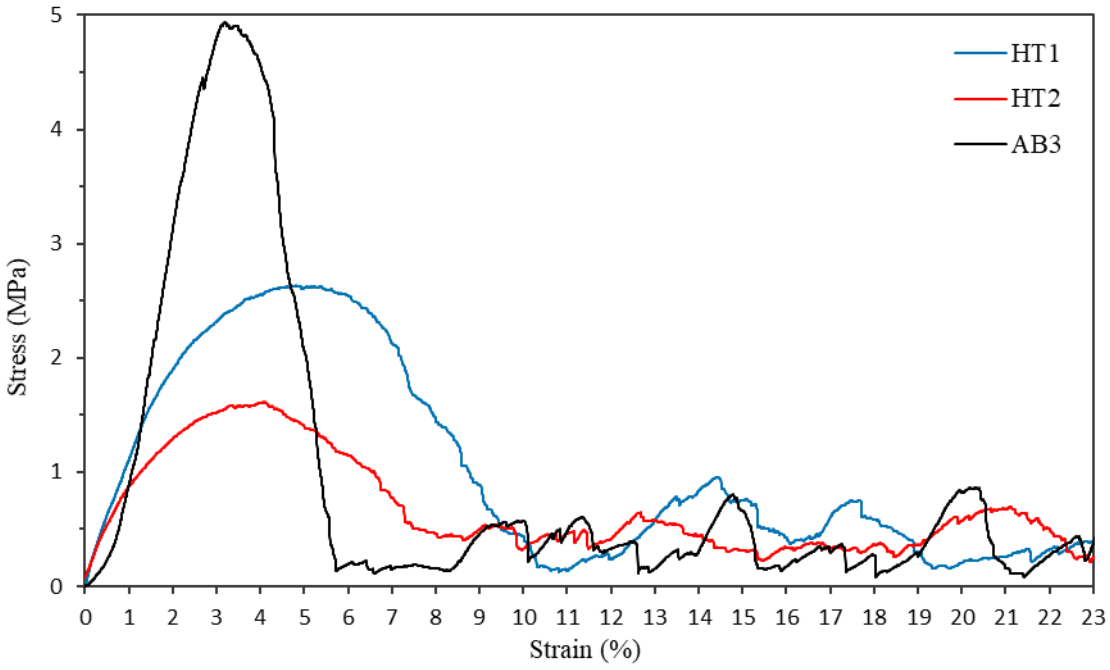

Figure 7.7. *Compression stress-strain curve of heat-treated samples and AB3.*

Figure 7.8 illustrates the stress-strain curves of the two re-entrant lattices that were subjected to compression testing. It is evident that the load-bearing capacity and elastic modulus of this geometry are significantly smaller, being approximately 10 times lower than the one from the previous lattice geometry. These samples were tested in the scanning direction, which is perpendicular to the build direction. This difference could potentially explain the substantial disparity in properties observed. However, it is worth noting that the bulk sample tested in the scanning direction exhibited a higher elastic modulus compared to the one tested in the building direction.

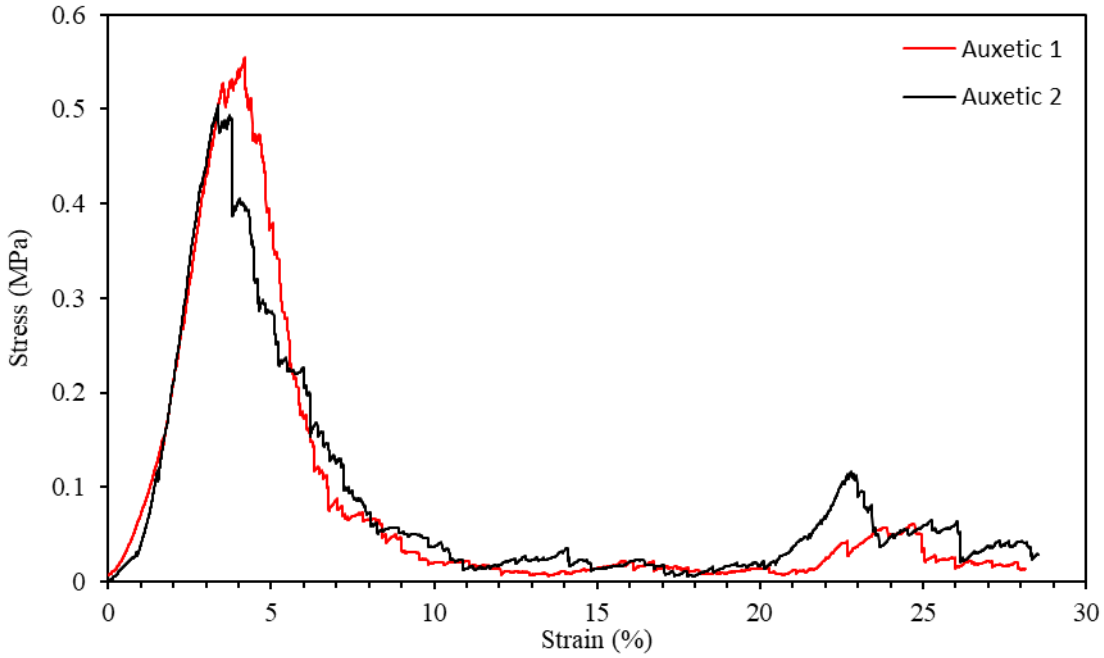

Figure 7.8. *Compression stress-strain curves of re-entrant auxetic lattices.*

Gaitzsh et al. [133] conducted a study on the impact of magneto-mechanical training on polycrystalline 10M cubes fabricated through directional solidification and subsequently annealed at 600 ºC for 14 hours. The stress-strain curves displayed a flattening of the slope at the initial stages of the compression test, attributed to the twin boundary motion and therefore the MFIS in the study. It is interesting to note that this effect was observed in all the as-built lattice curves in the present study but was absent in both the curves from the bulk samples (which is expected due to the large amount of grain boundaries and defects constraining the twin boundary motion) and the curves of the heat-treated lattices. However, drawing definitive conclusions regarding the flattening of the slope being attributed (at least partially) to the twin boundary motion is impossible, as we cannot rule out the possibility of artifacts arising from lack of parallelism of the samples and/or slightly uncalibrated load cells. Therefore, to corroborate this theory, an additional method is necessary to measure the MFIS.

3.3. Nanoidentation

The nanoindentation results obtained from the as-built lattice sample revealed a hardness (H) value of 6.35 ± 0.35 GPa and a reduced elastic modulus (E_r) value of 111.77 ± 6.99 GPa. These findings are in agreement with the outcomes of a previous nanoindentation investigation conducted on arc melted samples by Zhou et al. [134], which reported hardness ranging from 3.5 to 6 GPa and a reduced elastic modulus from 85 to 135 GPa. The variation in Zhou et al.'s data was attributed to different martensitic variants in the samples. In the present study, the lattice samples exhibited a consistent 14M martensite structure and therefore with different variants as well, while a small scatter of the data is observed. Remarkably, this small scatter in the data suggests the presence of a textured structure, as the values do not differ much from one grain to another, suggesting a uniform crystallographic direction which is also confirmed by the pole figures in Figure 7.3 showing a small preferential <100> crystallographic direction in the as-built condition and a stronger texture in the heat-treated condition. Additionally, the obtained hardness and reduced elastic modulus values also align with those reported by Liu et

al. [135] in their study on nanoindentation of thin films, where a hardness value of 5.5 GPa and a reduced elastic modulus of 155 GPa were documented.

The values of E_r and H obtained from the heat-treated sample, from different grains, are documented in Table 7.3. Some grains were too small to accommodate a sufficient number of indents, and the table also specifies the count of indents for each grain. Notably, grains G3 and G5 possessed enough indents to get robust data regarding their orientation, and their obtained values of elastic modulus closely approximate the elastic modulus of the as-built sample. This outcome deviates from the results of compression experiments where the heat treatment increased the ductility and decreased the strength.

Table 7.3. *Elastic modulus and hardness of different grains of a heat-treated sample.*

Grain	Euler Angles			Misorientation (°)	E_r (GPa)		H_r (GPa)	Number of indents
	phi1	phi	phi2					
G1	92.76	29.96	67.24	0.51	77	± 0.37	3.3	3
G2	216.29	35.97	23.74	0.41	71	± 2.98	3.5	5
G3	73.80	45.75	21.65	0.50	102	± 10.69	5.6	14
G4	-72.00	15.64	72.04	0.54	110	± 6.98	8.3	3
G5	120.47	51.25	39.77	0.45	109	± 8.76	6.4	25

Figure 7.9 shows the values of E_r and H_r depicted in the $Fm\bar{3}m$ inverse pole figure. This figure was plotted by referencing the grain's position in the inverse pole figure using EBSD data, followed by the inclusion of either E_r in Figure 7.9a or H_r in Figure 7.9b, employing a gradual colour scheme (green for lower values, yellow for intermediate values, and pink for higher values). This methodology was adopted from [136]. No significant correlation is discernible between the crystallographic orientation and the mechanical properties. It is essential to underscore that this study represents a preliminary investigation, and to draw definitive conclusions in this regard, a more extensive analysis a larger number of grains needs to be analysed.

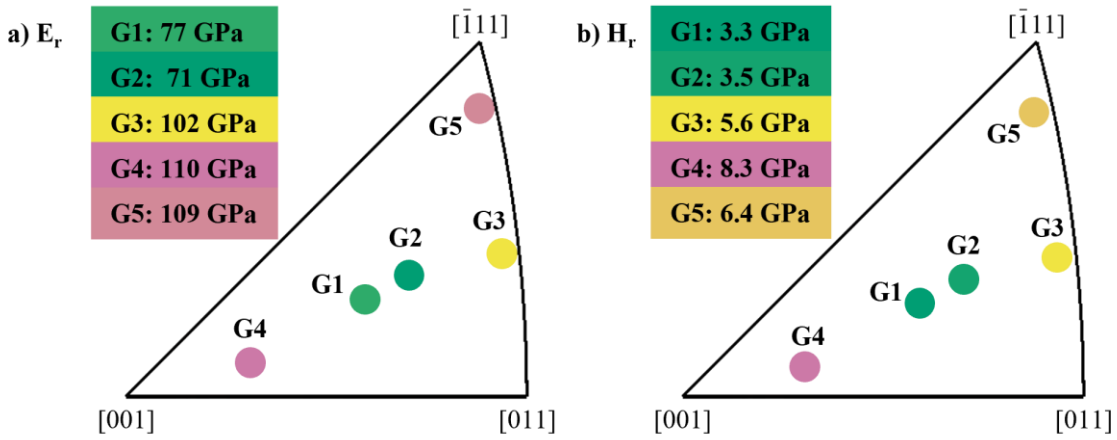

Figure 7.9. *(a) elastic modulus inverse pole figure and (b) hardness inverse pole figure of the heat-treated sample.*

The substantial disparity between the data obtained from nanoindentation and compression tests raises questions regarding their divergent outcomes. For the lattice samples, the measured elastic modulus is determined for the

entire lattice structure rather than the material itself. Consequently, these measurements cannot be accepted as an intrinsic value of the material. On the other hand, the bulk samples should theoretically exhibit values closer to those measured by nanoindentation. However, the bulk samples present a high density of cracks, leading to a decrease in their mechanical performance. To assess the displacement of the bulk material, DIC has been used, and the obtained results validated the measurements from the Instron. In contrast, the lattice struts remain crack-free, suggesting a potential advantage in their mechanical behaviour. Moving forward, a viable approach to enhance the mechanical performance of this material involves exploring the influence of different lattice geometries, strut sizes, and strut angles on its mechanical properties. However, it is essential to recognise that such investigations may also impact grain size and grain morphology, thereby influencing the shape memory effect of the material. A finite element model using the elastic modulus measured from nanoindentation would be interesting to optimise a lattice geometry.

4. Conclusion

In this study, the first investigation into the mechanical performance of Ni-Mn-Ga lattices produced via L-PBF has been undertaken. The following conclusions were drawn from our research:

- Nanoindentation of the lattice struts obtained a hardness of 6.35 GPa and a reduced elastic modulus of 111.77 GPa. These values are consistent with the existing literature on arc melted and thin film samples, providing validation for our experimental results.
- The compression tests performed on the bulk material demonstrated a highly brittle behaviour.
- The as-built lattices fractured along a 45º diagonal. The maximum stress observed ranged from 2.37 to 9.77 MPa, at elongation of 3.16 % and 5.27 % respectively. The elastic modulus (between σ_{20}-σ_{70}) was found to vary between 113 and 300 MPa.
- The heat treatment enhanced ductility and reduced strength in both bulk and lattice samples. The 45º diagonal fracture was not observed and the heat-treated lattices fractured layer-by-layer, though further testing is required to draw definitive conclusions.
- A different lattice geometry, a negative Poisson's ratio re-entrant lattice, was also examined and exhibited considerably lower strength compared to other lattice geometries.

The lattice geometry has a great influence of the mechanical performance of the sample, including factors such as the unit cell type, strut size, strut angle, and lattice density. The elastic moduli of the lattice samples seem to follow the Gibson-Ashby model and therefore opens the possibility for inverse engineering and structural optimisation. Further investigation through finite element analysis could provide deeper insights into how these geometric parameters affect mechanical properties. However, it is important to acknowledge that our current understanding is limited concerning the impact of lattice geometry on the material's magnetic and shape memory properties. Moreover, any enhancement in mechanical performance may potentially come at the cost of the shape memory characteristics. Therefore, it is essential to optimise the lattice design while considering its impact on the shape memory effect. For instance, a straightforward approach to improve the lattice's strength could involve increasing the strut diameter. However, this action would inevitably compromise the bamboo-like structure, consequently affecting the shape memory properties.

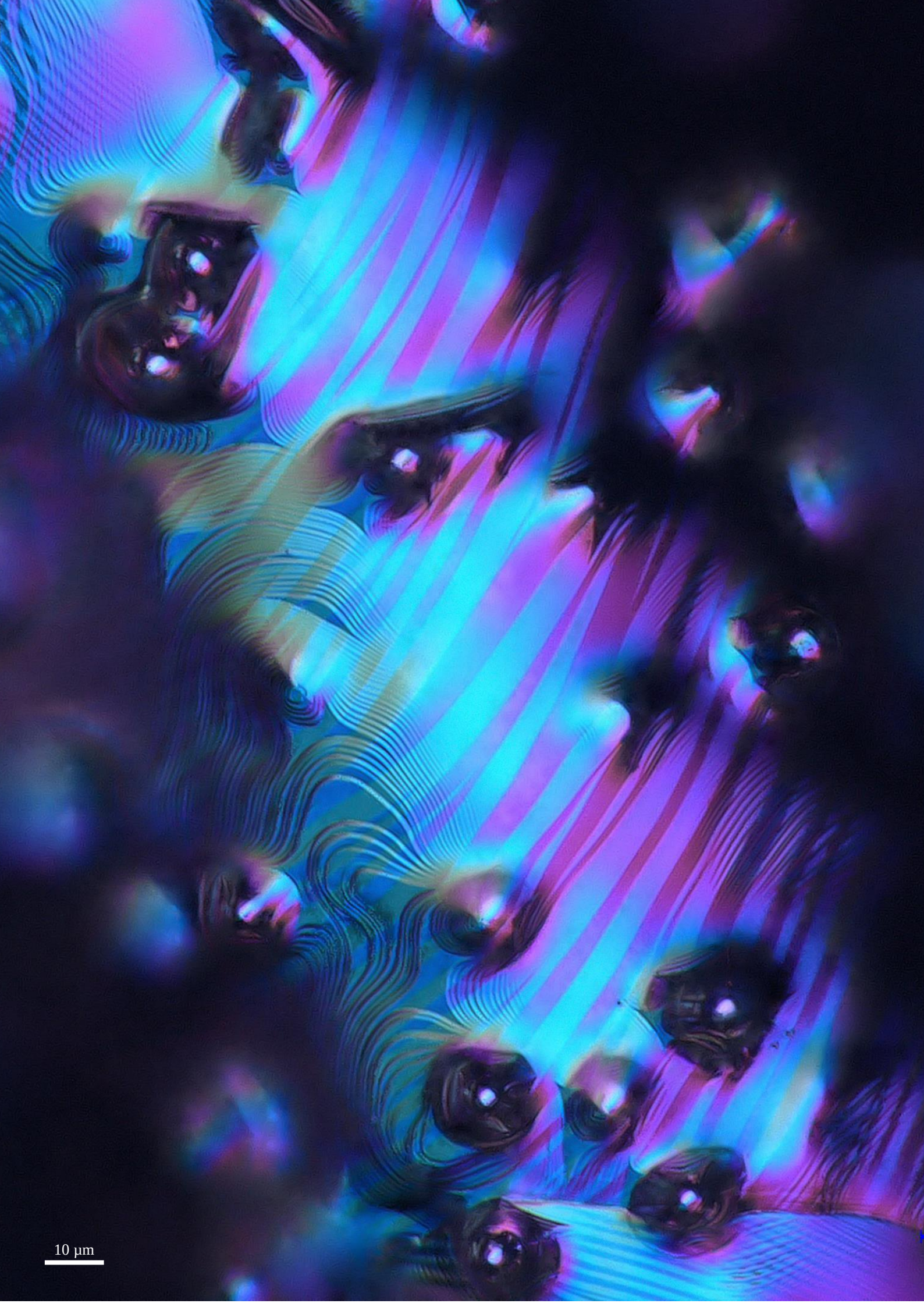
10 µm

Polarised light microscopy of Ni-Mn-Ga twins on a non-flat lattice strut
3D printed using L-PBF process.

Chapter 8

Magnetic-field-induced twin boundary motion observed in 10M Ni-Mn-Ga lattices fabricated through laser powder bed fusion

This chapter serves as the crowning achievement of the research conducted throughout this project, successfully achieving a large magnetic-field-induced strain in a fully functional Ni-Mn-Ga lattice structure. This chapter is intended to be part of a forthcoming publication.

Abstract:

This study investigates the magnetic-field-induced strains (MFIS) in Ni-Mn-Ga lattice samples fabricated using laser powder bed fusion (L-PBF) with bamboo-like grain structures. The lattice samples exhibit a 10M crystallographic structure with a phase transformation temperature of 58 ºC and a Curie temperature at around 100 ºC. The magnetic characterisation reveals anisotropic behaviour, with the build direction being the easy axis of magnetisation. Digital Image Correlation (DIC) microscopy observations indicate the presence of twin structures, demonstrating the lattice's response to magnetic fields of varying orientations. A maximum MFIS of 6.6% is achieved, offering promising possibilities for magnetic shape memory applications.

1. Introduction

Large magnetic-field-induced strains (MFIS) are commonly observed in Ni-Mn-Ga-based magnetic shape memory alloys [2] making them good candidates for applications such as ultrafast actuators [9], sensors [10], micro-pumps [11], and energy harvesters [12]. In single crystals, the MFIS can range from 6 to 12% [3,137] depending on the alloy composition. However, in polycrystalline materials, the shape memory effect is constrained by grain boundaries, limiting the achievable strain [5]. To mitigate this constraint, the use of foam-like materials have been investigated [6,100] reaching up to 8.7% strain [6] in polycrystalline foams manufactured by casting replication method. These porous materials exhibit a hierarchical grain structure, often referred to as bamboo-like grains, which span the diameter of individual structural features (struts or fibres). This structure reduces the constraining effects of grain boundaries and enhances the MFIS.

Additive manufacturing techniques have been employed to produce porous Ni-Mn-Ga samples with bamboo-like grain structures. One approach utilises the inherent porosity generated during the additive manufacturing process and tunes it using specific process parameters. This method has been applied in binder jetting, achieving a 0.01% MFIS [15,35], and in laser powder bed fusion (L-PBF) using an island scan strategy [25]. Another approach involves leveraging the design freedom offered by L-PBF to create lattices with 'engineered porosity'[40,86]. However, L-PBF can result in high residual stresses due to its rapid cooling rates, ranging from approximately 10^4 to 10^6 K/s [45]. Laitinen et al. [41] reduced these residual stresses in fully dense samples through heat treatment [41]. This sample exhibited a giant 5.8% strain within a large grain (approximately 1.7×1.1×0.35 mm³), a strain level very close to the ones found in single crystals with similar compositions, and notably higher than the 0.01% strain achieved via binder jetting. The twin mobility in this sample was studied by Saren et al. [43]. The twinning stress was determined to be approximately 1.4 MPa and 0.6 MPa for different boundary types, values higher than what is typically observed in single crystals of similar composition. The velocity of twin boundaries in these L-PBF-fabricated samples was also lower than in conventionally manufactured single crystals, with values of 1.5 m/s and 24 m/s. These differences in results were attributed to the presence of small keyhole defects resulting from trapped argon or oxygen, as well as Mn evaporation. The study also revealed that the twin boundaries started moving at a magnetic field strength of 0.1 T and achieved full displacement at 0.7 T.

Lattice structures with struts made of bamboo-like grain [86] have been successfully produced with optimised parameters. However, these lattices did not display a MFIS due to a compositional offset. Additionally, the microstructure in L-PBF can be controlled through process parameters and scanning strategy [138], creating highly textured bamboo-like structures. Furthermore, the Mn content can be tailored through process parameter adjustments, enabling the production of compositionally graded samples [86].

This study aims to measure the MFIS in Ni-Mn-Ga lattice samples produced via L-PBF for the first time.

Various methods have been employed to quantify the MFIS, such as a rotating field in combination with a mechanical mechanism to measure displacement in one direction [6], and the use of a solenoid and laser to measure displacement in a single direction [41]. However, these quantitative methods are limited to measuring displacement in only one direction, while lattices are likely to deform along the length of the struts. In this study, we propose to measure MFIS using optical imaging ex-situ the magnetic field similarly to [100].

2. Experimental procedure

Lattice samples with a composition $Ni_{50.25}Mn_{28.89}Ga_{20.86}$ (at.%) and a 10M crystallographic structure were produced using a M2 Concept Laser Cusing system, operated with a 400 W continuous-wave fibre laser with a wavelength of 1.064 µm, a maximum beam traverse speed of 4 m/s, and a fixed laser beam focal point diameter of approximately 67 µm. The fabrication process occurred in a protective argon atmosphere with O_2 levels below 100 ppm, utilising a 40 × 40 mm^2 316L substrate shown in Figure 8.1. The process parameters used were based on those reported in [86], with a laser power of 70 W, a scanning speed of 450 mm/s and a contour distance of 75 µm. A single contour scanning strategy with a 25 µm layer thickness was employed. Two lattice geometries were tested in this study, as depicted in Figure 8.2. One lattice sample was a 1 mm diameter cylinder (sample 1), while the other was a 2D wall (sample 2) with dimensions 7.4 × 0.25 × 8 mm^3 similar to those studied in [86]. Both lattices were designed with 75º strut angle and a height of 8 mm. Both the lattices studied here was chosen because of their 75º strut angle and the minimum number of nods, involving longer struts and to ease the formation of bamboo-like grains.

Figure 8.1. *Picture of the build platform with 10M lattices.*

Following fabrication, the lattice structures were separated from the substrate using electrical discharge machining (EDM). Subsequently, electropolishing was conducted by immersing the samples in an electrolyte solution with a 4:1 volumetric ratio of ethanol to 70% HNO_3, applying a constant 12 V voltage at -20 °C. Heat treatment was performed at 1080 ºC for 12 hours, followed by ordering at 800 ºC for 4 hours, in accordance with the procedures described in [56]. The lattice sample compositions were determined with an absolute accuracy of 0.3 at.% using the x-ray fluorescence (XRF) analyser X-Strata 960 from Oxford Instruments, calibrated with a reference sample of known composition. Phase transformation temperatures were determined using a low-field AC magnetic susceptibility device (LFMS) with a constant ~5 mT field and a 6 °C/min heating/cooling rate. X-ray diffraction (XRD) analysis was conducted using a PANalytical Empyrean 3 diffractometer with Co tube and λ = 0.17890 nm, equipped with poly-capillary optics and a PIXcel3D-Medipix3 detector.

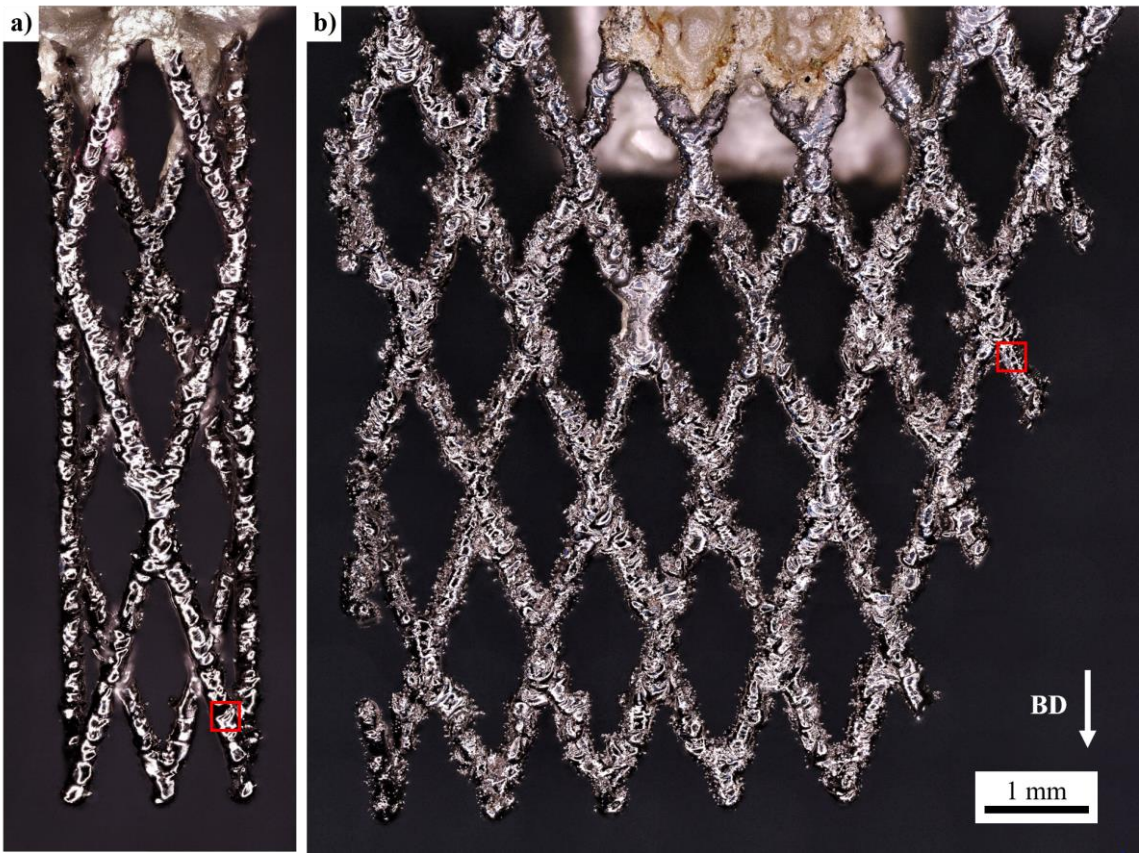

Figure 8.2. *10M lattice samples 1 (a) and 2 (b) tested for MFIS glued with silver paint on the sample holder in the building direction (BD). The red scares depict the areas observed in Figure 8.7.*

For magnetic testing, the lattice samples were affixed to a substrate designed for this purpose using silver paint. The substrate was 3D-printed using a Formlabs Form 3 printer filled with High Temp v2 resin. The mounted samples were then heated up to 150 ºC using a precision heat gun to ensure a complete phase transformation, followed by cooling in a 1 T magnetic field using a LakeShore 8600 Series vibrating sample magnetometer (VSM). The temperatures of the sample and the poles were monitored using three thermocouples, as illustrated in Figure 8.3. This training process was repeated three times to promote the growth of a preferential variant in the direction of the applied magnetic field, along the build direction (BD). Each hysteresis loop was performed 10 times to avoid any error in the measurements. The demagnetisation factor was considered with the shape of the samples simplified to rectangles and cylinders.

The lattice samples were observed at room temperature (~20 ºC) using a Keyence VHX-7000 4K digital microscope equipped with polarised light and differential interference contrast (DIC) between different orientations of the applied magnetic field. The sample was magnetised first in the direction perpendicular to BD, then taken out with the sample holder to the microscope for MFIS observation. The procedure was repeated with the magnetic field aligned with BD and aligned with the strut angle. A microscope stage was designed, and 3D printed to ensure the same sample position after magnetising it. The MFIS was quantified by measuring the distance between two distinctive points on the sample. This measurement was made 6 times between the same points to evaluate the error.

Efforts were made to measure the MFIS in-situ using a high-speed camera. This setup involved recording the sample rotating in the magnetic field, which would provide data on the activation angle and strain. Unfortunately, the results obtained from this setup were inconclusive, primarily due to alignment issues with the camera. Detailed information about this setup can be found in Chapter 3.5.6 for future reference.

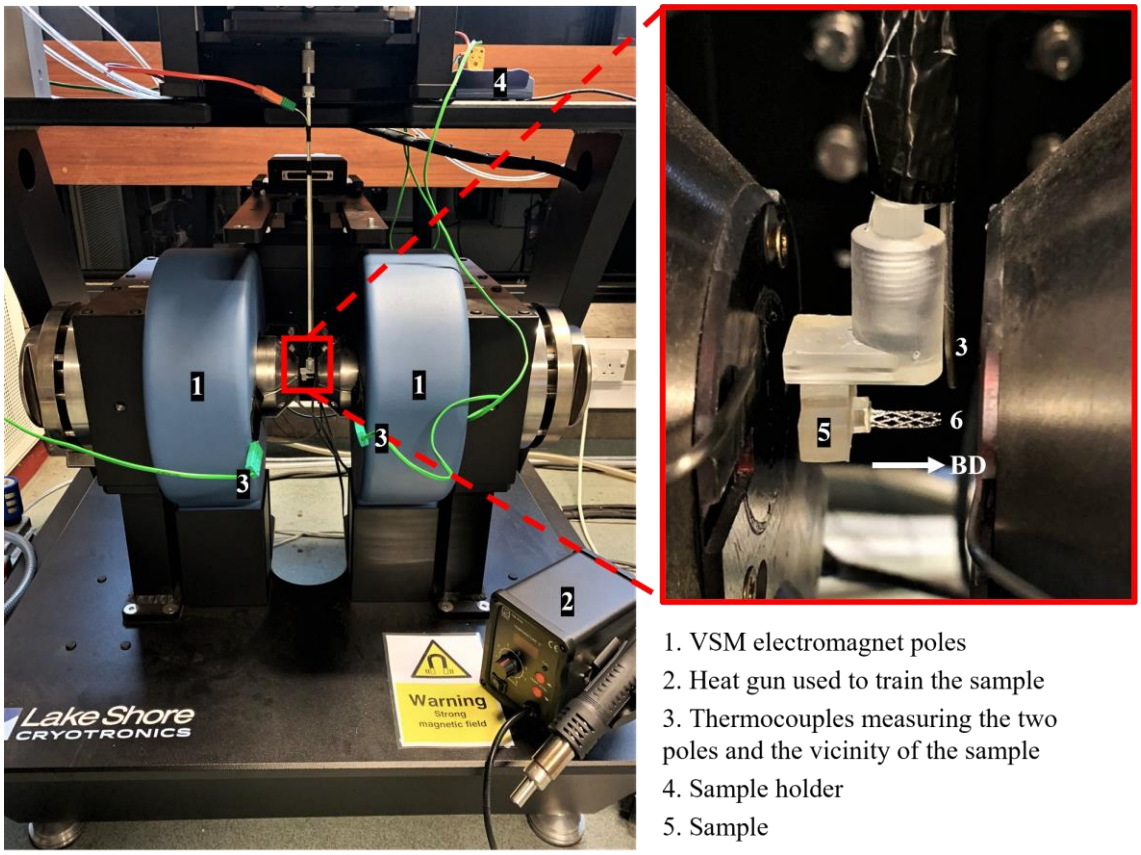

***Figure 8.3**. Setup with the VSM for applying the magnetic field and train the samples.*

3. Results and discussion

The samples' composition was measured as $Ni_{50.25}Mn_{28.89}Ga_{20.86}$ using XRF, a composition typically aligned with a 10M structure. This conclusion is supported by the XRD measurements, as shown in Figure 8.4, revealing a consistent 10M structure marked by characteristic planes (400), (040), and (004), along with lattice parameters a = 5.974 Å, b = 5.935 Å, c = 5.567 Å, and $\gamma = 90.43^{o}$. The c/a-ratio of this lattice approximates 0.93, suggesting a theoretical maximum MFIS of around 6.8 %. The LFMS data presented in Figure 8.4 exhibits the typical plateau-like curve associated with 10M structures. The austenite start temperature, measured during heating, registers at 59 ºC, while the martensite finish temperature, observed during cooling, is at 51 ºC. Additionally, the sample manifests a Curie temperature at 100.5 ºC. These temperatures are slightly elevated compared to results from Chmielus et al. [6] (phase transformation at 33 ºC and Curie temperature at 88 ºC), but very close to the ones found in L-PBFed samples made from the same powder but other machine setup in [43] (phase transformation at 51 ºC and Curie temperature at 99 ºC).

Figure 8.5 depict the results from the VSM measurements. Hysteresis loops for sample 2 were captured at different angles: 90º aligns with the configuration where the magnetic field coincides with the building direction (as depicted in Figure 8.3), 0º represents the direction perpendicular to the building direction, and 75º corresponds to the orientation along the strut length. Observable magnetic anisotropy in the samples indicates that the build direction (90º) is the easy axis of magnetisation, with a saturation magnetisation (M_s) of 68.44 Am^2/kg, while the 0º orientation is the hard axis of magnetisation, saturating at 62.15 Am^2/kg. Notably, the easy axis of magnetisation aligns with the build direction and not with the struts. The measured M_s and the coercivity (H_c) of 6.5 mT concur with data reported for similar compositions [56]. Moreover, there is no rapid magnetisation changes observable in the curves, suggesting that pinning effects are present, and the twin boundaries are not freely movable. This might be overcome by more training.

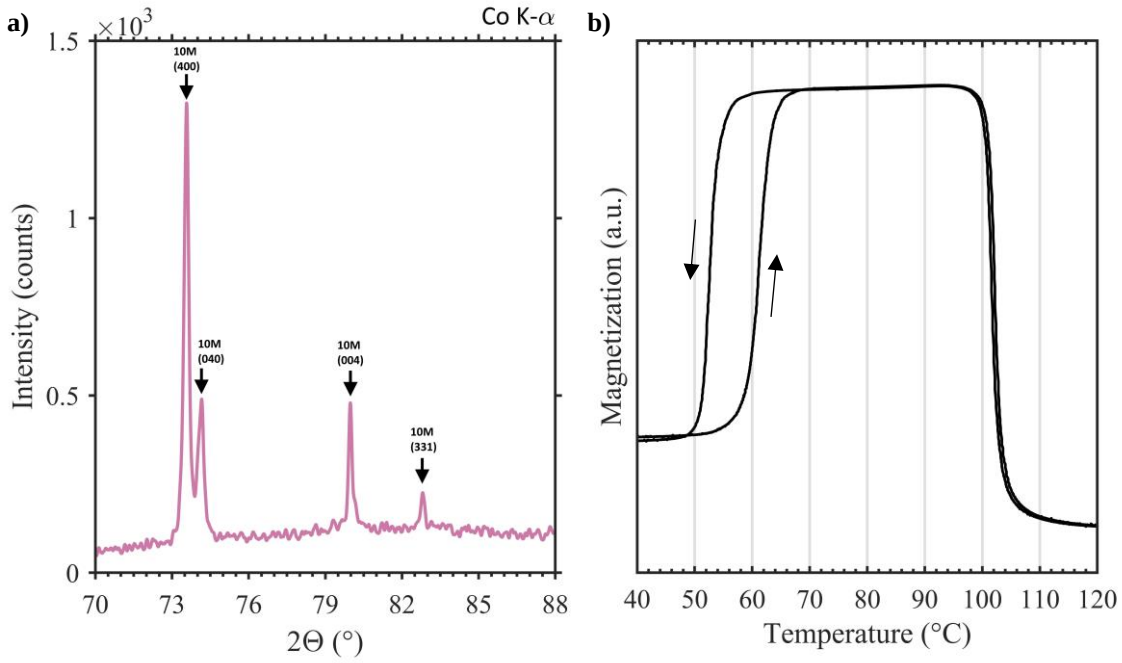

Figure 8.4. *(a) XRD pattern obtained from the heat-treated lattice. The background has been removed and the baseline is offset. All peaks have been indexed with respect to the unit cell coordinate system of the cubic parent phase. (b) Phase transformations of heat-treated lattice obtained via LFMS.*

Figure 8.6 presents a detailed microstructural analysis of a strut with a bamboo-like grain structure with twins crossing the grain boundaries. The use of differential interference contrast (DIC) microscopy facilitates the clear visualisation of these twins, which manifest as distinctive stripe patterns and are inherent to the 10M martensitic crystal structure. The micrographs were obtained from non-mechanically polished surfaces, resulting in non-flat regions with numerous defects such as partially melted powder particles, appearing as large dark circular features on the micrograph. Moreover, small defects are observed on the surface, which can be attributed to pinning effects during electropolishing.

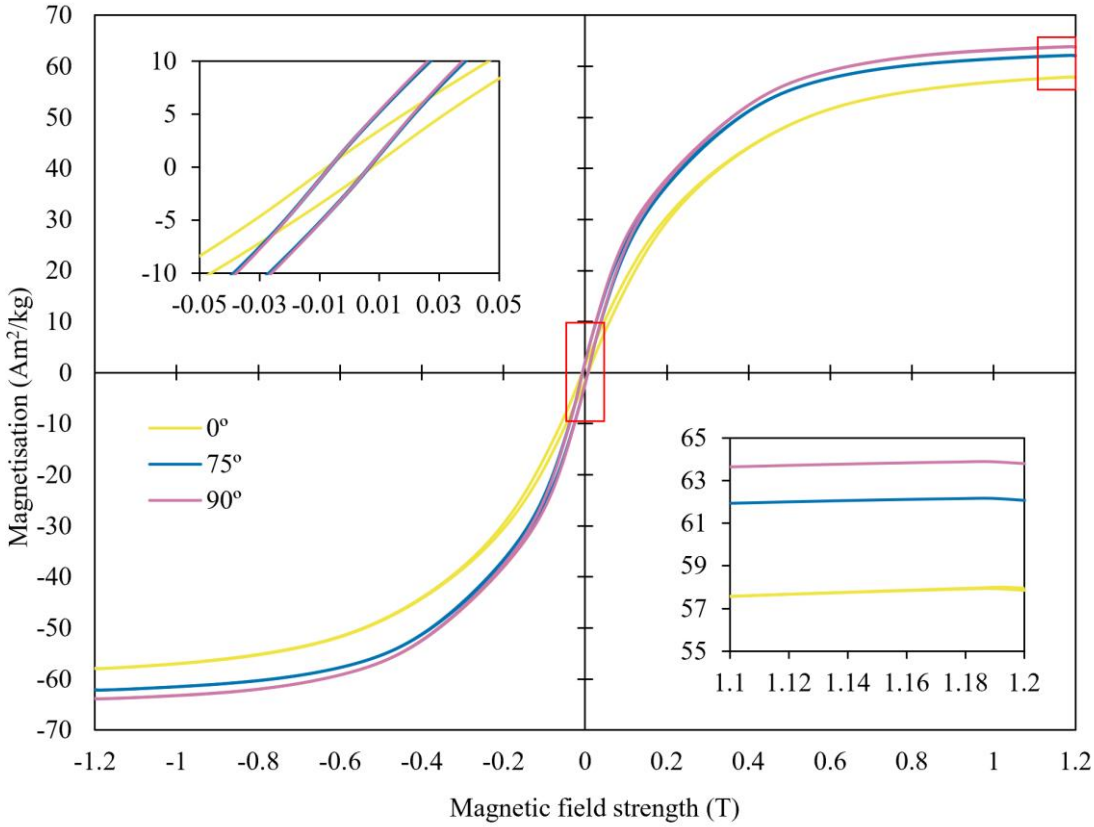

Figure 8.5. *Magnetisation hysteresis loop obtained at ambient temperature from the VSM measurements on heat-treated 10M lattice (sample 2) with different angles. The insets show a magnified view of the two red squares.*

Figure 8.7 displays DIC micrographs of the lattice samples depicted in Figure 8.2b. The micrographs were captured in the same area after subjecting the samples to a 1T magnetic field in two orientations: perpendicular to the building direction (a, c) and along the struts at an angle of 75º (b, d). Upon examination of the micrographs, distinct configurations of twins are observed, some of which are highlighted using red circles. These observations provide evidence of twin boundary motion activated by the magnetic field. The presence of twin boundaries and their response to the applied magnetic field offer valuable insights into the magnetic shape memory effect of the Ni-Mn-Ga lattice.

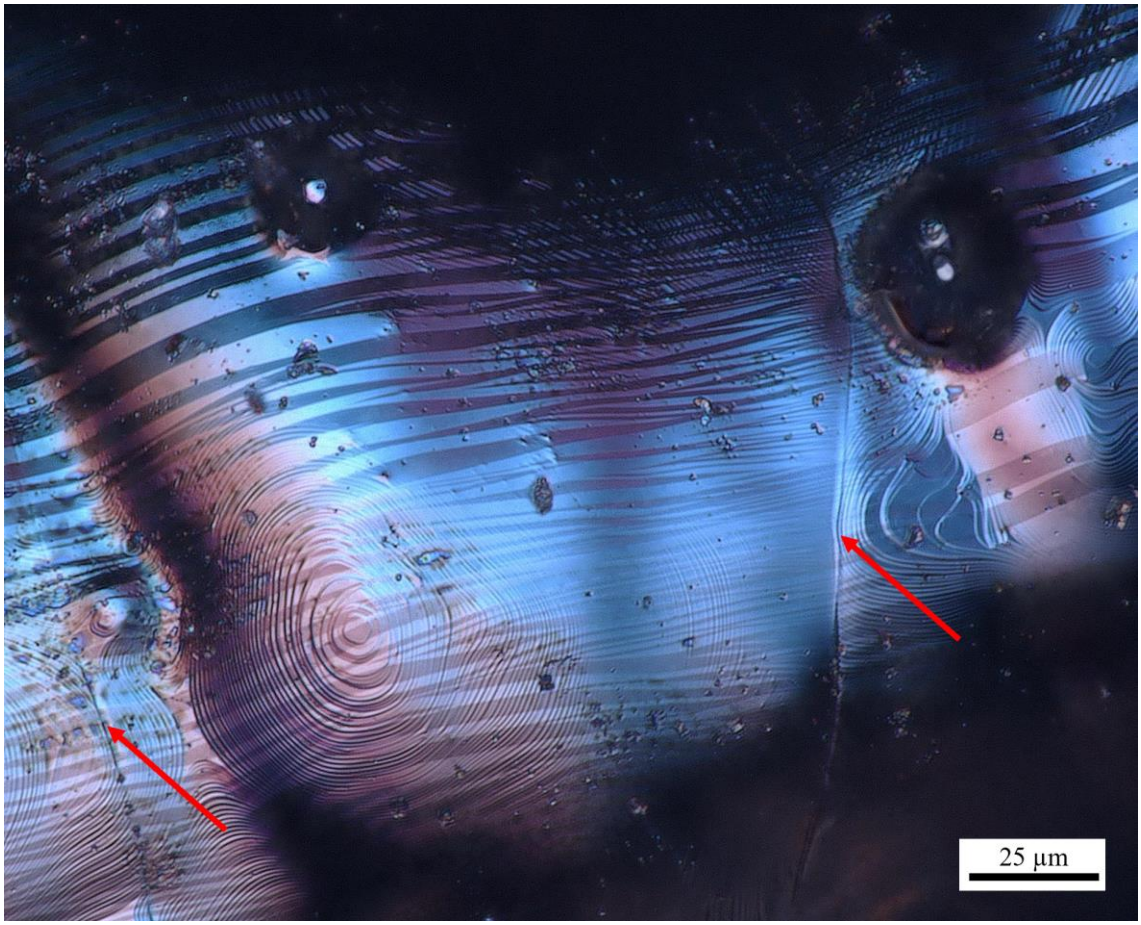

Figure 8.6. *DIC micrograph showing bamboo-like grains with twins crossing the grain boundaries shown with the red arrows.*

Furthermore, specific points within the micrographs were tracked, and distances were measured to evaluate the MFIS. A yellow line illustrates this method in Figure 8.7a,b. The lines exhibit a length difference of 7.5 µm ± 0.2 µm, corresponding to a deformation of 5.7 %, consistent with findings in prior literature for 10M samples [6,28,41]. In additional micrographs, the MFIS was recorded up to 6.6 %, corresponding to a difference of 16 µm ± 0.2 µm (see appendix). It is pertinent to acknowledge that these samples are likely to experience deformation along three directions and could potentially manifest greater strain in a direction perpendicular to the observed plane. Evidently, certain regions within the micrographs appear more focused in one image compared to another. This observation implies that there might be deformation occurring in the direction perpendicular to the observed plane. However, it is important to consider that such variations could also arise from slight movements in the sample positioning on the microscope stage.

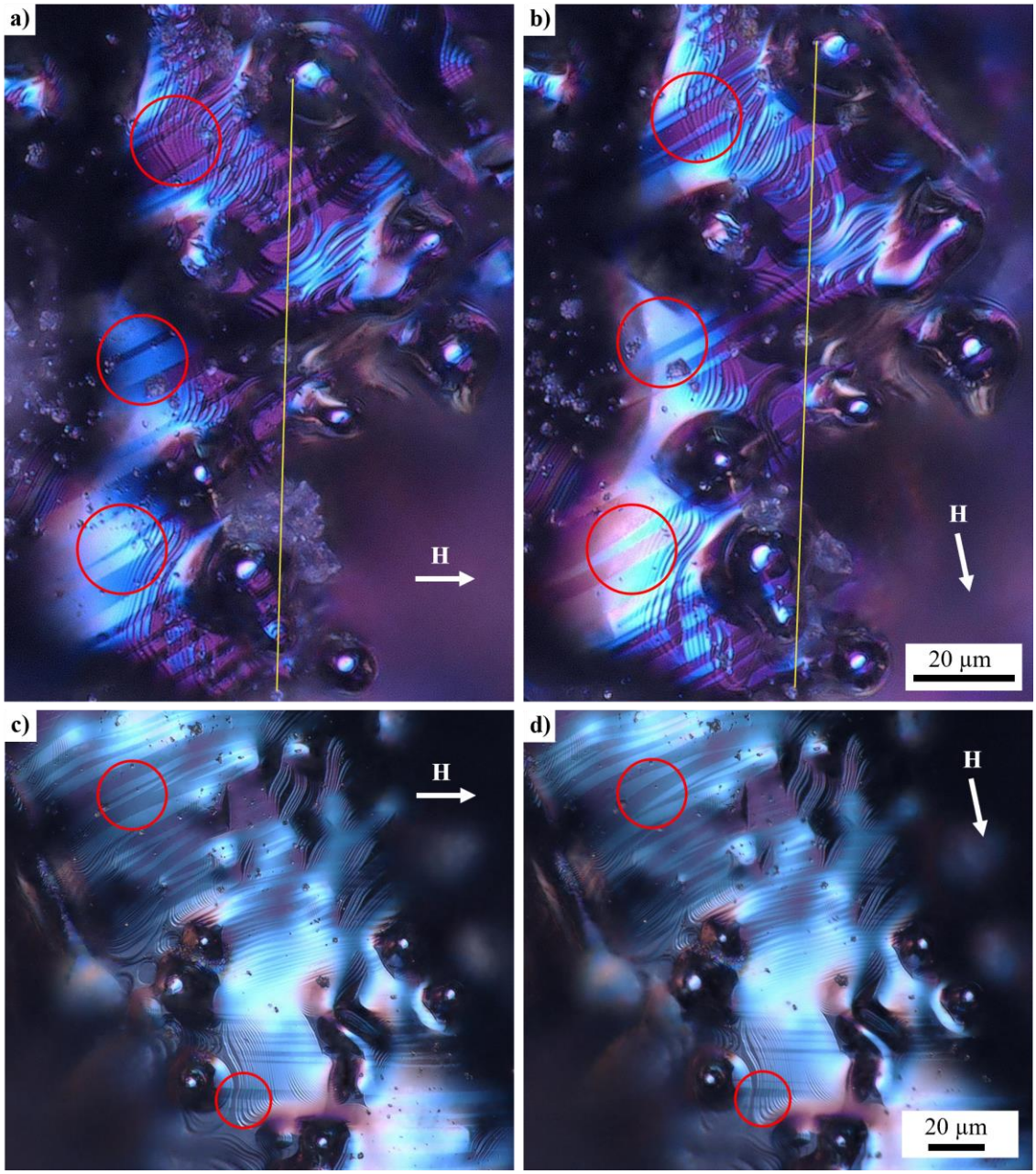

Figure 8.7. *DIC micrographs of twin boundary motion in two areas shown with a red squares in Figure 8.2 from sample 1 (a,b) and sample 2 (c,d). The samples are observed with the build direction vertically, as shown in Figure 8.2 and after being magnetised perpendicularly to the build direction (a,c) and along the struts at 75º (b,d). Some areas with twin boundary motion are highlighted with red circles.*

4. Conclusion

This study presents a giant MFIS of up to 6.6 % (± 0.1 %) in a lattice sample with bamboo-like grains, fabricated through L-PBF. The sample exhibits a 10M crystallographic structure with a phase transformation occurring around 58 ºC, a Curie temperature at approximately 100 ºC, and a saturation magnetisation (Ms) value of 68.44 Am^2/kg. Through Digital Image Correlation (DIC) microscopy, the acquired micrographs provide visual insights into the presence of twin structures, enhancing our comprehension of how the lattice responds to external magnetic fields under varying orientations. There exists potential for further enhancing the MFIS via additional sample training. Employing the same methodology but with in-situ visualisation would provide supplementary insights regarding the lattice's response to magnetic fields in diverse directions.

Appendix – Chapter 8

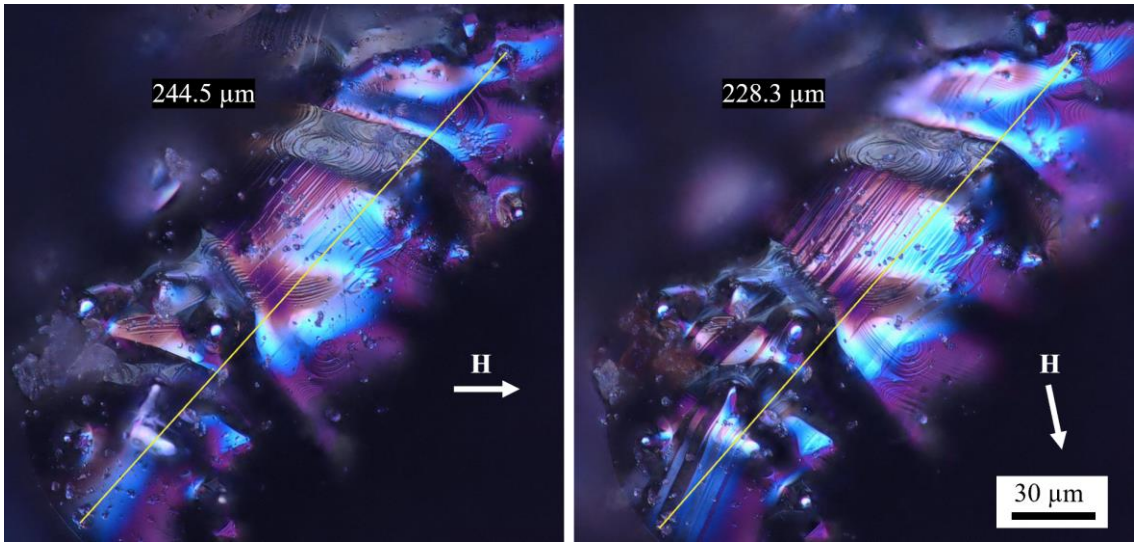

DIC micrographs showing giant 6.6% MFIS measured on a lattice sample (yellow line) exposed to different magnetic field directions.

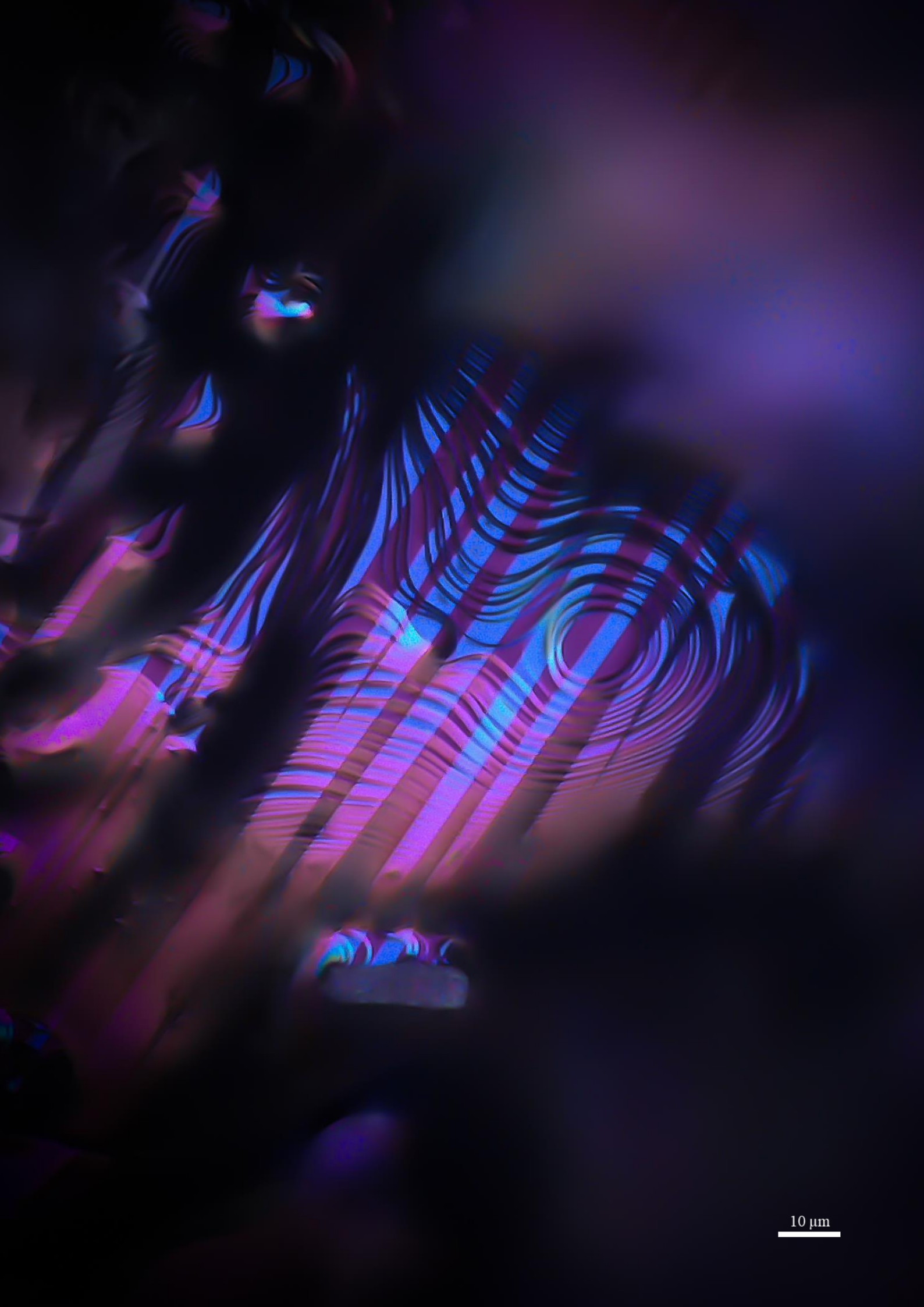
10 µm

Polarised light microscopy of Ni-Mn-Ga twins on a non-flat lattice strut
This image was submitted to the Royal Society Publishing Photography Competition 2023

Chapter 9

Conclusion

1. Overall conclusions

This study presents the development of functional Ni-Mn-Ga magnetic shape memory alloy lattices manufactured via laser powder bed fusion (L-PBF). Initially, an in-situ alloying approach was employed in order to have a better control over the composition (Mn especially), which resulted in segregations within the final parts. Subsequent experiments used pre-alloyed gas atomised powder to address this issue. The L-PBF process parameters were optimised for both bulk and lattice samples, focusing on Mn evaporation, porosity, and geometrical integrity. Further investigations were conducted to explore the control of microstructure through heated platform, double scanning strategy, and build orientation. These investigations revealed that the heated platform and double scanning had minimal impact on the microstructure. However, the strut angle, and consequently the building orientation, exerted an important influence on the texture. Struts aligned closely with the building direction exhibited a more pronounced texture. A preliminary study of the mechanical behaviour of bulk and lattice samples was carried out through compression testing and nanoindentation. This provided initial data on strength, elastic modulus, and microhardness. In a final experiment, a proof of concept demonstrated the functionality of Ni-Mn-Ga lattices produced by L-PBF, achieving up to 6.6% magnetic-field-induced strain (MFIS).

Key findings include:

- Bulk samples exhibited cracking and low density (around 90%) with the following parameters: laser power of 90 W, scanning speed of 500 mm/s, and hatch distance of 75 µm while the lattice samples were crack free with an internal strut density of 99% using the following parameters: laser power of 70 W, scanning speed of 450 mm/s, and contour distance of 75 µm. Lower energy was required to melt thin structures compare to bulk. These parameters were used successfully with other powder batches showing their repeatability. Heat treatment enhanced the formation of beneficial bamboo-like grain structures in lattice struts.
- Mn content was found to be strongly influenced by process parameters with higher energy increasing the Mn evaporation and could be controlled through adjustments of the parameters. This opens the possibility of printing compositionally graded structures with both actuated and non-actuated elements by changing the process parameters during the build.
- The crystallographic orientation of grains was observed to align with the orientation of the struts, allowing for control through the strut angle. Struts closer to the building direction (75º) exhibited a stronger texture, which increase the chances of inter-grains twin boundary motion advantageous for achieving large MFIS;
- Nanoindentation of the lattice struts showed a hardness of 6.35 GPa and a reduced elastic modulus of 111.77 GPa, very close to previous reported in arc-melted samples. Compression testing of lattices was performed for the first time and revealed a maximum stress ranging from 2.37 to 9.77 MPa, at elongation

of 3.16% and 5.27% respectively. The elastic modulus (between σ_{20}-σ_{70}) was found to vary between 113 and 300 MPa. The heat treatment enhanced ductility and reduced strength.

- A giant MFIS of up to 6.6% was achieved in a 10M lattice sample with bamboo-like grains after only 3 magnetic training cycles.

2. Scientific contribution

This study marks a significant milestone by demonstrating a giant MFIS in an additive-manufactured Ni-Mn-Ga sample. While previous research had shown MFIS values of up to 5.8% in large-grain walls fabricated using L-PBF, this investigation extends the material's capabilities to lattice structures with a 6.6% MFIS. Moreover, it contributes to a deeper understanding of several critical aspects, including the influence of lattice geometry on microstructure, the material-laser interaction in Ni-Mn-Ga lattices, and the resulting mechanical behaviour. These insights are important steps toward advancing the development of functional Ni-Mn-Ga devices for applications in actuators, micro-pumps, and energy harvesters.

3. Future work

Future research should delve deeper into the microstructure and the mechanisms governing grain growth. Smaller-scale studies, like in-situ synchrotron experiments, will provide valuable insights into the diffusion mechanisms essential for tailoring lattice geometries with specific textures. Moreover, testing various lattice geometries to ascertain their impact on mechanical properties is essential. As our understanding of the relationship between microstructure and strut orientation grows, computational models can be employed to analyse how lattice geometry influences both texture (and, consequently, MFIS) and mechanical properties. Additionally, the incorporation of alloying elements, such as Co, Cu, Fe, and Cr, holds the potential to further increase grain size, thereby enhancing the magnitude of MFIS. These future investigations promise to advance our comprehension and utilisation of Ni-Mn-Ga alloys in functional applications.

REFERENCES

[1] K. Ullakko, J.K. Huang, C. Kantner, R.C. O'Handley, V. V. Kokorin, Large magnetic-field-induced strains in Ni2MnGa single crystals, Appl. Phys. Lett. 69 (1996) 1966–1968. https://doi.org/10.1063/1.117637.

[2] K. Ullakko, Magnetically controlled shape memory alloys: A new class of actuator materials, J. Mater. Eng. Perform. 5 (1996) 405–409. https://doi.org/10.1007/BF02649344.

[3] S.J. Murray, M. Marioni, S.M. Allen, R.C. O'Handley, T.A. Lograsso, 6% magnetic-field-induced strain by twin-boundary motion in ferromagnetic Ni-Mn-Ga, Appl. Phys. Lett. 77 (2000) 886–888. https://doi.org/10.1063/1.1306635.

[4] A. Sozinov, A.A. Likhachev, N. Lanska, K. Ullakko, Giant magnetic-field-induced strain in NiMnGa seven-layered martensitic phase, Appl. Phys. Lett. 80 (2002) 1746–1748. https://doi.org/10.1063/1.1458075.

[5] P. Lázpita, G. Rojo, J. Gutiérrez, J.M. Barandiaran, R.C. O'Handley, Correlation between magnetization and deformation in a NiMnGa shape memory alloy polycrystalline ribbon, Sens. Lett. 5 (2007) 65–68. https://doi.org/10.1166/SL.2007.033.

[6] M. Chmielus, X.X. Zhang, C. Witherspoon, D.C. Dunand, P. Müllner, Giant magnetic-field-induced strains in polycrystalline Ni-Mn-Ga foams, Nat. Mater. 8 (2009) 863–866. https://doi.org/10.1038/nmat2527.

[7] M. Namvari, V. Laitinen, A. Sozinov, A. Saren, K. Ullakko, Effects of 1 at.% additions of Co, Fe, Cu, and Cr on the properties of Ni-Mn-Ga-based magnetic shape memory alloys, Scr. Mater. 224 (2023) 115116. https://doi.org/10.1016/j.scriptamat.2022.115116.

[8] A. Sozinov, N. Lanska, A. Soroka, W. Zou, 12% magnetic field-induced strain in Ni-Mn-Ga-based non-modulated martensite, Appl. Phys. Lett. 102 (2013). https://doi.org/10.1063/1.4775677.

[9] J. Tellinen, I. Suorsa, I. Aaltio, K. Ullakko, Basic Properties of Magnetic Shape Memory Actuators, 8th Int. Conf. ACTUATOR 2002. Bremen, Ge (2002) 10–12. https://www.researchgate.net/publication/265288374_Basic_properties_of_magnetic_shape_memory_actuators.

[10] A. Hobza, C.L. Patrick, K. Ullakko, N. Rafla, P. Lindquist, P. Müllner, Sensing strain with Ni-Mn-Ga, Sensors Actuators, A Phys. 269 (2018) 137–144. https://doi.org/10.1016/j.sna.2017.11.002.

[11] A. Saren, A.R. Smith, K. Ullakko, Integratable magnetic shape memory micropump for high-pressure, precision microfluidic applications, Microfluid. Nanofluidics. 22 (2018) 1–10. https://doi.org/10.1007/s10404-018-2058-0.

[12] I. Karaman, B. Basaran, H.E. Karaca, A.I. Karsilayan, Y.I. Chumlyakov, Energy harvesting using martensite variant reorientation mechanism in a NiMnGa magnetic shape memory alloy, Appl. Phys. Lett. 90 (2007) 1–4. https://doi.org/10.1063/1.2721143.

[13] J. Ping Liu, O. Gutfleisch, E. Fullerton, D.J. Sellmyer, Nanoscale magnetic materials and applications, chap14: Magnetic Shape Memory Phenomena, 2009. https://doi.org/10.1007/978-0-387-85600-1.

[14] M. Benedetti, A. du Plessis, R.O. Ritchie, M. Dallago, S.M.J. Razavi, F. Berto, Architected cellular materials: A review on their mechanical properties towards fatigue-tolerant design and fabrication, Mater. Sci. Eng. R Reports. 144 (2021) 100606. https://doi.org/10.1016/j.mser.2021.100606.

[15] M.P. Caputo, A.E. Berkowitz, A. Armstrong, P. Müllner, C.V. Solomon, 4D printing of net shape parts made from Ni-Mn-Ga magnetic shape-memory alloys, Addit. Manuf. 21 (2018) 579–588. https://doi.org/10.1016/j.addma.2018.03.028.

[16] M.P. Caputo, C. V. Solomon, A facile method for producing porous parts with complex geometries from ferromagnetic Ni-Mn-Ga shape memory alloys, Mater. Lett. 200 (2017) 87–89. https://doi.org/10.1016/j.matlet.2017.04.112.

[17] A. Mostafaei, P. Rodriguez De Vecchis, E.L. Stevens, M. Chmielus, Sintering regimes and resulting microstructure and properties of binder jet 3D printed Ni-Mn-Ga magnetic shape memory alloys, Acta Mater. 154 (2018) 355–364. https://doi.org/10.1016/j.actamat.2018.05.047.

[18] A. Mostafaei, K.A. Kimes, E.L. Stevens, J. Toman, Y.L. Krimer, K. Ullakko, M. Chmielus, Microstructural evolution and magnetic properties of binder jet additive manufactured Ni-Mn-Ga magnetic shape memory alloy foam, Acta Mater. 131 (2017) 482–490. https://doi.org/10.1016/j.actamat.2017.04.010.

[19] S.L. Taylor, R.N. Shah, D.C. Dunand, Ni-Mn-Ga micro-trusses via sintering of 3D-printed inks containing elemental powders, Acta Mater. 143 (2018) 20–29. https://doi.org/10.1016/j.actamat.2017.10.002.

[20] S.L. Taylor, R.N. Shah, D.C. Dunand, Microstructure and porosity evolution during sintering of Ni-Mn-Ga wires printed from inks containing elemental powders, Intermetallics. 104 (2019) 113–123.

https://doi.org/10.1016/j.intermet.2018.10.024.
[21] J. Toman, P. Müllner, M. Chmielus, Properties of as-deposited and heat-treated Ni-Mn-Ga magnetic shape memory alloy processed by directed energy deposition, J. Alloys Compd. 752 (2018) 455–463. https://doi.org/10.1016/j.jallcom.2018.04.059.
[22] V. Laitinen, A. Salminen, K. Ullakko, First investigation on processing parameters for laser powder bed fusion of Ni-Mn-Ga magnetic shape memory alloy, J. Laser Appl. 31 (2019) 022303. https://doi.org/10.2351/1.5096108.
[23] V. Laitinen, A. Sozinov, A. Saren, A. Salminen, K. Ullakko, Laser powder bed fusion of Ni-Mn-Ga magnetic shape memory alloy, Addit. Manuf. 30 (2019) 100891. https://doi.org/10.1016/j.addma.2019.100891.
[24] F. Nilsén, I.F. Ituarte, M. Salmi, J. Partanen, S.P. Hannula, Effect of process parameters on non-modulated Ni-Mn-Ga alloy manufactured using powder bed fusion, Addit. Manuf. 28 (2019) 464–474. https://doi.org/10.1016/j.addma.2019.05.029.
[25] I.F. Ituarte, F. Nilsén, V.K. Nadimpalli, M. Salmi, J. Lehtonen, S.P. Hannula, Towards the additive manufacturing of Ni-Mn-Ga complex devices with magnetic field induced strain, Addit. Manuf. 49 (2022). https://doi.org/10.1016/j.addma.2021.102485.
[26] M. Acet, L. Mañosa, A. Planes, chapter4: Magnetic-Field-Induced Effects in Martensitic Heusler-Based Magnetic Shape Memory Alloys, in: Handb. Magn. Mater., 2011: pp. 231–289. https://doi.org/10.1016/B978-0-444-53780-5.00004-1.
[27] A.A. Likhachev, A. Sozinov, K. Ullakko, Modeling the strain response , magneto-mechanical cycling under the external stress , work output and energy losses in Ni – Mn – Ga, 38 (2006) 551–563. https://doi.org/10.1016/j.mechmat.2005.05.022.
[28] E. Pagounis, R. Chulist, M.J. Szczerba, M. Laufenberg, Over 7% magnetic field-induced strain in a Ni-Mn-Ga five-layered martensite, Appl. Phys. Lett. 105 (2014). https://doi.org/10.1063/1.4892633.
[29] L. Zhou, M.M. Schneider, A. Giri, K. Cho, Y. Sohn, Microstructural and crystallographic characteristics of modulated martensite, non-modulated martensite, and pre-martensitic tweed austenite in Ni-Mn-Ga alloys, Acta Mater. 134 (2017) 93–103. https://doi.org/10.1016/j.actamat.2017.05.050.
[30] V.A. Chernenko, Compositional instability of β-phase in Ni-Mn-Ga alloys, Scr. Mater. 40 (1999) 523–527. https://doi.org/10.1016/S1359-6462(98)00494-1.
[31] D.C. Dunand, P. Müllner, Size effects on magnetic actuation in Ni-Mn-Ga shape-memory alloys, Adv. Mater. 23 (2011) 216–232. https://doi.org/10.1002/adma.201002753.
[32] T. Niendorf, F. Brenne, P. Krooß, M. Vollmer, J. Günther, D. Schwarze, H. Biermann, Microstructural Evolution and Functional Properties of Fe-Mn-Al-Ni Shape Memory Alloy Processed by Selective Laser Melting, Metall. Mater. Trans. A Phys. Metall. Mater. Sci. 47 (2016) 2569–2573. https://doi.org/10.1007/s11661-016-3412-z.
[33] Y. Boonyongmaneerat, M. Chmielus, D.C. Dunand, P. Müllner, Increasing magnetoplasticity in polycrystalline Ni-Mn-Ga by reducing internal constraints through porosity, Phys. Rev. Lett. 99 (2007) 14–17. https://doi.org/10.1103/PhysRevLett.99.247201.
[34] E. Stevens, K. Kimes, D. Salazar, A. Mostafaei, R. Rodriguez, A. Acierno, P. Lázpita, V. Chernenko, M. Chmielus, Mastering a 1.2 K hysteresis for martensitic para-ferromagnetic partial transformation in Ni-Mn(Cu)-Ga magnetocaloric material via binder jet 3D printing, Addit. Manuf. 37 (2021). https://doi.org/10.1016/j.addma.2020.101560.
[35] P.R. De Vecchis, A. Mostafaei, M. Chmielus, Densification Kinetics and Microstructural Evolution of Binder Jet Printed and Sintered Porous Ni-Mn-Ga Magnetic Shape-Memory Alloys, Acta Mater. (2023) 119323. https://doi.org/10.1016/j.actamat.2023.119323.
[36] U. Gaitzsch, R. Chulist, L. Weisheit, A. Böhm, W. Skrotzki, C.G. Oertel, H.G. Brokmeier, T. Lippmann, I. Navarro, M. Pötschke, J. Romberg, C. Hürrich, S. Roth, L. Schultz, Processing routes toward textured polycrystals in ferromagnetic shape memory alloys, Adv. Eng. Mater. 14 (2012) 636–652. https://doi.org/10.1002/adem.201200084.
[37] E. Flitcraft, P.R. De Vecchis, Effect of rapid solidification and post-processing on microstructure, magnetic and structural transition temperatures and magnetic properties in Ni50Mn29Ga21 magnetic shape-memory alloy, Acta Mater. (2023) 119325. https://doi.org/10.1016/j.actamat.2023.119325.
[38] A. Deltell, A.E.M.A. Mohamed, P. Álvarez-Alonso, M. Ipatov, J.P. Andrés, J.A. González, T. Sánchez, A. Zhukov, M.L. Escoda, J.J. Suñol, R. López Antón, Martensitic transformation, magnetic and magnetocaloric properties of Ni-Mn-Fe-Sn Heusler ribbons, J. Mater. Res. Technol. 12 (2021) 1091–1103. https://doi.org/10.1016/j.jmrt.2021.03.049.
[39] J. Emsley, The elements, Energy Explor. Exploit. 16 (5) (1998). https://doi.org/10.1177/014459879801600530.
[40] K. Ullakko, V. Laitinen, A. Saren, A. Sozinov, D. Musiienko, M. Chmielus, A. Salminen, Ni-Mn-Ga Actuating Elements Manufactured Using 3D Printing, 11th Eur. Symp. Martensitic Transform. (2018).

https://www.researchgate.net/publication/329556511_Ni-Mn-Ga_Actuating_Elements_Manufactured_Using_3D_Printing.
[41] V. Laitinen, A. Saren, A. Sozinov, K. Ullakko, Giant 5.8% magnetic-field-induced strain in additive manufactured Ni-Mn-Ga magnetic shape memory alloy, Scr. Mater. 208 (2021) 114324. https://doi.org/10.1016/j.scriptamat.2021.114324.
[42] J. Zou, Y. Gaber, G. Voulazeris, S. Li, L. Vazquez, L.F. Liu, M.Y. Yao, Y.J. Wang, M. Holynski, K. Bongs, M.M. Attallah, Controlling the grain orientation during laser powder bed fusion to tailor the magnetic characteristics in a Ni-Fe based soft magnet, Acta Mater. 158 (2018) 230–238. https://doi.org/10.1016/j.actamat.2018.07.064.
[43] A. Saren, V. Laitinen, M. Vinogradova, K. Ullakko, Twin boundary mobility in additive manufactured magnetic shape memory alloy 10M Ni-Mn-Ga, Acta Mater. 246 (2023) 118666. https://doi.org/10.1016/j.actamat.2022.118666.
[44] X. Wang, Y. Zhou, S. Wen, Y. Shi, Enhanced magnetic-field-induced strain of Ni-Mn-In alloy by altering laser scanning strategy during laser powder bed fusion, Mater. Lett. 349 (2023) 134740. https://doi.org/10.1016/j.matlet.2023.134740.
[45] P.K. Gokuldoss, S. Kolla, J. Eckert, Additive manufacturing processes: Selective laser melting, electron beam melting and binder jetting-selection guidelines, Materials (Basel). 10 (2017). https://doi.org/10.3390/ma10060672.
[46] S. Huang, W.Y. Yeong, Laser re-scanning strategy in selective laser melting for part quality enhancement: A review, Proc. Int. Conf. Prog. Addit. Manuf. 2018-May (2018) 413–419. https://doi.org/10.25341/D4GP4J.
[47] K.G. Prashanth, H. Shakur Shahabi, H. Attar, V.C. Srivastava, N. Ellendt, V. Uhlenwinkel, J. Eckert, S. Scudino, Production of high strength Al 85 Nd 8 Ni 5 Co 2 alloy by selective laser melting, Addit. Manuf. 6 (2015) 1–5. https://doi.org/10.1016/j.addma.2015.01.001.
[48] H. Meier, C. Haberland, Experimentelle Untersuchungen zum Laserstrahlgenerieren Metallischer Bauteile, Materwiss. Werksttech. 39 (2008) 665–670. https://doi.org/10.1002/mawe.200800327.
[49] K.G. Prashanth, S. Scudino, T. Maity, J. Das, J. Eckert, Is the energy density a reliable parameter for materials synthesis by selective laser melting?, Mater. Res. Lett. 5 (2017) 386–390. https://doi.org/10.1080/21663831.2017.1299808.
[50] L. Thijs, F. Verhaeghe, T. Craeghs, J. Van Humbeeck, J.P. Kruth, A study of the microstructural evolution during selective laser melting of Ti-6Al-4V, Acta Mater. 58 (2010) 3303–3312. https://doi.org/10.1016/j.actamat.2010.02.004.
[51] X. Wang, K. Chou, Electron Backscatter Diffraction Analysis of Inconel 718 Parts Fabricated by Selective Laser Melting Additive Manufacturing, Jom. 69 (2017) 402–408. https://doi.org/10.1007/s11837-016-2198-1.
[52] N. Nadammal, S. Cabeza, T. Mishurova, T. Thiede, A. Kromm, C. Seyfert, L. Farahbod, C. Haberland, J.A. Schneider, P.D. Portella, G. Bruno, Effect of hatch length on the development of microstructure, texture and residual stresses in selective laser melted superalloy Inconel 718, Mater. Des. 134 (2017) 139–150. https://doi.org/10.1016/j.matdes.2017.08.049.
[53] F. Liu, X. Lin, C. Huang, M. Song, G. Yang, J. Chen, W. Huang, The effect of laser scanning path on microstructures and mechanical properties of laser solid formed nickel-base superalloy Inconel 718, J. Alloys Compd. 509 (2011) 4505–4509. https://doi.org/10.1016/j.jallcom.2010.11.176.
[54] J. Toman, D.C. Pagan, P. Müllner, M. Chmielus, Epitaxial re-solidification of laser-melted Ni-Mn-Ga single crystal, Acta Mater. 219 (2021) 117236. https://doi.org/10.1016/j.actamat.2021.117236.
[55] D.L. Schlagel, Y.L. Wu, W. Zhang, T.A. Lograsso, Chemical segregation during bulk single crystal preparation of Ni-Mn-Ga ferromagnetic shape memory alloys, J. Alloys Compd. 312 (2000) 77–85. https://doi.org/10.1016/S0925-8388(00)01161-0.
[56] V. Laitinen, A. Sozinov, A. Saren, M. Chmielus, K. Ullakko, Characterization of as-built and heat-treated Ni-Mn-Ga magnetic shape memory alloy manufactured via laser powder bed fusion, Addit. Manuf. 39 (2021) 101854. https://doi.org/10.1016/j.addma.2021.101854.
[57] S. Palanivel, A.K. Dutt, E.J. Faierson, R.S. Mishra, Materials Science & Engineering A Spatially dependent properties in a laser additive manufactured Ti – 6Al – 4V component, 654 (2016) 39–52. https://doi.org/10.1016/j.msea.2015.12.021.
[58] K. Safaei, M. Nematollahi, P. Bayati, F. Kordizadeh, M.T. Andani, H. Abedi, B. Poorganji, M. Elahinia, On the crystallographic texture and torsional behavior of NiTi shape memory alloy processed by laser powder bed fusion: Effect of build orientation, Addit. Manuf. 59 (2022) 103184. https://doi.org/10.1016/j.addma.2022.103184.
[59] H. Jia, B. Liu, Z. Zhao, S. Duan, P. Wang, H. Lei, Experimental investigation and numerical modeling of laser powder bed fusion process-induced angle-dependent defects in strut-based lattice structure, Mater. Des. 224 (2022) 111354. https://doi.org/10.1016/j.matdes.2022.111354.

[60] S. Murchio, M. Dallago, F. Zanini, S. Carmignato, G. Zappini, F. Berto, D. Maniglio, M. Benedetti, Additively manufactured Ti–6Al–4V thin struts via laser powder bed fusion: Effect of building orientation on geometrical accuracy and mechanical properties, J. Mech. Behav. Biomed. Mater. 119 (2021) 104495. https://doi.org/10.1016/j.jmbbm.2021.104495.
[61] P. Delroisse, P.J. Jacques, E. Maire, O. Rigo, A. Simar, Scripta Materialia Effect of strut orientation on the microstructure heterogeneities in AlSi10Mg lattices processed by selective laser melting, Scr. Mater. 141 (2017) 32–35. https://doi.org/10.1016/j.scriptamat.2017.07.020.
[62] N. Takata, H. Kodaira, A. Suzuki, M. Kobashi, Materials Characterization Size dependence of microstructure of AlSi10Mg alloy fabricated by selective laser melting, Mater. Charact. 143 (2018) 18–26. https://doi.org/10.1016/j.matchar.2017.11.052.
[63] A. Leicht, U. Klement, E. Hryha, Effect of build geometry on the microstructural development of 316L parts produced by additive manufacturing, Mater. Charact. 143 (2018) 137–143. https://doi.org/10.1016/j.matchar.2018.04.040.
[64] S.Y. Ahn, E.S. Kim, G.M. Karthik, K.R. Ramkumar, S.G. Jeong, R.E. Kim, G.H. Gu, H.S. Kim, Thickness effect on the microstructures, mechanical properties, and anisotropy of laser-powder bed fusion processed 316L stainless steel, J. Mater. Sci. 57 (2022) 18101–18117. https://doi.org/10.1007/s10853-022-07516-x.
[65] X. Wang, J.A. Muñiz-Lerma, O. Sánchez-Mata, M. Attarian Shandiz, M. Brochu, Microstructure and mechanical properties of stainless steel 316L vertical struts manufactured by laser powder bed fusion process, Mater. Sci. Eng. A. 736 (2018) 27–40. https://doi.org/10.1016/j.msea.2018.08.069.
[66] X. Wang, J.A. Muñiz-Lerma, O. Sanchez-Mata, M. Attarian Shandiz, N. Brodusch, R. Gauvin, M. Brochu, Characterization of single crystalline austenitic stainless steel thin struts processed by laser powder bed fusion, Scr. Mater. 163 (2019) 51–56. https://doi.org/10.1016/j.scriptamat.2018.12.032.
[67] O. Sanchez-Mata, X. Wang, J.A. Muñiz-Lerma, S.E. Atabay, M. Attarian Shandiz, M. Brochu, Characterization of the microstructure and mechanical properties of highly textured and single crystal Hastelloy X thin struts fabricated by laser powder bed fusion, J. Alloys Compd. 901 (2022) 163465. https://doi.org/10.1016/j.jallcom.2021.163465.
[68] P. Peyre, J. Rodrigues, D. Silva, M. Dal, Size and build strategy effects for the L-PBF process applied to Inconel 625 vertical struts : a combined numerical and experimental approach, 2024.
[69] T. Niendorf, F. Brenne, Communication Lattice Structures Manufactured by SLM : On the Effect of Geometrical Dimensions on Microstructure Evolution During Processing, 45 (2014) 1181–1185. https://doi.org/10.1007/s11663-014-0086-z.
[70] P. Müllner, V.A. Chernenko, M. Wollgarten, G. Kostorz, Large cyclic deformation of a Ni-Mn-Ga shape memory alloy induced by magnetic fields, J. Appl. Phys. 92 (2002) 6708–6713. https://doi.org/10.1063/1.1513875.
[71] L. Straka, O. Heczko, Magnetic anisotropy in Ni-Mn-Ga martensites, J. Appl. Phys. 93 (2003) 8636–8638. https://doi.org/10.1063/1.1555982.
[72] R.D. James, K.F. Hane, Martensitic transformations and shape-memory materials, Acta Mater. 48 (2000) 197–222. https://doi.org/10.1016/S1359-6454(99)00295-5.
[73] B. Kiefer, D.C. Lagoudas, Magnetic field-induced martensitic variant reorientation in magnetic shape memory alloys, Philos. Mag. 85 (2005) 4289–4329. https://doi.org/10.1080/14786430500363858.
[74] M. Veligatla, P. Lindquist, C.J. Garcia-Cervera, P. Mullner, Energy conversion in Ni-Mn-Ga with asymmetrical bias magnetic field, J. Magn. Magn. Mater. 551 (2022) 169183. https://doi.org/10.1016/j.jmmm.2022.169183.
[75] J. Wang, Z. Zhang, Variant reorientation in a single-crystalline Ni–Mn-Ga sample induced by a quasi-static rotating magnetic field: Mechanism analyses based on configurational forces, J. Alloys Compd. 825 (2020) 153940. https://doi.org/10.1016/j.jallcom.2020.153940.
[76] M. Support, Minitab support - Analysis of Variance table for One-Way ANOVA, (2023). https://support.minitab.com/en-us/minitab/21/help-and-how-to/statistical-modeling/anova/how-to/one-way-anova/interpret-the-results/all-statistics-and-graphs/analysis-of-variance-table/#:~:text=The total degrees of freedom,much information that term uses.
[77] V. Laitinen, Laser powder bed fusion for the manufacture of Ni-Mn-Ga magnetic shape memory alloy actuators, 2021.
[78] M. Vinogradova, A. Sozinov, L. Straka, P. Veřtát, O. Heczko, M. Zelený, R. Chulist, E. Lähderanta, K. Ullakko, Constant plane shift model: Structure analysis of martensitic phases in Ni50Mn27Ga22Fe1 beyond non-modulated building blocks, Acta Mater. 255 (2023). https://doi.org/10.1016/j.actamat.2023.119042.
[79] J. Blaber, B. Adair, A. Antoniou, Ncorr: Open-Source 2D Digital Image Correlation Matlab Software, Exp. Mech. 55 (2015) 1105–1122. https://doi.org/10.1007/s11340-015-0009-1.
[80] A. Milleret, V. Laitinen, K. Ullakko, N. Fenineche, M.M. Attallah, Laser powder bed fusion of (14 M)

Ni-Mn-Ga magnetic shape memory alloy lattices, Addit. Manuf. 60 (2022) 1–14. https://doi.org/10.1016/j.addma.2022.103231.
[81] A. Milleret, 4D printing of Ni–Mn–Ga magnetic shape memory alloys: a review, Mater. Sci. Technol. (2022) 1–14. https://doi.org/10.1080/02670836.2022.2062655.
[82] U. Gaitzsch, J. Drache, K. McDonald, P. Müllner, P. Lindquist, Obtaining of Ni-Mn-Ga magnetic shape memory alloy by annealing electrochemically deposited Ga/Mn/Ni layers, Thin Solid Films. 522 (2012) 171–174. https://doi.org/10.1016/j.tsf.2012.08.019.
[83] P. Zheng, P. Lindquist, B. Yuan, P. Müllner, D.C. Dunand, Fabricating Ni-Mn-Ga microtubes by diffusion of Mn and Ga into Ni tubes, Intermetallics. 49 (2014) 70–80. https://doi.org/10.1016/j.intermet.2014.01.014.
[84] M.S. Knieps, W.J. Reynolds, J. Dejaune, A.T. Clare, A. Evirgen, In-situ alloying in powder bed fusion: The role of powder morphology, Mater. Sci. Eng. A. 807 (2021) 140849. https://doi.org/10.1016/j.msea.2021.140849.
[85] S. Ewald, F. Kies, S. Hermsen, M. Voshage, C. Haase, J.H. Schleifenbaum, Rapid Alloy Development of Extremely High-Alloyed Bed Fusion, Materials (Basel). (2019) 1–15.
[86] A. Milleret, V. Laitinen, K. Ullakko, N. Fenineche, M.M. Attallah, Laser powder bed fusion of (14 M) Ni-Mn-Ga magnetic shape memory alloy lattices, Addit. Manuf. 60 (2022) 103231. https://doi.org/10.1016/j.addma.2022.103231.
[87] W.M. Haynes, CRC Handbook of Chemistry and Physics. 97th Edition, 1942.
[88] D. Musiienko, A. Saren, L. Straka, M. Vronka, J. Kopeček, O. Heczko, A. Sozinov, K. Ullakko, Ultrafast actuation of Ni-Mn-Ga micropillars by pulsed magnetic field, Scr. Mater. 162 (2019) 482–485. https://doi.org/10.1016/j.scriptamat.2018.12.009.
[89] N. Lanska, O. Söderberg, A. Sozinov, Y. Ge, K. Ullakko, V.K. Lindroos, Composition and temperature dependence of the crystal structure of Ni-Mn-Ga alloys, J. Appl. Phys. 95 (2004) 8074–8078. https://doi.org/10.1063/1.1748860.
[90] V. Laitinen, M. Merabtene, E. Stevens, M. Chmielus, J. Van Humbeeck, K. Ullakko, Additive Manufacturing from the Point of View of Materials Research, Tech. Econ. Soc. Eff. Manuf. 4.0. (2020) 43–83. https://doi.org/10.1007/978-3-030-46103-4_3.
[91] B. Attard, A.E.-M.A. Mohamed, M.M. Attallah, New materials development, Fundam. Laser Powder Bed Fusion Met. (2021) 529–562. https://doi.org/10.1016/B978-0-12-824090-8.00025-1.
[92] Q. Zhong, K. Wei, T. Ouyang, X. Li, X. Zeng, Effect of rotation angle on surface morphology, microstructure, and mechanical properties of Inconel 718 alloy fabricated by high power laser powder bed fusion, J. Mater. Sci. Technol. 154 (2023) 30–42. https://doi.org/10.1016/j.jmst.2023.01.021.
[93] M. Leary, Design for additive manufacturing, Des. Addit. Manuf. (2019). https://doi.org/10.1016/C2017-0-04238-6.
[94] A. Çakir, L. Righi, F. Albertini, M. Acet, M. Farle, S. Aktürk, Extended investigation of intermartensitic transitions in Ni-Mn-Ga magnetic shape memory alloys: A detailed phase diagram determination, J. Appl. Phys. 114 (2013). https://doi.org/10.1063/1.4831667.
[95] O. Heczko, L. Straka, Temperature dependence and temperature limits of magnetic shape memory effect, J. Appl. Phys. 94 (2003) 7139–7143. https://doi.org/10.1063/1.1626800.
[96] D. Musiienko, F. Nilsén, A. Armstrong, M. Rameš, P. Veřtát, R.H. Colman, J. Čapek, P. Müllner, O. Heczko, L. Straka, Effect of crystal quality on twinning stress in Ni–Mn–Ga magnetic shape memory alloys, J. Mater. Res. Technol. 14 (2021) 1934–1944. https://doi.org/10.1016/j.jmrt.2021.07.081.
[97] A.G. Demir, P. Colombo, B. Previtali, From pulsed to continuous wave emission in SLM with contemporary fiber laser sources: effect of temporal and spatial pulse overlap in part quality, Int. J. Adv. Manuf. Technol. 91 (2017) 2701–2714. https://doi.org/10.1007/s00170-016-9948-7.
[98] J. Kim, S. Ji, Y.-S. Yun, J.-S. Yeo, A Review: Melt Pool Analysis for Selective Laser Melting with Continuous Wave and Pulse Width Modulated Lasers, Appl. Sci. Converg. Technol. 27 (2018) 113–119. https://doi.org/10.5757/asct.2018.27.6.113.
[99] C.A. Biffi, J. Fiocchi, P. Bassani, A. Tuissi, Continuous wave vs pulsed wave laser emission in selective laser melting of AlSi10Mg parts with industrial optimized process parameters: Microstructure and mechanical behaviour, Addit. Manuf. 24 (2018) 639–646. https://doi.org/10.1016/j.addma.2018.10.021.
[100] N. Scheerbaum, O. Heczko, J. Liu, D. Hinz, L. Schultz, O. Gutfleisch, Magnetic field-induced twin boundary motion in polycrystalline Ni-Mn-Ga fibres, New J. Phys. 10 (2008). https://doi.org/10.1088/1367-2630/10/7/073002.
[101] P. Zheng, N.J. Kucza, Z. Wang, P. Müllner, D.C. Dunand, Effect of directional solidification on texture and magnetic-field-induced strain in Ni-Mn-Ga foams with coarse grains, Acta Mater. 86 (2015) 95–101. https://doi.org/10.1016/j.actamat.2014.12.005.
[102] Z. Li, B. Yang, N. Zou, Y. Zhang, C. Esling, W. Gan, X. Zhao, L. Zuo, Crystallographic characterization on polycrystalline Ni-Mn-Ga alloys with strong preferred orientation, Materials (Basel).

10 (2017) 1–20. https://doi.org/10.3390/ma10050463.
[103] T. Niendorf, S. Leuders, A. Riemer, H.A. Richard, T. Tröster, D. Schwarze, Highly anisotropic steel processed by selective laser melting, Metall. Mater. Trans. B Process Metall. Mater. Process. Sci. 44 (2013) 794–796. https://doi.org/10.1007/s11663-013-9875-z.
[104] K. Kempen, L. Thijs, B. Vrancken, S. Buls, J. Van Humbeeck, J.-P. Kruth, Application of base plate preheating during selective laser melting, (2013).
[105] I.A. Roberts, INVESTIGATION OF RESIDUAL STRESSES IN THE LASER MELTING OF METAL POWDERS IN ADDITIVE LAYER, Thesis. (2012).
[106] M. Shiomi, K. Osakada, K. Nakamura, T. Yamashita, F. Abe, Residual stress within metallic model made by selective laser melting process, CIRP Ann. - Manuf. Technol. 53 (2004) 195–198. https://doi.org/10.1016/S0007-8506(07)60677-5.
[107] R. Mertens, S. Dadbakhsh, J. Van Humbeeck, J. Kruth, Application of base plate preheating during selective laser melting, Procedia CIRP. 74 (2018) 5–11. https://doi.org/10.1016/j.procir.2018.08.002.
[108] N.T. Aboulkhair, N.M. Everitt, I. Ashcroft, C. Tuck, Reducing porosity in AlSi10Mg parts processed by selective laser melting, Addit. Manuf. 1 (2014) 77–86. https://doi.org/10.1016/j.addma.2014.08.001.
[109] M.A. Obeidi, A. Conway, A. Mussatto, M.N. Dogu, S.P. Sreenilayam, H. Ayub, I.U. Ahad, D. Brabazon, Effects of powder compression and laser re-melting on the microstructure and mechanical properties of additively manufactured parts in laser-powder bed fusion, Results Mater. 13 (2022) 100264. https://doi.org/10.1016/j.rinma.2022.100264.
[110] P. Krakhmalev, I. Yadroitsava, G. Fredriksson, I. Yadroitsev, In situ heat treatment in selective laser melted martensitic AISI 420 stainless steels, Mater. Des. 87 (2015) 380–385. https://doi.org/10.1016/j.matdes.2015.08.045.
[111] J.P. Kruth, J. Deckers, E. Yasa, R. Wauthlé, Assessing and comparing influencing factors of residual stresses in selective laser melting using a novel analysis method, Proc. Inst. Mech. Eng. Part B J. Eng. Manuf. 226 (2012) 980–991. https://doi.org/10.1177/0954405412437085.
[112] E. Yasa, J. Deckers, J.P. Kruth, The investigation of the influence of laser re-melting on density, surface quality and microstructure of selective laser melting parts, Rapid Prototyp. J. 17 (2011) 312–327. https://doi.org/10.1108/13552541111156450.
[113] E. Yasa, J.P. Kruth, Microstructural investigation of selective laser melting 316L stainless steel parts exposed to laser re-melting, Procedia Eng. 19 (2011) 389–395. https://doi.org/10.1016/j.proeng.2011.11.130.
[114] P. Promoppatum, B. Chayasombat, A. Nyein Soe, A. Sombatmai, Y. Sato, T. Suga, M. Tsukamoto, In-situ modification of thermal, microstructural, and mechanical responses by altering scan lengths in laser powder bed fusion additive manufacturing of Ti-6Al-4V, Opt. Laser Technol. 164 (2023) 109525. https://doi.org/10.1016/j.optlastec.2023.109525.
[115] I. Aaltio, A. Soroka, Y. Ge, O. Söderberg, S.P. Hannula, High-cycle fatigue of 10M Ni-Mn-Ga magnetic shape memory alloy in reversed mechanical loading, Smart Mater. Struct. 19 (2010). https://doi.org/10.1088/0964-1726/19/7/075014.
[116] L. Straka, O. Heczko, H. Seiner, N. Lanska, J. Drahokoupil, A. Soroka, S. Fähler, H. Hänninen, A. Sozinov, Highly mobile twinned interface in 10 M modulated Ni-Mn-Ga martensite: Analysis beyond the tetragonal approximation of lattice, Acta Mater. 59 (2011) 7450–7463. https://doi.org/10.1016/j.actamat.2011.09.020.
[117] N. Zou, Z. Li, Y. Zhang, B. Yang, X. Zhao, C. Esling, L. Zuo, Plastic deformation of Ni–Mn–Ga 7M modulated martensite by twinning & detwinning and intermartensitic transformation, Int. J. Plast. 100 (2018) 1–13. https://doi.org/10.1016/j.ijplas.2017.07.006.
[118] M. Chmielus, C. Witherspoon, R.C. Wimpory, A. Paulke, A. Hilger, X. Zhang, D.C. Dunand, P. Müllner, Magnetic-field-induced recovery strain in polycrystalline Ni-Mn-Ga foam, J. Appl. Phys. 108 (2010). https://doi.org/10.1063/1.3524503.
[119] P. Zheng, N.J. Kucza, C.L. Patrick, P. Müllner, D.C. Dunand, Mechanical and magnetic behavior of oligocrystalline Ni-Mn-Ga microwires, J. Alloys Compd. 624 (2015) 226–233. https://doi.org/10.1016/j.jallcom.2014.11.067.
[120] M.F. Ashby, The properties of foams and lattices, Philos. Trans. R. Soc. A Math. Phys. Eng. Sci. 364 (2006) 15–30. https://doi.org/10.1098/rsta.2005.1678.
[121] L.J. Gibson, M.F. Ashby, Cellular solids: Structure and, 1997. https://doi.org/10.1016/0021-9290(89)90056-0.
[122] S. Zhou, H. Liu, J. Ma, X. Yang, Deformation behaviors and energy absorption characteristics of a hollow re-entrant auxetic lattice metamaterial, Aerosp. Sci. Technol. 1 (n.d.) 108583. https://doi.org/10.1016/j.ast.2023.108583.
[123] H. Gu, A. Shterenlikht, M. Pavier, Brittle fracture of three- dimensional lattice structure, Eng. Fract. Mech. 219 (2019).

[124] C. Qiu, S. Yue, N.J.E. Adkins, M. Ward, H. Hassanin, P.D. Lee, P.J. Withers, M.M. Attallah, Influence of processing conditions on strut structure and compressive properties of cellular lattice structures fabricated by selective laser melting, Mater. Sci. Eng. A. 628 (2015) 188–197. https://doi.org/10.1016/j.msea.2015.01.031.
[125] S. McKown, Y. Shen, W.K. Brookes, C.J. Sutcliffe, W.J. Cantwell, G.S. Langdon, G.N. Nurick, M.D. Theobald, The quasi-static and blast loading response of lattice structures, Int. J. Impact Eng. 35 (2008) 795–810. https://doi.org/10.1016/j.ijimpeng.2007.10.005.
[126] X. Liu, T. Wada, A. Suzuki, N. Takata, M. Kobashi, M. Kato, Understanding and suppressing shear band formation in strut-based lattice structures manufactured by laser powder bed fusion, Mater. Des. 199 (2021) 109416. https://doi.org/10.1016/j.matdes.2020.109416.
[127] S.Y. Choy, C.N. Sun, K.F. Leong, J. Wei, Compressive properties of Ti-6Al-4V lattice structures fabricated by selective laser melting: Design, orientation and density, Addit. Manuf. 16 (2017) 213–224. https://doi.org/10.1016/j.addma.2017.06.012.
[128] Y.K. Gao, Auxetic metamaterials and structures, Cailiao Gongcheng/Journal Mater. Eng. 49 (2021) 38–47. https://doi.org/10.11868/j.issn.1001-4381.2019.000391.
[129] H.M.A. Kolken, A.F. Garcia, A. Du Plessis, A. Meynen, C. Rans, L. Scheys, M.J. Mirzaali, A.A. Zadpoor, Mechanisms of fatigue crack initiation and propagation in auxetic meta-biomaterials, Acta Biomater. 138 (2022) 398–409. https://doi.org/10.1016/j.actbio.2021.11.002.
[130] S. Li, H. Hassanin, M.M. Attallah, N.J.E. Adkins, K. Essa, The development of TiNi-based negative Poisson's ratio structure using selective laser melting, Acta Mater. 105 (2016) 75–83. https://doi.org/10.1016/j.actamat.2015.12.017.
[131] R.S. Lakes, Foam Structures with a Negative Poisson's Ratio, Science (80-.). 435 (1987) 0–2. https://doi.org/10.1126/science.235.4792.1038.
[132] L. Yang, O. Harrysson, H. West, D. Cormier, Compressive properties of Ti-6Al-4V auxetic mesh structures made by electron beam melting, Acta Mater. 60 (2012) 3370–3379. https://doi.org/10.1016/j.actamat.2012.03.015.
[133] U. Gaitzsch, M. Pötschke, S. Roth, B. Rellinghaus, L. Schultz, A 1% magnetostrain in polycrystalline 5M Ni-Mn-Ga, Acta Mater. 57 (2009) 365–370. https://doi.org/10.1016/j.actamat.2008.09.017.
[134] L. Zhou, A. Giri, K. Cho, Y. Sohn, Mechanical anomaly observed in Ni-Mn-Ga alloys by nanoindentation, Acta Mater. 118 (2016) 54–63. https://doi.org/10.1016/j.actamat.2016.07.029.
[135] C. Liu, Z.Y. Gao, X. An, H.B. Wang, L.X. Gao, W. Cai, Surface characteristics and nanoindentation study of Ni-Mn-Ga ferromagnetic shape memory sputtered thin films, Appl. Surf. Sci. 254 (2008) 2861–2865. https://doi.org/10.1016/j.apsusc.2007.10.031.
[136] C. Fizanne-Michel, M. Cornen, P. Castany, I. Péron, T. Gloriant, Determination of hardness and elastic modulus inverse pole figures of a polycrystalline commercially pure titanium by coupling nanoindentation and EBSD techniques, Mater. Sci. Eng. A. 613 (2014) 159–162. https://doi.org/10.1016/j.msea.2014.06.098.
[137] A. Sozinov, N. Lanska, A. Soroka, W. Zou, 12% magnetic field-induced strain in Ni-Mn-Ga-based non-modulated martensite, Appl. Phys. Lett. 102 (2013). https://doi.org/10.1063/1.4775677.
[138] B. Attard, S. Cruchley, C. Beetz, M. Megahed, Y.L. Chiu, M.M. Attallah, Microstructural control during laser powder fusion to create graded microstructure Ni-superalloy components, Addit. Manuf. 36 (2020) 101432. https://doi.org/10.1016/j.addma.2020.101432.